Kinetics and Mechanism of Phase-Transfer Catalysed Fluorination

Yuan Gao

Doctor of Philosophy

The University of Edinburgh

2024

Abstract

Phase-transfer catalysis (PTC) enormously enhances the reaction rate between reagents located in immiscible phases. The main advantages of PTC are mild reaction conditions, inexpensive reagents, and simple work-up, which lead to the possibility of large-scale production, and make PTC appealing to industrial applications. However, due to the inherent challenges associated with monitoring a heterogeneous system *in situ*, there is a lack of mechanistic investigation on PTC and most of the efficient phase-transfer catalysts have been developed by trial and error, which restricts their applications. To address this, a plunger-based *in-situ* mixing device has been designed and developed, which is portable and can be easily adapted to any NMR spectrometer to enable *in-situ* reaction monitoring of heterogeneous reaction that requires agitation. The effect of key parameters, such as plunger type, mixing speed and settling time on the mixing efficiency and spectral resolution was explored to guide the selection of optimum settings. The robustness of this system was demonstrated by measuring the kinetics for a range of reactions and comparison of these with that obtained by conventional *ex-situ* monitoring method.

The reaction mechanism of a novel phase-transfer catalysed asymmetric nucleophilic fluorination developed by the Gouverneur group in 2018 has then been investigated using extensive reaction monitoring by both *in-situ* and *ex-situ* ^{19}F NMR spectroscopy followed by kinetic modelling. Formation of substrate-alkylated catalyst was identified and supported by degradation experiment and ESI-MS. Its catalytic activity varied between catalysts. Two pathways of fluorine delivery were identified, and incorporation of both was essential to correctly simulate the reaction evolution from low to high catalyst loadings. The rate of ionisation of substrate, β-bromosulfide, was measured by magnetisation transfer, and both catalysts were found to accelerate this process by more than two orders of magnitude. The fluorination of β-chloramine was enabled by the same type of catalyst. Its mechanism has been explored using similar approaches and compared with that of β-bromosulfide. In this case, the formation of substrate-alkylated catalyst was much less pronounced, the catalysts had negligible effects on the rate of ionisation of substrate, and a simpler catalytic cycle has been proposed. Understanding these fluorinations provides useful insights for further optimisation of catalysts and mechanistic studies of similar reactions. Furthermore, the development of the mixing device will promote mechanistic investigations of PTC reactions in general.

Lay summary

Phase-transfer catalysis (PTC) helps speed up reaction between substances that do not mix. It is popular in industrial processes because it uses cheap substances, works under mild conditions, and is easy to scale up. However, it is difficult to study how PTC works because the reaction involves different substances that don't naturally mix well, and without stirring, the reaction slows down or even stops. As a result, many PTC methods have been developed through trial and error, limiting their effectiveness.

To solve this issue, our group developed a mixing device that allows reactions to be mixed well within a constrained place. This device can be used with NMR spectroscopy, a powerful tool that helps scientists observe how molecules change and measure their amount. A range of tests were conducted to ensure the device is reliable. After that, this device was used to study a reaction that produces a fluorinated compound. Fluorinated compounds are very useful and can be found in things like packaging, medicines, and batteries. With the help of the mixing device, NMR spectroscopy and other techniques, we explained and compared the role of the catalysts in two similar fluorinations. This better understanding can help chemists make these fluorinations more efficient and improve the design of similar reactions. Additionally, the mixing device can make studying other PTC reactions easier.

Acknowledgements

It is my tenth year in the UK, and I certainly did not expect to stay this long when I started my undergraduate studies in Durham. I am very lucky to be surrounded by people who are extremely friendly, smart, and have great passion for life and/or for research. Their passion is infectious and sparks my life here.

First, I would like to thank my master supervisor, Prof. AnnMarie O'Donoghue, who introduced me to the beauty of catalysis and mechanism and encouraged me to apply for a PhD. I would like to thank Prof. Guy Lloyd-Jones, who is a fine mentor, knowledgeable, supportive, and very generous about his time. He lets me freely explore the project, while provides me with insightful suggestions when I needed. It has been a delight to work with him. I would like to thank Lloyd Mitchell, George Steadman, and Stuart Johnstone for all the technical support they provided me throughout the years.

I would like to extend my appreciation to the Lloyd-Jones research group, both present and past members --- they feel more like a family rather than colleagues. I still remember the day that I first visited the group, Dr Havey Dale and Dr Hannah Hayes showed me around the city and mentioned the ‘a little bit early’ 8 am group meetings. I would like to thank Dr Andrés García-Domínguez for multiple techniques he has trained me and all the pep talks, Dr Andrew Hall for patiently explaining the basic of NMR and sharing fun facts, Dr Patrick Boaler for being a kinetic expert and always willing to help, Dr Yael Ben-Tal for being a solid board game buddy, Dr Maciej Kucharski for having a special touch of humours, Dr Ran Wei for being vivid and optimistic, Dr Katie Grant for her caring heart and ability to finding everything in internet or anyone in Edinburgh, Pedro Helou de Oliveira for being a such a good lab neighbour and a late night lab buddy, Dr Nicole Fohn for all the supportive chats and hugs, Hannah Minshull for being thoughtful and organising events. I would also like to thank Dr Lukas Hoff, Dr Christina Wartmann, Chen Li, Annabel Flook, Roisin O'Dea, and Ben Grills. It has been a pleasure working with you.

I would also like to thank my friends, Dr Chunchun Ye, for being such a nice flatmate and being one of the few people who sharing the love for bread with me, to Jiayi Wu and Xuerui Yi, for many relaxing times that we spent together.

Finally, I would like to thank my parents, Fei Gao and Chunmin Zhao, for their constant support and everlasting love. It is hard to imagine how much effort you have put in to allow me the freedom to choose my lifestyle and become who I am today. I would like to thank my husband, Dr Tianren Xie, who always sees the best in me, accompanies me when I feel blue, encourages me when I feel down. I would like to thank my son, Yian Xie, who, though he cannot speak yet, has already brought immense joy and laughter into my life.

Abbreviations

BINAP	2,2'-bis(diphenylphosphino)-1,1'-binaphthyl
BTB	bromothymol blue
DAST	diethylaminosulfur trifluoride
DBFOX	dibenzofuran-4,6-bis(oxazoline)
DBU	1,8-diazabicyclo(5.4.0)undec-7-ene
DCM	dichloromethane
DFT	density functional theory
e.r.	enantiomeric ratio
ee	enantiomeric excess
ESI	electrospray ionization
ETFE	ethylene tetrafluoroethylene
FID	free induction decay
FWHM	full width at half maximum
glyme	dimethoxyethane
HPLC	high-performance liquid chromatography
ID	inner diameter
IR	infrared
mol%	mole percentage
MR-SHARPER	multiple resonance SHARPER
MS	mass spectra
MTBE	methyl-*tert*-butyl ether
NFSI	*N*-fluorobenzene-sulfonimide

NLE	non-linear effect
NMR	nuclear magnetic resonance
OD	outside diameter
PEEK	polyetheretherketone
PET	positron emission tomography
PT	phase-transfer
PTC	phase-transfer catalysis
PTFE	polytetrafluoroethylene
rpm	revolutions per minute
sel	selective
SHARPER	sensitive, homogeneous, and resolved peaks in real time
SPFGSE	single-pulsed field gradient spin-echo
TBAF	tetrabutylammonium fluoride
TTL	transistor-transistor logic
UV-Vis	ultraviolet and visible

Table of Contents

1. Introduction

1.1 Phase-transfer catalysis

Phase-transfer catalysis (PTC) enhances the rate of reaction by bringing reagents in different phases into proximity. It is a versatile tool for organic synthesis and has been applied in a variety of reactions such as alkylation,[1] cyclisation,[2] oxidation,[3] and asymmetric reactions.[4,5] This strategy commonly features mild reaction conditions, inexpensive reagents, and simple work-up, leading to the possibility of large-scale production and has therefore found applications in many industrial processes, including manufacturing of pharmaceuticals, agrichemicals, additives, dyes, and polymers.[6–8] Pioneering works done by Stark, Makosza, and Brändström in late 1960s laid the foundation of PTC, [9–13] which was first introduced as a concept in 1971, whereas the Reactions between reagents that are located in immiscible phases are frequently inhibited. One common way to enable these reactions is to find a mutual solvent, which can be expensive and is not always feasible. Alternatively, phase-transfer (PT) catalyst acts like a shuttle bus. It promotes these reactions by continually delivering one reagent as an active species to the other phase or the interface of two phases, where reactions can occur. One example is the cyanation of 1-chloro-octane (**Scheme 1.1**).[14] Without catalyst, no product was observed after several days of mixing, whereas addition of 1 mol% of quaternary ammonium salt (QCl) led to 100% yield within two hours. The key for this rate enhancement is the formation of an ammonium cyanide ion pair (QCN), which makes cyanide soluble in the organic phase and nucleophilic enough for the following displacement reaction. QCl is regenerated upon product formation and the catalytic cycle continues.

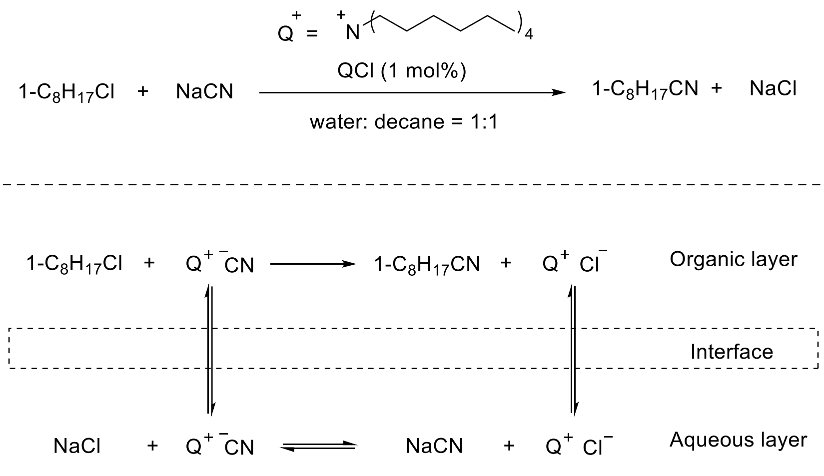

Scheme 1.1. Quaternary ammonium salt catalysed cyanation.

1.1.1 Classification and general mechanisms

PTC reactions are generally classified by the solubility of the catalyst and the nature of the phases (**Figure 1.1**).[8] While early examples use soluble PT catalysts with biphasic systems, insoluble catalysts were soon developed to enable easy separation and recovery of catalyst.[15–18] The catalyst is either immobilised on a solid support (LSLPTC) or concentrated in dense layer between two phases (TLPTC). Typical PTC involves transportation of anions to the organic phase, but there are also PT catalysts transporting reagents into the aqueous phase[19,20] and transporting of cations [21,22], which are termed inverse and reverse PTC respectively.

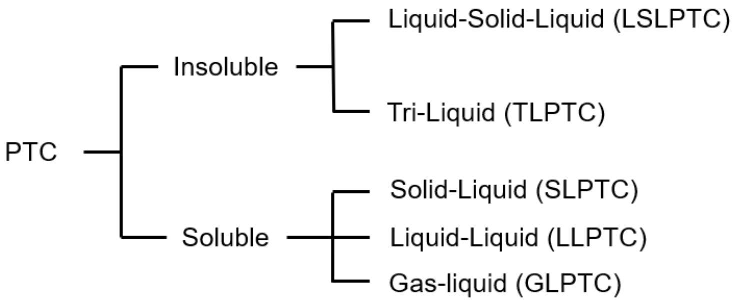

Figure 1.1. Classification of PTC.

Two general mechanisms have been proposed for PTC: the extractive type and the interface type (**Scheme 1.2**). Here, a Liquid-Liquid biphasic system is used as an example, but similar mechanisms can be adapted to other systems, e.g. the aqueous layer can instead be solid or gas phase. Both mechanisms involve the formation of catalytically active species between the PT catalyst (Q^+) and the anion of the inorganic salt (Y^-), which then reacts with the substrate (RX) in the organic phase to form product (RY). The main distinction between the two mechanisms is the solubility of the transferred species. In the extractive type, Q^+Y^- is partitioned between both organic and aqueous phases, whereas in the interface type, Q^+Y^- is only dissolvable in the organic phase and the ion exchange occurs in the interface layer. In practice, a combined mechanism is frequently observed, i.e. the reaction occurs both in the bulk and in the interface, but one can be dominant.[23,24] For example, the cyanation shown in **Scheme 1.1** is widely accepted to be described by extractive mechanism. The rate of cyanation is affected by the hydration energy of X^- (Cl^-) and Y^- (CN^-): much slower rates were observed when alkyl iodide was used instead of chloride, as a consequence of the lower hydration energy of iodide anions. In general, alkylation, esterification, and simple displacement reaction follow the extractive mechanism.

Extractive type:

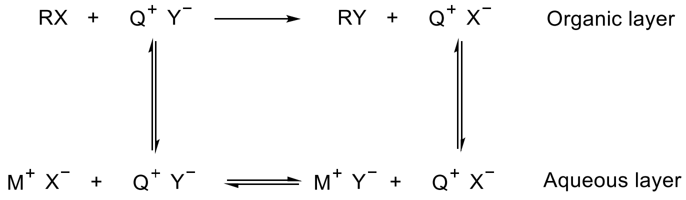

Interface type:

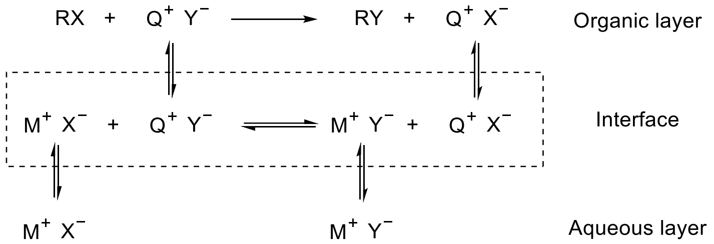

Scheme 1.2. General mechanisms of PT catalysed reactions with liquid-liquid biphasic system as examples.

On the other hand, reactions involving carbenes and carbanions are best described by the interface mechanism.[25] One example is the dichloropropanation of alkenes (**Scheme 1.3**).[26] Deprotonation of chloroform leads to the formation of trichloromethyl carbanions in the interfacial region. Ion exchange between $NaCCl_3$ and quaternary ammonium salt (QCl) generates ion pair, $Q^+CCl_3^-$, which is sufficient lipophilic to migrate into organic phase and generate dichlorocarbene for subsequent dichloropropanation. [27]

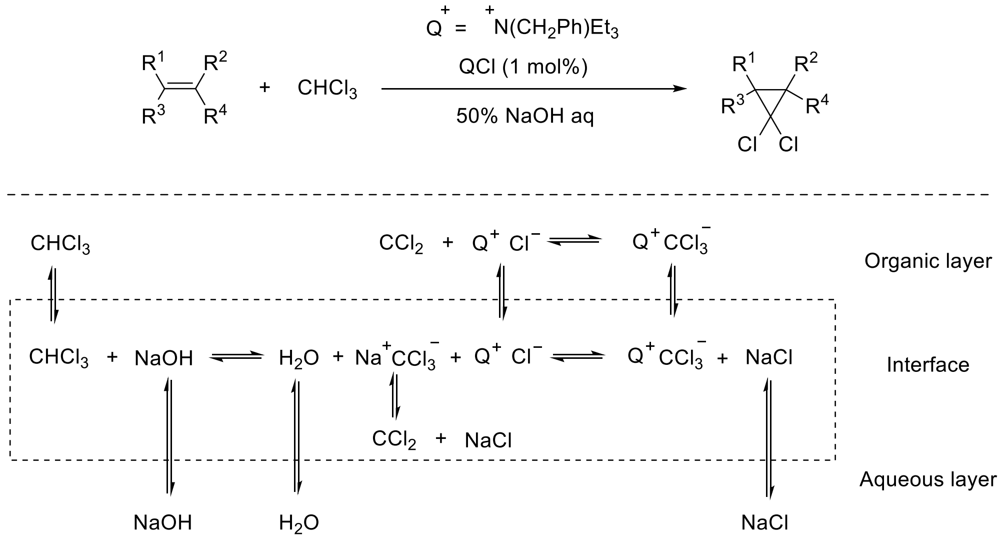

Scheme 1.3. PT catalysed dichloropropanation of alkenes.

1.1.2 Types of catalysts

To achieve effective catalysis, PT catalysts need to have certain degree of lipophilicity and the binding between the catalyst and the reagent needs to be strong enough to bring the reagent into another phase but loose enough to achieve high reactivity.[14] Common PT catalysts are onium salts (mostly ammonium and phosphonium salts), macrocyclic and macrobicyclic ethers and aza compounds and open chain polyethers.[28] Some examples are shown in **Figure 1.2**.

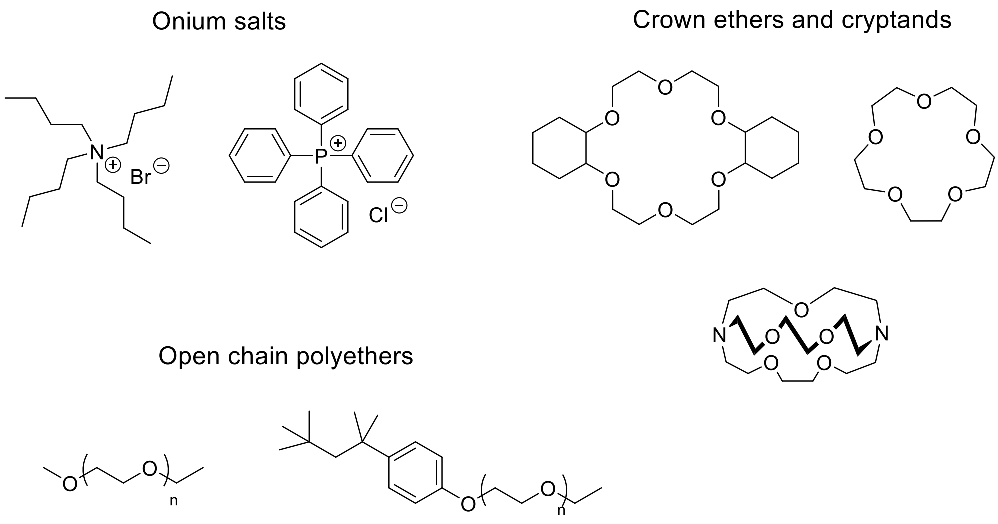

Onium salts

Crown ethers and cryptands

Open chain polyethers

Figure 1.2. Common types of PT catalysts.

The ability to form an ion pair also makes asymmetric PTC feasible. Potentially, a bulky chiral onium cation can induce asymmetry on the associated anion, and thus control the stereochemical outcome of the reaction. Early examples of asymmetric PTC are dominated by cinchona alkaloid-derived ammonium salts[29–33] as they are cheap and can be easily prepared, but examples involving crown ethers also exist (**Figure 1.3**).[34–36] More recently, tetraalkyl onium salts containing a binaphthyl moiety has been developed by Maruoka.[37–40] These catalysts provide high enantioselectivity in various transformations[41] with typical catalytic loading in the range of 1 mol%, and in some cases as low as 0.01 mol %.[42,43] These findings offered new insight into the design of asymmetric phase-transfer catalysts, and since then, a more diverse range of cationic and neutral asymmetric PT catalysts have been developed. Only selected examples are shown in **Figure 1.3**,[44–47] and comprehensive classifications and applications can be found in recent reviews.[4,41,48] On the other hand, limited research has been conducted on the analogous charge-inverted strategy.[49,50] The first successful application of asymmetric anionic PTC did not emerge until 2011, in which Toste's group reported asymmetric fluorocyclisation reactions with bulky chiral phosphates as phase-transfer catalysts and Selectfluor as fluorinating agent (see Section 1.2.1 for further discussion).[51] In 2015, Hamashima's group developed carboxylic acid precatalysts for asymmetric fluorolactonisation, again with Selectfluor.[52] Later, dianionic variants have been developed and applied in fluorination and fluorocyclisation.[53]

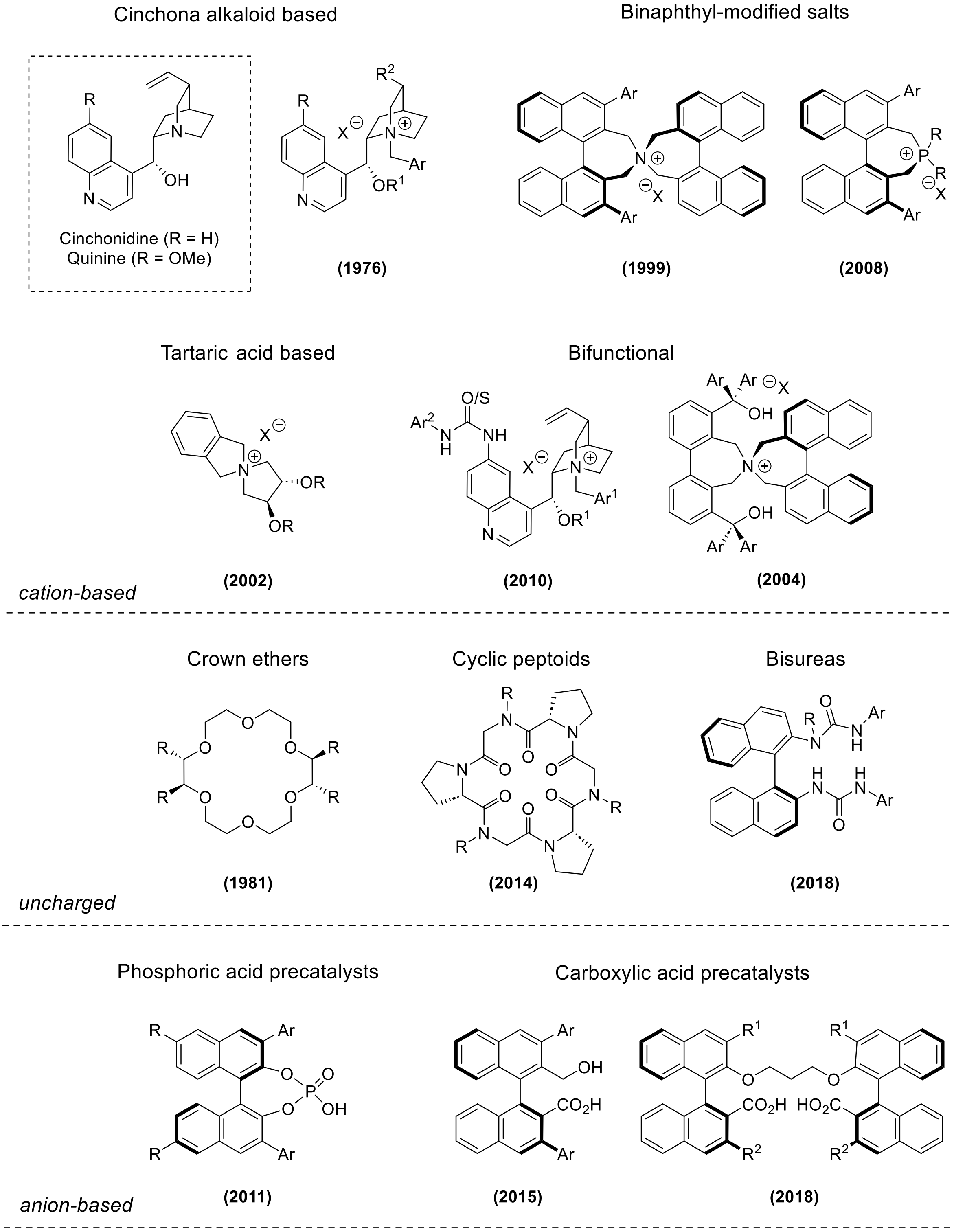

Figure 1.3. Selected examples of commonly used classes of chiral PT catalysts.

1.2 Asymmetric fluorination

Fluorine has the highest electronegativity among all elements. The C-F bond is one of the strongest single bonds in chemistry.[54] It is highly polarised and stable towards oxidising and reducing conditions. Fluorinated materials are ubiquitous from food packages,[55,56] lithium-ion batteries[57–59] to aerospace.[60,61] Organofluorine compounds have also found widespread applications in pharmaceutical science as the introduction of fluorine atom(s) into a molecule can substantially alter its chemical and physical properties, leading to an enhanced stability, bioavailability, and hydrophobicity.[62–65] Furthermore, fluorine-19, which has a 100% natural abundance, spin half, and a gyromagnetic ratio close to that of hydrogen, is an ideal nuclide for nuclear magnetic resonance (NMR) spectroscopy. [66–68] Its unnatural isotope, fluorine-18, is frequently used in positron emission tomography (PET) imaging.[69–71]

Although fluorine is abundant, it mostly presents in ores and minerals as an inorganic salt, and organofluorine compounds are rarely found in nature.[72,73] Almost all organofluorine compounds require synthesis by using fluorinating agents sourced from fluorspar (CaF_2).[74] Since the early 20th century, fluorination has mainly relied on corrosive or explosive reagents, such as fluorine gas, HF, and SbF_3, which made fluorine chemistry a rather specialised area.[75] Given the utility of fluorine, much effort has been made to develop economic, facile, and safe fluorination methods. In late 20th century, there was a boost in new fluorination agents, for instance, diethylaminosulfur trifluoride (DAST), Selectfluor, *N*-fluorobenzenesulfonimide (NFSI) and *N*-fluoropyridiunium salts (**Figure 1.4**). These reagents are easier to handle, milder, and more selective. Since then, many fluorination strategies have been developed. Detailed discussions on recent advance in fluorination can be found in multiple textbooks and review articles.[75–79] As this work concentred on mechanistic investigation of asymmetric fluorination under PTC, this section will give an overview of the field of asymmetric fluorination, focusing on functional groups that allow fluorine delivery, followed by discussions on prior mechanistic studies on some of these systems.

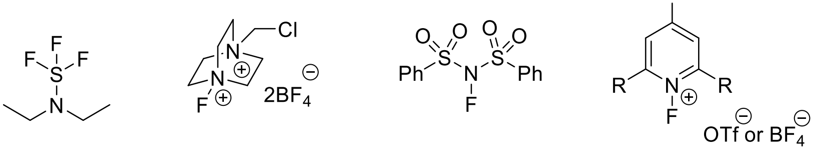

DAST Selectfluor NFSI *N*-Fluoropyridinium salts

Figure 1.4. Common fluorinating agents.

1.2.1 Electrophilic fluorination

Earlier strategies in asymmetric electrophilic fluorination are almost exclusively based on using β-keto esters as substrates and rely on formation of bidentate transition metal enolates to achieve a rigid chiral environment and thus a high enantioselectivity. Transition metal complexes of Ti(IV),[80,81] Pd(II),[82–84] Ni(II),[85,86] and Cu(II)[85,87] are mostly used. One example is shown in **Scheme 1.4**. In 2002, Sodeoka's group reported asymmetric fluorination of cyclic and acyclic β-keto esters by using NFSI and cationic palladium-BINAP complexes (**Figure 1.5**).[82] The coordination between palladium and β-keto esters increased the acidity of the α-proton, leading to the generation of the corresponding chiral palladium enolates, which were detected by ^{1}H NMR. It was proposed that the bulky *tert*-butyl group will be located at the *Si* face, away from the aromatic ligands to minimise the steric repulsion, forcing the NFSI to approach from the *Re* face of the enolate.[83] In 2008, Shibata and co-workers extended this strategy to less acidic dicarbonyl substrates using nickel-DBFOX complexes (**Scheme 1.4**).[88] Addition of 2,6-lutidine was found to be essential to accelerate the reaction from days to hours. In the initial report, fluorinated products were obtained with moderate enantioselectivities (56−78% ee). Later, enhanced enantioselectivities (92−98% ee) were achieved by using catalytic amounts of HFIP (1,1,1,3,3,3-hexafluoroisopropanol) and a lower temperature (−60 °C).[89]

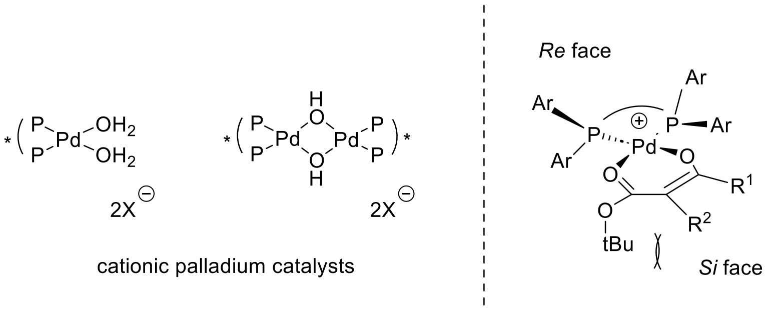

Figure 1.5. left: cationic palladium catalyst; X = OTf or BF_4. Right: proposed structure of Pd-enolate complex. Figures are reproduced from Hamashima *et al.*, 2006.[83]

Similar types of fluorinations can also be achieved via cationic PTC. The first example was reported by Kim and Park in 2002.[90] Using 10 mol% of cinchona alkaloid-based quaternary ammonium salts (**Scheme 1.4**), NFSI and a base in toluene, the corresponding α-fluoro esters were afforded in high yield with moderate enantioselectivities (48−69% ee). As expected, the reaction proceeded without enantioselectivity when the base or the PT catalyst were absent.

Later, the Maruoka and Lu groups further optimised the PT catalysts, improving the enantioselectivity to up to 98% ee.[91,92]

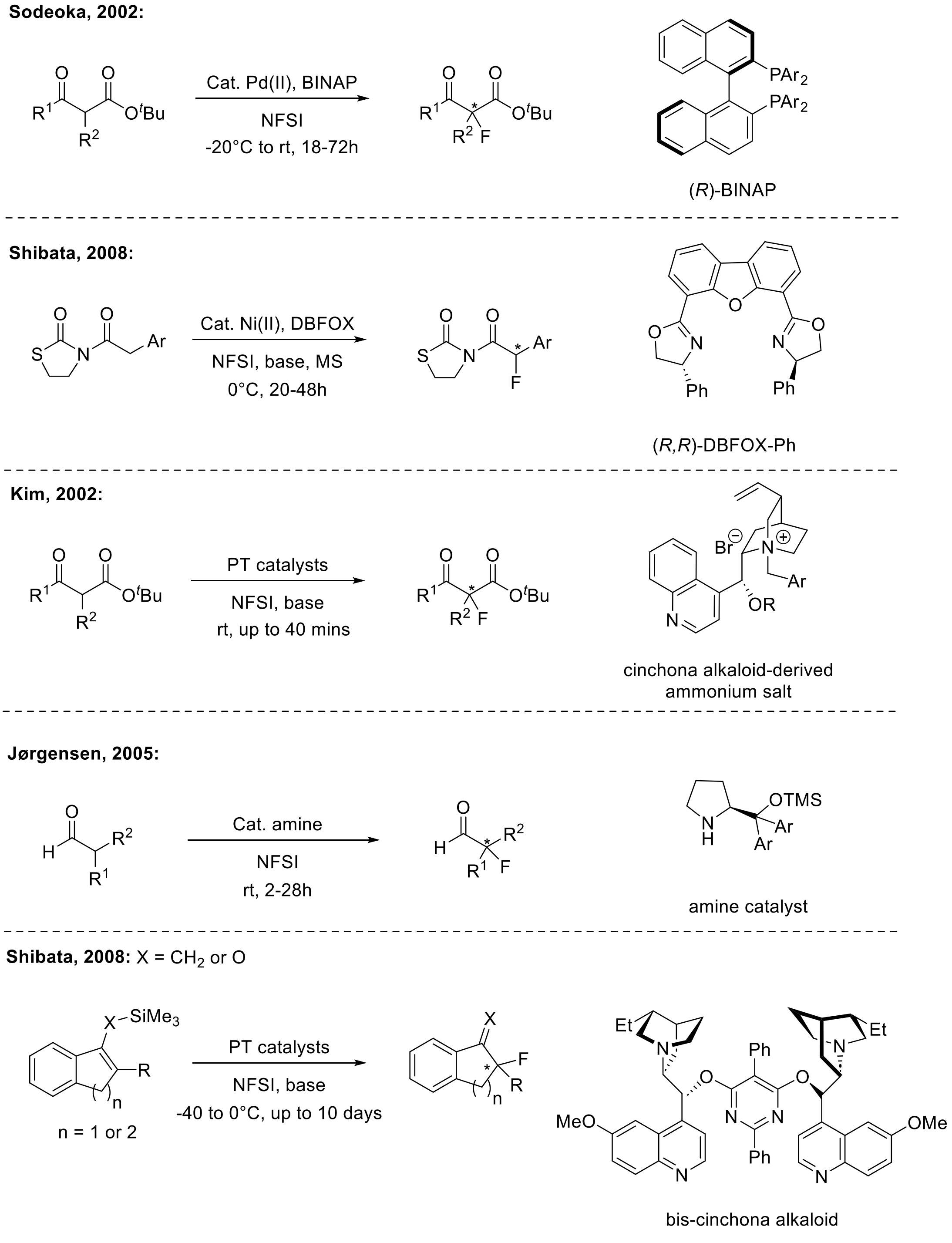

Scheme 1.4. Common strategies for enantioselective electrophilic fluorination with selected examples.

Enantioselective α-fluorination of aldehyde was achieved with enamine catalysis. [93–96] Despite multiple strategies having been reported, the method developed by Jørgensen's group in 2005 is still the method of choice for direct α-fluorination of aldehydes due to its efficiency.[96] This method uses silylated secondary amine catalyst, NFSI, and methyl-*tert*-butyl ether (MTBE) as solvent (**Scheme 1.4**). Using a low catalytic loading (1 mol% or lower) and an excess of aldehyde was essential to prevent the formation of difluorinated product and afforded the desired product in high yield and enantioselectivity (91−97% ee). It is worth noting that the fluorinated aldehydes are very unstable and more volatile than their parent aldehydes. Therefore, they were reduced to the corresponding alcohol *in situ* for analysis. The authors suggested that the *E*-configured enamine **A** was preferably formed and the *Re* face of the enamine shielded by the sterically-demanding aromatic groups (Ar = Ph-3,5-(CF_3)$_2$), leading to the formation of (*S*,*S*)-**B**, and then (*S*)-**E** (**Scheme 1.5**). The hydrogen in (*S*,*S*)-**B** was again shielded by the surrounding sterically demanding groups, making deprotonation an unlikely event and allowing (*S*)-**E** to be formed as the major product. This hypothesis was supported by a kinetic resolution experiment: mixing racemic mixture of α-fluoroaldehyde **E** with 0.5 equivalent of NFSI and 1 mol% catalyst led to formation of difluorinated product **D** with (*R*)-**E** consumed faster than (*S*)-**E**. [96]

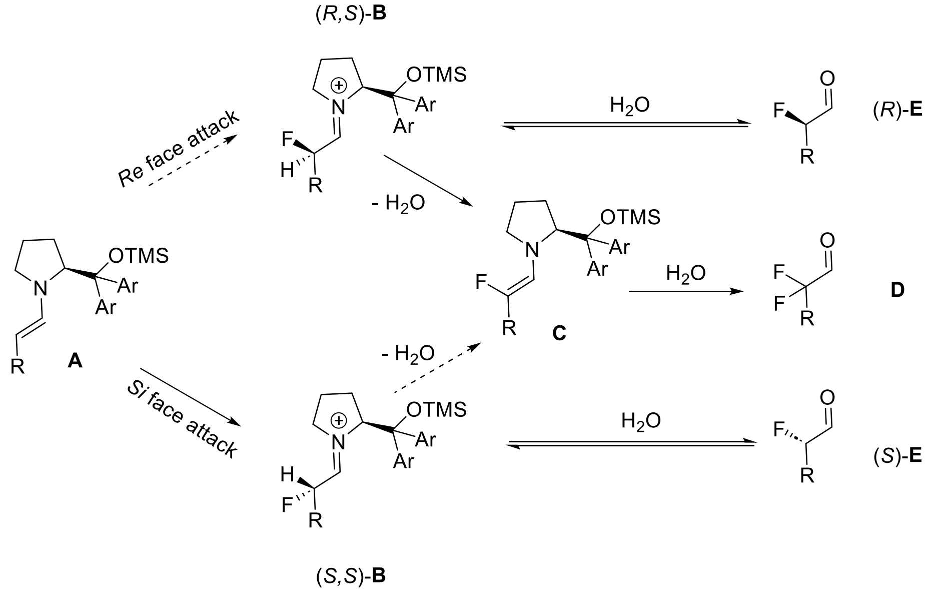

Scheme 1.5. Explanation for the stereoselectivity and stability of the α-fluoroaldehyde under reaction conditions. Kinetic resolution experiment (Ar = Ph-3,5-(CF_3)$_2$, R = Bn).

Moving away from carbonyl compounds, in 2008, Shibata and co-workers reported bis-cinchona alkaloid catalysed enantioselective fluorodesilylation of allyl silanes and silyl enol ethers.[97] In the presence of excess base, the corresponding fluorinated product can be obtained in moderate to high yield with up to 95% ee. One limitation of this approach is the requirement of a bulky R group. For example, when R = H, X = O, the product was obtained with 58 % yield and 51 % ee. Previous research revealed that chiral *N*-fluoroammonium salts were formed when NFSI was reacted with cinchona alkaloid.[98] Asymmetric fluorination of allyl silanes can also be achieved by using stoichiometric bis-cinchona alkaloid under different conditions.[99] As both the catalytic and stoichiometric methods afforded the product with the same stereoselectivity, it was suggested that the formation of chiral *N*-fluoroammonium salt is the key for the enantiocontrol of the reactions. As the reaction proceeded much slower without the potassium carbonate, the following mechanism was proposed (**Scheme 1.6**). Fluorination of bis-cinchona alkaloid affords the chiral *N*-fluoroammonium salt **I**, which then acts as a PT catalyst and reacts with the potassium carbonate to form the salt **II**. The $[KCO_3]^-$ anion triggers the fluorodesilylation of substrate, which leads to formation of product and regeneration of catalyst. A reasonable transition state was also proposed based on the crystal structure of the catalyst to explain the stereo outcome. However, none of the intermediates have been isolated.

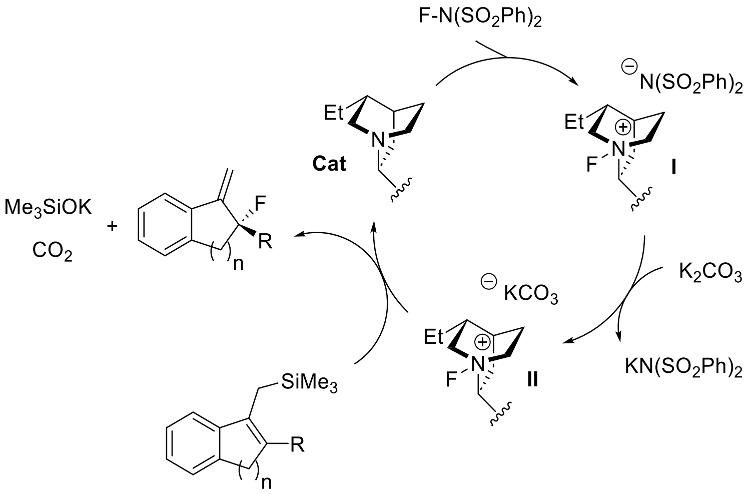

Scheme 1.6. Proposed mechanism for bis-cinchona alkaloid catalysed enantioselective fluorodesilylation.

The development of anionic PTC has greatly extended the substrate scope of asymmetric fluorination.[100–106] Selected examples are shown in **Scheme 1.7**. Using a combination of chiral phosphoric acid and Selectfluor, a range of transformations, including asymmetric fluorocyclisation,[51] fluorination of enamides[101] and fluorinative dearomatisation of phenols[102] can be achieved with high enantioselectivity. The first example of anionic PT catalysed asymmetric fluorination was reported in 2011 by Rauniyar *et al.*[51] As shown in **Scheme 1.7**a, asymmetric fluorocyclisation of dihydropyran derivatives was achieved by using 5 mol% chiral phosphoric acid **1** as precatalyst in combination with Selectfluor. In most cases, the corresponding fluorinated product was obtained in moderate to high yield with high enantio- and diastereoselectivity. As expected, the installation of hydrophobic octyl chain was beneficial. Although small, the spirocyclic product (R = H) was obtained with increased ee when phosphoric acid **1** (92% ee) was used instead of **2** (87% ee).

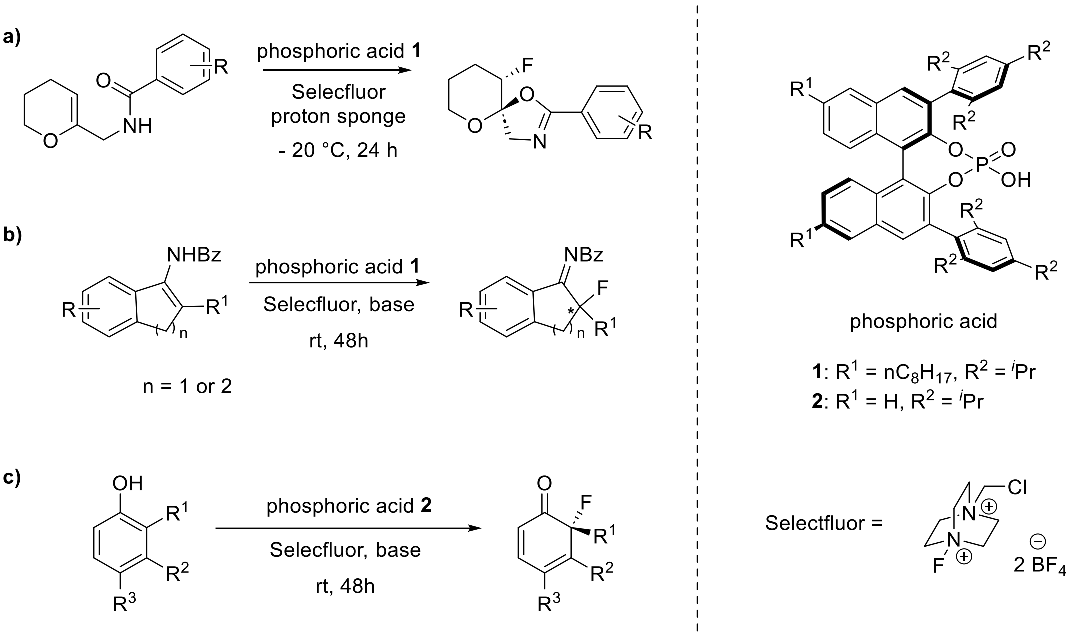

Scheme 1.7. Selected examples of asymmetric fluorination under anionic PTC. a) fluorocyclisation; b) fluorination of cyclic enamides; c) fluorinative dearomatisation of phenols.

Furthermore, this strategy was found effective towards less electron-rich substrates such as dihydronaphthalene and chromene derivatives (**Figure 1.6**). [51] Although an increased amount of catalyst was required (10 mol%), the corresponding spirocyclic products were obtained with high yield and enantioselectivity at room temperature. It should be mentioned that Selectfluor is approximately 10^4-fold more reactive than NFSI.[107] However, the background racemic reaction was completely suppressed due to the insolubility of Selectfluor in fluorobenzene, leading to the observed high enantioselectivity. A small negative non-linear effect (NLE) was observed when plotting the enantiopurity of the products against catalyst, which suggested that more than one chiral component was involved in reaction transition state.[108] Therefore, it was concluded that both tetrafluoroborate anions of Selectfluor were replaced by the chiral phosphate anions prior to the fluorocyclisation. [51]

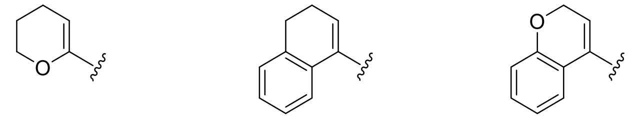

dihydropyran dihydronaphthalene chromene

Figure 1.6. Activated and non-activated alkenes.

1.2.2 Nucleophilic fluorination

Unlike asymmetric electrophilic fluorination, the development of asymmetric nucleophilic fluorination has been more sluggish, partially due to the poor nucleophilicity and basicity of fluoride, as well as the lack of chiral nucleophilic fluorinating reagents. To date, most approaches rely on the ring-opening of three-membered heterocycles (**Scheme 1.8**). Pioneering works were reported by Burns and Haufe, where moderate enantioselective ring opening of a *meso*-epoxide was achieved using stoichiometric amount of (*S,S*)-(salen)chromium chloride complex, and KHF_2/18-crown-6,[109] or AgF.[110] Although use of a sub-stoichiometric amount was attempted, very low yields were obtained because of the catalyst poisoning. In 2010, a catalytic version of the same transformation was reported by Kalow and Doyle (**Scheme 1.8**).[111]

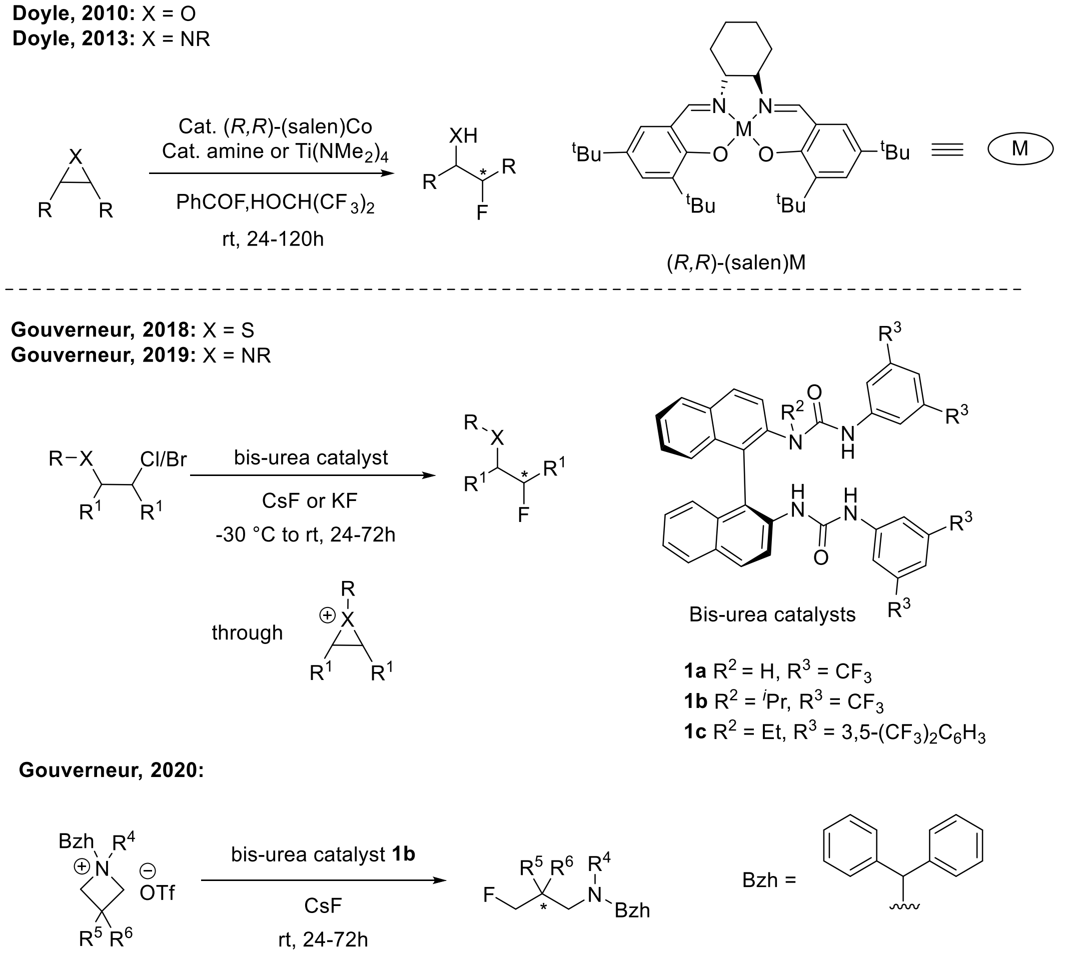

Scheme 1.8. Strategies for catalytic asymmetric ring-opening fluorination with selected examples.

Benzoyl fluoride was used as fluoride source, which slowly released HF in the presence of alcohols and chiral amine. In combination with a chiral (salen)cobalt complex, a range of fluorohydrin can be synthesised in high yield and enantioselectivity from corresponding fiveto eight-membered cyclic epoxide at room temperature. Functional groups such as alkene, esters, and protected amines were well-tolerated. The use of alternative fluoride sources, such as CsF, $Et_3N\cdot3HF$, and tetra-butylammonium fluoride (TBAF) all led to low yield or enantioselectivity, suggesting that the formation of a chiral HF-containing complex is the key. The use of either achiral amine or Lewis acid catalyst led to a substantial loss in enantioselectivity, and a pronounced matched/mismatched effect was observed between two catalysts. Kinetic studies using 4-fluororstyrene oxide as substrate revealed that the reaction was first order in both catalysts.[112] A positive-order dependence was observed for substrate, in which saturation was observed at high initial concentrations, indicating a pre-equilibrium between catalyst and substrate. Hammett study was performed with a range of *para*-substituted styrene oxides. A large positive ρ value (+1.98 ± 0.19) was obtained, which was consistent with a rate-limiting ring-opening step (a buildup of negative charge during the transition state). Both NLE experiments and experiments with linked dimeric (salen)Co, suggested that the reaction proceeded via a bimetallic mechanism (**Scheme 1.9**).[112] Further kinetic experiments suggested that a (salen)Co-F dimer was in a resting state, responsible for the apparent first-order in substrate concentration. The amine acted as an axial ligand on Co, generating active monomeric species from the (salen)Co dimer.

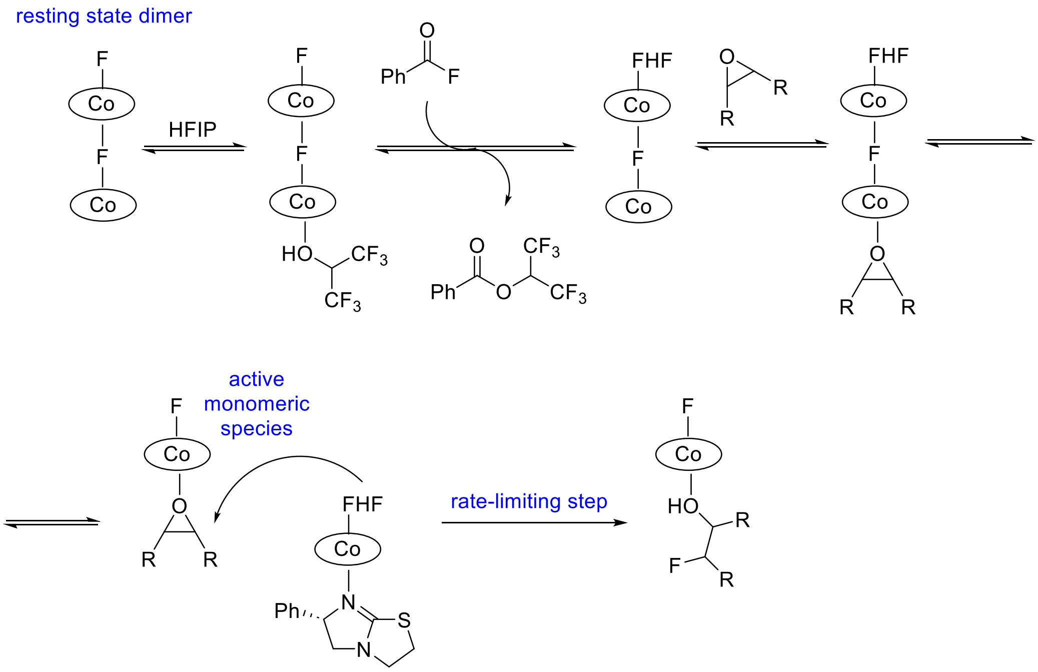

Scheme 1.9. Proposed mechanism for (salen)Co and amine cocatalysed ring opening reaction of epoxide.

In 2012, the Doyle group reported asymmetric ring opening of aziridines using a similar strategy, affording medicinally-valuable β-fluoroamines in moderate yield and enantioselectivity (**Scheme 1.8**).[113] In this case, an achiral Ti(IV) complex was used to activate the aziridines.

In 2018, the Gouverneur group reported a novel asymmetric fluorination using SLPTC and alkaline metal as fluorinating agent.[47] With this strategy, asymmetric nucleophilic fluorination of episulfonium and aziridinium[114] precursors, i.e. β-bromosulfides and β-chloroamine, was achieved using 5–10 mol% bis-urea catalysts **1b** and **1c** (**Scheme 1.8**). From racemic trans starting materials, the corresponding fluorides were obtained in moderate to high yield and enantioselectivity (70−95% ee). In 2020, the same strategy was applied to synthesis of enantioenriched γ-fluoroamines from azetidinium triflates (**Scheme 1.8**). Over 30 examples were reported with up to 95% ee.[115] Comparing with other fluorinating agents, alkali metal fluorides are abundant, cheaper, safer, and easier to use. However, their applications are normally limited by their low solubility and high basicity, which frequently leads to undesirable side reactions.[116] The key to the success of this strategy was using insoluble metal fluorides to suppress the background racemic reactions and using hydrogen bonding to mediate the basicity of the fluoride.

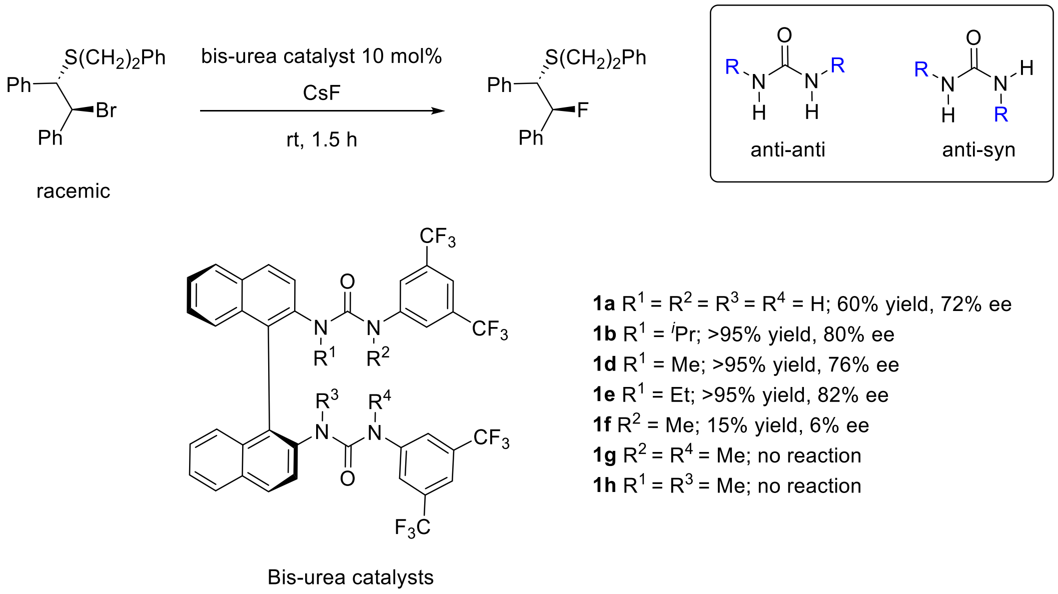

1a $R^1 = R^2 = R^3 = R^4 = H$; 60% yield, 72% ee
1b $R^1 = {}^{i}Pr$; >95% yield, 80% ee
1d $R^1 = Me$; >95% yield, 76% ee
1e $R^1 = Et$; >95% yield, 82% ee
1f $R^2 = Me$; 15% yield, 6% ee
1g $R^2 = R^4 = Me$; no reaction
1h $R^1 = R^3 = Me$; no reaction

Scheme 1.10. Asymmetric fluorination catalysed by different bis-urea compounds; all R groups = H, unless otherwise stated. Two possible conformations of urea.

Initially, bis-urea **1a** was designed, synthesised and tested. It was proposed that the two urea moieties could act as hydrogen bonding donors to complex with the fluoride, and thus bring the fluoride into solution. Initial experiments confirmed the viability of this strategy. With 10 mol% of **1a**, the corresponding product was obtained with 60% yield and 72% ee, and no fluorination was observed in the absence of catalyst. To identify the key H-bonding interactions, a range of alkylated catalysts were prepared, and their catalytic abilities were evaluated (**Scheme 1.10**). It was found that methylation at the R^2 position (**1f**) significantly lowered the yield and enantioselectivity, and dimethylation (**1g** and **1h**) led to no reaction. In contrast, methylation at the R^1 position (**1d**) was found to be beneficial, and the enantiocontrol was further enhanced when a bulkier ethyl group (**1e**) or isopropyl group (**1b**) was installed. Molecular dynamic simulations suggested that one of the ureas in **1b** isomerised to anti-syn when complexing with the fluoride (**Scheme 1.10**). The formation of tridentate H-bonding between *N*-alkylated catalyst and fluoride was further supported by density functional theory (DFT) calculations[47] and, later, by detailed $^1H/^{19}F$ NMR studies and single-crystal X-ray diffraction analysis.[117] The following reaction mechanism was proposed (**Scheme 1.11**). Upon hydrogen bonding, complex **I** was formed as a soluble chiral source of fluoride. Ionisation of substrate led to formation of episulfonium salt **II**, which then reacted with **I** to generate ion pair **III** and caesium bromide. Subsequent fluoride delivery afforded the enantioenriched product.

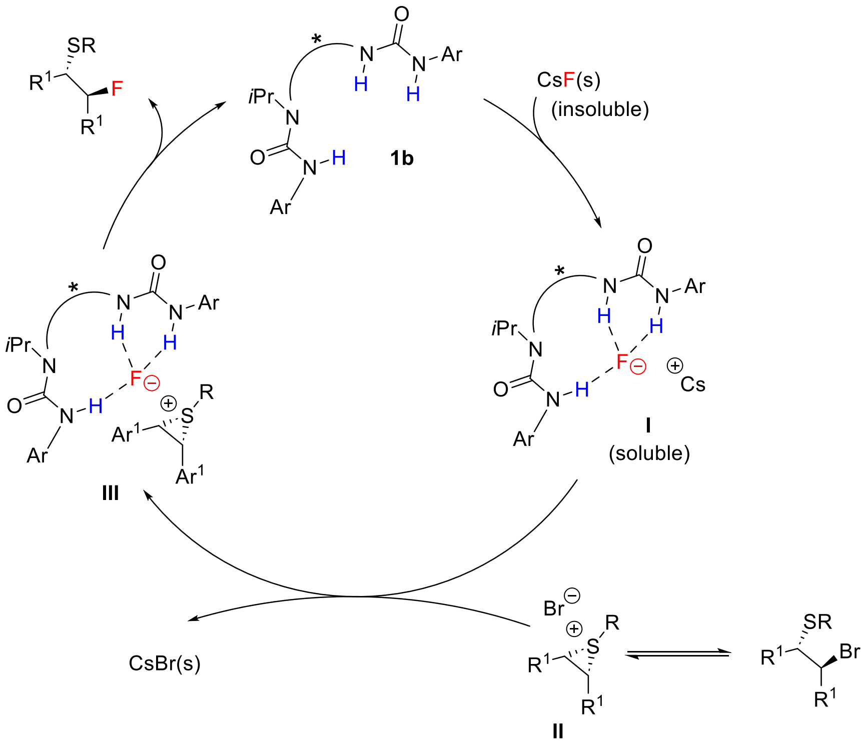

Scheme 1.11. Proposed mechanism for the asymmetric nucleophilic fluorination of racemic β-bromosulfides under PTC.

Strategies for the asymmetric nucleophilic fluorination of other types of precursors are less explored. In 2010, Katcher and Doyle reported palladium-catalysed asymmetric fluorination of cyclic allylic chloride with sliver fluoride as fluorinating agent (**Scheme 1.12**a).[118] The corresponding allylic fluoride was obtained in high enantioselectivity (87−96% ee) with retention of stereochemical configuration. Although the reaction proceeded without the palladium catalyst, it was rather slow, therefore had a small impact on the chemo- and stereo-selectivity. Later, the same group extended this strategy to regio- and enantioselective fluorination of acyclic allylic chlorides (**Scheme 1.12**b).[119] It was found that bidentate phosphines with large bite angles gave higher regioselectivity towards the branched product, with the best regioselectivity achieved by naphthyl ligand **L2** (b:l > 20:1). With these conditions, good regioselectivity was achieved with a range of substrates. However, good enantioselectivity was only obtained with limited branched substrates, while low to moderate enantioselectivity was obtained with linear substrates (R^1 = H).

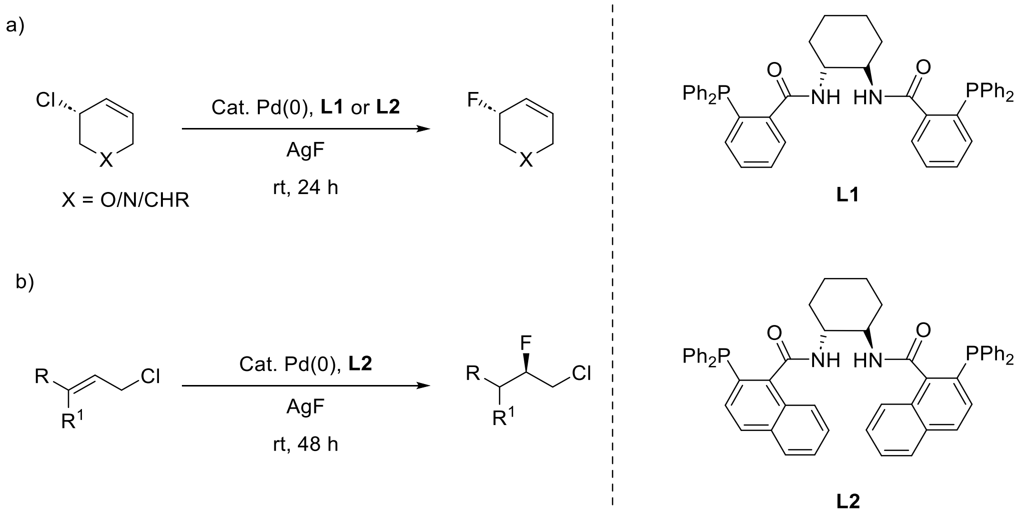

Scheme 1.12. Palladium-catalysed asymmetric allylic fluorination.

1.3 Project aims

Organofluorine compounds have found wide applications in many aspects of chemical industry. Although the field of fluorination is becoming more mature, there are few strategies available for the highly demanding asymmetric fluorination. There is no doubt that PT catalysed asymmetric fluorination with PTC has become one of the major enabling strategies for asymmetric fluorination over the last decades. Although new phase-transfer catalyst with novel features have been designed, there is a lack of mechanistic understanding, and most of the present efficient phase-transfer catalysts are developed based on trial and error. The lack of mechanistic understanding restricts the application of catalysis to a small range of substrates, and in some cases, a subtle change in the structure of the substrate can profoundly diminish the yield and enantioselectivity. Additionally, with a different substrate, re-optimisation of solvent, base, and temperature can be required to obtain optimised results.

A more fruitful way would be understanding the reaction mechanism, and then using this to design and tailor catalyst for different categories of substrates. However, it is technically challenging to monitor a PT catalysed reaction *in situ* and conventional *ex situ* monitoring methods possesses inherent disadvantages. Hence, it would be beneficial to develop an NMR-based *in-situ* monitoring system for reactions with PTC, which will enable more accessible kinetic studies, shed light on the reaction mechanism of PTC, and guide the structural development of the novel catalyst.

This project aimed to conduct detailed mechanistic investigations on asymmetric nucleophilic fluorinations under PTC (Chapter 3). To accelerate kinetic data acquisition, a novel *in-situ* NMR mixing device has been designed and developed, which can also be applied to monitor other biphasic solid-liquid reactions that requires vigorous agitation (Chapter 2).

2. *In-situ* NMR mixing device

2.1 Introduction

Mechanistic study is essential for understanding the chemical process, optimising the reaction conditions towards higher yield and selectivity, and guiding the design of new reactions and catalysts.[120] Reaction monitoring is informative. By systematically studying the concentration changes occurring during a chemical process, one can obtain information of reaction kinetics and the role of each chemical species, which can then be used to direct further mechanistic analysis.[121–123] A range of analytic techniques, including NMR, infrared (IR), Raman and UV-Vis spectroscopy, mass spectrometry, and reaction calorimetry can be applied to monitor reactions *in situ*. [123–128] Among all, liquid-state NMR spectroscopy is probably the most popular method. It is non-invasive, applicable for a range of nuclei, and provides rich chemical structural information. Quantitative data can be implemented by designed experimental settings.[129,130] However, not all reaction systems are readily amenable to routine NMR. For instance, reactions that requires high pressure, high temperatures, and/or light requires specialised techniques.[131–135]

In comparison with homogeneous reactions, heterogeneous reactions are more challenging to study by NMR because the reaction contains two or more phases, and all or part of the reaction occurs at phase interfaces.[136,137] The former leads to localised magnetic inhomogeneity as the magnetic susceptibility normally differs between different phases, resulting in severe peak broadening and distortions. The latter means that efficient mass transport is essential for the reaction to proceed and for meaningful kinetic data to be collected, i.e. the apparent rate is a consequence of chemical processes rather than mass transfer rate.[138–141] In terms of heterogeneous solid-liquid reactions, continuous and vigorous agitation is required to overcome this mass transfer limit, which is trivial in normal glassware / reactors but is difficult to achieve within the probe of standard NMR spectrometers. The long and narrow geometry of standard NMR tube prohibits good mass transport through the sample volume. Furthermore, the sample is not readily accessible as it located in a position that is approximately a metre deep inside the magnet bore.

The effect of magnetic inhomogeneity can be alleviated by employing tailored NMR pulse sequences. [142–144] However, most methods do not work in real time, i.e. acquisition of multiple free induction decays (FIDs) is needed, and are therefore not optimal for *in-situ* reaction monitoring. SHARPER is a pure-shift method that is designed for the analysis of reactions and equilibria.[145,146] It greatly enhances the spectral resolution by removing all heteronuclear and homonuclear couplings with repetitive refocusing between chunks of data acquisition. Whereas the initial SHARPER only allows one resonance to be studied at a time, the recently reported MR-SHARPER (Multiple Resonance SHARPER) allows multiple resonances (examples with up to three resonances were demonstrated) to be monitored simultaneously without a trade-off of sensitivity. One example is shown in **Figure 2.1**, where α and β are two protons with distinct chemical shifts and MR-sel-SHARPER allows simultaneous observation of both protons.[146,147] MR-SHAPER is more appealing for reaction monitoring as multiple species (e.g. reactant, intermediate, products) are normally of interest.

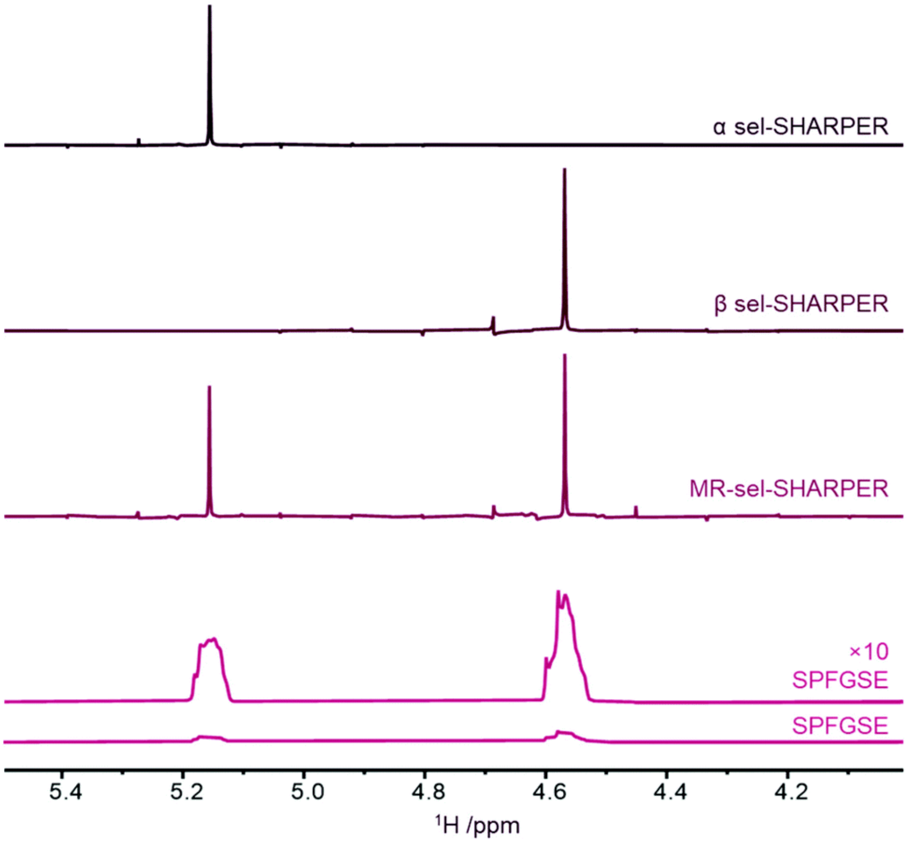

Figure 2.1. Overlay of ^{1}H spectra acquired in an inhomogeneous magnetic field with z shim corrections offset by +200 units from the optimal values using sel-SHARPER (focusing on different protons), MR-sel-SHARPER and SPFGSE pulse sequences. α and β are two protons with distinct chemical shifts. All spectra were plotted with the same scale unless labelled. Image is taken from Davy *et al.*, 2022.[146]

Line-broadening caused by field inhomogeneity can also be compensated by post-acquisition processing. One efficient method is reference deconvolution. [148,149] The principle of this method has been developed independently by multiple groups since 1960s.[150–153] It is a purely mathematical operation without changing any built-in information. Assuming that the distortions caused by field inhomogeneity affect all signals in the same way, by referencing to a singlet with known theoretical form, the discrepancies between the theoretical and experimental line shape of this singlet can be used to calculate a correction function, which then can be applied to the full spectrum to give a better spectral resolution.[148] One example is shown in **Figure 2.2**. Narrower lines can be obtained when shorter linewidth was set for reference deconvolution, with a gradual trade-off of sensitivity.

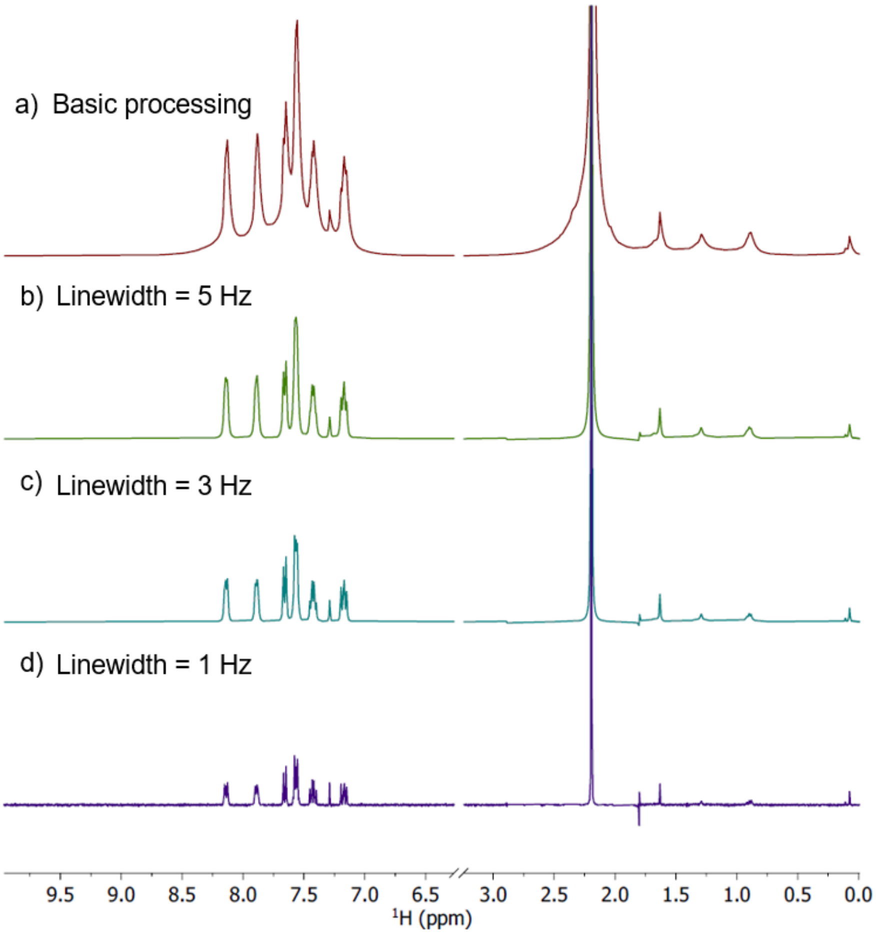

Figure 2.2. Overlay of partial ^{1}H spectra of a mixed solution of 1-fluoronaphthalene (100 mM), acetone (100 mM) and magnesium sulfate (0.040 g) in $CDCl_3$ (800 µL), processed with a) phase and baseline correction, b-d) based on the first spectrum using reference deconvolution with acetone peak as reference singlet, reference line-shape as a Lorentzian peak and a linewidth set to 5, 3, 1 Hz respectively. All spectra were plotted with the same scale.

Although methods have been developed to mediate the poor resolution, there is no general way to achieve efficient agitation inside an NMR spectrometer. Therefore, heterogeneous reactions are commonly monitored using *ex-situ* sampling method, where reaction is conducted in laboratory under standard conditions, and aliquots are taken out at various recorded time and then immediately quenched for analysis.[120] In comparison with the *in-situ* monitoring method, the *ex-situ* sampling method has less constraints on reaction conditions and allows reactions to be studied under realistic conditions. The sample can also be analysed by multiple techniques, providing that an efficient way of quench is identified; for heterogeneous reaction a filtration is normally sufficient. However, the quench process is normally irreversible, i.e. one aliquot only provides information on one time point, thus, *ex-situ* sampling method tends to be tedious and laborious, especially in the case of kinetics studies where large amount of data is desired. To address this, platforms have been developed for automated sampling and data acquisition.[154–157] In 2017, Rougeot *et al.* developed a sampling system for monitoring heterogeneous liquid-solid reactions.[154] By using two parallel sampling channels, one with filter and one without, information of both the liquid phase and the mixed phase can be obtained (**Figure 2.3**). This system is effective and can perform sampling at maximum 1 per minute over a long period of time (up to 90 hours). However, care needs to be taken as the solid-free solution is continuously withdrawn from the reaction mixture during the sampling process, which means the percentage of the solid components is increasing overtime. This may lead to changes in the observed kinetic profile, in comparison with manual *ex-situ* sampling, where both phases are taken out at the same time. Later, the same group extended their platform for monitoring liquid-liquid biphasic reactions using both phase-selective and heterogeneous sampling methods.[155,157]

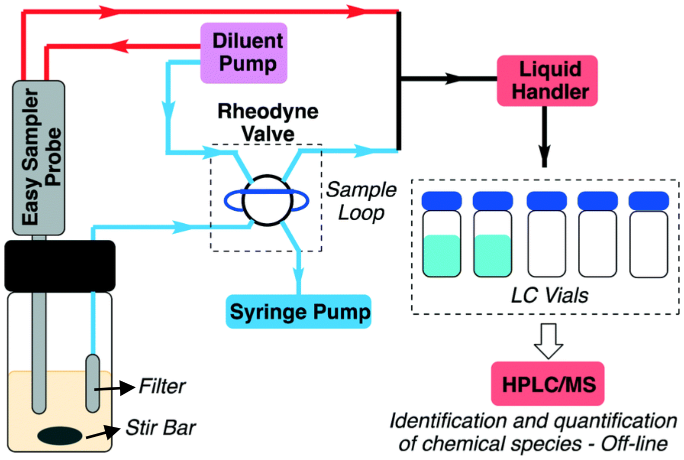

Figure 2.3. Schematic of automatic sampling device. Image is taken from Rougeot *et al.*, 2017.[154]

In contrast to the *ex-situ* method, the *in-situ* reaction monitoring method only requires a small amount of sample and allows high data-density to be collected; it can also avoid decomposition of fragile reaction components as no manual processing is involved. Overall, it is highly desirable to develop a general method to allow *in-situ* monitoring of a heterogeneous reactions by NMR spectroscopy. As this project aimed to study the reaction mechanism of phase-transfer catalysed fluorination involving solid reagents, we specifically want to develop a method that will allow us to monitor solid-liquid biphasic reactions *in situ*. To fulfil this goal, an efficient way of agitation and data acquisition procedures needed to be identified.

2.2 Mode of agitation

For heterogenous solid-liquid reactions, efficient agitation is essential for the reaction to proceed and to overcome the mass transfer limit (see Section 2.4.4 for examples). We first investigated different agitation modes. One way to generate agitation is by sparging inert gases throughout the sample (**Figure 2.4**A). This set-up was initially used to introduce gas reagents for heterogenous gas-liquid reactions.[140,158] Recently, Neto *et al.* used a similar approach to homogenise a liquid-liquid biphasic system.[159] The gas was injected into the bottom of the NMR tube though a Teflon tube. While the gas flows, it promotes the mixing between the two liquids. Gas sparging needs to be halted before data acquisition as bubbles also cause field inhomogeneity and lead to poor resolution. We excluded this method because it would accelerate evaporation of solvent, which would lead to change in concentration and affect the validity of the data, especially when volatile solvents are used. Furthermore, it is hard to identify an optimal flow rate --- the flow rate needs to be fast enough to bring solids up but not too vigorous to remove the solid from the solution.

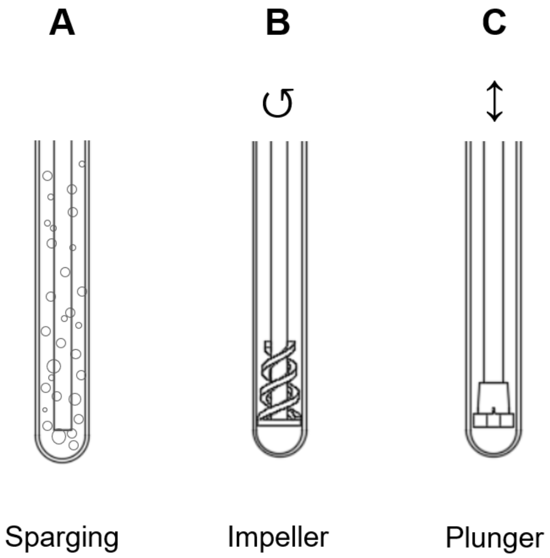

Figure 2.4. Schematic representations of three modes of agitation within a standard 5 mm NMR tube (OD = 5 mm), with A: gas sparging, B: rotating impeller, and C: a plunger that moves in vertical direction. Figures reproduced from Gao *et al.*, 2023.[160]

Another option is using a rotating impeller, which is widely used in industrial processes to agitate heterogenous mixtures.[161,162] Considering the strong magnetic field of NMR, a titanium impeller was used (**Figure 2.4**B). When tested using a solution of acetone with addition of powder of magnesium sulfate, we found that very high rotation rate (> 10 000 rpm) was required to bring the solid up to most of the sample. After one minute of agitation, the solution has been heated up, by the frictional forces, and abrasion of the glass wall was observed. Furthermore, when the titanium impeller was inserted in the NMR tube in the active volume, severe peak broadening was observed (**Figure 2.5**c), which was primarily attributed to increased electrical conductance in the active volume.

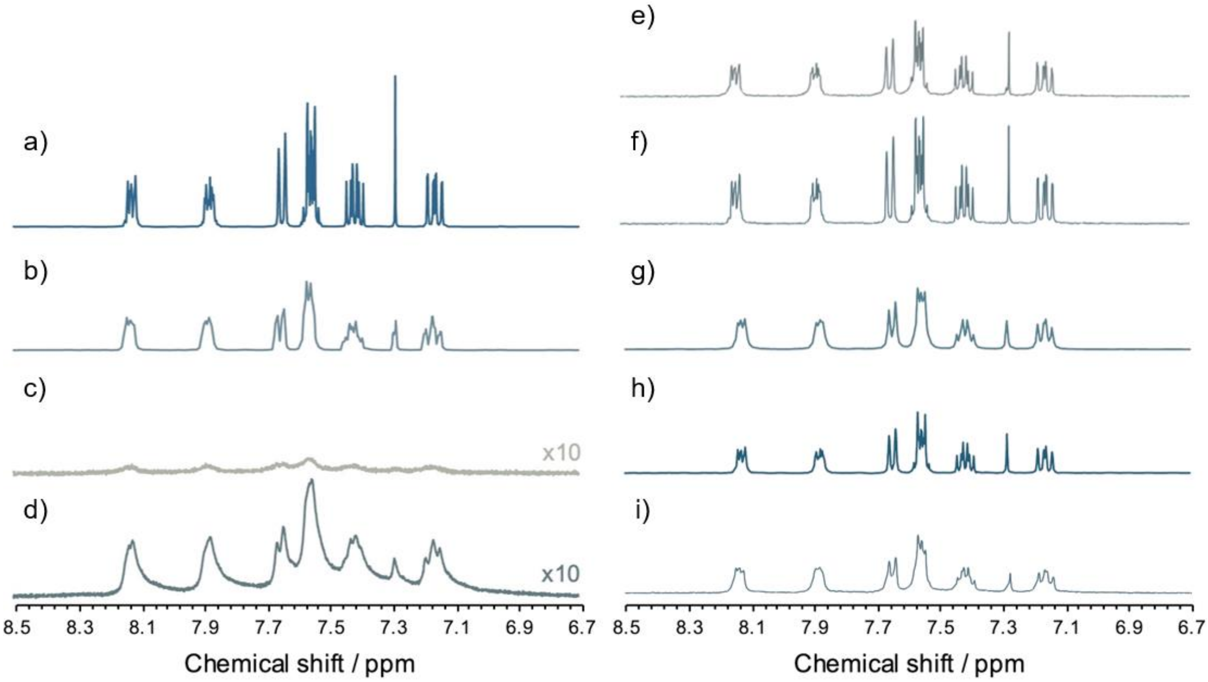

Figure 2.5. Overlay of partial ^{1}H spectra of a solution of 1-fluoronaphthalene (100 mM) and acetone (100 mM) in $CDCl_3$ (800 µL) recorded in a standard 5 mm NMR tube (OD = 5 mm), under different conditions: a) no modification, b-h) with 0.04 g of magnesium sulfate; c) with a titanium impeller in the active volume; d) with plunger in the active volume; e) with plunger at the bottom of the NMR tube and the sample was re-shimmed; f) with plunger at 1 cm above the active volume and the sample was re-shimmed; g) with plunger at 1 cm above the active volume with the same shimming setting as in spectrum a; h) based on spectrum g using reference deconvolution with acetone peak as reference singlet, reference line-shape as a Lorentzian peak and a linewidth set to 1.2 Hz respectively; i) with plunger moving in the active volume with the same shimming setting as in spectrum e. All spectra were recorded with the same receiver gain, processed with 64K points zero filling and plotted with the same scale unless labelled. Figure reproduced from Gao *et al.*, 2023.[160]

While removing the impeller from the NMR tube, we noticed that the impeller lifted up some of the solids, which led us to test a plunger-type mixer (**Figure 2.4**C). The initial plunger-tip was modified from a HPLC fitting (made of ethylene tetrafluoroethylene (ETFE)), which had a diameter close to the inner diameter of NMR tube and was grooved on the side. When tested with the same mixture of acetone and solids, we found that rising and lowering the plunger very effectively distributed the solid through the whole solution phase. When the plunger was in the active volume, sever peak broadening was also observed due to the mismatch of magnetic susceptibility between ETFE and acetone (**Figure 2.5**d). Neither automated nor manual shimming could improve the spectral resolution. Alternatively, when the plunger was lifted out of the active volume, a reasonable spectral resolution was obtained (**Figure 2.5**g). Re-shimming the sample (**Figure 2.5**f) or reprocessing the spectrum with reference deconvolution (**Figure 2.5**h) further improves the spectral resolution. Placing the plunger at the bottom of the NMR tube also leads to severe spectral distortion because the glass capillary that connected to the plunger tip is now in the active volume. Re-shimming the sample helps (**Figure 2.5**e), but in comparison with **Figure 2.5**f, a decrease in signal intensity was observed as the sample in the active volume is reduced. It is also possible to obtain spectra with reasonable resolution while the plunger is constantly moving (**Figure 2.5**i). However, only one out of several that has good resolution, and signal intensity varies as the amount of sample in the active volume constantly changes over a range of 207 to 280 μL. Therefore, in the final design, the plunger is halted and held above the active volume during data acquisition to give optimal result.

2.3 General design and workflow

Centred on a plunger-based mixer, a mixing system has been developed for monitoring heterogeneous solid-liquid reactions by *in-situ* NMR. A scheme of the system is shown in **Figure 2.6**a. The system has an NMR insert block (**Figure 2.6**b), a linear stepper motor, a motor controller compartment (motor drive, TTL signals, etc.) and a control panel.

The NMR insert block contains a part that resembles a standard spinner, allowing the sample to sit steadily within the spectrometer. A truncated NMR tube with a 5 mm diameter is attached to the spinner via a compression fitting with a nut and an O-ring[163] which enable easy exchange of samples, addition of reagents, and cleaning. The liquid reagent can also be added through the glass capillary. The headspace above the sample can be purged with inert gas via the two gas ports on the top, allowing air-sensitive reactions to be studied.

A Bowden cable is used to connect the NMR insert block and the linear stepper motor. It consists of a polyetheretherketone (PEEK) inner cable (OD = 1.59 mm, ID = 1.0 mm) and a Nylon outer cable (OD = 4 mm, ID = 2.5 mm). By fixing both ends of the outer cable, mechanical movement can be transmitted through the movement of the inner cable. The motion is further transmitted to the glass capillary tube via a coupling, allowing the plunger to move up and down. This combination of material and diameter was selected to provide sufficient stiffness to limit the bending angle and reduce the friction, while keeping the cable flexible enough to allow the NMR insert block to be easily loaded into the spectrometer (**Figure 2.6**c). Limiting the bending angle is also beneficial for reducing the "backlash", which is a lost motion in a mechanism caused by gaps between different parts.[164] However, after initial optimisation, we still observed backlash (1–2 mm) after several cycles because the cables are not strictly co-centred and there is a 90° bend in the set-up to mount the motor (**Figure 2.6**d). Since backlash is cumulative when the moving directions is altered, it will lead to irreproducible results and may lead to damage of the spectrometer. To prevent this, a non-magnetic spring was installed to keep the cable under constant tension, which proved to be very effective --- no backlash was observed after 2 hours' operation (approximately 6500 cycles of plunger movement). As a further safety precaution, two distance sensors were installed on both side of the motion platform (see Section 6.1 for further details) to stop the motor in the case of malfunction.

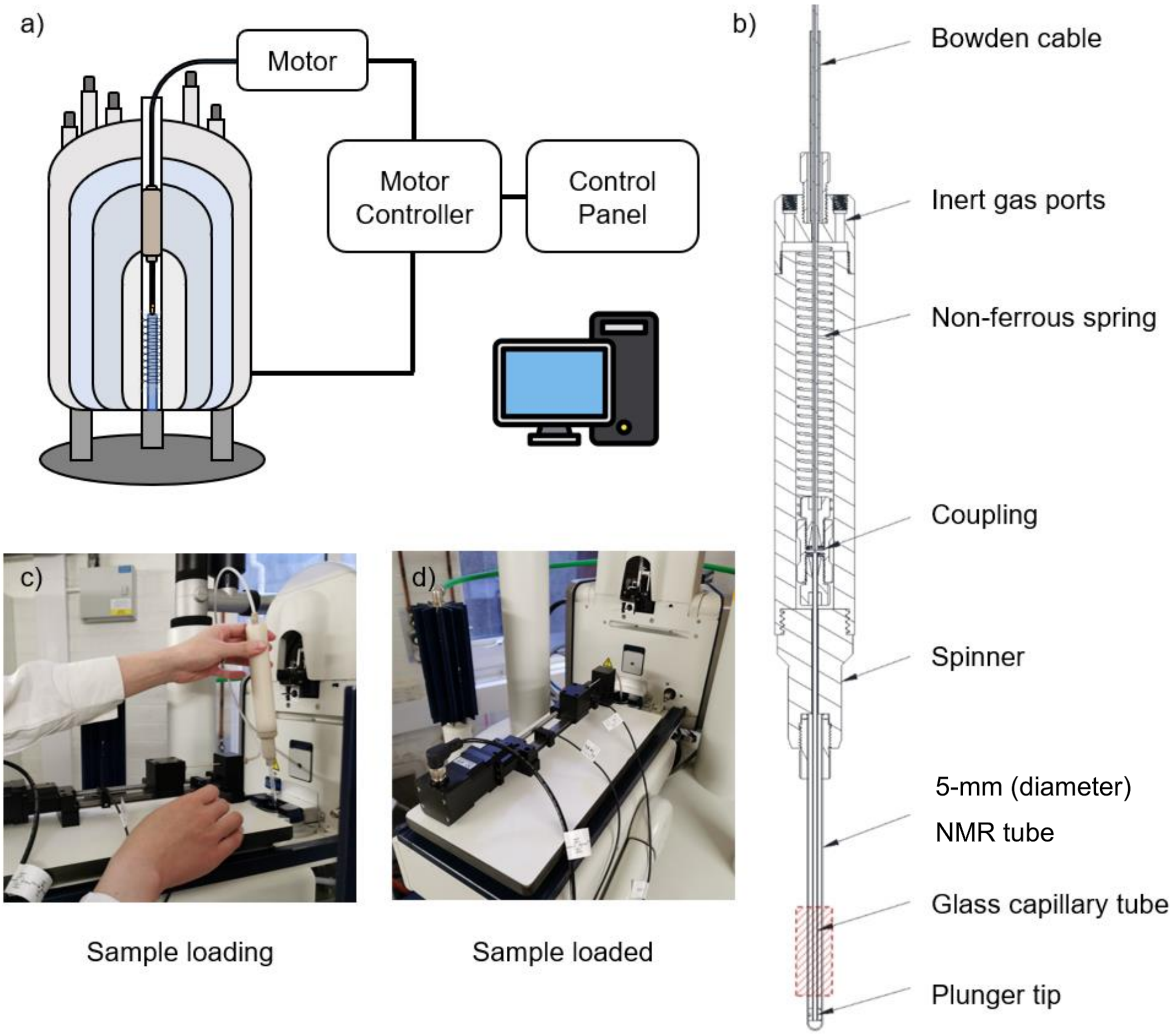

Sample loading

Sample loaded

Figure 2.6. Schematic representations of a) the NMR-based *in-situ* mixing system; b) the insert section of the mixing system, where the active volume is highlighted in red. c) Photograph showing the sample loading process, the motor is positioned on the sample changer platform (with the sample changer removed). The sample is manually inserted into the bore of the magnet. d) Photograph of the mixing system when sample is loaded. c) –d) figures reproduced from Gao *et al.*, 2023.[160]

The linear stepper motor allows the plunger to move at a speed up to 120 mm/s, which is more than sufficient to achieve efficient mixing for all the reactions that we have tested. The speed is not limited by the stepper motor but rather the processing speed of the microcontroller. A higher speed can be achieved by using a more advanced microcontroller. Although adjustable, the plunger is normally moved in the range of 40 mm, to keep the plunger tip within the solution and reduce the formation of bubbles.

The general workflow of the NMR mixing device can be divided into three stages: mixing, settling and data acquisition, with the pulse program shown in **Figure 2.7**. In the first stage, the motor is on with the set parameters, mixing the solids and liquids to allow the reaction to proceed for a period, τ_{mix}. Then the spectrometer sends a TTL trigger to the motor to stop the mixing and halt the plunger above the active volume for a period, τ_{settle}, allowing the solid particles to partially settle down. The settling time is crucial to get a reasonable spectral resolution. It could vary depending on the experimental settings and size of the particle but should be set much shorter than the mixing time to minimise the disturbance of reaction kinetics (see section 2.4.2 for further discussion). After that, a spectrum is acquired as normal and TTL trigger is turned off to resume the mixing. The whole process is repeated throughout the reaction.

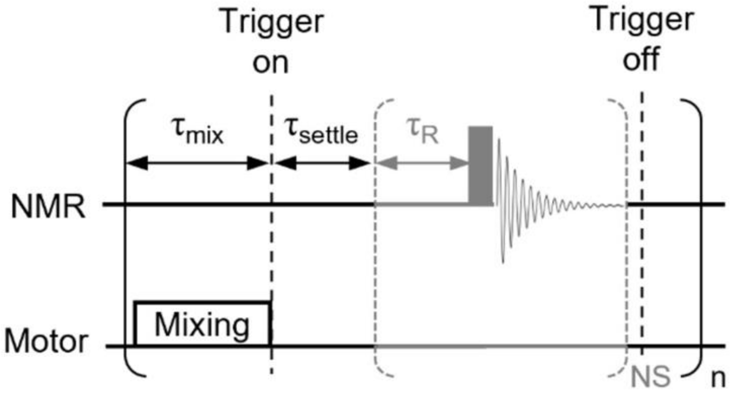

Figure 2.7. The pulse program used for NMR acquisition with in-situ NMR mixing device. The sample is first mixed for a period, τ_{mix}. Then, a TTL signal is used to stop the movement of the motor and lift the plunger above the active volume. The solids are allowed to settle for a period, τ_{settle}, before the data acquisition, where τ_R = relaxation delay, and NS = number of scans. After that, the trigger is turned off and the mixing resumes. The whole process is repeated n times for the duration of the reaction. See section 6.2 for pulse program. Image is taken from Gao *et al.*, 2023.[160]

A custom software interface was developed by Dr. Andrew Hall, allowing other key parameters such as moving speed and moving distance to be easily changed (see Section 6.1 for further details). The device can also be operated without receiving TTL trigger signal by presetting the mixing time and settling time in the software. In this mode, the motor also sends a TTL signal out, to allow the reaction to be monitored by alternative techniques, such as UV-Vis spectroscopy.

2.4 Performance and optimisation

2.4.1 Mixing efficiency

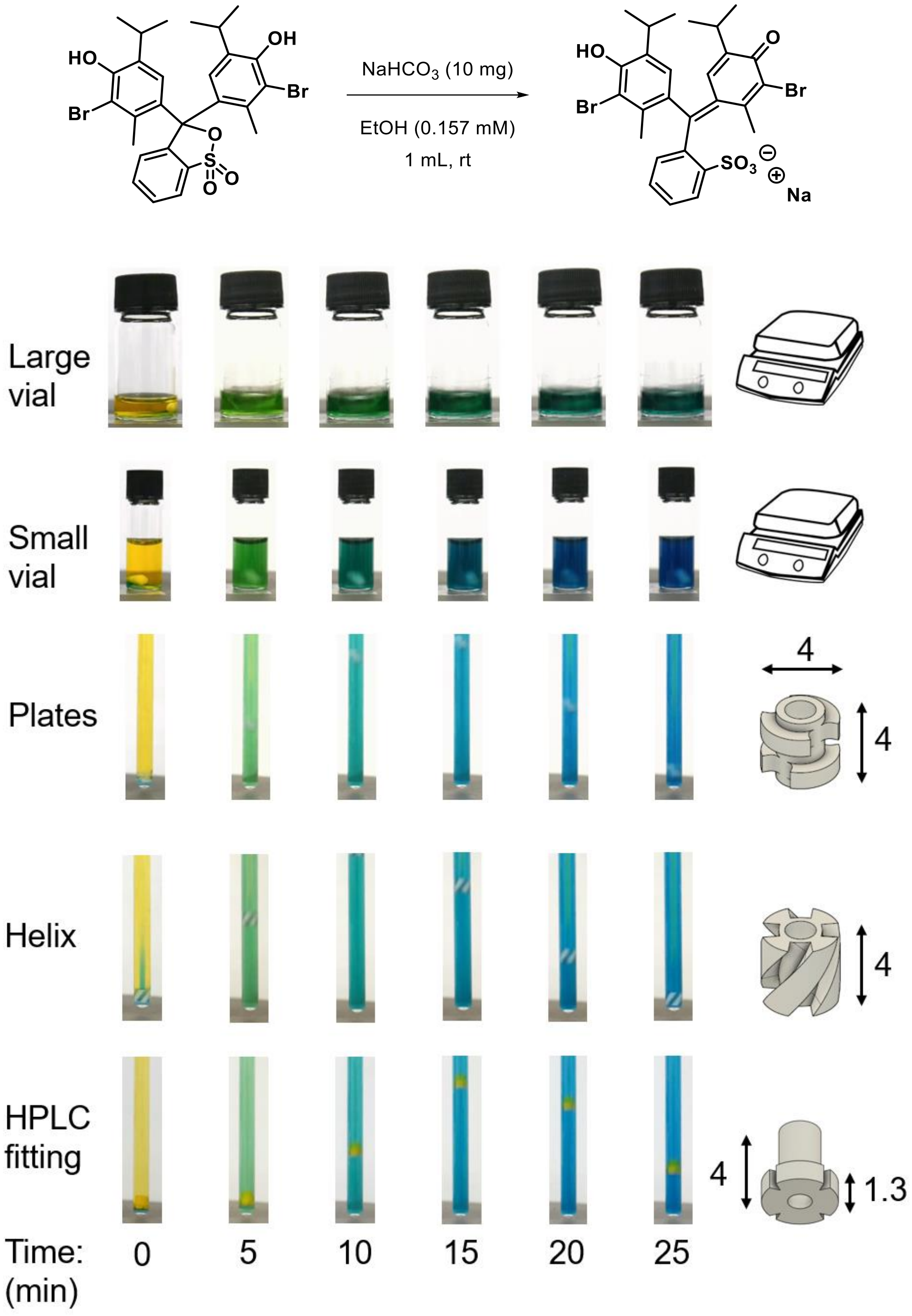

Figure 2.8. Heterogenous reaction of solution of bromothymol blue in ethanol and solid sodium bicarbonate. The protonated BTB is yellow and gradually deprotonated by base and turning green and eventually a blue solution. The same reaction was set up in small (1.7 mL) and large (7 mL) sample vials equipped with magnetic stirrer bar (1500 rpm) and in the NMR tube with mixing device (100 mm/s) equipped with either plates, helix or modified

HPLC fitting plunger tips. The design of each plunger tip was showing on side, with all dimensions in mm. The reactions were recorded for 25 minutes and selected images at different time points were shown.

It is critical that the reaction is well-mixed, so that the rate of the reaction is not limited by the mass transfer but is an indication of the inherent reaction processes. To improve the mixing efficiency, three different plunger tips were designed, and their performance were assessed using the acid-base reaction between bromothymol blue (BTB) in ethanol with solid sodium bicarbonate. This reaction proceeds with a pronounced colour change from yellow to green to blue (**Figure 2.8**), allowing the reaction to be assessed visually and by UV-Vis spectroscopy. The initial plunger tip was a grooved HPLC fitting made of ETFE. The close fit between the NMR tube (ID = 4.2 mm) and the tip forced the solids to pass through the grooves and mix with the liquid. The plates and helix plunger tips were machined from polytetrafluoroethylene (PTFE), intended to create radial or tangential vortices. All plunger tips have a centre bore, which allows them to connect with the capillary via a friction-based "push-fit".

The same reactions were set up in small (1.7 mL) and large (7 mL) sample vials stirred at 1500 rpm and in the NMR tube with mixing device (100 mm/s) equipped with different plunger tips. As shown in **Figure 2.8**, all plunger tips performed well, with similar colour changes observed when reaction were conducted in a small vial. The reaction in large vial proceeds slower because the solids were partially trapped at the edge during stirring.

The effect of different types of plunger tips and mixing speed on the mixing efficiency was further investigated by monitoring the same reaction by UV-Vis spectroscopy (different reaction conditions were used to accommodate UV-Vis measurements, (see section 5.3.1 for experimental details). UV-Vis spectra of BTB ethanol solution (0.0314 mM) with different extent of deprotonation by addition of sodium hydroxide were acquired as references (**Figure 2.9**a). Negative absorbances were observed as the BTB ethanol solution before addition of sodium hydroxide was acquired as background absorbance. The spectra obtained with the reaction between BTB and sodium bicarbonate were more noisy (**Figure 2.9**b). The absorbances at 432 and 497 nm were extracted for each time point, and relative absorbance was calculated using **Eq. 2.1**. To reduce the noise level, ten data points were acquired after each pause and their values were averaged (**Figure 2.9**c, d). The rate constant of formation of deprotonated BTB was estimated by fitting with a pseudo-first order kinetics (**Eq. 2.2**). The relative absorbance for the deprotonated BTB ethanol solution, A_2, is non-zero, and thus need to be deduced from the observed A_t. The results are shown in **Figure 2.10**. The absorbances at 627 nm were also used to calculate the rate constant of formation of deprotonated BTB; while similar value of rate constant was obtained, there was no improvement in the noise level, which was likely due to light scattering of the suspended solid.

$$A_{rel} = \frac{A_{432}}{A_{497}} \tag{2.1}$$

Where A_{rel}, A_{432} and A_{497} are relative absorbance, absorbance at 432 nm and 497 nm respectively.

$$A_t - A_2 = A_1 \exp(-kt) \tag{2.2}$$

Where A_t is the absorbance at time t, A_1 and A_2 are the absorbance of BTB and deprotonated BTB ethanol solution respectively, *k* is the rate constant.

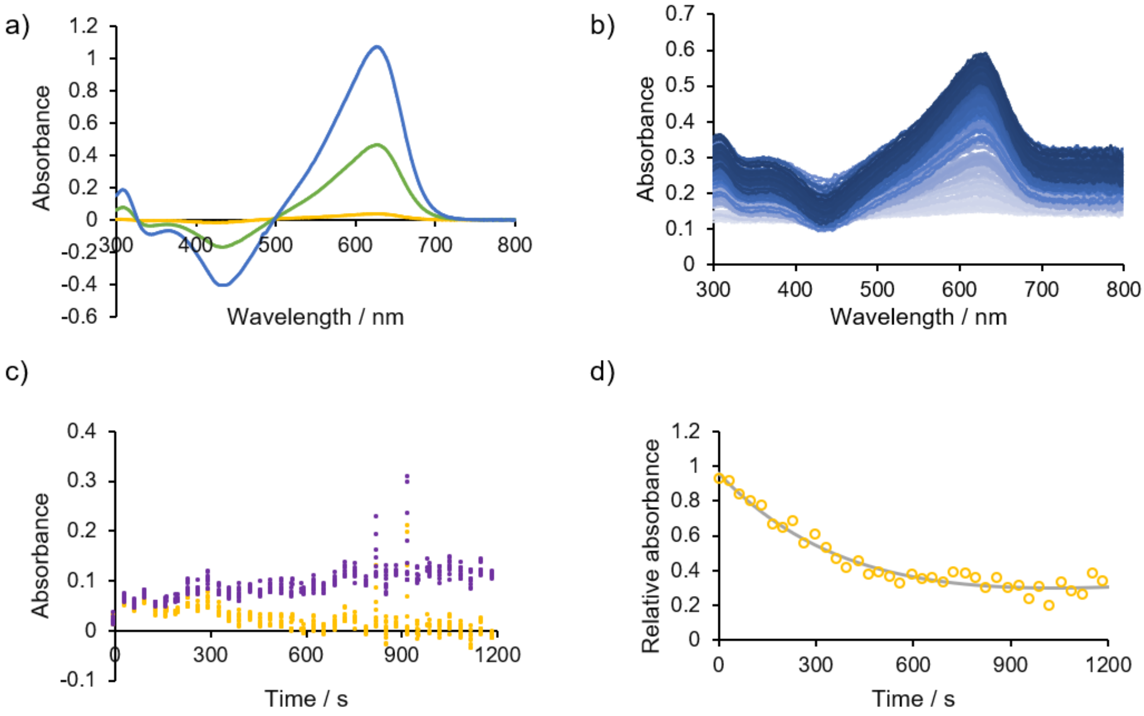

Figure 2.9. a) UV-Vis spectra of a BTB ethanol solution before (yellow) and after addition of different amount of NaOH (green, blue). b) Representative UV-Vis spectra of one reaction between protonated BTB ethanol solution and sodium bicarbonate. c) Representative plot of absorbance at isosbestic point (497 nm, purple) and 432 nm (yellow) against time. d) Representative plot of relative absorbance against time (experimental data: yellow dots, fitted: grey line).

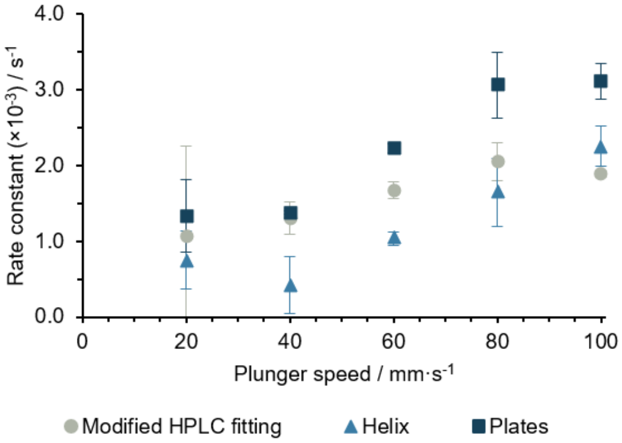

Figure 2.10. The mixing efficiency of different plunger tips at various moving speed was assessed by comparing the rate constant of formation of deprotonated BTB in the reaction of BTB ethanol solution and solid sodium bicarbonate. Figure is taken from Gao *et al.*, 2023.[160]

In general, the mixing efficiency improves with faster plunger speed. The plate design has the best performance, with the helix and modified HPLC fitting performing similarly. The current design also allows using a stack of plunger tips. The mixing efficiency can be further improved if a stack of plate style plunger tips is used (**Figure 2.11**). The use of three helix or a combination of helix and plate style plunger tips did not improve the mixing efficiency. When using the mixing device for reaction monitoring of phase-transfer catalysed fluorination, we found that one plate style plunger tip is sufficient to overcome the mass transfer limit.

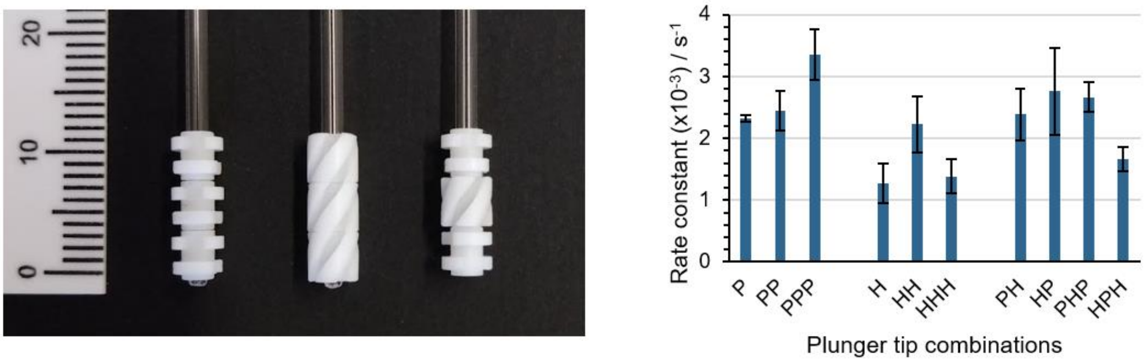

Figure 2.11. Left: picture of stacked plunger tips, from left to right: PPP, HHH, PHP. P = plate style plunger tip, H = helix style plunger tip. Right: the mixing efficiency of different combinations of plunger tips at plunger speed = 60 mm/s, with design counting from bottom end, i.e. PH = plate at bottom, helix at top. Figures are taken from Gao *et al.*, 2023.[160]

2.4.2 Settling time

During the initial tests, we noticed that having a settling time prior to data acquisition can greatly improve the spectral resolution. To quantitatively assess this, we measured the full width at half maximum (FWHM) of an acetone signal in a sample containing caesium fluoride in DCM with a settling delay between 2 to 120 seconds (**Figure 2.12**). With the plunger moved at 100 mm/s (**Figure 2.12**, red), the linewidth improved substantially when the delay time was increased from 0 to 5 seconds (from 28 Hz to 4 Hz), the improvement became less significant after 5 seconds (1.4 Hz). Although suspension of fine particles was still observed after more than ten minutes after mixing is stopped, there was no further improvement on the linewidth with delay time longer than 60 seconds. Therefore, it is not necessary to wait for all the solid particles to settle down to get reasonable spectral resolution. The settling time can be further reduced if the spectral components of the reaction system allow the application of reference deconvolution methods.[160]

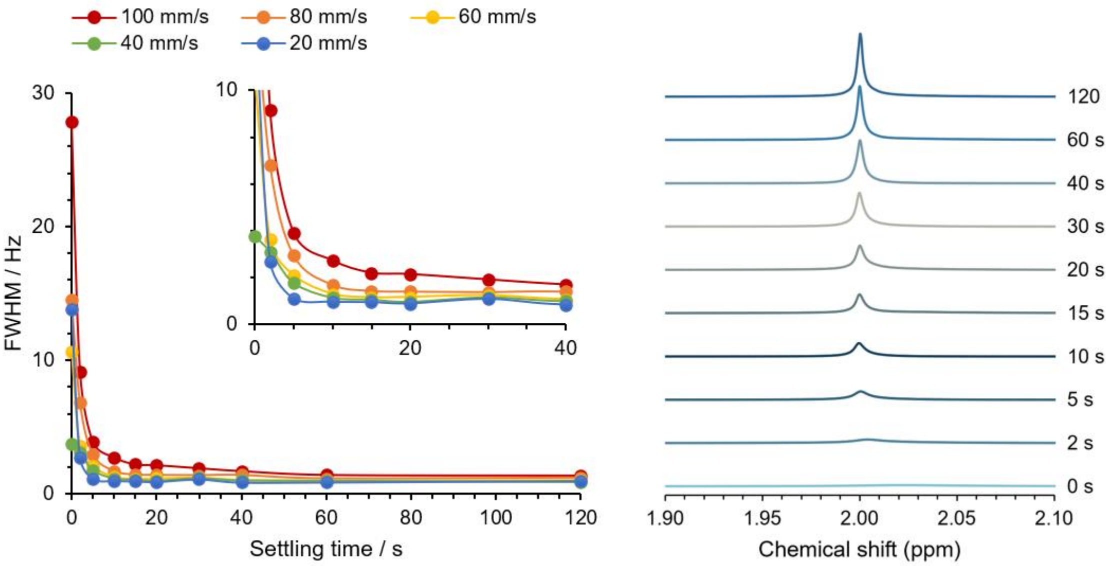

Figure 2.12. Left: effect of settling time on the FWHM of the proton signal of acetone (163 mM) in deuterated DCM (800 μL) containing fine powder of CsF (61 mg). The sample was mixed for a 60 s period at a plunger speed of 20, 40, 60, 80, or 100 mm/s, before mixing was stopped for a delay time between 2 to 120 s and a spectrum was acquired. Right: Overlay of ^{1}H spectra acquired at a plunger speed = 100 mm/s with different delay timed labelled on the side, zoomed in for the acetone peak. All spectra were acquired with 1 scan, processed with 64k points zero filling and without apodization. The figure on the right is taken from Gao *et al.*, 2023.[160]

We then examined the effect of different plunger speed. As expected, slower plunger speeds caused less disturbance to the spectral resolution and resulted in sharper initial peaks, with a shorter settling time required to reach optimum linewidth. This trend is consistent within all data sets apart from the first blue point (**Figure 2.12**, left).

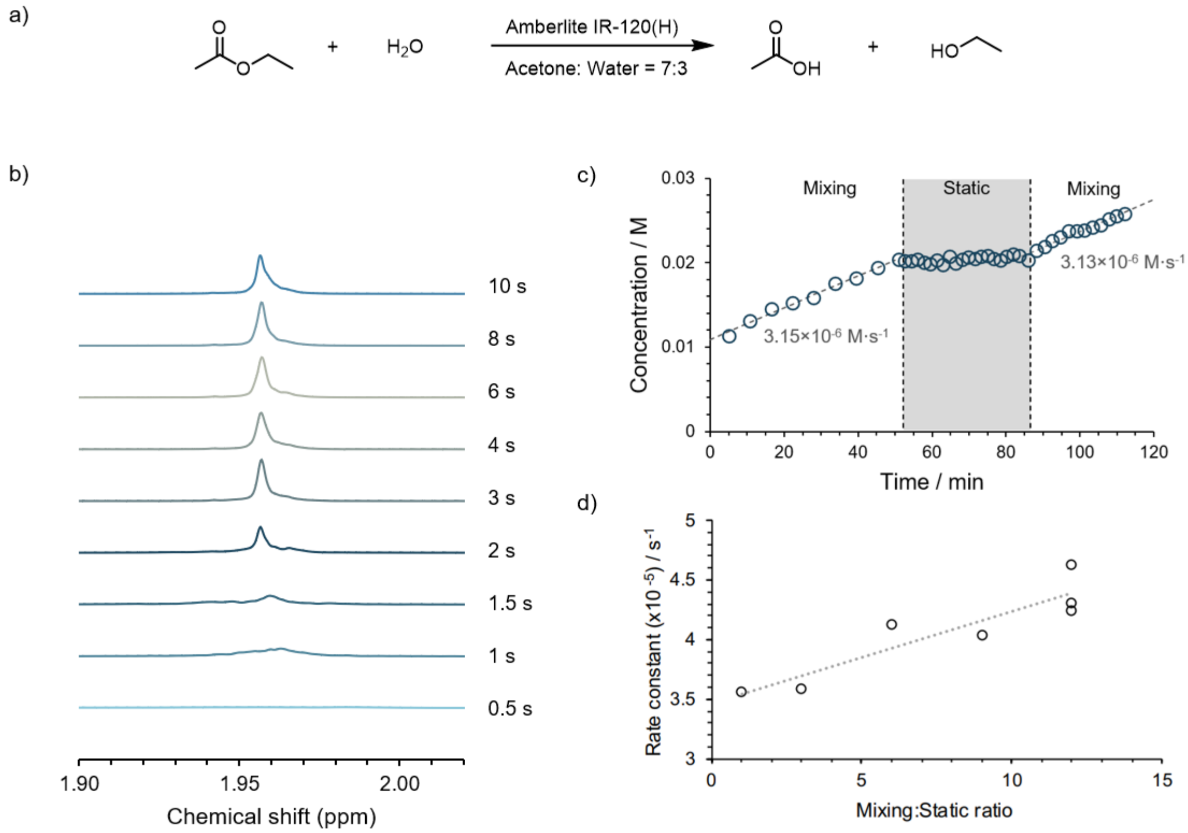

Figure 2.13. a) Hydrolysis of ethyl acetate catalysed by Amberlite IR-120(H). b) Overlay of ^{1}H spectra acquired at a plunger speed = 100 mm/s with different delay timed labelled on the side, zoomed in for the methyl peak. All spectra in b) were acquired with 1 scan, processed with 64k points zero filling and without apodization. c) The hydrolysis ([ethyl acetate] = 0.5 M, resin = 0.0200 g, solvents = 600 µL) was monitored with in-situ mixing device with a plunger speed of 100 mm/s, 0 – 50 mins: settling time = 2 s, data acquired every 5 minutes; 50 – 90 mins: mixing halted, data acquired every 2 minutes; 90 – 115 mins: settling time = 2 s, data acquired every 2 minutes. d) Plot of rate constant against mixing: static ratio. The rate constant was extracted from different time region of a single reaction ([ethyl acetate] = 0.5 M, resin = 0.0160 g, solvents = 600 µL) where the mixing and static time were varied to get different ratios. The figures c and d are taken from Gao *et al.*, 2023.[160]

A shorter settling time was required for hydrolysis of ethyl acetate using Amberlite IR-120(H), an acidic cation exchange resin with a sphere shape and a diameter around 1 mm (**Figure 2.13**a).[165] As shown in **Figure 2.13**b, reasonable line-width was obtained when settling time = 2 seconds, and no significant improvement was observed for settling time longer than 3 seconds. No reaction was observed when the mixing was halted (**Figure 2.13**c), and similar reaction rates were observed when spectra was acquired at 5 mins and 2 mins time intervals with settling time = 2 seconds. Both rates are in good agreement with those obtained using the *ex-situ* sampling method (3.30×10^{-6} $M \cdot s^{-1}$). However, the measured rate constant decreased when the mixing: static ratio was decreased, i.e. increased sampling frequency with the same settling time, especially when the mixing time is less than 6-fold of the settling time (**Figure 2.13**d). Therefore, the static time (the sum of settling time and acquisition time) should be kept much shorter than the mixing time, to allow reliable kinetic data measurement. As settling time will vary depending on the particle size, tests similar to that shown in **Figure 2.13**b should be performed for each new reaction system to identify the optimum settling time.

2.4.3 Solvent evaporation

Evaporation of solvent causes changes in reaction concentration, which may lead to changes in the reaction rate. To investigate the effect of agitation, we monitored the absorbances of a dye under various conditions by visible light spectroscopy and deduced the solvent loss by application of the Beer–Lambert law (Eq. 2.3 – 2.6).

$$A = \varepsilon\, c\, l = \varepsilon\, \frac{n}{V}\, l \qquad (2.3)$$

A is absorbance, ε is the molar extinction coefficient of the absorbing compound, c is the concentration, l is the path length of the light, n is number of moles and V is the volume of the solution.

The number of moles of dye in the solution is constant. The pathlength was kept constant, and calibration curves were measured for all solvents to confirm linearity of the extinction coefficients over the range of concentrations measured (see section 5.3.2). Thus, the change in volume can be calculated from the change in absorbance.

$$\frac{A_0\, V_0}{\varepsilon\, l} = \frac{A_1\, V_1}{\varepsilon\, l} \qquad (2.4)$$

$$A_0\, V_0 = A_1\, V_1 \qquad (2.5)$$

$$\Delta V = \frac{V_0 - V_1}{V_0} = \frac{A_1 - A_0}{A_1} \qquad (2.6)$$

As expected, agitation of the reaction mixture accelerates evaporation, with greater solvent loss observed with higher mixing speed, solvent with lower boiling point and larger total volume (**Figure 2.14**). Therefore, while ensuring efficient mixing and reasonable spectral resolution, a slower mixing speed and smaller sample volume should be used, especially when the system contains volatile solvent and/or reagents.

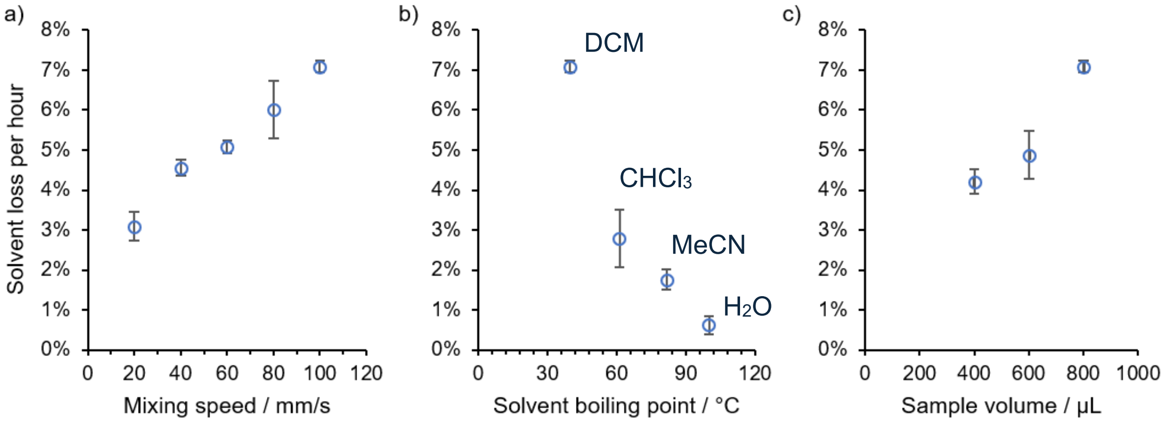

Figure 2.14. Percentage of solvent loss per hour due to evaporation as a function of a) mixing speed (DCM, 800 µL), b) solvent boiling point; the solvent name are shown in Figure (mixing speed = 100 mm/s, 800 µL), and c) sample volume (DCM, mixing speed = 100 mm/s). All experiments were performed at 21 °C, using plates style plunger tip, 40 mm plunger travel distance, 25 s mixing time, 4 s settling time. 5:1 mixing: static ratio. The figures a and b are taken from Gao *et al.*, 2023.[160]

2.4.4 Case studies

To validate the effectiveness of the mixing device, phase-transfer catalysed fluorination[47] was monitored by ^{19}F NMR with both *in-situ* mixing device and conventional *ex-situ* sampling method (**Figure 2.15**). All reaction components except caesium fluoride are in the liquid phase, whereas caesium fluoride is a fine powder and insoluble in DCM. As shown in **Figure 2.15**, the kinetics data obtained by both methods are in excellent agreement. The *in-situ* monitoring method features higher data density and requires less reagents (0.8 mL instead of 4 mL). Although the spectral resolution obtained *in situ* is poorer than that obtained via *ex-situ* sampling method, reliable data can be retrieved through standard spectral analysis (see Section 5.4.1 for further details).

To ensure the measured rate is not mass transfer limited, the reaction was conducted under stirring rate ranged from 150 to 1400 rpm and the rate of product formation was compared (**Figure 2.16**). For stirring speed below 900 rpm, the reaction rate increased with increasing stirring speed, indicating that the reaction was limited by mass transfer. When the stirring speed was higher than 1000 rpm, the reaction rate plateaued and reflected the inherent reaction kinetics. A stirring rate of 1200 rpm was used when the reaction was monitored by ex-situ sampling method. Thus, one can confidently conclude that the reaction was beyond mass transfer limit for both experiments shown in **Figure 2.15**.

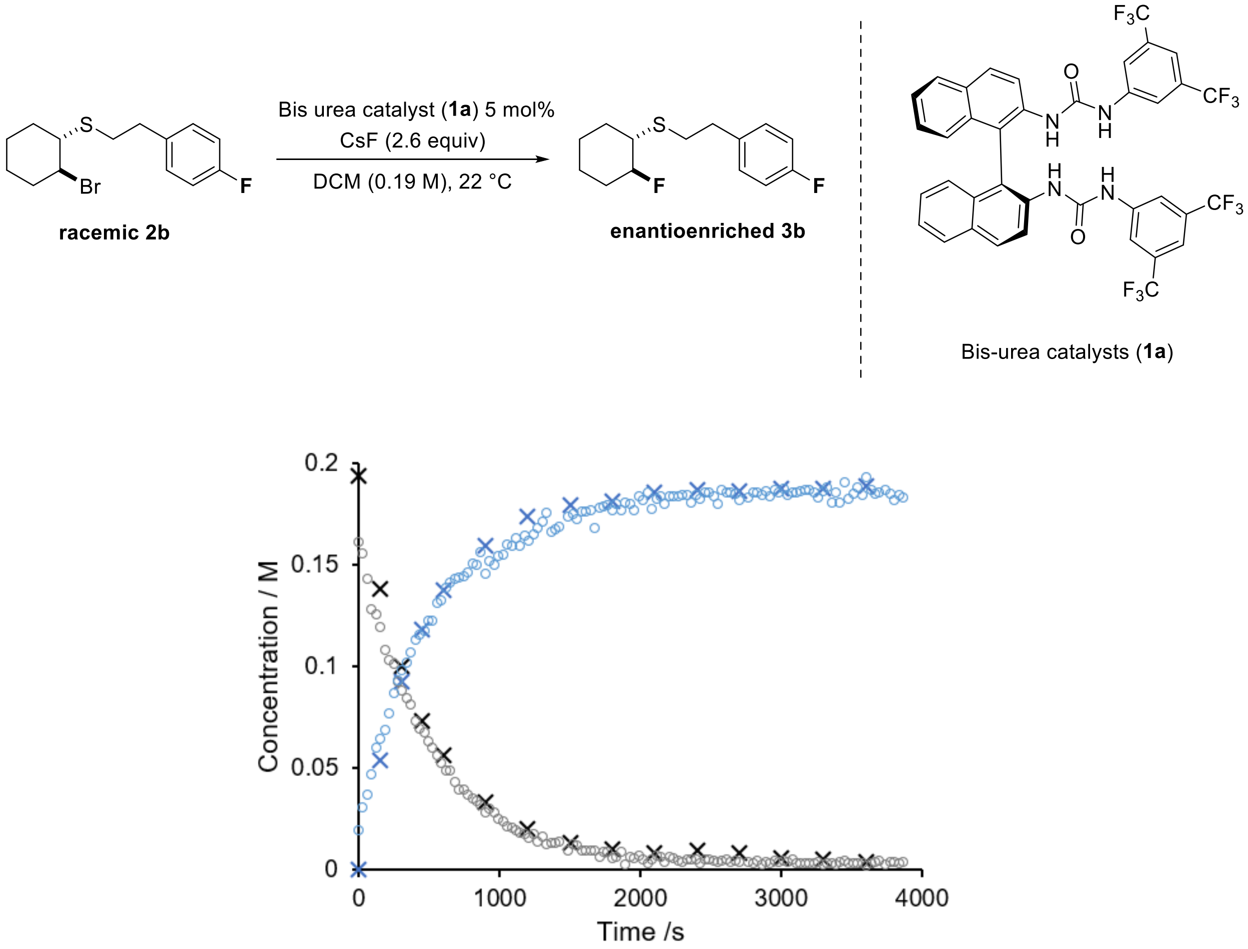

Figure 2.15. The reaction kinetics of phase-transfer catalysed fluorination of β-bromosulfide **2b**, with data acquired by using ^{19}F NMR with *in-situ* mixing device (open circles, mixing speed = 100 mm/s, mixing time = 20 s, settling time = 2 s) or with *ex-situ* sampling method (crosses, stirring speed = 1200 rpm). Plots show the consumption of β-bromosulfide **2b** (grey) and formation of β-fluorosulfide **3b** (blue).

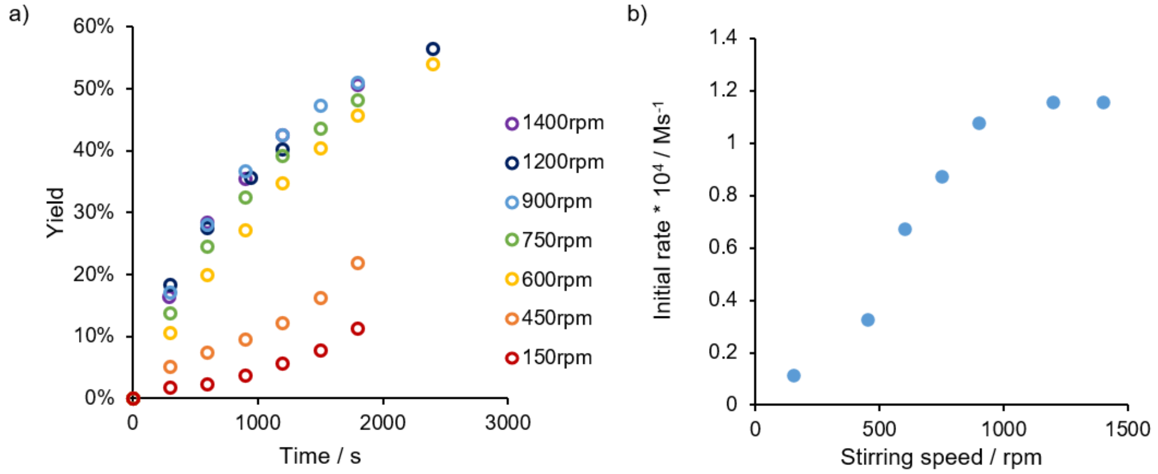

Figure 2.16. Phase-transfer catalysed fluorination of β-bromosulfide ([**2b**] = 0.19 M, [**1a**] = 1.3 mol%) were monitored by *ex-situ* sampling method. a) overlay of percentage yield evolution with varying stirring speed. b) initial rate (*d*[Product]/*dt*) dependence on stirring speed. Figures are taken from Gao *et al.*, 2023.[160]

The *in-situ* NMR mixing device was designed to be compatible with air-sensitive reactions; two gas ports on the top of insert section allow purging of inert gas throughout the device before and during the reaction (**Figure 2.6**b). To test this, an oxygen-sensitive nickel catalysed homocoupling reaction was conducted with *in-situ* mixing device and compared with the same process run in a Schlenk flask (**Figure 2.17**).[166,167] In this reaction, zinc is used as a heterogeneous reductant and the active Ni(0) catalyst is generated in-situ from [$NiCl_2$(glyme)] by mixing with zinc and PPh_3 at 60 °C. Upon activation of catalyst, a deep red solution is formed. If oxygen is present, the catalyst will be deactivated, and the red colour will disappear. After activation of catalyst, substrate was added under a flow of argon and the reaction was monitored by using ^{19}F NMR with *in-situ* mixing device (**Figure 2.17**a). A flow of nitrogen was used throughout the experiment to maintain an inert atmosphere. Though severe peak broadening and thus peak overlap was observed for some of peaks due to mutual effect of mixing and presence of paramagnetic Ni species, peak deconvolution can be applied to acquire reasonably good kinetic data (**Figure 2.17**b).

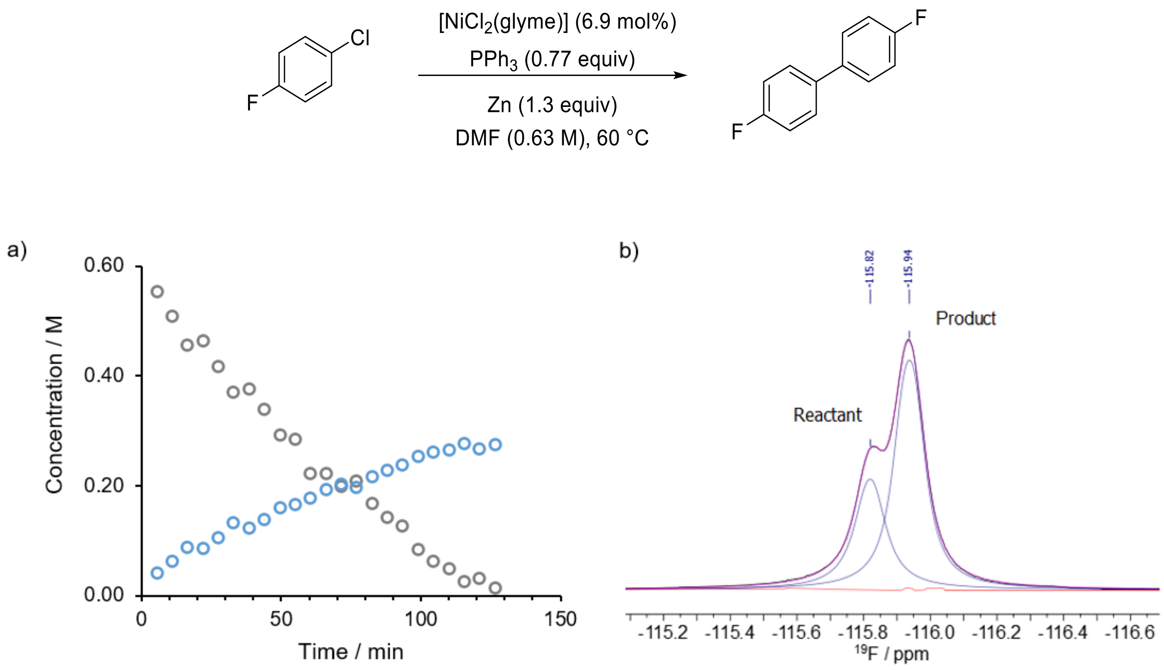

Figure 2.17. Nickel-catalysed Ullmann homocoupling reaction. a) kinetic profile obtained by using ^{19}F NMR and *in-situ* mixing device (mixing speed = 100 mm/s, mixing time = 300 s, settling time = 30 s). Plot shows the consumption of 1-chloro-4-fluorobenzene (grey) and formation of 4,4'-difluorobiphenyl (blue). b) representative peak deconvolution of fluorine peaks of reactant (δF = −115.82 ppm) and product (δF = −115.94 ppm). Each peak was fitted to single generalized Lorentzian function. Figures are reproduced from Gao *et al.*, 2023.[160]

Experiments that similar to the one shown in **Figure 2.16** were conducted to ensure that the apparent rate is not limited by mass transfer.[168] The rates of product formation obtained from *in-situ* and *ex-situ* monitoring methods are in a good agreement, which are 3.0 × 10^{-2} and 3.3 × 10^{-2} M·s^{-1} respectively, indicating that the mixing device is suitable for study of air-sensitive reactions.

3. Phase-transfer catalysed fluorination

3.1 Introduction

In 2018, Pupo *et al.* reported the first example of asymmetric nucleophilic fluorination under PTC.[47] Under optimised conditions, the desired (*S,S*)-β-fluorosulfides **3** were obtained in moderate to high yield and high enantioselectivity. Later, the same group successfully extended this method for synthesis of β-fluoroamines **7** (**Scheme 3.1**).[114] Both products are medicinally valuable. Comparing with other asymmetric fluorination methods, this strategy does not require transition metals or expensive fluorinating agents, and instead uses alkaline metals fluorides, which are abundant, cheap and easy-to-handle. Moreover, the catalysts can be prepared on multigram scale,[169] and the process is scalable, as demonstrated by a 200-g synthesis.[170] All of these make the process synthetically valuable. Whereas previous studies investigated the hydrogen-bonding interactions between the fluoride and the bis-urea catalysts in depth through NMR spectroscopy and single-crystal X-ray diffraction,[117] a detailed mechanistic investigation of the full catalytic cycle is absent.

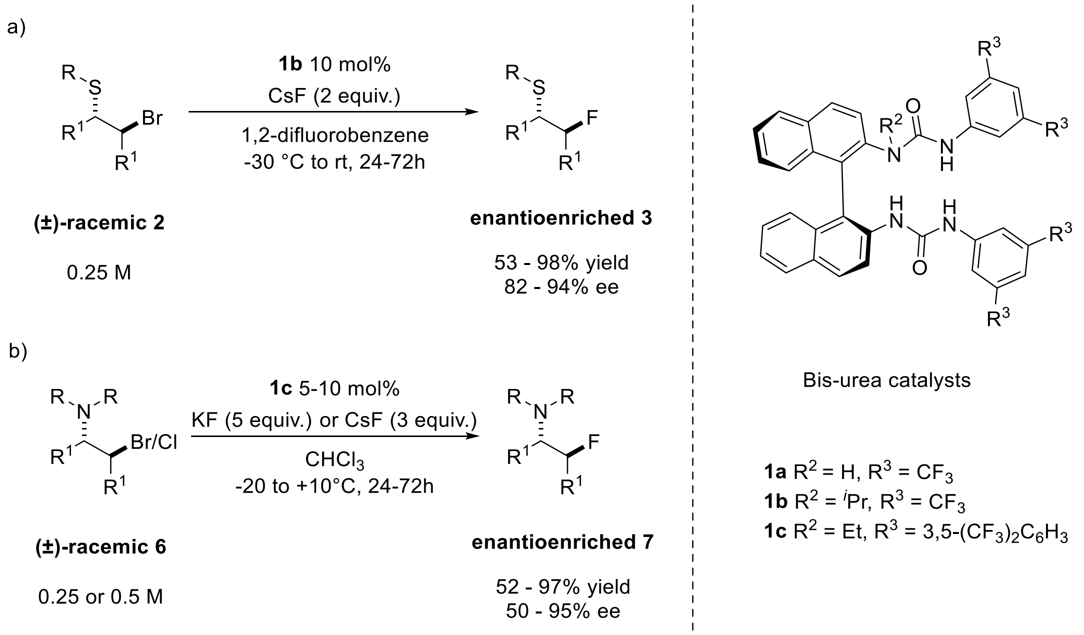

Scheme 3.1. Asymmetric nucleophilic fluorination of β-bromosulfides and β-haloamine with PTC.

3.2 Preliminary studies

3.2.1 Fluorination of β-bromosulfide

The fluorination of racemic β-bromosulfide **2** with chiral bis-urea catalysts **1** was investigated (**Scheme 3.2**). The reaction was run in DCM, using solid CsF as fluorinating agent, and afforded enantioenriched β-fluorosulfide **3** as product. This substrate was selected as it is reported to react with low enantioselectivity (63.5:36.5 e.r.), which allows the formation of each enantiomer to be followed.[47] The performance of catalysts **1a** and **1b** was investigated and compared. Previous studies suggested that non-alkylated catalyst **1a**, though has available four NH groups, forms bidentate complex with fluoride, whereas the *N*-alkylated catalyst **1b** interacts with the fluoride through three hydrogen bonding.[117] High yields (>95%) were obtained when using either catalyst, but the *N*-isopropyl catalyst **1b** gives the highest enantioselectivity among all the tested catalysts.[47]

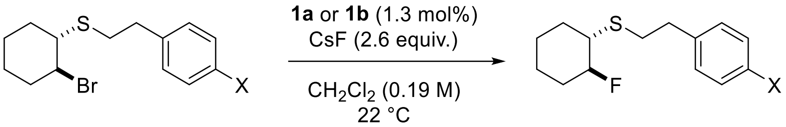

(±)-racemic 2

enantioenriched 3

2a/3a X = H
2b/3b X = F

Scheme 3.2. Fluorination of β-bromosulfide under PTC.

The reaction was first conducted using **1a** and **2a** under the reported literature conditions (**Table 3.1**, entry 1). The purchased CsF was in varied particle size, which was found to affect the reproducibility of the experiments, therefore, ground CsF was used in all following experiments. No reaction was observed in the absence of catalyst (entry 3) or agitation (entry 4), indicating that there is no significant background reaction. Water is detrimental to the yield (entry 4,5). Later investigations revealed that addition of water into the solvent has a negligible impact on the rate of the reaction (see Section 5.4.4.1), whereas water absorbed on CsF significantly slows down the reaction. As CsF is hygroscopic, we suspected that a water shell is formed upon the absorption of water, which reduces the accessibility and reactivity of CsF. CsF is also soluble in water, so increasing amounts of water will promote the background reaction and leads to extra complications. Therefore, dry CsF and anhydrous DCM were used in all studies.

Entry	Catalyst loading / mol%	CsF[a]	Stirring speed / rpm	Yield[b] / %
1	10	dry, direct from bottle	1200	99
2	10	dry, ground	1200	100
3	0	dry, ground	1200	0
4	10	dry, ground	0	0
5	10	14 wt% water, ground	1200	66
6	10	108 wt% water, ground	1200	6

For all runs, [**2a**] = 0.25 M, solvent = anhydrous DCM, temperature = 22 °C, reaction time = 1.5 hours. [a]The purchased CsF is in varied particle sizes. wt% = weight percentage. [b]The end-point yield was determined using ^{19}F NMR with 1-fluoronaphthalene as internal standard.

Table 3.1. The effect of varying reaction conditions on the yield.

Preliminary reaction monitoring revealed that the reaction reached 90% conversion within 10 minutes, making it inconvenient to be followed by conventional *ex-situ* sampling method; preparing each sample is time-consuming (see Section 5.4.1 for more details) and thus leads to scarce kinetic information. Although interleaved experiments can be performed to reconstruct a more data-dense reaction profile, it is labour-intense, and introduces more uncertainty to the data, especially for fast process, as the reactions need to be repeated with identical conditions and sampled at accurate time. [120,171] Thus, a reduced catalytic loading was used in the model reaction to slow down the process, whereas later the development of *in-situ* mixing device allows reactions with higher catalytic loadings to be monitored.

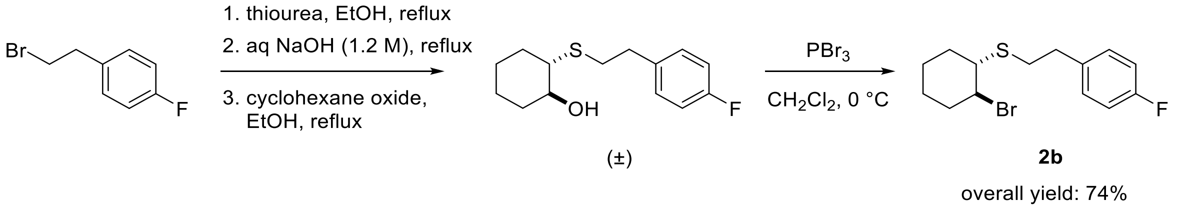

Scheme 3.3. Synthesis of F-labelled substrate **2b**. See Section 5.2 for further details.

While initial investigations were performed with substrate **2a**, F-labelled substrate **2b** was prepared from 4-fluorophenethyl bromide following modified literature procedures (**Scheme 3.3**)[47,172] and used for subsequent reactions to allow all reaction components to be monitored by ^{19}F NMR spectroscopy. The ^{19}F nucleus has comparable sensitivity to that of ^{1}H (83.4%). In comparison with ^{1}H NMR, it has a wider chemical shifts range, less complex spectra (less F atoms per molecule) and does not require the use of deuterated solvent. The ^{19}F NMR is very sensitive to chemical environment, allowing structural similar compounds to be distinguished.

For instance, despite the installed fluorine being remote from the reaction centre, substrate **2b** and product **3b** have distinct chemical shifts (**Figure 3.1**).

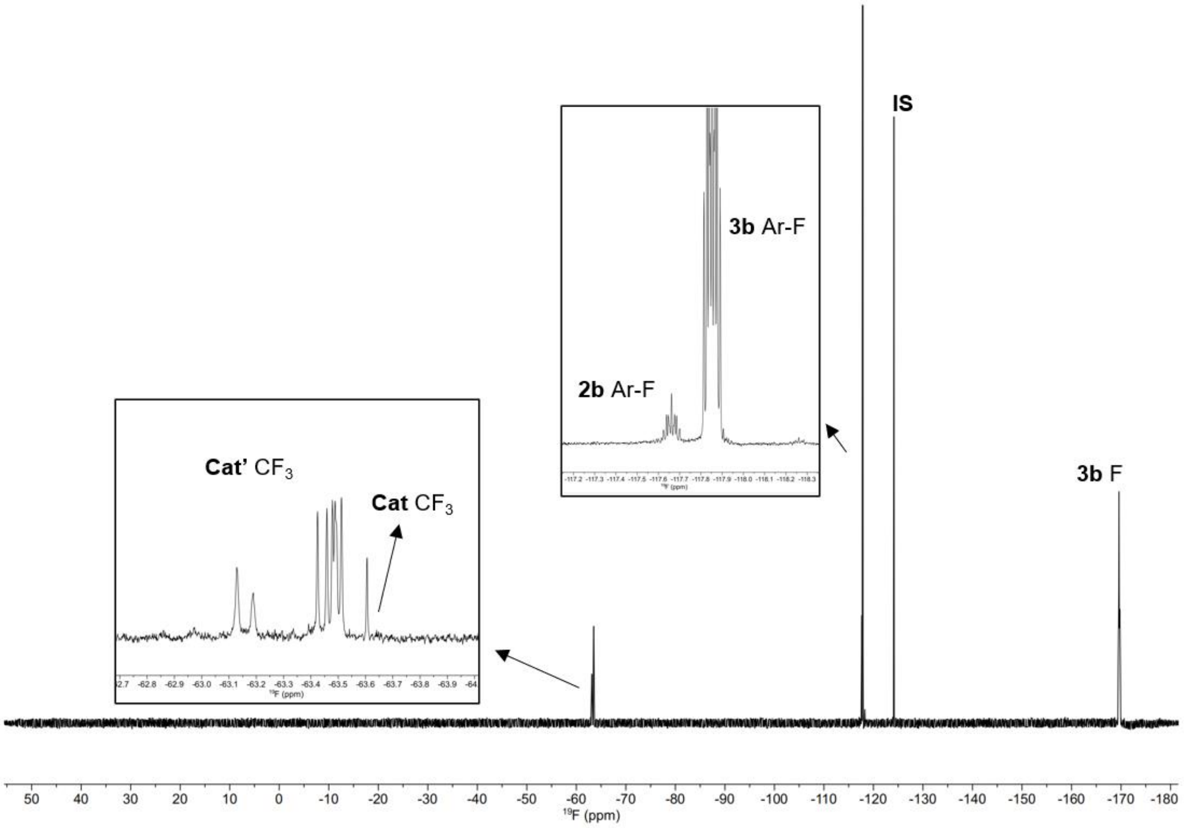

Figure 3.1. A representative ^{19}F NMR spectrum of an *ex-situ* sample of nearly completed reaction mixture, with all reaction components labelled: Cat' = substrate-alkylated catalysts, Cat = catalyst, IS = internal standard.

Before the reaction started, a singlet was observed for catalyst **1a**, corresponding to the four CF_3 groups. During the reaction, the concentration of **1a** decreased, while several peaks with chemical shifts similar to that of **1a** emerged. $^{19}F\{^1H\}$ spectra confirmed that all peaks are singlets. The relative integration of the peaks under varied conditions suggested that they arise from at least two compounds. Later experiments suggested that these peaks corresponded to the CF_3 group of substrate-alkylated catalysts **4a** and **5a** (see Section 3.3). Typical kinetic profiles are shown in **Figure 3.2**. There was no effect of premixing the reaction mixture without substrate, CsF or catalyst. The filtration of reaction mixture effectively quenched the reaction, however we found that **4a** and **5a** were slowly converted back to **1a** after quenching and their speciation was altered during the sampling processes, i.e. filtration, dilution (see Section 5.4.5.5). To minimize these effects, all NMR spectra were taken directly after sampling (within 10 minutes), and the sum of **4a** and **5a**, i.e. Cat', were used in kinetic modelling. The formation of Cat' was not observed in the absence of CsF or substrate under experimental conditions or in the presence of solely catalyst and products **2b** and/or CsBr. Although bis-urea catalysts **1a** and **1b** are known to be complexed with fluoride in DCM, these studies were conducted with either a soluble source of fluoride (TBAF), or a large excess of CsF (50 equiv.) and prolonged sonication.[117] Under the reaction conditions, the formation of [CatFCs] was not observed by NMR spectroscopy, indicating its low concentration and/or fast consumption.

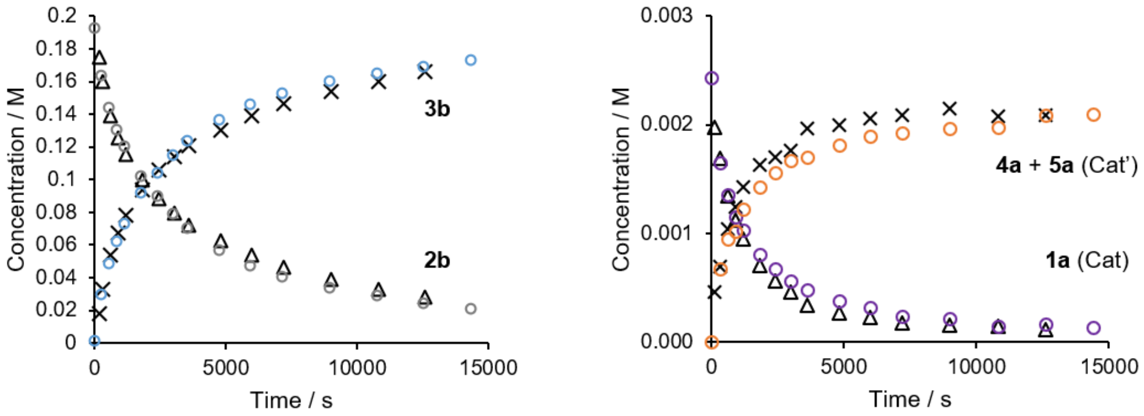

Figure 3.2. Overlayed kinetic profiles of standard reaction and premixed reaction, in which all reaction components except catalyst were mixed for 20 mins before the start of reaction. Initial conditions: [**2b**] = 0.190 M, [Cat] = 0.00245 M. Catalyst related species have lower concentration and are shown separately on the right.

Furthermore, as discussed in Chapter 2, for phase-transfer catalysed reactions, it is important that the reaction is well mixed, and the rate of reaction is not limited by the mass transfer. To ensure that, a series of experiments were conducted in flask (*ex-situ*) or NMR tube (*in-situ*) with varied mixing speed, and plots of initial rate against mixing speed were constructed for each combination of substrate and catalyst to guide the selection of mixing speed (see Section 2.4.4 and 5.4.3.1).

3.2.2 Fluorination of β-chloroamine

The same bis-urea catalysts also promote fluorination of β-chloramines.[114] The fluorination of stilbene-derived β-chloroamine **6a** with 2 equivalent CsF, catalysed by **1a** or **1b** in chloroform was investigated (**Figure 3.3**). Compound **6a** was chosen because it is a previously reported substrate for this transformation and contains fluorine, which facilitates reaction monitoring. **6a** was prepared following literature procedures (see Section 5.2). Again, no reaction was observed in the absence of catalyst or agitation, confirming that there is no background reaction. Wet solvent with water concentration higher than that of catalyst has no impact on the rate of the reaction (see Section 5.4.4.2). To get reproducible results, dry ground CsF and anhydrous acid-free chloroform were used in all studies. This reaction proceeds slower than that of β-bromosulfide, allowing the reaction to be monitored under the reported catalyst loadings.[114] As shown in **Figure 3.3**, the concentration of catalyst remained constant during the reaction.

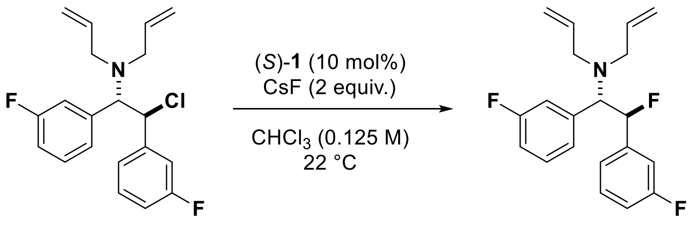

(±)-6a **enantioenriched 7a**

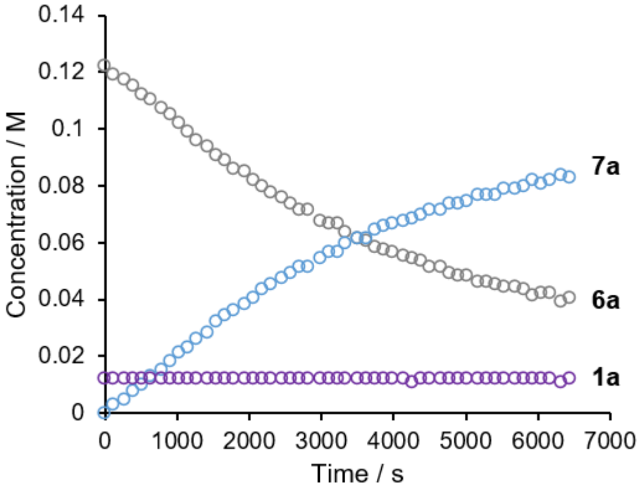

Figure 3.3. A kinetic profile of phase-transfer catalysed fluorination of β-chloroamine.

3.3 Substrate-alkylated catalyst

CsF is moderate basic, therefore it is reasonable to propose that it deprotonates the catalyst to facilitate its nucleophilic attack of the episulfonium bromide and leads to the formation of substrate-alkylated catalyst species. There have multiple possible structures as both catalysts have multiple NH groups, and the substrate is racemic. One possible structure for Cat' is shown in **Scheme 3.4**.

Although Cat' species are relatively stable under reaction conditions, they tend to decompose when exposed to water and acidic conditions. Isolation of Cat' by crystallisation or column chromatography failed and led to recovery of catalyst in all cases. However, several experiments supported this postulation: 1) the decomposition of Cat' leads the quantitative formation of **1a** and β-hydroxyl sulfide **8** (**Figure 3.4**), which was verified by spiking; 2) electrospray ionisation mass spectra (ESI-MS) of the catalyst and reaction mixture at 0, 50 and 90% conversion showed gradual formation of a species with a mass that is consistent with that of substrate-alkylated catalyst; 3) species with similar chemical shifts were formed when tetramethylguanidine was added to a solution of catalyst and substrate; 4) Cat' derived from **1a** can also catalyse the fluorination with a slower but not insignificant rate --- incorporation of this in the mechanism is important to get an overall fit for reactions with varied catalytic loading. For all experiments, further details are discussed in Section 5.4.5.

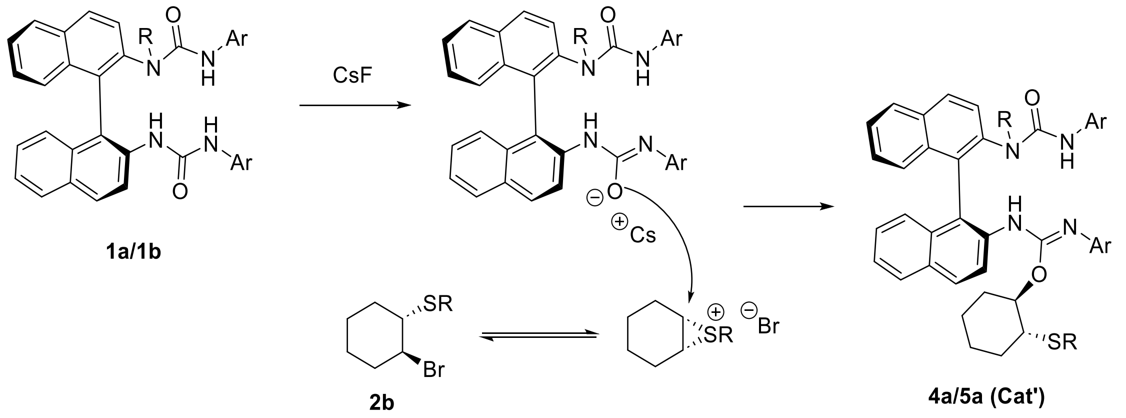

Scheme 3.4. Formation of substrate-alkylated catalyst. One possible structure of Cat' is shown.

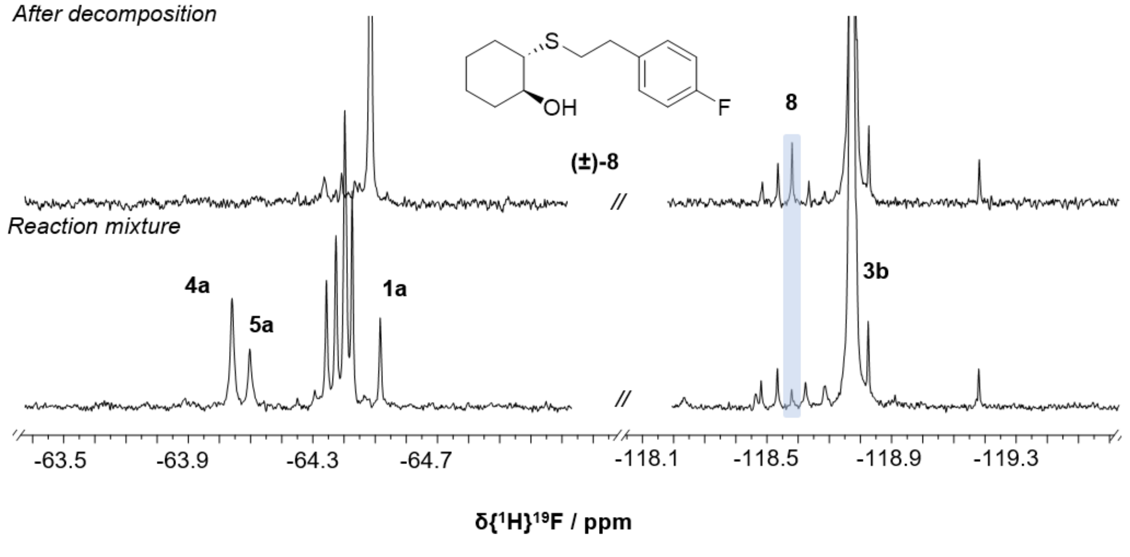

Figure 3.4. $^{19}F\{^1H\}$ NMR spectra of the reaction mixture after reaching completion, and the same mixture after decomposition of Cat'.

3.4 Ionisation of substrate

Previous density functional theory (DFT) calculations based on β-bromosulfide **2c** and urea catalyst **9** suggested the fluorination was initiated by ionisation of β-bromosulfide to give a tight episulfonium-bromide ion pair, **2-i**, followed by ion pair dissociation, anion exchange, ion pair recombination and fluorination (**Scheme 3.5**).[173] Due to the much higher lattice energy of CsF compared to CsBr, the halide exchange was prohibited for the uncatalysed route. Urea type catalysts promoted the fluorination by coordinating with the bromide and favouring the halide exchange, since stronger H-bonding occurs between the catalyst and fluoride then that with bromide. To get further insights of this ionisation process, we performed magnetisation transfer experiments to measure the rate of formation, k_1, of episulfonium-bromide ion pair under various conditions.

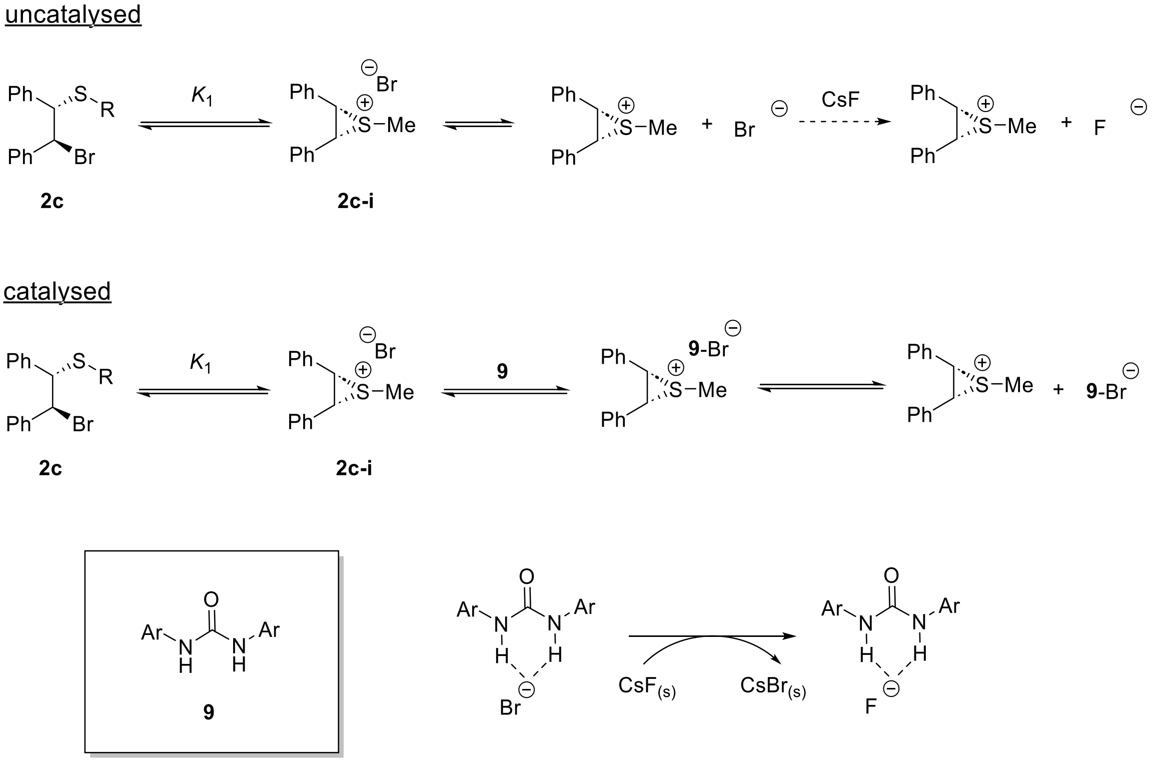

Scheme 3.5. Ionisation of substrate and catalyst promoted anion exchange.[47]

The pulse sequence of magnetisation transfer experiment is shown in **Figure 3.5**a: after a relaxation delay, RD, a soft 180° pulse was used to selectively inverted a range of frequencies covering one of the exchange peaks (spin A), followed by a variable delay time, VD, a 90° pulse and data acquisition.[173] During the variable delay time, the magnetisation evolves according to both chemical exchange kinetics and longitudinal relaxation of all of the involved spins. A kinetic model for a typical two-spin system is shown in **Figure 3.5**b. By monitoring the intensities of both spins at varied delay time, and a knowledge of longitudinal relaxation, T_1, of both spins, the rate of exchange, k_1, can be measured.

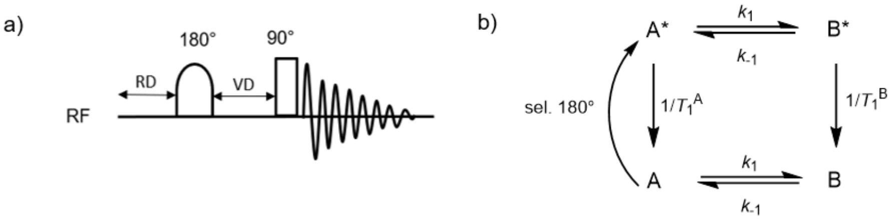

Figure 3.5. Magnetisation transfer experiment. a) Pulse sequence, where RD = relaxation delay, VD = varied delay. b) Kinetic model for a two-spin system, where spin A is inverted by the selective 180° soft pulse to A* and undergoes chemical exchange with B*, and both A* and B* undergo relaxation.

The ionisation of β-bromosulfide **2b** involves a slightly more complex scenario than that described in **Figure 3.5**b because spin A and B undergo exchange through an intermediate S (**Figure 3.6**a). For **2b**, S is the episulfonium-bromide intermediate. We didn't observe a separate set of peaks for S during the magnetisation transfer experiments, indicating that the concentration of this intermediate is very low with respect to β-bromosulfide. Therefore, it is reasonable to assume that the relaxation of S* has a negligible effect on the overall kinetics.

Since **2b** is racemic, the ionisation of both enantiomers needs to be considered. The ionisation of (*S*,*S*)-**2b** is shown in **Figure 3.6**b as an example. H_a and H_b have distinct chemical shifts ($\Delta\delta_H$ = 1.3 ppm). H_a in **2A** undergoes intramolecular exchange with H_b in **2B** through the closing and opening of episulfonium ring. This rate of exchange is unmeasurable without magnetisation transfer because **2A** and **2B** are enantiomers and we are unable to differentiate H_a in **2A** and **2B**. With a selective 180° pulse, the magnetisation of H_a is inverted, i.e. magnetically labelled. Thus, the H_a and H_a* in **2A*** and **2B*** can be distinguished. The intensities of H_a and H_b are determined by k_1, the longitudinal relaxation time, T_1, of both H_a and H_b and the delay time between inversion and measurement, as long as the proportion of **2S/2S*** in solution is insignificant. T_1^A and T_1^B were measured under experimental conditions. k_{-1} can be determined by measuring the integration of both protons with varied delay time, and then fitting to the kinetic model described in **Figure 3.6**b (see Section 5.5.3). The k_1 is equal to two times of k_{-1} since only half of the ring opening process measurable, i.e. change from **2S*** to **2A*** won't affect the magnetisation of H_a and H_b.

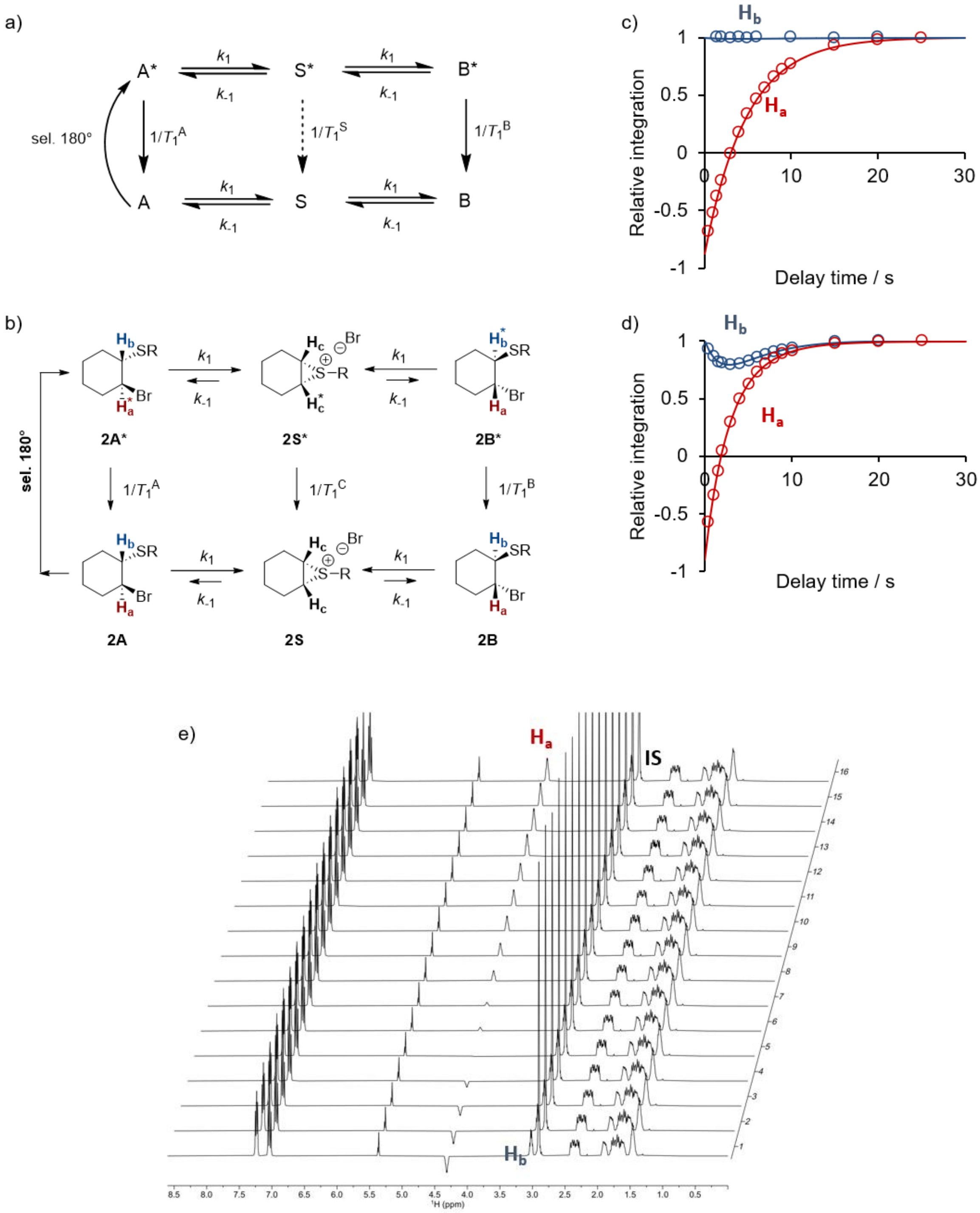

Figure 3.6. a) Kinetic model for a three-spin system, where spin A is inverted by the selective 180° soft pulse to A* and undergoes chemical exchange with B* through intermediate S*, and A*, B* and S* all undergo relaxation. b) Kinetic model for the same scenario as that in b) with one enantiomer of β-bromosulfide **2b** as an example. c) Typical plot when k_1 is two orders of magnitude smaller than $1/T_1$; [**2b**] = 0.19 M, T = 300 K, $k_1 < 0.004$ s^{-1}. d) Typical plot when k_1 is comparable to the rate of relaxation, $1/T_1$; [**2b**] = 0.19 M, [**1a**] = 0.196 M, T = 300 K, $k_1 = 0.11 \pm 0.01$ s^{-1}. For c) and d), experimental data (circle) and kinetic simulations (line) were indicated for both H_a (red) and H_b (blue). e) A representative stack of spectra of magnetisation transfer experiments ([**2b**] = 0.19 M, T = 300 K.). A random delay list was used during the experiment. The obtained spectra were reordered according to delay time (the delay time increased from 0 s to 25 s from bottom to top).

Since the inverted magnetisation is constantly being relaxed back to its ground state during the whole experiment, it is important that k_1 is in the range of $10^{-2} - 10^{3}$ ($1/T_1$) to allow accurate measurement of the rate. A typical plot for small k_1 is shown in **Figure 3.6**c: the intensity of H_b stayed at its maximum and was almost unaffected by the exchange. Whereas for a larger k_1, an asymmetric V-shape was observed (**Figure 3.6**d).[120] A representative stack of spectra of magnetisation transfer experiments is shown in **Figure 3.6**e, with descending delay time. A random delay list was used during the experiment to minimise any artifacts caused by experimental setting. An unaffected proton was selected as internal standard and the relative integration for H_a and H_b was calculated by referring to the integration of internal standard and standardised with respect to their maximum intensity (see Section 5.5.2).

The rate of ionisation of 0.19 M **2b** in anhydrous deuterated DCM with varied catalyst concentrations under different temperature was measured and the results are plotted in **Figure 3.7**. Both catalysts significantly accelerate the rate of ionisation. The ionisation rate of **2b** at 300 K is 3×10^{-3} s^{-1}. At the same temperature, the non-alkylated catalyst **1a** enhances the rate by 1.11 $s^{-1}M^{-1}$ and the *N*-isopropyl catalyst **1b** enhances the rate by 3.62 $s^{-1}M^{-1}$, which is more than three-fold that of catalyst **1a**.

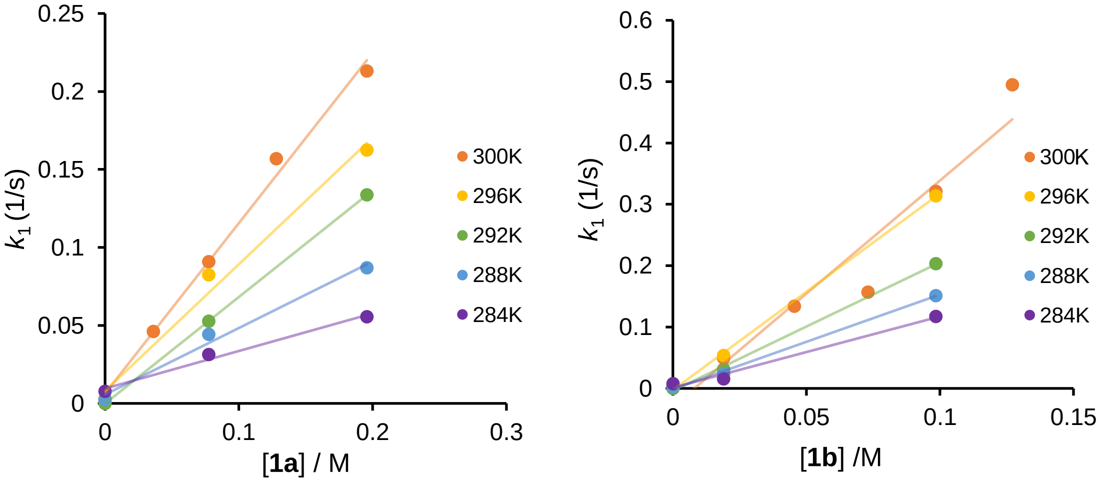

Figure 3.7. Plots of ionisation rate, k_1, of **2b** against catalyst concentration under different temperatures. [**2b**] = 0.19 M.

Eyring plots (**Figure 3.8**) were then used to estimate the enthalpy of activation, $\Delta H^{\ddagger}$, and entropy of activation, $\Delta S^{\ddagger}$, of uncatalysed and catalysed ionisation. For uncatalysed ionisation, k_1 values measured under different temperatures were used directly to construct the plot (triangle, right y-axis). For catalysed ionisation, a catalyst concentration averaged k_1 was calculated for each temperature, which was then used to construct the plots (**1a** square, **1b** circle, left y-axis). The general form of Eyring equation is shown in Eq. 3.1, which can be rearranged into Eq. 3.2 to calculate the values of $\Delta H^{\ddagger}$ and $\Delta S^{\ddagger}$. The results are shown in **Table 3.2**.

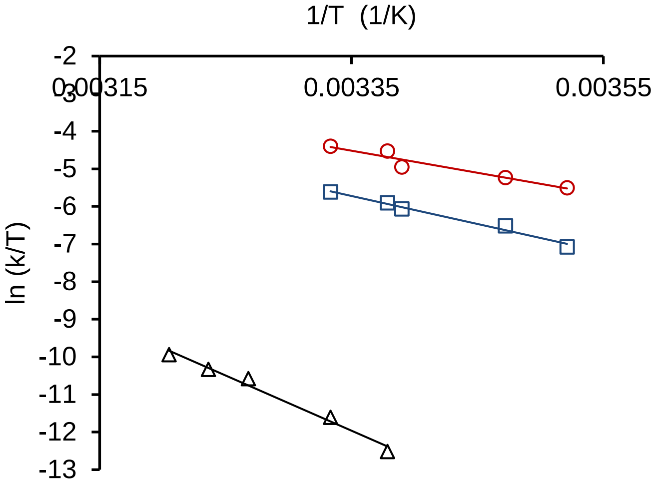

Figure 3.8. Eyring plots of only substrate **2b** (triangle), with **1a** (square), with **1b** (circle).

$$k = \frac{k_B T}{h} e^{\frac{\Delta S^{\ddagger}}{R}} e^{\frac{-\Delta H^{\ddagger}}{RT}} \tag{3.1}$$

$$\ln k/T = \frac{-\Delta H^{\ddagger}}{R}\frac{1}{T} + \ln\frac{k_B}{h} + \frac{\Delta S^{\ddagger}}{R} \tag{3.2}$$

	$\Delta H^{\ddagger}$/ kJ mol^{-1}	$\Delta S^{\ddagger}$/ J mol^{-1} K^{-1}
***2b** only*	122 ± 9	112 ± 11
*with **1a***	62 ± 5	−38 ± 4
*with **1b***	49 ± 8	−72 ± 16

Table 3.2. Enthalpy and entropy of activation for catalysed and uncatalyzed ionization.

A small positive $\Delta H^{\ddagger}$ is consistent with a simultaneous formation and breakage of bond, and a better solvation of partially charged activated complex. The presence of the catalyst further lowers the $\Delta H^{\ddagger}$ as the breakage of C-Br bond is compensated by the formation of hydrogen bonding between the bromide and catalyst. A positive $\Delta S^{\ddagger}$ was observed for the uncatalysed ionisation, which indicated that the activated complex comprises a loosely bonded ion pair. On the contrary, negative $\Delta S^{\ddagger}$ values were observed for catalysed ionisation as preorganization of catalyst is required for forming the desirable hydrogen bonding.

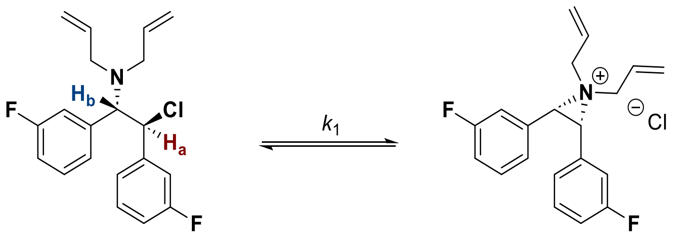

(±)-6

6-i

Scheme 3.6. Investigation of ionisation of β-chloroamine by magnetisation transfer. H_a is the inverted proton, H_b is the exchanged proton.

A similar approach was used to measure the rate of ionisation of β-chloroamine (**Scheme 3.6**). The proton adjacent to the chloride was inverted (H_a, δ_H = 5.3 ppm), which exchanged with the proton adjacent to the amine group (H_b, δ_H = 4.3 ppm). Deuterated anhydrous chloroform was used to mirror the experimental conditions. The rate of ionisation of 0.19 M **2b** with varied catalyst concentrations under different temperature was measured. Representative relative integration-delay time plots with only substrate, with 100 mol% catalyst **1a**, and with 100 mol% of catalyst **1b** are shown in **Figure 3.9**a to c respectively.

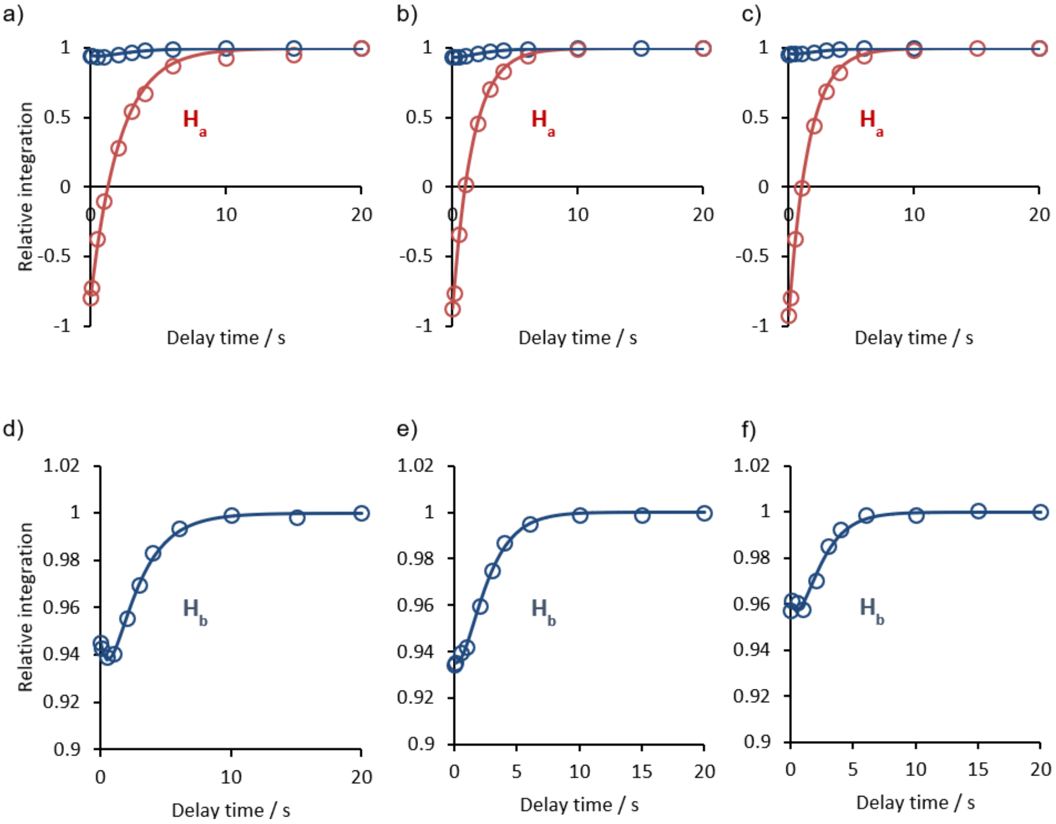

Figure 3.9. Representative integration-delay time plots for a) [**6**] = 0.19 M, $CDCl_3$, T = 300 K, $k_1 = 0.11 \pm 0.01\ s^{-1}$; b) [**6**] = 0.19 M, [**1a**] = 0.19 M, $CDCl_3$, T = 300 K, $k_1 = 0.07 \pm 0.01\ s^{-1}$; c) [**6**] = 0.19 M, [**1b**] = 0.19 M, $CDCl_3$, T = 300 K, $k_1 = 0.06 \pm 0.01\ s^{-1}$. The change in the relative integration of H_b is small, therefore, a zoomed in version for plots a) to c) are shown in d) to f) respectively.

Unlike that observed with β-bromosulfide, both catalysts have no impact on the rate of ionisation of β-chloroamine (**Figure 3.10**, left). The process is also not sensitive to temperature (**Figure 3.10**, right). Fluctuation of data was observed because the measured rate is subject to large percentage of error --- the ionisation rate is slow with respect to the relaxation of the measured protons. Whereas the reported error is propagated from the fitting (see Section 5.5.3), a larger error was introduced during the standard spectral processing, e.g. phase correction and baseline correction.

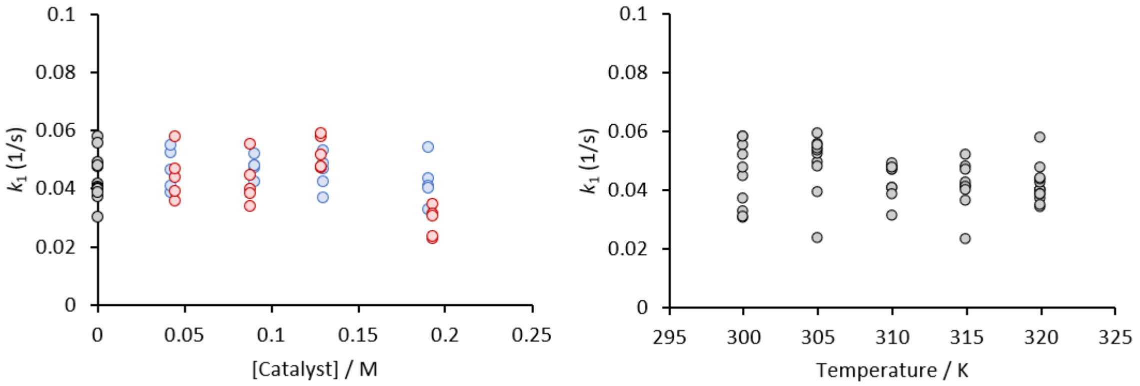

Figure 3.10. Plots of ionisation rate, k_1, against catalyst concentration (left, with **1a** = blue, with **1b** = red) and against temperature (right) for β-chloroamine.

3.5 Systemic kinetic variation

To investigate the kinetic behaviour of these fluorinations, temporal concentration profiles of over 40 reactions with different initial conditions were obtained either by *in-situ* or *ex-situ* monitoring technique with NMR spectrometer. The effect of varying initial concentration of substrate, catalyst and the amount of CsF was investigated for each combination of substrate (**2b** and **6a**) and catalyst (**1a** and **1b**). Selected datasets are shown below to aid the discussion of general trends, whereas all datasets were used in kinetic modelling to facilitate identification of general mechanisms.

3.5.1 Fluorination of β-bromosulfide

Experiments were performed using different initial concentrations of β-bromosulfide **2b**, under otherwise the same conditions (**Figure 3.11**). For all experiments, the total concentration of the substrate and the product was constant overtime, and no formation of side products were observed. The initial rate of the reaction does not follow simple zero- or first-order behaviour.

Changing the substrate concentration has a negligible impact on the catalyst speciation. The total concentration of catalyst **1a** and **Cat'** decreases over time, which could be due to decomposition of catalyst or formation of substrate-alkylated catalysts other than **4a** and **5a**. Very small peaks were observed with chemical shifts near (± 1 ppm) the ^{19}F peak of **1a**, and when these peaks were taken into total concentration, the mass lost became less.

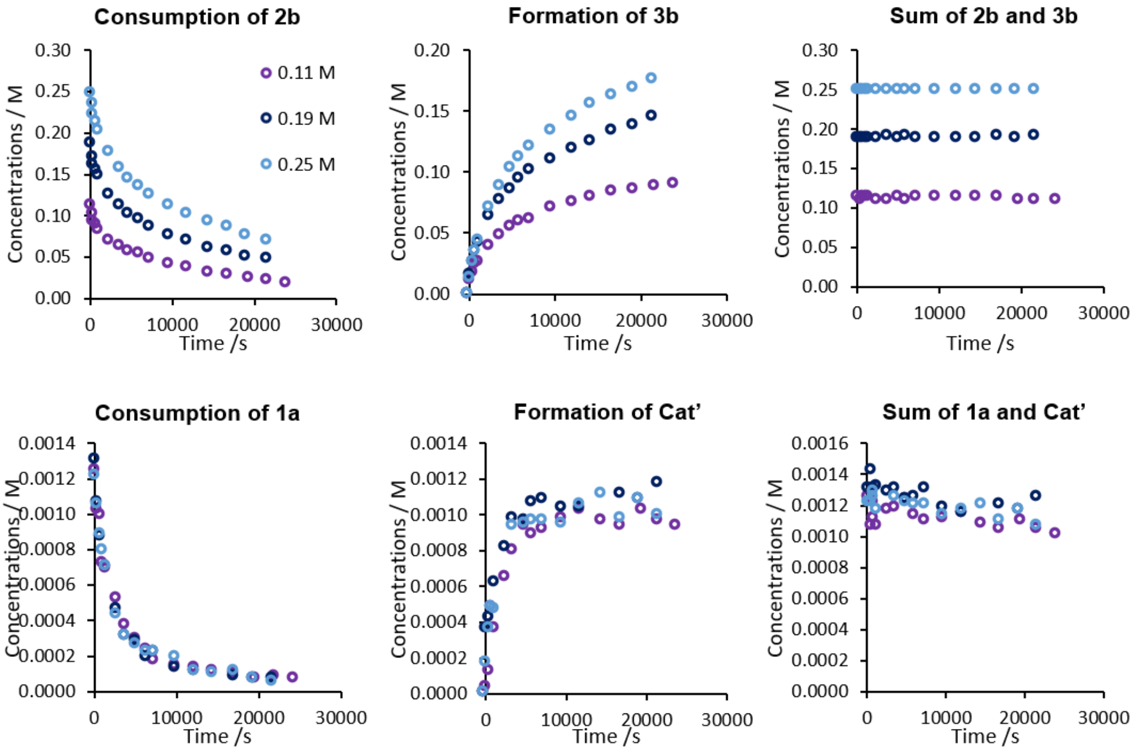

Figure 3.11. Overlaid plots detailing the effect of varying starting substrate concentration, [**2b**]$_0$, on the major species present during the reaction against the time. Each colour represents a different initial substrate concentration with [**1a**]$_0$ = 1.25 mM, initial amount of CsF equivalent to 0.5 M.

Experiments were performed using catalyst loading varying from 0.7 mol% to 5.1 mol%, under otherwise the same conditions (**Figure 3.12**). The reaction is faster with higher catalyst concentration, but initial rate does not have a simple dependence on the total catalyst concentration. A logarithm plot of initial rate and [**1a**]$_0$ is shown in **Figure 3.12**. The fitted line has a gradient of 1.15, and it is obvious that the last two points, corresponding to 3.2 and 5.1 mol% catalyst, deviate from the line. Due to the complexity of the reaction and the constantly consumption of **1a** (**Figure 3.12**), the actual value of the gradient does not reflect the order of the catalyst in the reaction. Therefore, kinetic modelling was used to further probe the overall reaction mechanism (see Section 3.6.1). Varying the initial amount of CsF has a small impact on the reaction rate (**Figure 3.13**). Using excess amounts of CsF leads to a slower product formation at higher conversion, and a slightly faster consumption of catalyst **1a**. Both can be attributed to the basic nature of CsF.

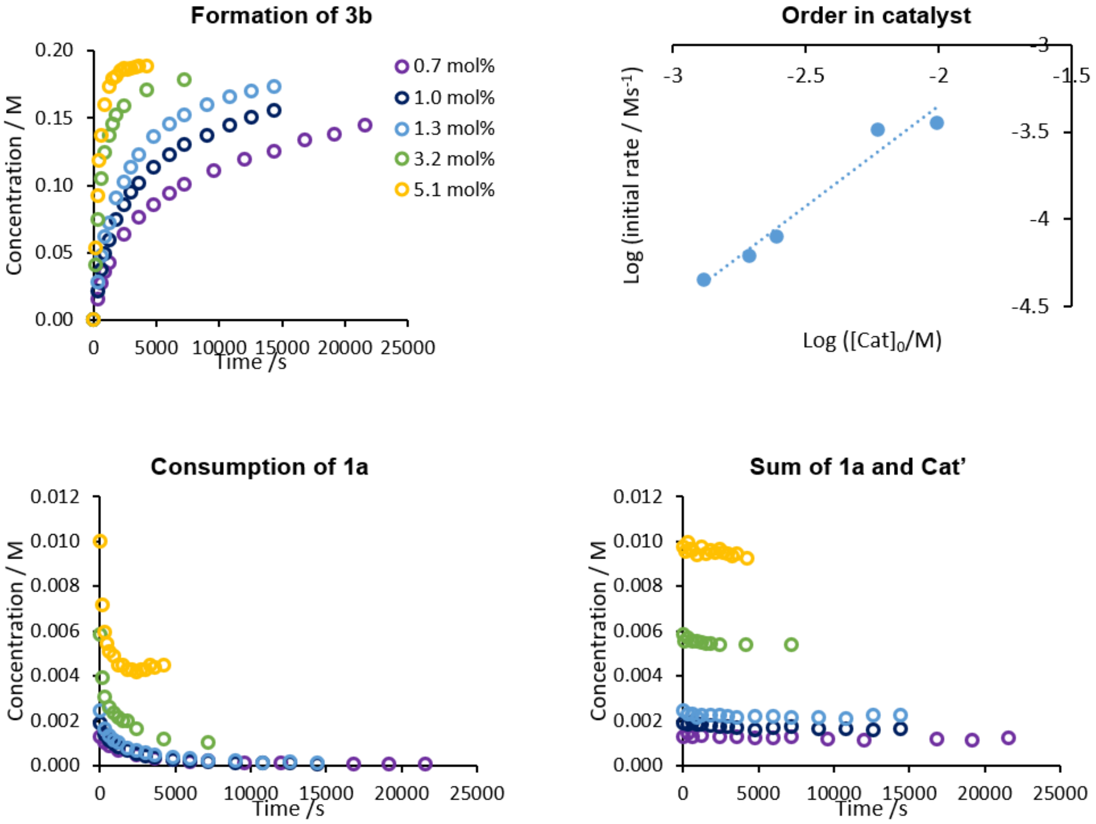

Figure 3.12. Overlaid plots detailing the effect of varying starting catalyst concentration on the concentrations of product, catalyst, and sum of **1a** and **Cat'** during the reaction against the time. Each colour represents a different initial catalyst concentration with [**2b**]$_0$ = 190 mM, initial amount of CsF equivalent to 0.5 M. Top right: a logarithm plot of initial rate against initial catalyst concentration.

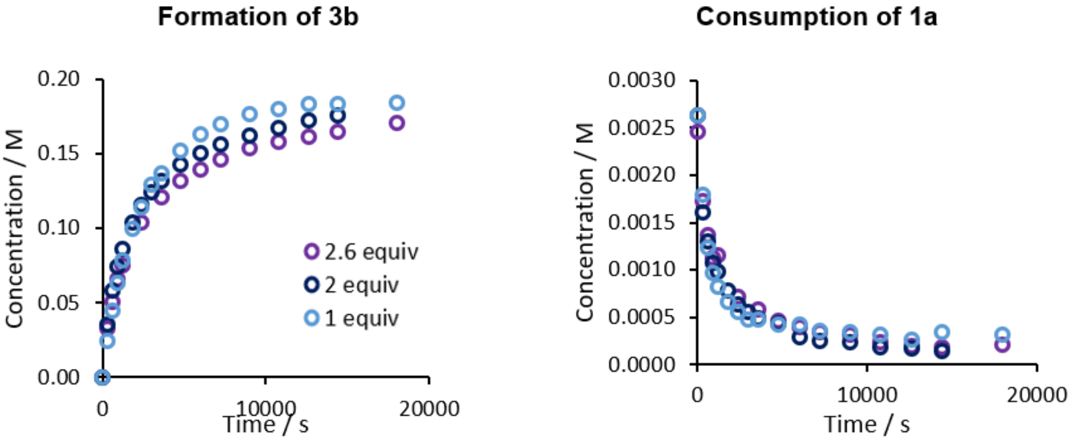

Figure 3.13. Overlaid plots detailing the effect of varying starting CsF amount on the concentrations of product, and catalyst during the reaction against the time. Each colour represents a different initial amount of CsF with [**2b**]$_0$ = 190 mM, [**1a**]$_0$ = 2.6 mM.

Similar experiments were conducted using β-bromosulfide **2b** and catalyst **1b** (**Figure 3.14, Figure 3.15**). Unlike that with **1a**, the change in temporal concentration of catalyst **1b** is much smaller (**Figure 3.14**). The four CF_3 groups of the catalyst appear as a doublet in the ^{19}F NMR spectrum. Although small peaks with chemical shifts similar to that of **1b** emerged, their concentrations are very low and subject to large error, making it hard to group them based on relative integrations. Decomposition experiments showed that some of these peaks corresponds to substrate-alkylated catalyst (see **Figure 5.16**), but the total concentration of **Cat'** cannot be calculated. Therefore, only the concentration of catalyst **1b** was measured. With the same concentration of catalyst, more catalyst is lost with lower substrate concentration. As shown in **Figure 3.15**, the reaction is faster with higher catalyst concentration. Varying the initial amount of CsF from 1.2 equivalent to 4.0 equivalents has a negligible effect on the rate of product formation.

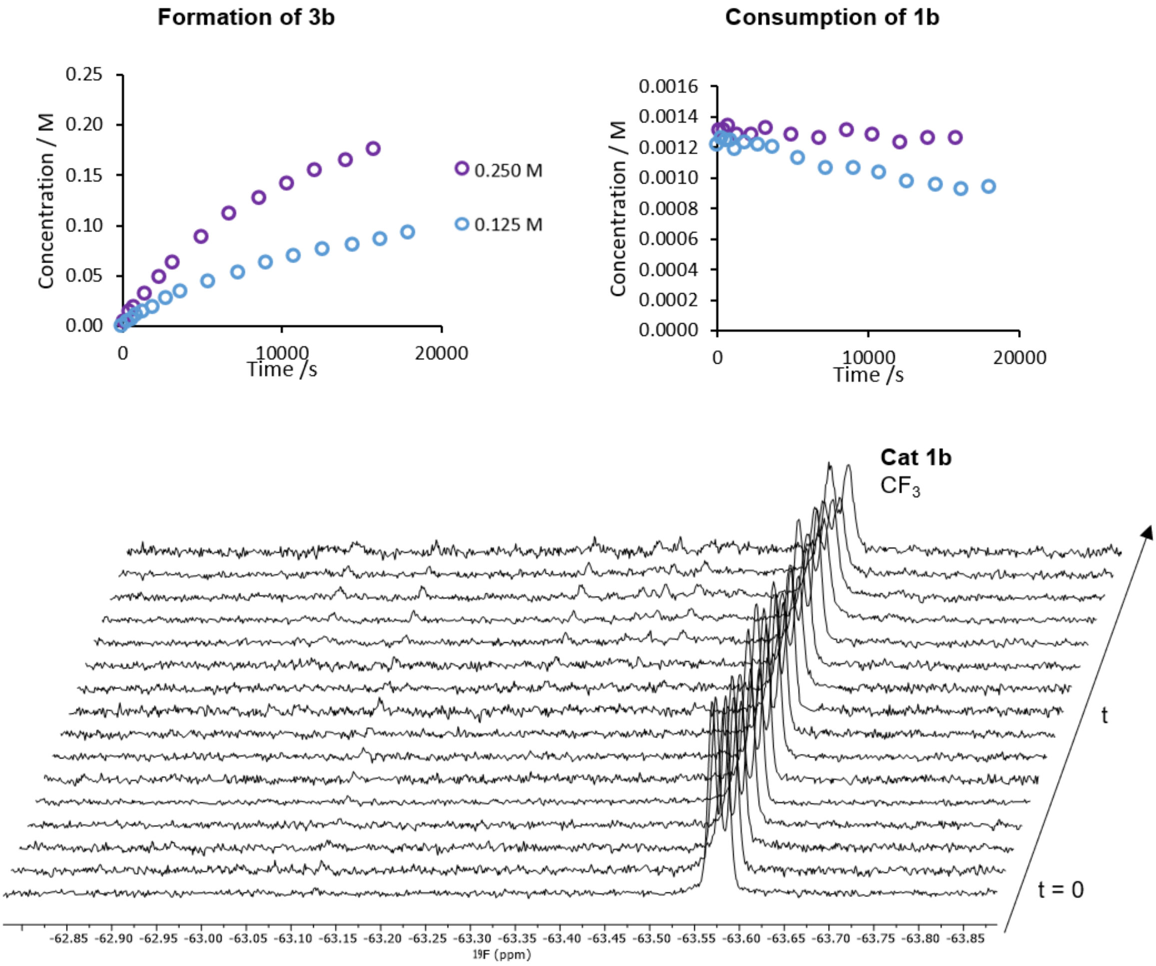

Figure 3.14. Above: overlaid plots detailing the effect of varying starting substrate concentration, $[\mathbf{2b}]_0$, on the concentrations of product, and catalyst during the reaction against the time. Each colour represents a different initial substrate concentration with $[\mathbf{1b}]_0$ = 1.25 mM, initial amount of CsF equivalent to 0.5 M. Below: a stack of partial ^{19}F NMR spectra focusing on the catalyst signals. Initial conditions: [**2b**] = 0.250 M, [**1b**] = 1.25 mM.

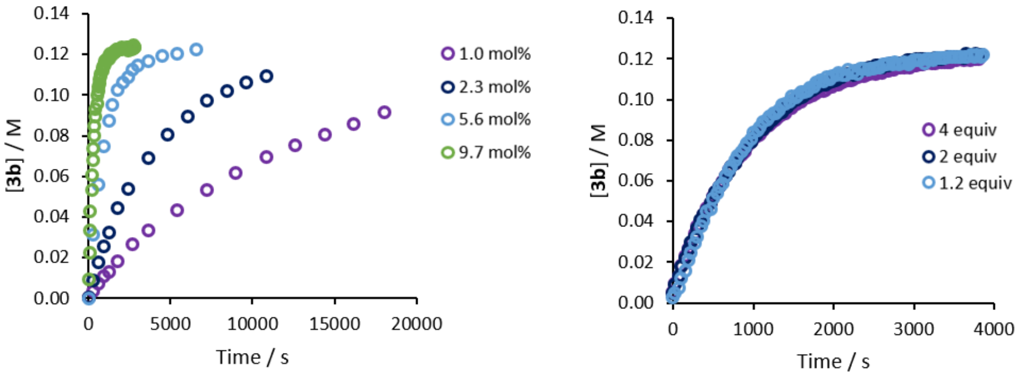

Figure 3.15. Overlaid plots detailing the effect of varying starting catalyst concentration **1b** (left) or starting CsF amount (right) on concentration of products during the reaction against the time. Each color represents a different initial catalyst concentration or starting CsF with [**2b**]$_0$ = 0.125 M. For left plot, CsF equivalent to 0.5 M. For right plot, [**1b**]$_0$ = 6.3 mM.

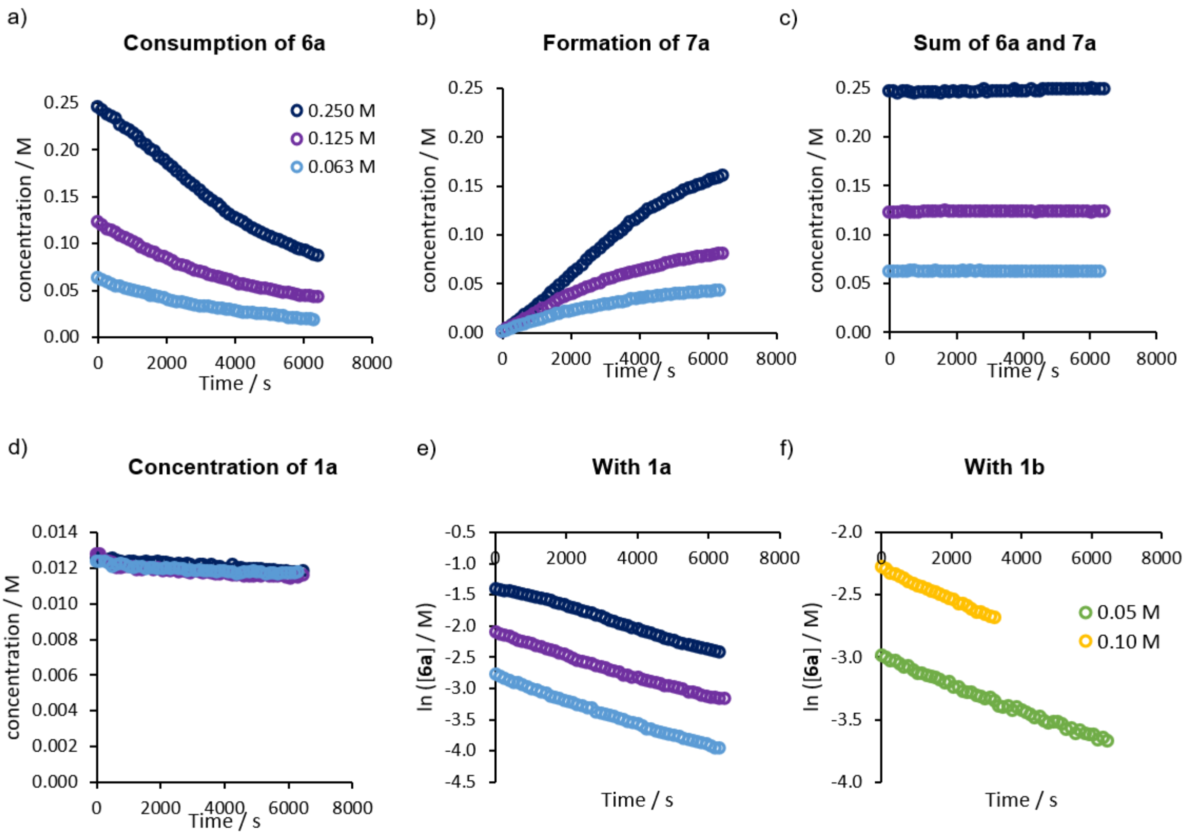

Figure 3.16. a) – d) Overlaid plots detailing the effect of varying starting substrate concentration, [**6a**]$_0$, on the major species present during the reaction against the time. e) Semi-logarithmic plot of ln ([**6a**]$_t$) against time. Each colour represents a different initial substrate concentration with [**1a**]$_0$ = 12.5 mM, initial amount of CsF equivalent to 0.5 M. f) Semi-logarithmic plot of ln ([**6a**]$_t$) against time. Each colour represents a different initial substrate concentration with [**1b**]$_0$ = 10 mM, initial amount of CsF equivalent to 0.2 M.

3.5.2 Fluorination of β-chloroamine

Experiments were performed using different initial concentrations of β-chloroamine **6a**, under otherwise the same conditions (**Figure 3.16a–d**). For all experiments, the total concentration of the substrate and the product was constant overtime. Approximately 8% of catalyst was lost after 105 minutes of reaction, which may be due to the decomposition of catalyst as no new CF_3 peaks appear in the ^{19}F spectrum during the reaction. Also, there is no clear correlation between the amount of lost catalyst and the initial concentration of substrate. The reaction is first-order in substrate as a plot of the natural logarithm of the concentration of **6a** against time gives straight line (**Figure 3.16e**). This linearisation is based on the following rate law and integrated rate law (Eq. 3.3 to 3.5). This observation holds true when using catalyst **1b** (**Figure 3.16f**).

$$rate = \frac{d[\boldsymbol{6a}]}{dt} = k_{obs}\,[\boldsymbol{6a}] \tag{3.3}$$

$$[\boldsymbol{6a}] = [\boldsymbol{6a}]_0 e^{-k_{obs}t} \tag{3.4}$$

$$\ln[\boldsymbol{6a}] = \ln\,[\boldsymbol{6a}]_0 - k_{obs}t \tag{3.5}$$

Experiments were also performed using different catalyst concentration (**Figure 3.17**). Since the rate is first-order in substrate, the observed rate constant, k_{obs}, for different catalyst loading was calculated from the linear regression analysis of the semi-logarithmic plots (**Figure 3.17**b and d). To investigate the role of the catalyst, k_{obs} was plotted against the concentration of the catalyst. For non-alkylated catalyst **1a**, a linear relationship was observed (**Figure 3.17**c), which indicated that the reaction is first-order in catalyst. For *N*-isopropyl catalyst **1b**, the rate also increased with increased catalyst loading, but the rate enhancement is smaller at higher catalyst concentration (**Figure 3.17**f). This might be due to the formation of inactive or less reactive [(**1b**)$_2$FCs], as a peak at −97.8 ppm was observed at higher catalyst concentrations, i.e. when [**1b**] is larger than 10 mM. Representative spectra are shown in **Figure 3.18**. During the reaction, this complex slowly builds up until an equilibrium was reached, likely between [(**1b**)$_2$FCs] and [(**1b**)FCs]. The equilibrium position is proportional to the initial catalyst concentration (**Figure 3.19**). The formation of [(**1b**)$_2$FCs] was previously observed when 25 mM **1b** was sonicated with 50 equivalents of CsF in deuterated DCM, and the fluoride of this complex was reported to have a chemical shift at − 96 ppm.[117]

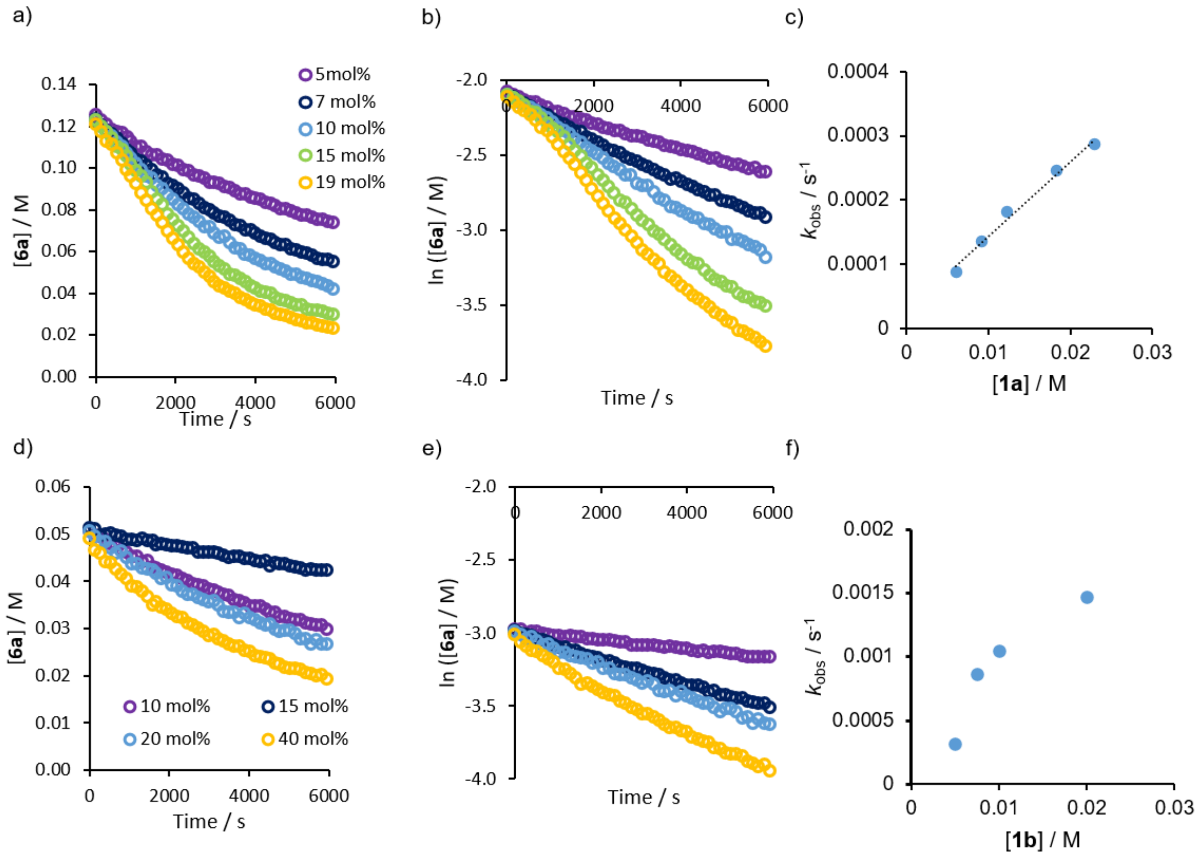

Figure 3.17. a) Overlaid plots detailing the effect of varying starting catalyst concentration **1a** on concentration of products during the reaction against the time. b) Semi-logarithmic plot of ln ([**6a**]$_t$) against time for reactions using **1a**. c) Plot of the observed rate constant, k_{obs}, against initial catalyst concentration [**1a**]. Each colour represents a different initial catalyst concentration with [**6a**]$_0$ = 125 mM, initial amount of CsF equivalent to 0.5 M. d) Overlaid plots detailing the effect of varying starting catalyst concentration **1b** on concentration of products during the reaction against the time. e) Semi-logarithmic plot of ln ([**6a**]$_t$) against time for reactions using **1b**. f) Plot of the observed rate constant, k_{obs}, against initial catalyst concentration [**1a**]. Each colour represents a different initial catalyst concentration with [**6a**]$_0$ = 50 mM, initial amount of CsF equivalent to 0.2 M.

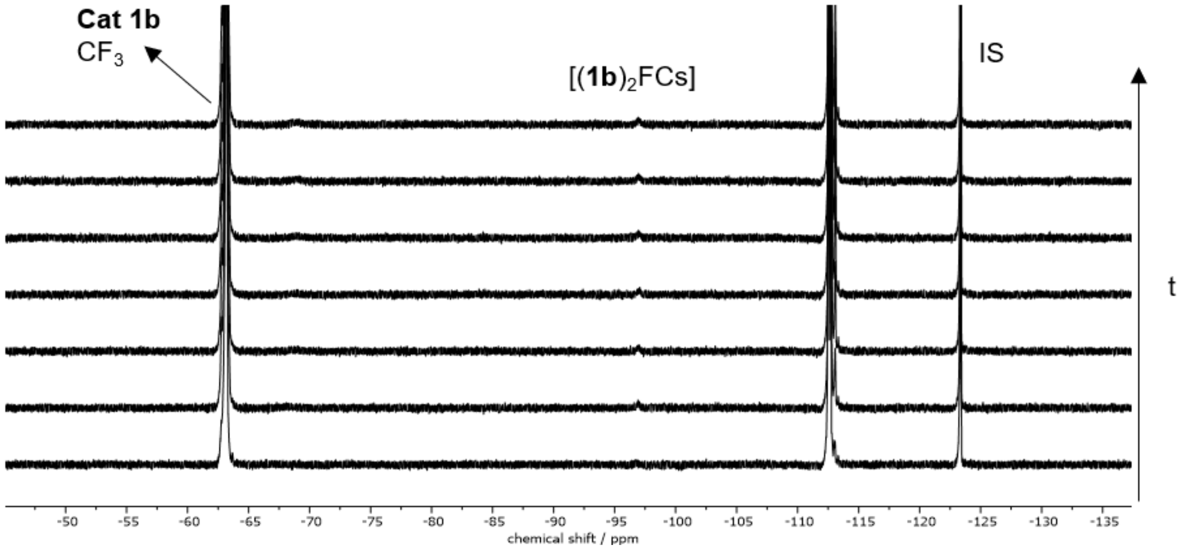

Figure 3.18. A stack of selected ^{19}F NMR spectra of the reaction mixture ($CHCl_3$) acquired using *in-situ* reaction monitoring method. Initial conditions: [**6a**] = 0.050 M, [**1b**] = 0.015 M.

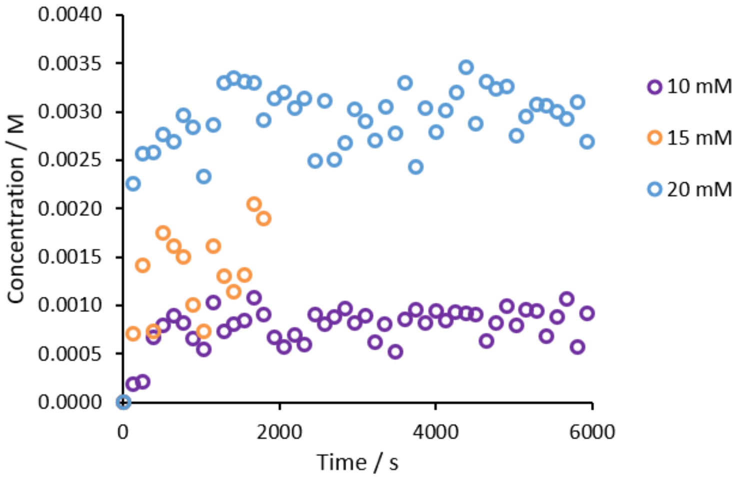

Figure 3.19. Temporal concentration of [(**1b**)$_2$FCs] at different initial concentration of **1b**.

The effect of CsF was also investigated. Similar to that with β-bromosulfide and **1a**, varying the initial amount of CsF only has a small effect on the rate of product formation. Using an excess amount of CsF leads to a slightly slower the rate of product formation. This observation also holds true when using catalyst **1b (Figure 3.20)**.

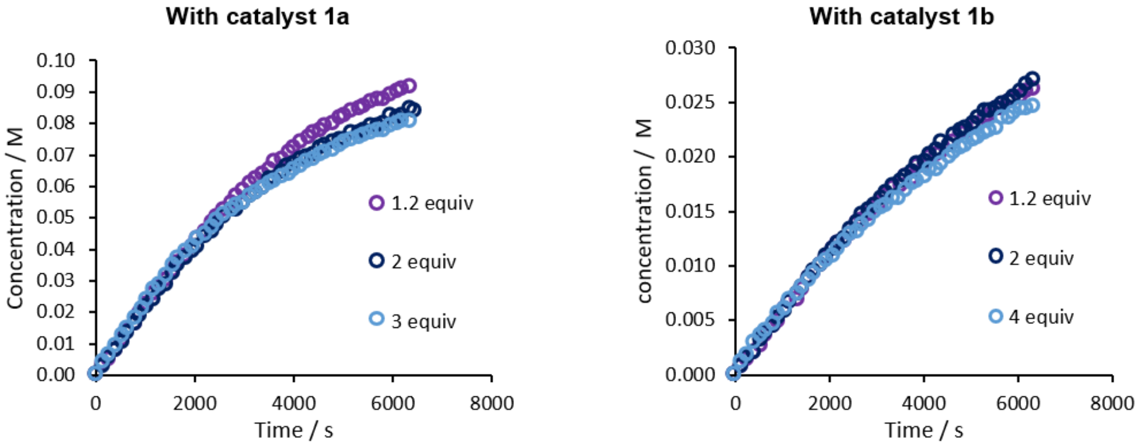

Figure 3.20. Overlaid plots detailing the effect of varying starting CsF amount on the product against the time. Each color represents a different initial amount CsF with a) [**6a**]$_0$ = 125 mM, [**1a**]$_0$ = 12.5 mM. b) [**6a**]$_0$ = 50 mM, [**1b**]$_0$ = 10 mM.

3.5.3 Investigation of product inhibition

For some experiments, as the reactions proceed, the reduction in rate is greater than that attenuated by the reduction in the quantities of the reactants. This reduction in rate could be due to product inhibition. Therefore, the effect of addition of product(s) at the beginning of the reaction was investigated for each combination of substrate (**2b** and **6a**) and catalyst (**1a** and **1b**). Unlike that was previously observed in asymmetric azidation,[125] none of products have a significant inhibitory effect on the rate of product formation (see Section 5.4.6 for further details).

3.5.4 Kinetic modelling

Kinetic models were built based on experimental observations and reasonable assumptions, then simulated using software that implements numerical integration techniques, converting a series of interconnected reactions into corresponding rate equations, approximating the full system, and solving it. The kinetic models were fitted to experimental data using a proprietary algorithm that gradually improves the estimates of the value of the rate constants by minimizing the errors between the simulated and experimental temporal concentration data. This algorithm was implemented in Excel through a scale-up systems add-in.

A kinetic model that poorly represent the reaction, even with the optimised rate constants, will not provide a satisfactory fit, whereas a good kinetic model provides a general fit to a series of experimental data with varied initial conditions, i.e. the discrepancy between the estimated rate constants among all data sets is small. To probe the generality, it is advantageous to include a large dataset. In most cases, a good general fit indicates that the used kinetic model reflects the key aspect(s) of the investigated reaction mechanism. It is important to avoid scenarios of underfitting and overfitting,[120] and to be aware that kinetically equivalent processes cannot be distinguished by kinetic modelling.

In this study, a series of kinetic models were evaluated to identify the one that is the simplest but can provide a general fit over a large dataset. Some kinetic models are discussed in Section 3.6.

3.6 Proposed mechanisms

Based on the experimental observations and extensive kinetic monitoring and kinetic modelling, a general reaction mechanism has been proposed for each fluorination. For each mechanism, an overall mechanism will first be presented, followed by discussion of experimental observations and kinetic modelling that supports the proposal. Selected datasets are shown below to aid the discussion of, whereas the full dataset that fitted to the kinetic model can be found in Section 6.4.

3.6.1 Fluorination of β-bromosulfide

The mechanism for the fluorination of β-bromosulfide by catalyst **1a** or **1b** can be described by the following set of interconnected catalytic cycles (**Figure 3.21**).

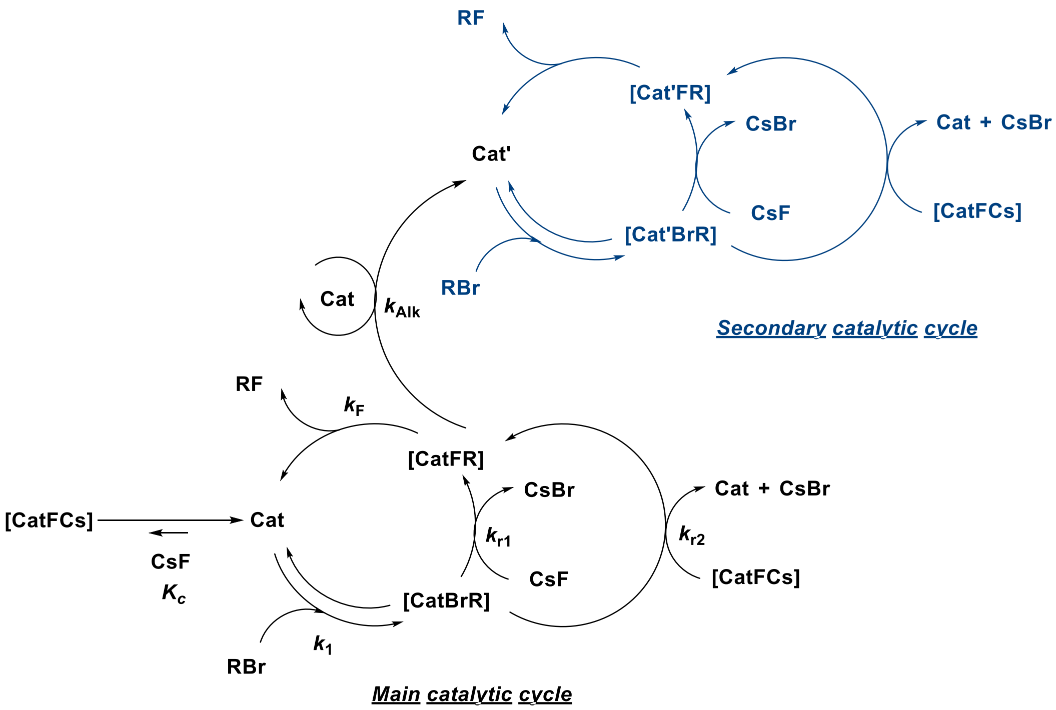

Figure 3.21. The proposed general mechanism for fluorination of β-bromosulfide, RBr, catalysed by PT catalyst **1a** or **1b**. Each catalytic cycle contains two pathways for generation of product, RF. The key intermediate [CatFR] is formed through anion exchange between CsF and [CatBrR], and through anion exchange between [CatFCs] and [CatBrR]. The secondary catalytic cycle (dark blue) only occurs for catalyst **1a**.

The reaction is initiated by ionisation of substrate, RBr. The ionisation process is accelerated by catalyst and leads to generation of an episulfonium-bromide ion pair, which then coordinates with catalyst to form [CatBrR]. The catalyst can also coordinate with CsF to form [CatFCs]. The catalyst bearing H-bonded bromide anion exchange its anion with [CatFCs] or with the solid CsF, and leads to generation of the key intermediate, a catalyst-bound fluoride-episulfonium ion pair [CatFR]. The formation of this intermediate is the rate-limiting step. Subsequently, this intermediate irreversibly generates the product, RF, and regenerates the catalyst or generate the substrate-alkylated catalyst, Cat'. For the *N*-isopropyl catalyst **1b**, the corresponding Cat' is not catalytically active. For non-alkylated catalyst **1a**, the corresponding Cat' is catalytically active, and goes through a secondary catalytic cycle that similar to that of the main catalytic cycle, except that unlike the original catalyst, the Cat' cannot efficiently bind to CsF.

The ionisation of β-bromosulfide was studied in detail by conducting magnetisation transfer experiments under varied concentration of catalyst and temperature (see Section 3.4). Based on the Eyring analysis, the rate of ionisation with catalyst **1a** or **1b** can be calculated using Eq. 3.2. The rate enhancement (k_1) at 295 K for catalyst **1a** and **1b** were determined to be 0.719 $s^{-1}M^{-1}$ and 2.55 $s^{-1}M^{-1}$, respectively. These values were used in the kinetic modelling (Eq. 3.6). The equilibrium constant, K_1, was set as 0.001 as [CatBrR] was not observed experimentally, indicating its low concentration.

$$\frac{d[[\mathrm{CatBrR}]]}{dt} = k_1\,[\mathrm{Cat}][\mathrm{RBr}] - k_{-1}\,\big[[\mathrm{CatBrR}]\big] \qquad (3.6)$$

It has been reported that these bis-urea catalysts are capable of complexing with CsF to form [CatFCs].[117] Both [CatFCs] and [Cat_2FCs] were formed when 25 mM **1b** and 50 equivalents of CsF was sonicated in deuterated DCM for two hours. Their formation was supported by low temperature (243 K) ^{1}H and ^{1}H DOSY NMR, and room temperature ^{19}F NMR.[117] Although the formation of neither [CatFCs] nor [Cat_2FCs] was observed under experimental conditions, or when sonicating 20 mM **1a** or **1b** with 2 equivalents of CsF for 4 hours in DCM, it is reasonable to assume that [CatFCs] was generated during the reaction but as the equilibrium is biased heavily towards the catalysts, the concentration of [CatFCs] was too low to be detected by NMR spectroscopy. The CsF is an insoluble solid and used in large excess, therefore the concentration of CsF is approximately constant during the reaction and the concentration of [CatFCs] is proportional to the concentration of catalyst (Eq. 3.7 to 3.9).

$$\frac{d[[\mathrm{CatFCs}]]}{dt} = k_{\mathrm{C}}\,[\mathrm{Cat}][\mathrm{CsF}] - k_{-C}\,\big[[\mathrm{CatFCs}]\big] \qquad (3.7)$$

$$\frac{d[[\mathrm{CatFCs}]]}{dt} \approx k_{\mathrm{C}}\,[\mathrm{Cat}][\mathrm{CsF}] = k_{\mathrm{C}}'\,[\mathrm{Cat}];\; k_{\mathrm{C}}' = k_{\mathrm{C}}\,[\mathrm{CsF}] \qquad (3.8)$$

$$[[\text{CatFCs}]]_t = k_\text{C}' \, [\text{Cat}]_t \qquad (3.9)$$

Kinetic modelling showed that for both catalysts, it is necessary to include two pathways for the generation of the key intermediate, [CatFR]. The fluorination using the *N*-isopropyl catalyst, **1b**, has a simpler model that that of **1a**, thus, was shown below as an example. When the kinetic model only incorporates generation of [CatFR] from anion exchange between [CatBrR] and CsF, a good fit can be obtained when the model was only fitted to one dataset (**Figure 3.22**a, b). However, this model cannot provide a general fit to experiments that has varied initial substrate and catalyst concentrations. Two examples are shown below: one with low catalyst loading (1 mol%, **Figure 3.22**c) and one with high catalyst loading (10 mol%, **Figure 3.22**d). The general fit of the model overestimated the rate of product formation of the former whereas underestimated that of the latter. When the kinetic model only incorporates generation of [CatFR] from anion exchange between [CatBrR] and [CatFCs], poor general fits were again observed (**Figure 3.22**e, f), but with an opposite direction of errors, i.e. the model underestimated the rate of product formation of runs with low catalyst loading. These observations indicate that the kinetic dependence on catalyst is between first-order to second-order. As expected, a kinetic model that contains both pathways gives a good general fit, even without considering experimental errors (**Figure 3.22**g, h).

For fluorination with bis-urea catalyst **1b**, the decrease in catalyst concentration during the reaction was less significant than that with **1a**. Although the corresponding *N*-alkylated catalyst was formed, the formation of other deactivated catalysts was not ruled out. A range of side-reactions were explored using kinetic modelling, independently or in combination. All the explored side-reactions are shown in **Figure 3.23** in blue. The substrate-alkylated catalyst, Cat’, can be generated from [CatFR] directly or catalytically. The CsF-bound catalyst can decompose to an inactive species, X, directly or catalytically. The CsF-bound catalyst can also interact with another equivalent of catalyst to generate inactive dimer species reversibly. Among all the tested models, only two gave good general fittings: one involved formation of a catalyst dimer and the other involved generation of Cat’, with the former performed slightly better. However, when probed experimentally, we found that prolonged mixing (4 hours) of catalyst **1b** and CsF in DCM prior to addition of substrate has no impact on the reaction profile. Additionally, the premixing did not lead to a decrease in the catalyst concentration. Therefore, we proposed that the main pathways contributing to catalyst deactivation are the formation of substrate-alkylated catalyst species.

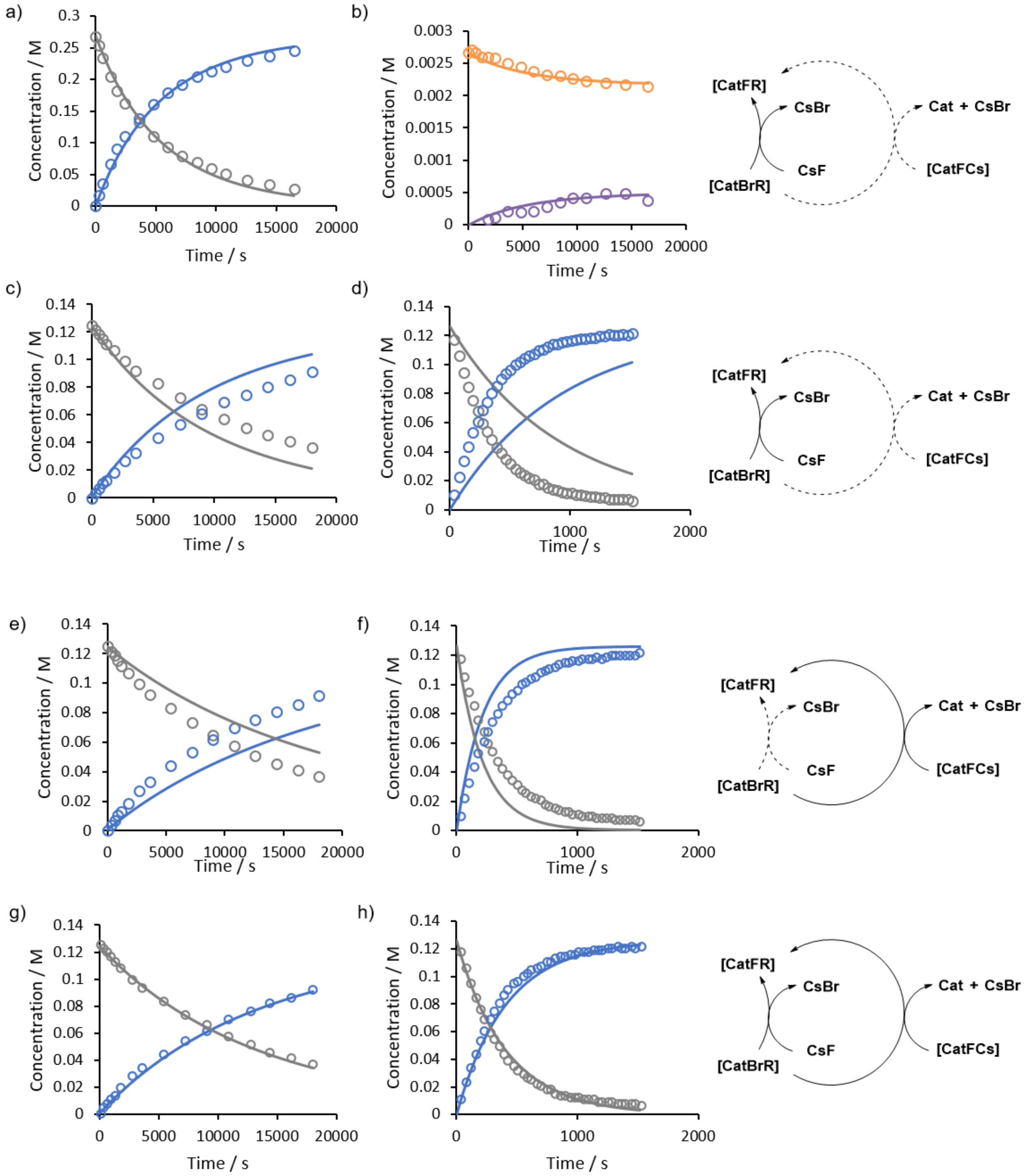

Figure 3.22. Kinetic simulations (solid lines) of $[\mathbf{2b}]_t$ (grey), $[\mathbf{3b}]_t$ (blue), $[\mathbf{1b}]_t$ (orange), and $[\mathbf{Cat'}]_t$ (purple) for different initial concentrations of β-bromosulfide, **2b**, and bis-urea catalyst, **1b**, as compared to values determined experimentally (open circles; determined by *in-situ* or *ex-situ* ^{19}F NMR spectroscopy). The kinetic models that used for simulations were partially shown on the right side of the plots, highlighting the key differences (solid lines: involved pathway; dash lines: not involved pathways). a) and b): kinetic model with rate constants that fitted to one experimental dataset with $[\mathbf{2b}]_0$ = 268.9 mM, $[\mathbf{1b}]_0$ = 2.66 mM. c) to h): kinetic model with rate constants that fitted to six experimental datasets. c), e) and g) $[\mathbf{2b}]_0$ = 125.2 mM, $[\mathbf{1b}]_0$ = 1.2 mM. d), f) and h) $[\mathbf{2b}]_0$ = 126.3 mM, $[\mathbf{1b}]_0$ = 12.3 mM.

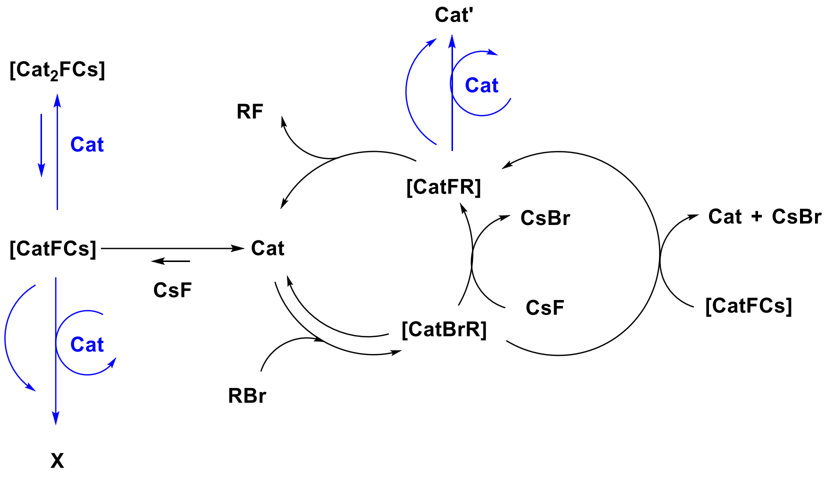

Figure 3.23. Potential pathways for generation of Cat' and other unknown deactivated catalyst-related species, X, for catalyst **1b**.

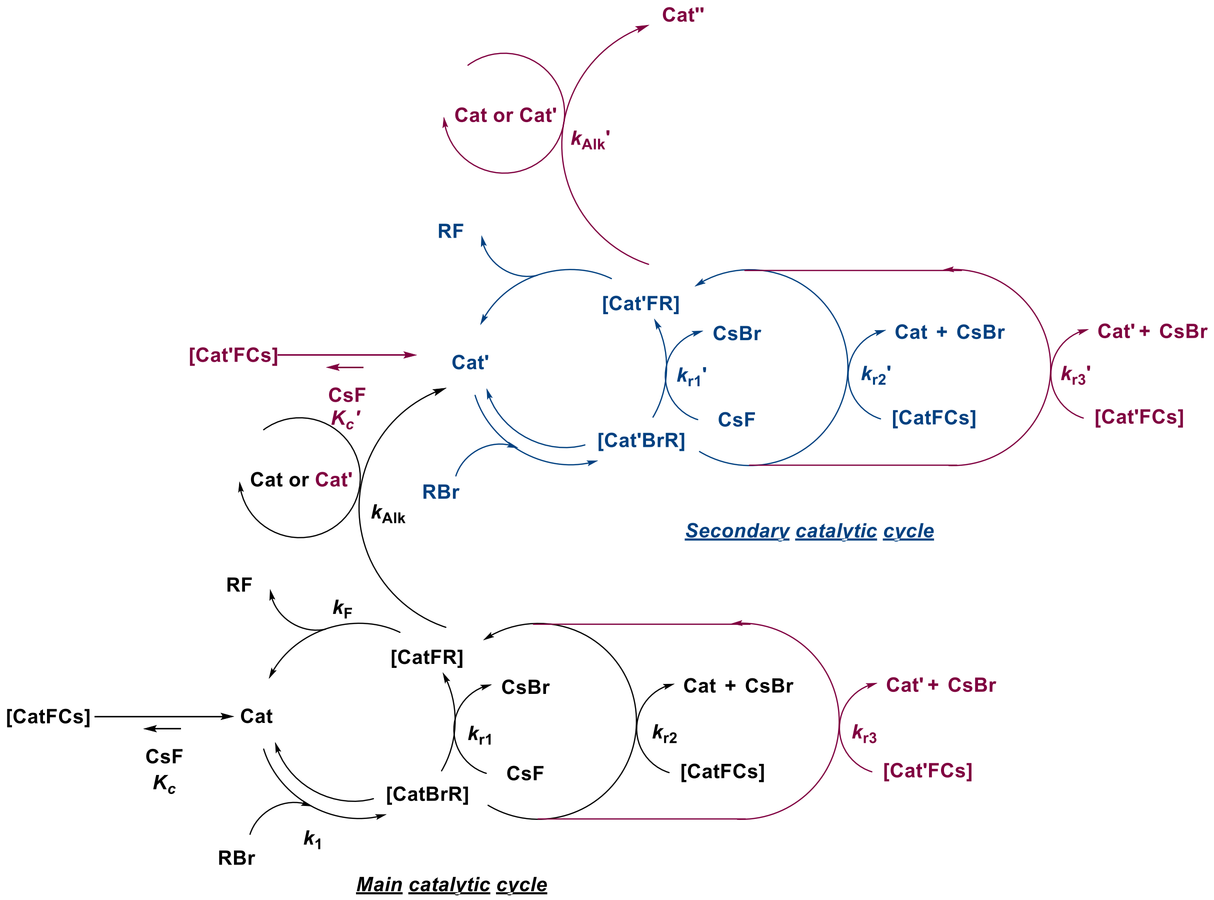

Figure 3.24. The proposed kinetic model for fluorination of β-bromosulfide, RBr, catalysed by PT catalyst **1a**. The main catalytic circle is shown in black; the secondary catalytic circle is shown in blue; the pathways that ruled out by kinetic modelling are shown in red.

The kinetic model for non-alkylated catalyst **1a** is more complex than that of **1b** because the substrate-alkylated catalyst, Cat', for **1a** is catalytically active and formation of Cat' is significant. Failing to include this effect leads to a kinetic model that poorly predicts the experimental data. Cat’ has three available NH groups and can in theory behave like bis-urea catalysts **1b**, i.e. capable of forming hydrogen bonding with fluoride and bromide and catalyse both fluorination and alkylation. Therefore, a secondary catalytic cycle (**Figure 3.24**, blue), which is an exact replica of the main catalytic cycle, was included in the kinetic model. Cat’ may bind to CsF to form [Cat’FCs], which can then act as a soluble source of fluoride and lead to generation of [CatFR] and [Cat’FR]. Additionally, Cat’ can be further alkylated to generate double substrate-alkylated catalyst, Cat” (**Figure 3.24**, red). A kinetic model that incorporates all the aforementioned transformations provided a good overall fit, but represents an overfitting, i.e. the model is too flexible as too many rate constants can be adjusted to optimise the fitting. To identify a minimal kinetic model that can provide a good general fit, the effect of removal of one or several related pathways was investigated. It was found that a good general fit can be obtained without all the pathways that are coloured in red (**Figure 3.24**). This kinetic model indicates that unlike the original catalyst, Cat’ cannot bind to CsF efficiently and cannot catalyse the generation of Cat’, likely due to its steric bulkiness. The formation of double substrate-alkylated catalyst, Cat”, is insignificant and has a negligible impact on the overall kinetic profile.

Furthermore, similar to that observed with catalyst **1b**, it is essential that [CatFR] can be generated from anion exchange of [CatBrR] with both CsF and [CatFCs]. On the other hand, there is no kinetic evidence that both generation pathways need to be included for [Cat’FR] as reasonable fitting can be obtained with either generation pathway.

3.6.2 Fluorination of β-chloroamine

The proposed reaction mechanism for the fluorination of β-chloroamine by catalyst **1a** or **1b** are shown in **Figure 3.25**. The catalyst can coordinate with CsF to form [CatFCs], which can further coordinate with another catalyst molecule to form [Cat_2FCs]. The ionisation of substrate, RCl, leads to formation of a chloride aziridinium ion pair, [R^+Cl^-]. The ion exchange between [CatFCs] and [R^+Cl^-] leads to generation of the key intermediate, a catalyst-bound fluoride-aziridinium ion pair [CatFR]. Subsequently, this intermediate irreversibly generates the product, RF, and regenerates the catalyst.

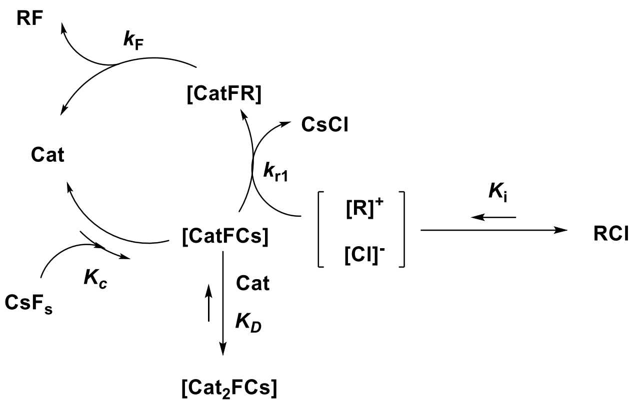

Figure 3.25. The proposed general mechanism for fluorination of β-chloroamine, RCl, catalysed by PT catalyst **1a** or **1b**. The key intermediate [CatFR] is formed through anion exchange between [CatFCs] and [R^+Cl^-].

Unlike that of β-bromosulfide, the rate of ionisation of β-chloroamine was not accelerated by catalysts **1a** or **1b**, and maintained at $k_1 = 0.045 \pm 0.015$ s^{-1} under varied conditions (see Section 3.4). This value was used in the kinetic modelling. The equilibrium constant, K_1, was set to an arbitrary value of 0.001 as the formation of chloride aziridinium ion pair, [R^+Cl^-] was not observed experimentally, indicating its low concentration. Although the formation of [CatFCs] was not observed, the formation of [(**1b**)$_2$FCs] was observed at higher catalyst concentrations. The formation of [CatFR], k_{r1}, is the rate determine step. The reaction is approximately first-order in catalyst, suggesting that the [CatFCs] reacts with the ion pair [R^+Cl^-] rather than the dissociated ions. For catalyst **1a**, the formation of [(**1a**)$_2$FCs] was not observed even at high catalytic loadings. This is consistent with the previous research into complexation between catalyst **1a** or **1b** with TBAF: higher binding constants of catalyst and fluoride, and [CatFCs] and fluoride were observed with catalyst **1b**.

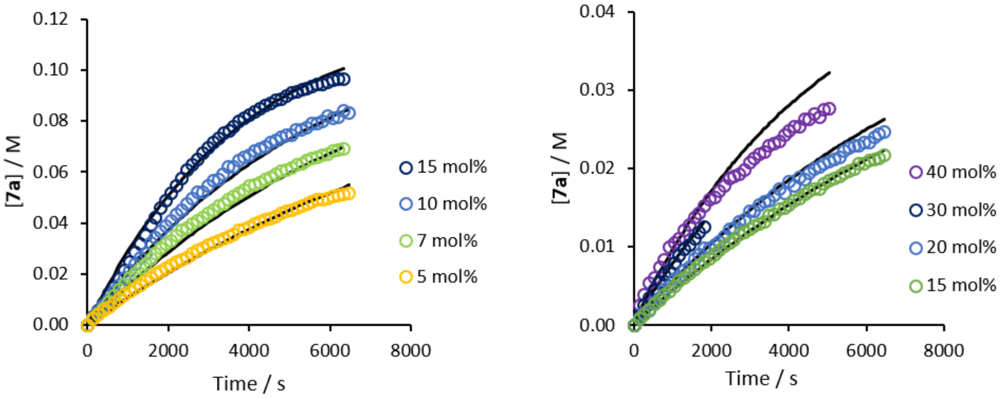

Figure 3.26. Kinetic simulations (solid lines) of product formation using bis-urea catalyst **1a** (left, [**2b**]$_0$ = 0.125 M) or **1b** (right, [**2b**]$_0$ = 0.05 M) under various catalyst concentrations, as compared to values determined experimentally (open circles; determined by *in-situ* ^{19}F NMR spectroscopy).

Kinetic modelling using the proposed mechanism gives a reasonably good general fit, except for the experiment with the highest catalyst loading, for which the rate of product formation was underestimated by the model (**Figure 3.26**, purple). A similar trend was observed with 20 mol% **1b**, but much less significant. There might be other pathways that leads to deactivation of catalyst **1b**, which has higher dependence in catalyst concentration and caused the observed decrease in rate.

4. Conclusion and Future Work

A plunger-based mixing device has been developed to facilitate *in-situ* kinetic monitoring of heterogenous solid-liquid reactions that requires continuous agitation. The plunger moves vertically within a truncated 5 mm NMR tube and is driven by a stepper motor through a Bowden cable. The design includes inert gas ports, enabling the investigation of air-sensitive reactions. A customised software is used to allow easy variation of parameters, such as plunger speed and position, and synchronised with the spectrometer to allow automated data acquisition. Other parameters, such settling time and measuring interval, can be adjust in the pulse sequence.

The effect of plunger type and mixing speed on the mixing efficiency was investigated by measuring the product formation rate of a deprotonate reaction via UV-Vis spectroscopy. While all three tested designs provide good mixing, the plate design performs the best. Further improvements in mixing efficiency can be achieved by using a faster plunger speed and/or stacking plunger tips. It was found that removing the plunger from the active volume and allowing a settling time prior to data acquisition greatly improves the spectral resolution. The optimum settling time can vary from a few seconds to tens of seconds across different systems. The pause has a negligible impact on the observed reaction kinetics as long as the acquisition time is relatively short. It should be noted that agitation accelerates solvent evaporation. Therefore, a slower mixing speed should be used to provide good mixing efficiency, especially when volatile solvents are involved. The mixing device has been used to measure the kinetics for two different systems. The reaction profiles and rate constants obtained via *in-situ* and conventional *ex-situ* monitoring method are in good agreement, while using less reagents and giving higher data density.

With the aid of this device and high-field NMR spectroscopy, kinetic studies were conducted on two phase-transfer-catalysed fluorinations, and the performance of two structurally similar PT catalysts were compared. Fluorine-labelled substrates were prepared, allowing the reaction to be monitored by ^{19}F NMR spectroscopy *in situ* and *ex situ*. Substrate-alkylated catalysts, Cat’, were formed during the fluorination of β-bromosulfide. The *N*-alkylated catalyst, **1b**, is more resistant to this side-reaction, whereas Cat’ of non-alkylated catalyst, **1a**, is catalytically active. Similar species were not observed during the fluorination of β-chloroamine.

It was proposed that both fluorinations were initiated by ionisation of the substrates, leading to the formation of cationic three-membered heterocycles. The rate of ionisation of both substrates were explored via magnetisation transfer and measured under a series of concentrations and temperature. The ionisation of β-bromosulfide was accelerated by both catalysts by more than two orders of magnitude. On the contrary, the ionisation rate of β-chloroamine was affected by neither the catalyst concentration nor the temperature. The experimentally measured rate constants were incorporated into the kinetic models.

Based on all the experimental observations and kinetic modelling, two reaction mechanism were proposed. In the fluorination β-bromosulfide, the catalyst accelerates the formation of episulfonium-bromide ion pair and complexed with the ion pair to generate [CatBrR], which can then exchange its anions with either solid CsF or [CatFCs] and leads to the formation of the key intermediate, [CatFR]. Further reaction of [CatFR] leads to the product formation and regeneration of catalyst. Additionally, the [CatFR] also undergoes alkylation and forming the catalytically less reactive or non-reactive substrate-alkylated catalysts. The Cat’ derived from **1a** goes through a secondary catalytic cycle, which is a replica of the main catalytic cycle, except that Cat’ cannot efficiently bind to CsF. The rate of product formation from the secondary catalytic cycle is slower than that from the main catalytic cycle; therefore, switching between different fluorination pathways within the secondary catalytic cycle has a minimal effect on the overall fit.

In the fluorination of β-chloramine, the catalyst first coordinates with CsF to form [CatFCs], which then reacts with chloride aziridinium ion pair, leading to the formation of the key intermediate [CatFR]. Further reaction of [CatFR] leads to the product formation and regeneration of catalyst. Whereas no noticeable formation of similar substrate-alkylated catalysts was observed, the formation of 2:1 catalyst-fluoride complex, [(**1b**)$_2$FCs] was observed at high catalyst loadings. It is proposed that this complex is not catalytically active, but in equilibrium with [CatFCs]. The kinetic profile of some experiments has a sigmoidal shape, and the reason behind it is unclear. The possibility of product inhibition was ruled out by controlled experiments.

The investigated bis-urea catalyst has found applications in a range of fluorinations using alkaline fluorides and recent work also shown that similar catalysts can be used for asymmetric reactions other than fluorination, i.e. azidation, using inexpensive sodium azide.[177] This work can be useful when exploring the reaction mechanism of existing and new reactivities of the bis-urea type catalysts or other similar PT catalysts. Furthermore, the catalytic ability of bis-urea catalysts can be optimised by reducing the formation of substrate-alkylated catalysts, and enhancing the coordination between catalysts, substrate and fluoride. In addition to catalytic ability, investigation into the enantioselectivity of the reaction can provide additional understanding of the reaction mechanism. For example, by determining the enantioselectivity of each fluorination pathway, we can differentiate if the fluorinated product was produced via the same or different [CatFR] intermediate, which are kinetically indistinguishable. With this information, we may be able to improve the enantioselectivity by favouring one fluorination pathway.

To date, the applications of bis-urea catalysts have relied on either the use of readily ionisable substrates to form cationic three-membered heterocycles or the use of azetidinium salts as substrates. In this study, the ionisation of β-bromosulfide and β-chloramine was investigated in detail using magnetisation transfer. This method provides a useful guide for studying the ionisation of other types of substrates. Furthermore, for the first time, we have found that bis-urea catalysts also participate in and accelerate the ionisation process, indicating that they can be applied to promote reactions of substrates that are not readily ionisable. Further research in this area will allow for a substantial broadening of the substrate scope.

As demonstrated in this work, by using *in-situ* NMR mixing device, SLPTC reactions can be monitored automatically and efficiently. The device is readily applicable for monitoring other liquid-solid heterogeneous processes, for instance, Mizoroki−Heck[178,179] and Suzuki−Miyaura[180–182] cross-coupling reactions, and other industrial important reactions.[183,184] With adaptations to the connections and size, this device should be easily adaptable to different NMR spectrometers. Future work will explore the application of this device in various liquid-solid reactions, extend its use to liquid-liquid heterogeneous systems, and integrate it with a more affordable benchtop NMR spectrometer for real-time reaction monitoring.[185]

5. Experimental

5.1 General considerations

NMR spectra were recorded on a Bruker Ascend 400 MHz NMR spectrometer equipped with a Prodigy cryoprobe at 300 K unless otherwise stated. MestReNova version 14 were used for processing all NMR spectra. Data are presented in the following format: chemical shift (ppm), integration, multiplicity (s = singlet, d = doublet, t = triplet, br = broad, m = multiplet) coupling constants (J = x Hz) and assignment (*o* = *ortho*, *m* = *meta*, *p* = *para*) where appropriate. ^{1}H and ^{13}C chemical shifts are reported related to residual solvent peaks whereas ^{19}F chemical shifts are reported related to 1-fluoronaphthalene (δF = –124.07) as an internal standard.

UV-Vis spectra were recorded in a plastic cuvette with 1cm path length on an Ocean-Optics Flame CCD Spectrometer connected via optical fibre to a DH2000-BALUV lamp. Acquisition was controlled by the Kinetic Studio software package (version 5). Data was processed and plotted using Excel.

Infrared (IR) spectra of neat compounds were recorded using a Bruker APLHA^{TM} ATR-FTIR spectrometer. Peaks were reported in cm^{-1}.

Electrospray ionisation (ESI+) and high-resolution mass spectra were recorded on a Bruker ESI Micro-Tof mass spectrometer. Data are reported in the form of m/z.

Analytical thin-layer chromatography was performed on precoated aluminium-backed plates (Merck Silica Gel 60 F$_{254}$), and visualisation was achieved using ultraviolet light (254 nm) and/or phosphomolybdic acid (PMA) stain. Flash column chromatography was performed using Merck Silica Gel 60 (40–63 µm).

Unless otherwise stated, all reagents were obtained from commercial sources (Sigma Aldrich, Alfa Aesar, Fischer Scientific, Acros Organics and Fluorochem) and used without purification, and solvents were used without prior drying or degassing. Anhydrous dichloromethane was obtained using an MBraun SPS-800 system directly into an MBraun glovebox and was further dried and stored over 4 Å molecular sieves. Anhydrous chloroform (Acros) was stored over 4 Å molecular sieves and passed on a column of basic alumina prior to use. CsF (99.9% trace metal basis, Sigma-Aldrich) was ground and stored in glovebox. The catalysts **1a** and **1b** were prepared and provided by Francesco Ibba and Claire Dooley from Gouverneur's group and dried *in vacuo* prior to use.

5.2 Synthetic procedures

(±)-(*S**,*S**)-2-(phenethylthio)cyclohexane-1-ol

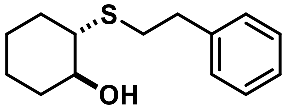

The title compound was prepared following literature procedure.[47] In a round bottom flask equipped with a reflux condenser and a magnetic stirring bar, cyclohexene oxide (1.0 mL, 10 mmol, 1 equiv.) was dissolved in EtOH (100 mL). NaOH (0.4 g, 10 mmol, 1 equiv.) and thiol (1.4 mL, 10 mmol, 1 equiv.) were added at room temperature, and the solution was heated to 90 °C in an oil bath for 4 hours. The reaction mixture was allowed to cool to room temperature before the solvent was removed *in vacuo*. The residue was treated with Et_2O and water, extracted with Et_2O (×2), dried ($MgSO_4$) and concentrated *in vacuo* to afford the crude product. Flash column chromatography (hexane: Et_2O = 85:15) afforded the pure product as a colourless oil (2.07 g, 88%). ATR FT-IR ν_{max} / cm^{-1} 3438, 2928, 2855, 1496, 1447, 1273, 1066, 962, 696, 556. ^{1}H NMR (400 MHz, $CDCl_3$), δ 7.36 – 7.27 (2H, m, *m*-Ar-*H*), 7.16 – 7.26 (3H, m, *o,p*-Ar-*H*), 3.29 (1H, td, *J* = 10.0, 4.4 Hz), 2.98 – 2.76 (4H, m, S*CH*$_2$*CH*$_2$), 2.39 (1H, ddd, *J* = 12.2, 10.0, 4.0 Hz), 2.18 – 2.03 (2H, m), 1.84 – 1.66 (2H, m), 1.51 – 1.37 (1H, m), 1.35 – 1.20 (3H, m). ^{13}C {^{1}H} NMR (101 MHz, $CDCl_3$), δ 140.47, 128.66, 128.62, 126.60, 72.39, 53.87, 36.91, 33.99, 33.10, 31.53, 26.50, 24.61. HRMS (ESI) calculated for $C_{14}H_{20}O^{32}S$ 236.12294, observed 236.123759.

(±)-(*S**,*S**)-2-bromocyclohexylphenethyl sulfide, 2a

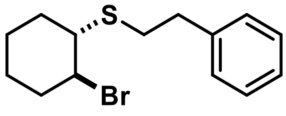

The title compound was prepared according to literature procedure.[47] In a flame-dried round bottom flask equipped with a magnetic stirring bar and under inert atmosphere, the hydroxysulfide (1.296 g, 5.489 mmol, 1 equiv.) was dissolved in CH_2Cl_2 (5.5 mL). The solution was cooled to 0 °C in an ice-bath and PBr_3 (0.19 mL, 2.0 mmol, 0.36 equiv.) was added dropwise. The reaction mixture was stirred at 0 °C for 2 hours. The reaction was quenched by the addition of ice-cold water, and extracted with Et_2O (×2), dried ($MgSO_4$) and concentrated *in vacuo* to afford the pure product as a colourless oil (1.345 g, 82%). ATR FT-IR ν_{max} / cm^{-1} 2933, 2856, 1496, 1444, 1180, 1000, 696, 662, 562, 492. ^1H NMR (400 MHz, $CDCl_3$), δ 7.34 − 7.27 (2H, m, *m*-Ar-*H*), 7.25 − 7.17 (3H, m, *o,p*-Ar-*H*), 4.29 (1H, q, *J* = 3.0 Hz), 3.05 – 2.69 (1H, m), 2.93 – 2.83 (4H, m, S*CH₂CH₂*), 2.40 – 2.23 (2H, m), 1.91 – 1.81 (1H, m), 1.79 – 1.55 (3H, m), 1.48 – 1.37 (2H, m). $^{13}C\ \{^1H\}$ NMR (101 MHz, $CDCl_3$), δ 140.48, 128.63, 128.62, 126.55, 57.24, 50.62, 36.57, 34.03, 33.66, 30.39, 23.42, 23.29. HRMS (ESI) calculated for $C_{14}H_{19}{}^{79}BrS$ 298.03854, observed 298.038707.

(±)-(*S**,*S**)-2-(4-fluorophenethylthio)cyclohexane-1-ol

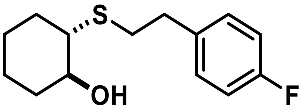

The title compound was prepared according to modified literature procedures.[47,172] In a round bottom flask equipped with a reflux condenser and a magnetic stirring bar, thiourea (0.762 g, 10.0 mmol, 1 equiv.) was dissolved in ethanol (20 mL) and 4-fluorophenethyl bromide (1.4 mL, 10 mmol, 1 equiv.) was added. After the reaction mixture became homogeneous, it was heated under reflux in an oil bath for 3 hours. The reaction mixture was allowed to cool to room temperature before the solvent was removed *in vacuo*. Aqueous NaOH (6.3 mL, 1.2 M, 15 mmol, 1.5 equiv.) was added to the residue. The solution was heated under reflux in an oil bath under inert atmosphere for 2 hours. The reaction mixture was allowed to cool to room temperature. EtOH (100 mL) and cyclohexene oxide (1.1 mL, 11 mmol, 1.1 equiv.) were added, and the solution was heated to 90 °C in an oil bath for 4 hours. The reaction mixture was allowed to cool to room temperature before the solvent was removed *in vacuo*. The residue was treated with Et_2O and brine, extracted with Et_2O (×2), dried ($MgSO_4$) and concentrated *in vacuo* to afford the crude product. Flash column chromatography (hexane: Et_2O = 7:3) afforded the pure product as a colourless oil (1.955 g, 79%). ATR FT-IR ν_{max} / cm^{-1} 3436 (O−H), 2929 (C−H), 2856 (C−H), 1508, 1219 (C−F), 822 (C−H). ^1H NMR (400 MHz, CD_3OD), δ 7.27 − 7.18 (2H, m, *o*-Ar-*H*), 7.04 − 6.93 (2H, m, *m*-Ar-*H*), 3.39 – 3.31 (1H, td, *J* = 9.2, 4.4 Hz, *H*(C)OH), 2.92 – 2.80 (4H, m, S*CH₂CH₂*), 2.45 (1H, ddd, *J* = 11.0, 9.2, 3.9 Hz, *H*(C)S), 2.11 –

1.92 (2H, m), 1.79 – 1.61 (2H, m), 1.41 – 1.19 (4H, m). ^{13}C NMR (101 MHz, CD_3OD), δ 162.95 (d, *J* = 242.7 Hz), 138.15 (d, *J* = 3.2 Hz), 131.27 (d, *J* = 8.0 Hz), 115.90 (d, *J* = 21.6 Hz), 74.96, 52.67, 36.92, 35.65, 33.77, 33.49, 26.70, 25.21. ^{19}F NMR (377 MHz, CD_3OD), δ – 117.51 (tt, *J* = 9.0, 5.4 Hz). HRMS (EI) calculated for $C_{14}H_{19}OF^{32}S$ 254.11352, observed 254.11339.

(±)-(*S**,*S**)-2-bromocyclohexyl-4-fluorophenethyl sulfide, 2b

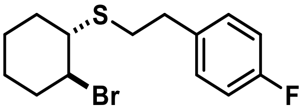

In a flame-dried round bottom flask equipped with a magnetic stirring bar and under inert atmosphere, the hydroxysulfide (0.88 g, 3.5 mmol, 1 equiv.) was dissolved in CH_2Cl_2 (3.5 mL). The solution was cooled to 0 °C in an ice-bath and PBr_3 (0.12 mL, 1.3 mmol, 0.37 equiv.) was added dropwise. The reaction mixture was stirred at 0 °C for 2 hours. The reaction was quenched by the addition of ice-cold water, and extracted with Et_2O (×2), dried ($MgSO_4$) and concentrated *in vacuo* to afford the crude product. The crude was dissolved in pentane and quickly plugged through a celite pad to afford the pure product as a pale-yellow oil (1.03 g, 94%). The product is prone to decomposition at elevated temperature (~ 50 °C) and reacts rapidly with methanol. ATR FT-IR ν_{max} / cm^{-1} 2934 (C−H), 2857 (C−H), 1508, 1220 (C−F), 822 (C−H), 505 (C−Br). ^{1}H NMR (400 MHz, CD_2Cl_2), δ 7.27 − 7.13 (2H, m, *o*-Ar-*H*), 7.07 − 6.90 (2H, m, *m*-Ar-*H*), 4.27 (1H, td, *J* = 7.0, 3.6 Hz, *H*(C)Br), 2.98 (1H, td, *J* = 7.0, 4.1 Hz, *H*(C)S), 2.91 – 2.81 (4H, m, SCH_2CH_2), 1.92 – 1.80 (1H, m), 1.78 – 1.52 (4H, m), 1.48 – 1.35 (1H, m). ^{13}C NMR (101 MHz, CD_2Cl_2), δ 161.96 (d, *J* = 243.3 Hz), 136.76 (d, *J* = 3.2 Hz), 130.44 (d, *J* = 7.9 Hz), 115.45 (d, *J* = 21.1 Hz), 57.95, 51.03, 35.89, 34.52, 34.19, 31.16, 24.04, 23.82. ^{19}F NMR (377 MHz, CH_2Cl_2), δ –117.59 (1F, tt, *J* = 8.9, 5.4 Hz). HRMS (EI) calculated for $C_{14}H_{18}{}^{79}BrF^{32}S$ 316.02911, observed 316.03000.

(±)-(*S**,*S**)-2-fluorocyclohexyl-4-fluorophenethyl sulfide, 3b

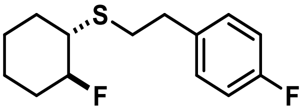

In a dark screw-cap vial equipped with a magnetic stirring bar, 2-bromocyclohexyl-4-fluorophenethyl sulfide (0.48 mg, 1.5 mmol, 1 equiv.) and AgF (0.38 mg, 3.0 mmol, 2 equiv.) were dissolved in MeCN (3 mL). The vial was sealed, and the reaction mixture was stirred at 1200 rpm at the room temperature overnight. The reaction mixture was then filtered and concentrated *in vacuo* to afford the crude product. The crude was dissolved in acetonitrile and plugged through a silica pad to afford the pure product as a pale-yellow oil (0.28 g, 73%). ATR FT-IR ν_{max} / cm^{-1} 2936, 2860, 1508, 1449, 1220, 1157, 1029, 957, 823. ^{1}H NMR (400 MHz, $CDCl_3$), δ 7.23 – 7.11 (m, 2H), 7.05 – 6.92 (m, 2H), 4.43 – 4.31 (m, 1H), 3.01 – 2.80 (m, 4H), 2.78 – 2.66 (m, 1H), 2.21 – 1.98 (m, 2H), 1.83 – 1.60 (m, 2H), 1.58 – 1.44 (m, 1H),1.41 – 1.21 (m, 3H).^{13}C NMR (101 MHz, $CDCl_3$) δ 161.69 (d, *J* = 244.1 Hz), 136.38 (d, *J* = 3.2 Hz), 130.07 (d, *J* = 7.9 Hz), 115.32 (d, *J* = 21.1 Hz), 96.52 (d, *J* = 176.4 Hz), 48.22 (d, *J* = 18.2 Hz), 35.92, 34.01 – 33.85 (m), 31.88 (d, *J* = 19.3 Hz), 31.02 (d, *J* = 5.3 Hz), 24.85 (d, *J* = 1.8 Hz), 23.24 (d, *J* = 9.5 Hz). ^{19}F NMR (377 MHz, CH_2Cl_2), δ –116.98 (tt, *J* = 8.8, 5.4 Hz), –169.54 (d, *J* = 49.0 Hz). HRMS (EI) calculated for $C_{14}H_{18}F_2{}^{32}S$ 256.10918, observed 256.10966.

bis(3-fluorophenyl)acetylene

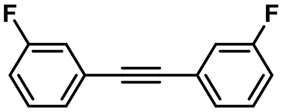

The title compound was prepared following literature procedure, from 1-fluoro-3-iodobenzene.[174] In a dry 100 mL Schlenk flask equipped with a magnetic stirring bar, CuI (0.19 g, 1.0 mmol, 0.20 equiv.), $PdCl_2(PPh_3)_2$ (0.44 g, 0.60 mmol, 0.12 equiv.) were dissolved in anhydrous and degassed benzene (50 mL). 1-fluoro-3-iodobenzene (2.2 g, 10 mmol, 2.0 equiv.), DBU (9.1 g, 60 mmol, 12 equiv.), trimethylsilylacetylene (9.1 g, 60 mmol, 12 equiv.) and water (72 µL, 4.0 mmol, 0.8 equiv.) were added in sequence. The flask was wrapped in aluminium foil and the reaction mixture was stirred at room temperature for 16 hours. The reaction mixture was quenched by adding saturated aqueous NH_4Cl solution (25 mL) and stirred for 10 minutes. The reaction mixture was partitioned in Et_2O and distilled water, extracted with Et_2O (50 mL

× 2), washed with brine (100 mL), dried ($MgSO_4$) and concentrated *in vacuo* to afford the crude product. Flash column chromatography (hexane) afforded the pure product as a white solid (0.94 g, 88%). All spectral data agreed with previously reported values.[174] ^{1}H NMR (400 MHz, $CDCl_3$), δ 7.37 – 7.28 (m, 4H), 7.25 – 7.20 (m, 2H), 7.11 – 7.01 (m, 2H). ^{19}F NMR (377 MHz, $CDCl_3$), δ −112.74 – −112.84 (m).

cis-3,3'-difluorostilbene

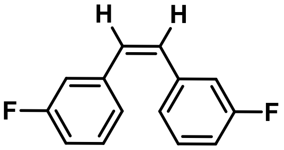

The title compound was prepared according to modified literature procedures.[174] In a dry 250 mL Schlenk flask equipped with a magnetic stirring bar and under inert atmosphere, the bis(3-fluorophenyl)acetylene (0.64 g, 3.0 mmol, 1 equiv.) was dissolved in THF (20.0 mL). The solution was cooled to –78 °C in an acetone/dry ice bath and $Ti(O^iPr)_4$ (0.98 mL, 3.3 mmol, 1.1 equiv.) was added. *n*-BuLi (4.1 mL 15% in hexane, 6.6 mmol, 2.2 equiv.) was added dropwise. After the solution was stirred for 15 minutes, it was heated to 50 °C and stirred for 3 hours. The reaction was cooled to 0 °C with an ice bath and quenched by adding saturated aqueous NH_4Cl solution (10.0 mL) and stirred for 5 minutes. The reaction mixture was extracted with Et_2O (3 × 25 mL), washed with brine (50.0 mL), dried ($MgSO_4$) and concentrated *in vacuo* to afford the crude product. Flash column chromatography (petrol ether) afforded the pure product as a clear oil (0.53 g, 82%). All spectral data agreed with previously reported values.[175] ^{1}H NMR (400 MHz, $CDCl_3$), δ 7.25 – 7.16 (m, 2H), 7.00 (dt, J = 7.7, 1.2 Hz, 2H), 6.95 – 6.86 (m, 4H), 6.60 (s, 2H). ^{13}C NMR (101 MHz, $CDCl_3$), δ 162.87 (d, J = 245.6 Hz), 139.06 (d, J = 7.9 Hz), 130.27 (d, J = 2.3 Hz), 129.95 (d), 124.76 (d, J = 2.9 Hz), 115.67 (d, J = 21.7 Hz), 114.46 (d, J = 21.1 Hz). ^{19}F NMR (377 MHz, $CDCl_3$), δ –113.29 (ddd, J = 10.0, 8.7, 6.1 Hz).

cis-2,3-Bis(3-fluorophenyl)oxirane

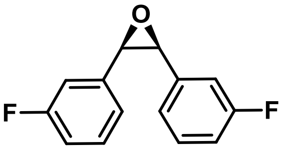

The title compound was prepared following literature procedure, from *cis*-3,3'-difluorostilbene.[175] In an open 25 mL flask equipped with a magnetic stirring bar, the cis-3,3'-difluorostilbene (0.34g, 1.6 mmol, 1 equiv.) was dissolved in CH_2Cl_2 (4 mL). The solution was cooled to 0 °C in an ice-bath, $MeReO_3$ (10 mg, 0.04 mmol, 0.025 equiv.), pyridine (17 µL, 0.21 mmol, 0.13 equiv.) and H_2O_2 (0.55 mL 30% in water, 4.8 mmol, 3.0 equiv.) were added consecutively. The flask was wrapped with aluminium foil. The reaction mixture was allowed to warm to room temperature and stirred for 48 hours. The reaction was quenched with MnO_2 (2.0 mg), extracted with CH_2Cl_2 (2.0 mL × 3), dried ($MgSO_4$) and concentrated *in vacuo* to afford the crude product. Flash column chromatography (petrol ether/ethyl acetate 30:1) afforded the pure product as a white solid (0.33 g ,88%). All spectral data agreed with previously reported values. [175] ^{1}H NMR (400 MHz, $CDCl_3$) δ 7.16 (tdd, *J* = 7.8, 5.8, 0.7 Hz, 2H), 6.97 (dt, *J* = 7.8, 1.3 Hz, 2H), 6.90 – 6.83 (m, 4H), 4.34 (s, 2H). ^{13}C NMR (101 MHz, $CDCl_3$) δ 162.58 (d, *J* = 249.5 Hz), 136.75 (d, *J* = 7.6 Hz), 129.71 (d, *J* = 8.1 Hz), 122.57 (d, *J* = 3.1 Hz), 114.90 (d, *J* = 21.0 Hz), 113.95 (d, *J* = 22.7 Hz), 59.28 (d, *J* = 2.3 Hz).

(±)-(*S**,*S**)-2-(diallylamino)-1,2-bis(3-fluorophenyl)ethan-1-ol

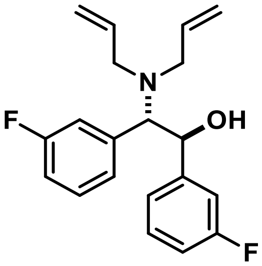

The title compound was prepared following literature procedure, from *cis*-2,3-bis(3-fluorophenyl) oxirane.[114] In a flame-dried two-neck round bottom flask equipped with a magnetic stirring bar and under inert atmosphere, the *cis*-2,3-bis(3-fluorophenyl) oxirane (1.1 g, 4.7 mmol, 1 equiv.), diallylamine (1.8 mL, 14 mmol, 3 equiv.) and $Y(OTf)_3$ (0.24g, 0.94 mmol, 0.2 equiv.) were dissolved in anhydrous THF (9.4 mL). The solution was refluxed for

24 hours. The reaction mixture was allowed to cool to room temperature and the solvent was removed in *vacuo*. The residue was dissolved in EtOAc, washed with saturated $NaHCO_3$, extracted with EtOAc, dried ($MgSO_4$) and concentrated *in vacuo* to afford the crude product. The crude was dissolved in hexane and Et_2O (1:1) and quickly plugged through a silica pad to afford the pure product as a white solid (1.24 g, 80%). All spectral data agreed with previously reported values.[114] ^{1}H NMR (400 MHz, $CDCl_3$), δ 7.24 – 7.21 (m, 1H), 7.13 – 7.04 (m, 1H), 7.00 – 6.92 (m, 2H), 6.91 – 6.76 (m, 4H), 5.94 – 5.81 (m, 2H), 5.30 – 5.14 (m, 4H), 4.98 (d, *J* = 10.3 Hz, 2H), 3.84 (d, *J* = 10.3 Hz, 1H), 3.51 (d, *J* = 14.0, 2H), 2.67 (dd, *J* = 14.0, 8.5 Hz, 2H). ^{19}F NMR (377 MHz, $CDCl_3$) δ −112.58 – −112.67 (m), −113.40 – −113.49 (m).

(±)-(*S,*S**)-*N*-allyl-*N*-2-chloro-1,2-bis(3-fluorophenyl)ethyl)prop-2-en-1-amine, 6a**

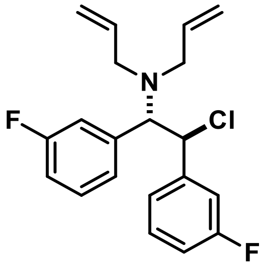

The title compound was prepared following literature procedure, from (±)-(*S**,*S**)-2-(diallylamino)-1,2-bis(3-fluorophenyl)ethan-1-ol.[114] In a flame-dried round bottom flask equipped with a magnetic stirring bar and under inert atmosphere, the alcohol (1.63 g, 4.95 mmol, 1 equiv.) was dissolved in anhydrous CH_2Cl_2 (25 mL). The solution was cooled to 0 °C in an ice-bath, and NEt_3 (1.1 mL, 7.5 mmol, 1.5 equiv.) was added. Then methanesulfonyl chloride (0.72 mL, 7.5 mmol, 1.5 equiv.) was added dropwise. The reaction mixture was allowed to warm to room temperature and stirred for 3 hours. The reaction was washed with saturated $NaHCO_3$ and brine, dried ($MgSO_4$) and concentrated *in vacuo* to afford the crude product. The crude product was purified with a short silica plug. The pure product is obtained as a white solid (1.58 g, 92%). ^{1}H NMR (400 MHz, $CDCl_3$), δ 7.22 – 7.04 (m, 2H), 7.02 – 6.91 (m, 2H), 6.90 – 6.79 (m, 2H), 6.78 – 6.73 (m, 1H), 6.73 – 6.66 (m, 1H), 6.00 – 5.83 (m, 2H), 5.40 – 5.28 (m, 2H), 5.27 – 5.16 (m, 3H), 4.30 (d, *J* = 10.9 Hz, 1H), 3.50 (d, *J* = 14.3, 2H), 2.73 (dd, *J* = 14.3, 8.0 Hz, 2H). ^{13}C NMR (101 MHz, $CDCl_3$) δ 162.58 (dd, *J* = 246.6, 5.8 Hz), 142.37 (d, *J* = 7.2 Hz), 137.70 (d, *J* = 6.2 Hz), 136.85, 129.79 (dd, *J* = 36.7, 8.2 Hz), 124.40

(dd, *J* = 95.1, 2.9 Hz), 117.60, 116.38 – 114.18 (m), 68.44 (d, *J* = 1.6 Hz), 62.46 (d, *J* = 1.9 Hz), 53.14. ^{19}F NMR (377 MHz, $CDCl_3$) δ −112.54 – −112.67 (m), −112.68 – −112.83 (m).

5.3 UV-Vis analysis

5.3.1 Mixing efficiency

A mixture of $NaHCO_3$ (7.0 mg) and stock solution of BTB in ethanol (1 mL, 0.0314 mM) were added to the NMR tube of the mixing device equipped with different plunger tips. The mixing device was adapted to the UV-Vis spectrometer via a custom curvet (**Figure 5.1**). The samples were mixed for 30 seconds (various speed, acceleration = 1200 mm/s^2, distance = 50 mm), and halted for 2 seconds, and then 10 spectra were recorded within 1 second (integration time = 0.007 s). The mixing was then resumed, and the process was repeated.

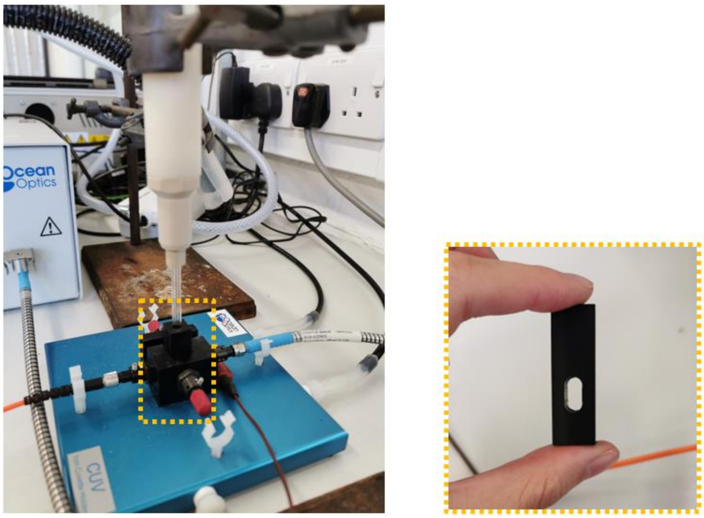

Figure 5.1. The set-up for UV-Vis experiment. The NMR tube was positioned in the centre of the custom cuvette adapter.

5.3.2 Solvent evaporation

Stock solutions of methyl red (0.0145 mM) in dichloromethane, chloroform, acetonitrile and of bromophenol blue (0.031 mM) in water were prepared. The solvent in NMR tube was used as background spectrum. A known amount of solution was added into the NMR tube via microsyringe. The NMR tube was connected to the mixing device using the same setup as in last section. The samples were mixed for 25 seconds (various speed, acceleration = 1200 mm/s^2, distance = 40 mm), and halted for 4 seconds, and then 10 spectra were recorded within 1 second (integration time = 0.007 s). The mixing was then resumed, and the process was repeated for a further 50 minutes. To avoid UV photobleaching of the dye, only the visible light source was switched on during these measurements. The absorbance at 490 nm (methyl red) or 593 nm (bromophenol blue) was extracted for each time point, and the solvent loss calculated as discussed in Section 2.4.3.

To ensure that the extinction coefficient is linear to the concentration in the studied range, calibration curves were run for each solvent (**Figure 5.2**).

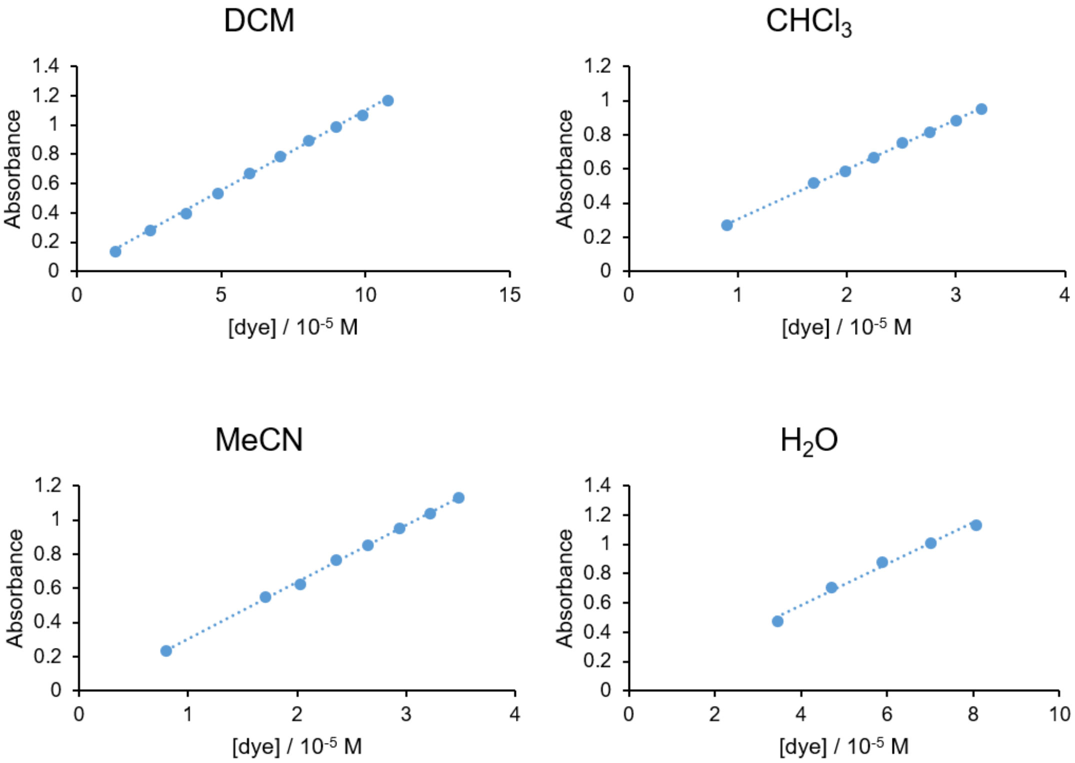
DCM

$CHCl_3$

MeCN

H_2O

Figure 5.2. Calibration curves for methyl red in dichloromethane, chloroform, acetonitrile and for bromophenol blue in water.

5.4 Kinetic studies

5.4.1 *Ex-situ* reaction monitoring

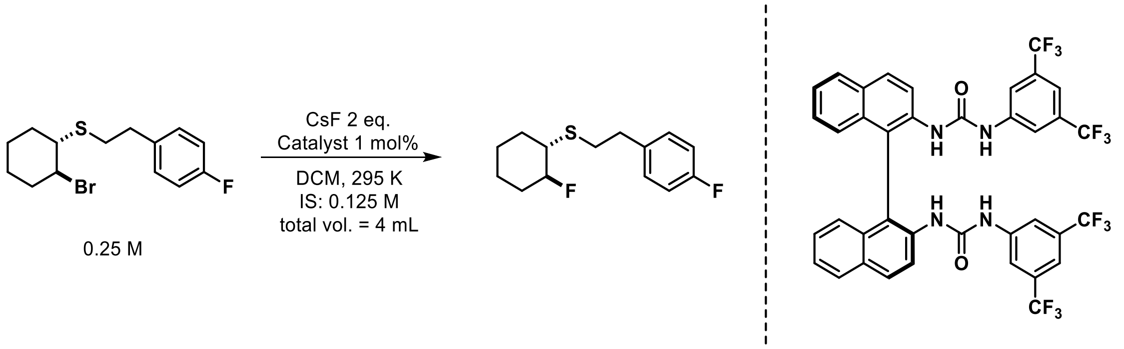

Scheme 5.1. Standard reaction conditions for *ex-situ* experiments.

In a N_2-filled glovebox, β-bromosulfide (0.3173 g, 1.00 mmol), catalyst (800 μL, 0.01 mmol), 1-fluoronaphthalene (240 μL, 0.50 mmol) and anhydrous dichloromethane (2960 μL) were added into a screw-cap vial equipped with a magnetic stirring bar. The vial was sealed by rubber septum and removed from the glovebox. The reaction mixture was kept at 295 K with a water bath, and the mixture was stirred at 1200 rpm for 10 minutes. By using a 1 mL plastic syringe, aliquot (0.2 mL) of the mixture was taken out and added into an NMR tube. The NMR sample was top-up to 0.6 mL with anhydrous dichloromethane, sealed and shaken vigorously, and a ^{19}F NMR spectrum was acquired as reference spectrum. CsF (0.2886 g, 1.9 mmol) was added to the vial, which initiated the reaction (t = 0). Aliquots of the reaction mixture were taken out at various recorded time. Each aliquot was quenched by filtered through syringe filter (Millex, 0.22 μm). The quenched aliquot and anhydrous dichloromethane were added into an NMR tube and mixed, and a ^{19}F NMR spectrum was acquired.

Experiments show that the aliquot was completely quenched after filtration, i.e. the amount of the product and reactant was constant after 3 days. However, after quenching, the intermediates generated during the reaction was slowly converted into original catalyst. To minimize this effect, all spectra were taken as fast as possible; unless otherwise stated, the ^{19}F NMR spectra used for investigation of intermediate were acquired within 10 minutes after sampling.

Stock solutions of 1-fluoronaphthalene (2.1 M) and catalyst (0.0125 M) were prepared using volumetric flasks, with solid weighted by microbalance and liquid measured by microsyringe. Both stock solutions were freshly made and used within 7 days. The bromosulfide was made a day before the experiment from corresponding hydroxide, dried and stored under nitrogen atmosphere in freezer at −20 °C.

Each spectrum was first processed separately, in the sequence of zero-filling, phase correction and baseline correction, then stacked and aligned referring to the internal standard. Each peak was integrated, and the concentration was calculated by referring to the integration and concentration of the internal standard. In the cases of peak overlapping, peak deconvolution was performed using manual regional line-fitting with constrains on chemical shifts and/or width of the peak.

Similar method was employed for monitoring β-bromosulfide with *N*-alkylated catalyst, and β-chloroamine with non-alkylated catalyst. Here, only β-bromosulfide with non-alkylated catalyst with conditions shown in **Scheme 5.1** was discussed as an example. Representative spectra and concentration-time profiles were shown in **Figure 5.3** to **Figure 5.5**.

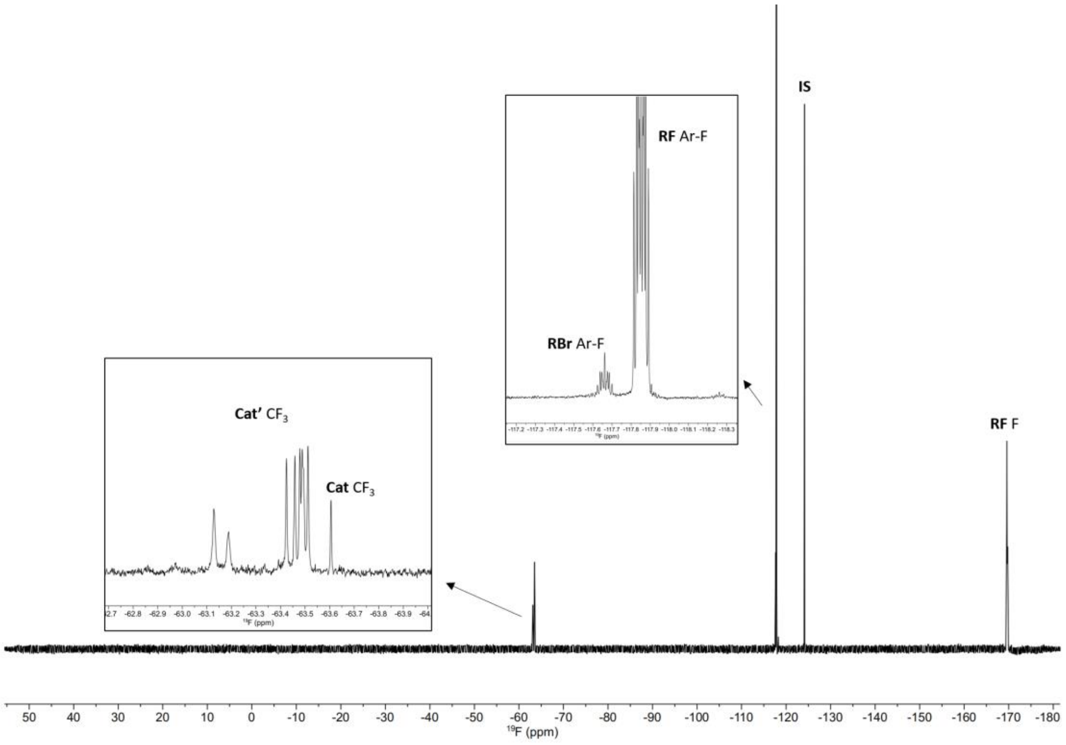

Figure 5.3. Single spectrum of nearly completed reaction, showing the locations of the reaction components: Cat' = substrate-alkylated catalyst, Cat = catalyst, RBr = β-bromosulfide, RF = β-fluorosulfide, IS = internal standard.

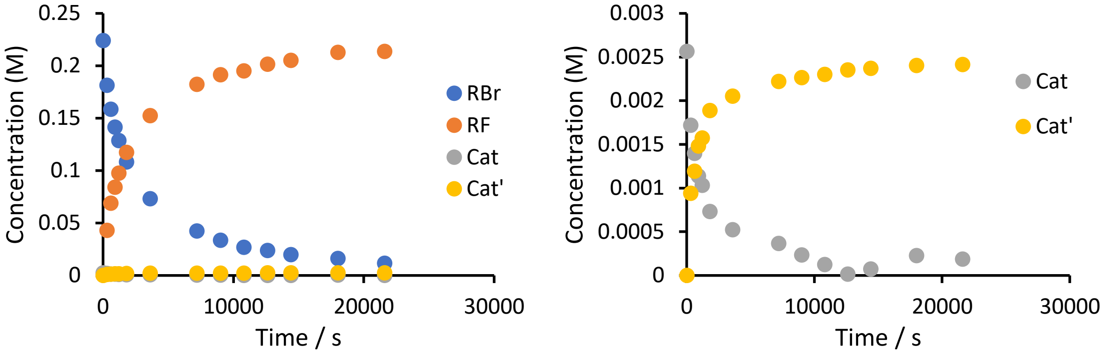

Figure 5.4. A representative concentration-time profile using NH catalyst. Initial conditions: [RBr] = 0.224 M, [Cat] = 2.56 mM. Catalyst related species have lower concentration and are shown in the right graph.

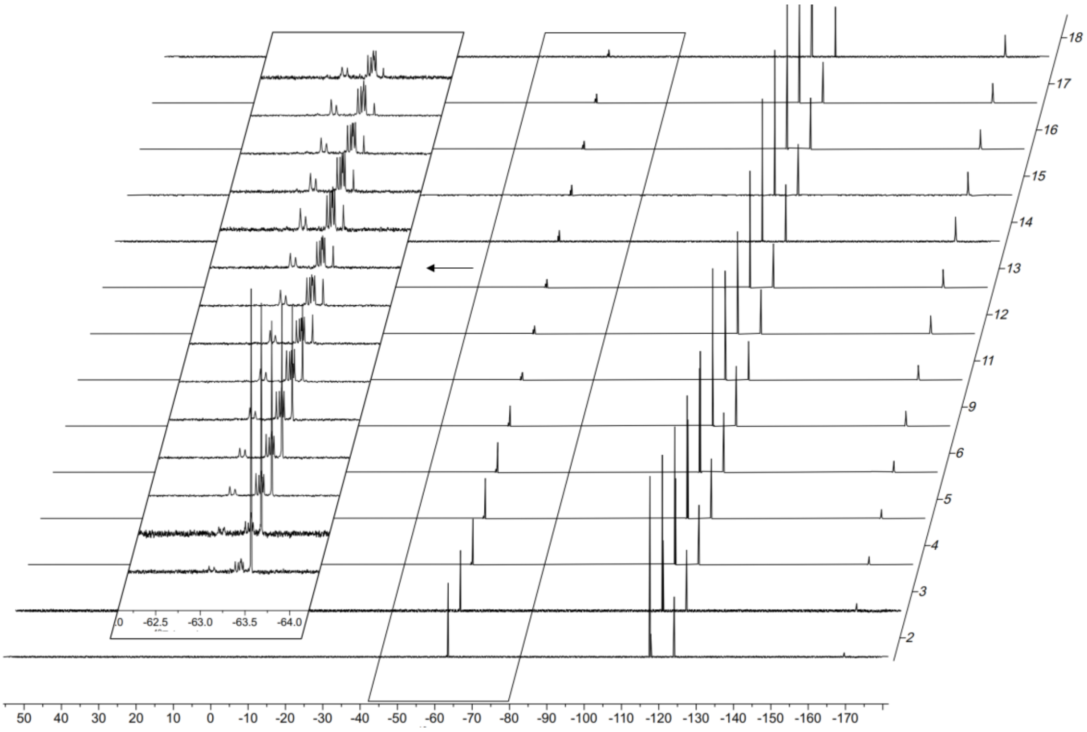

Figure 5.5. The stacked spectra of the same reaction.

5.4.2 *In-situ* reaction monitoring

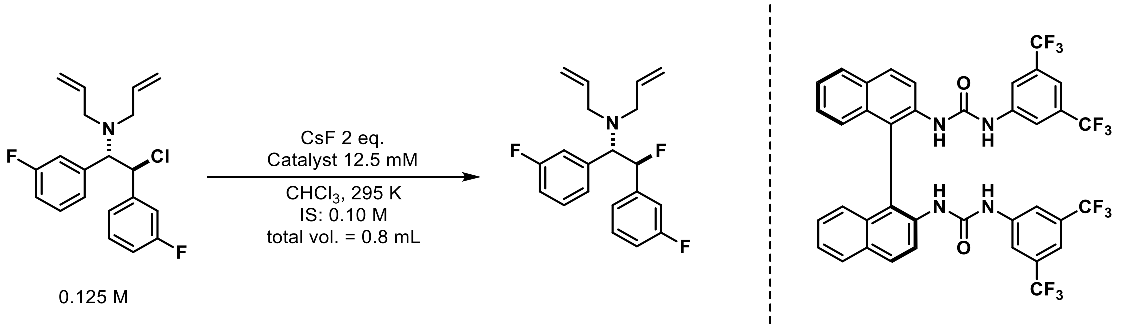

Scheme 5.2. Standard reaction conditions for *in-situ* experiments.

Stock solutions of β-chloroamine (0.3389 g, 0.4882 M), 1-fluoronaphthalene (0.0858 g, 0.294 M), and catalyst (0.1025 g, 0.06452 M) in anhydrous dichloromethane (2 mL) were freshly prepared prior the experiment. In a N_2-filled glovebox, stock solution of chloroamine (205 μL), 1-fluoronaphthalene (270 μL), dichloromethane (170 μL), and CsF (0.0304 g) were added into an NMR tube, capped, and removed from the glovebox. The solution was transferred to the NMR mixing device and a ^{19}F NMR spectrum was acquired as reference spectrum. A stock solution of catalyst (155 μL) was injected to the NMR tube, which initiated the reaction (t = 0). The reaction was mixed in situ at 295 K, with mixing paused at 120-second intervals to allow ^{19}F NMR spectra to be recorded (single scan, plunger speed = 80 or 100 mm/s, mixing time = 100 s, settling time = 20 s).

For each experiment, all spectra were stacked and processed together, in the sequence of zero-filling, phase correction and baseline correction. Each peak was integrated, and the concentration was calculated by referring to the integration and concentration of the internal standard. In the cases of peak overlapping, peak deconvolution was performed using manual regional line-fitting with constrains on chemical shifts and/or width of the peak.

Similar method was employed for monitoring β-chloroamine with *N*-alkylated catalyst, and β-bromosulfide with non-alkylated catalyst. Here, only β-chloroamine with non-alkylated catalyst with conditions shown in **Scheme 5.2** was discussed as an example. Representative spectra and concentration-time profiles were shown in **Figure 5.6** to **Figure 5.8**.

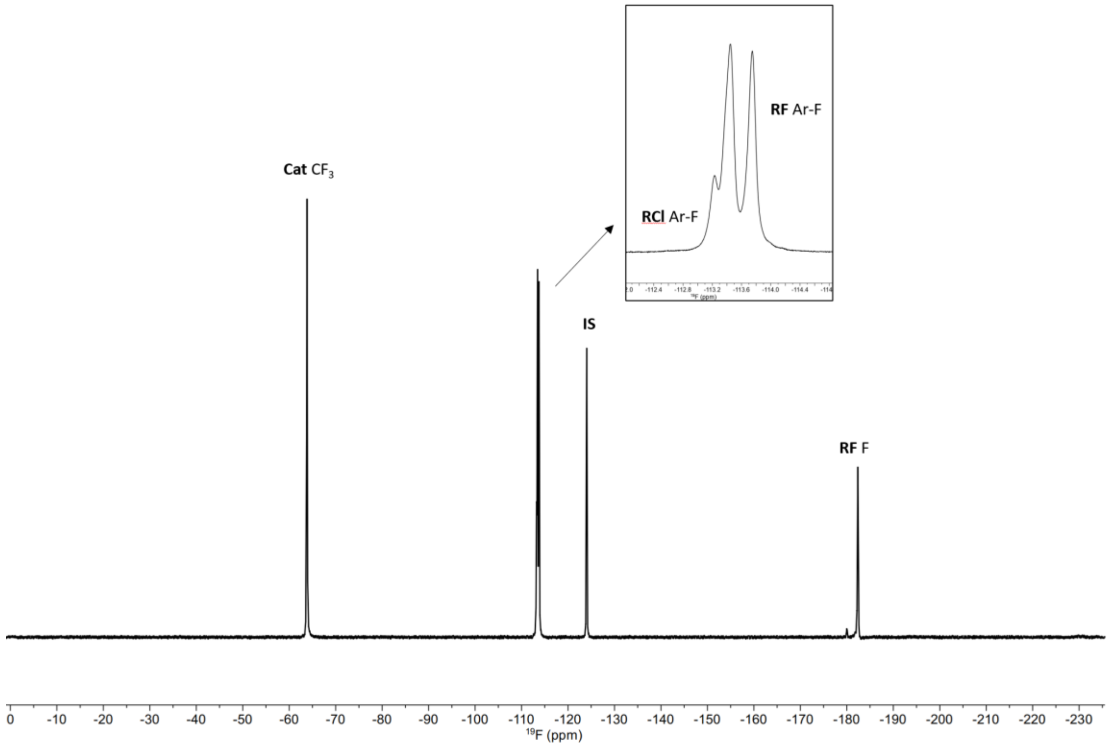

Figure 5.6. Single spectrum at 70% conversion of the substrate, showing the locations of the reaction components: Cat' = substrate-alkylated catalyst, Cat = catalyst, RCl = β-chloroamine, RF = β-fluoroamine, IS = internal standard.

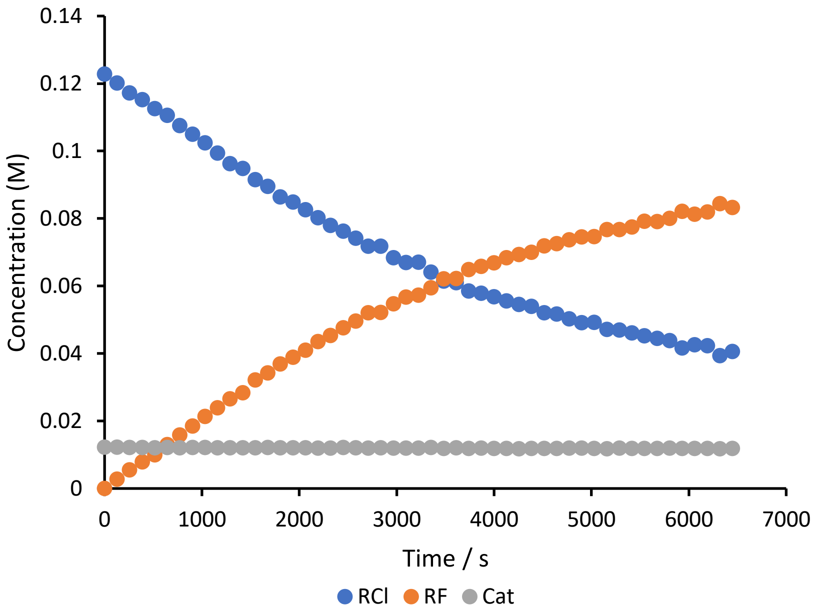

Figure 5.7. A representative concentration-time profile using NH catalyst. Initial conditions: [RCl] = 0.123 M, [Cat] = 12.3 mM.

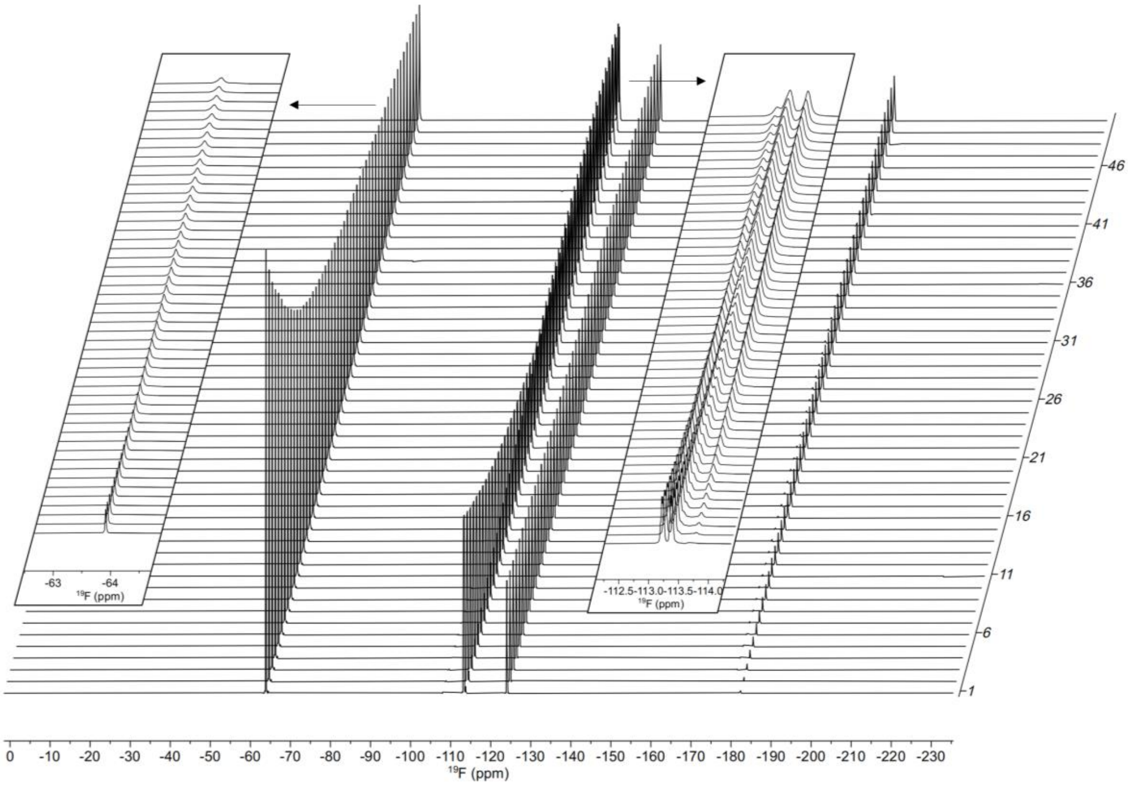

Figure 5.8. The stacked spectra of the same reaction.

5.4.3 Effect of mixing speed

5.4.3.1 β-bromosulfide

The stirring speed of each set of experiments was carefully selected to ensure that the rate of reaction was not limited by mass transfer, i.e. the observed rate is the true rate.

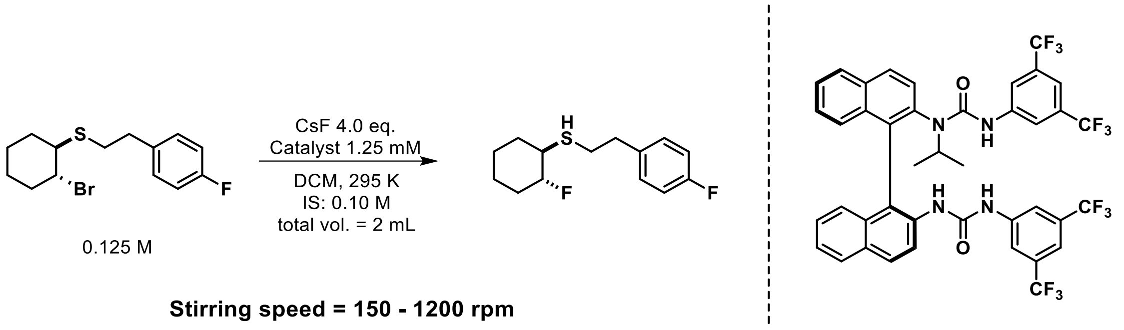

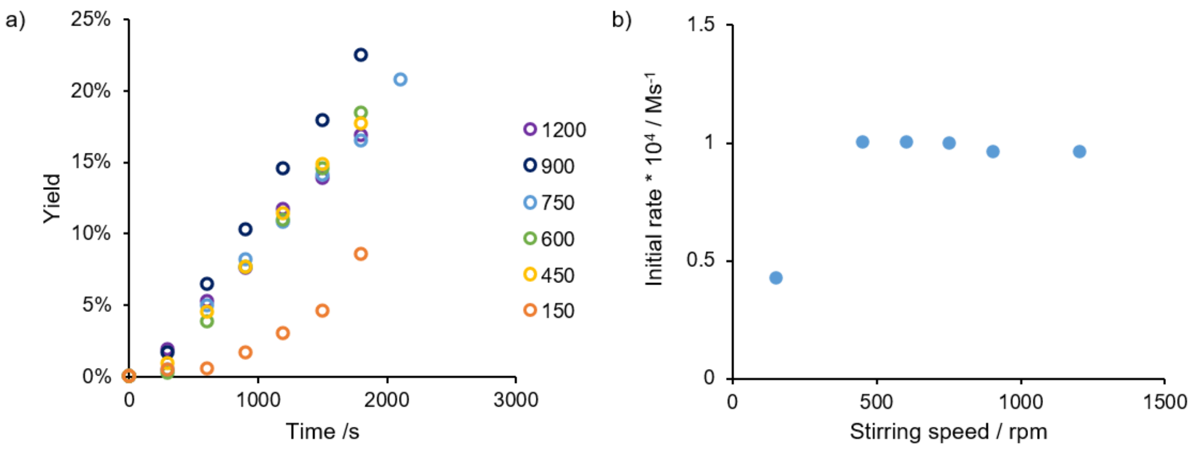

Figure 5.9. Phase-transfer catalysed fluorination of β-bromosulfide ([Substrate] = 0.125 M, [Catalyst] = 1 mol%) were monitored by *ex-situ* sampling method. a) overlay of percentage yield evolution with varied stirring speed. b) initial rate (*d*[Product]/*dt*) dependence on stirring speed.

5.4.3.2 β-chloroamine

The mixing speed of each set of experiments was carefully selected to ensure that the rate of reaction was not limited by mass transfer. Apart from the moving speed of plunger, all other parameters were kept the same: settling time = 20 s, mixing time = 100 s, moving distance = 50 mm.

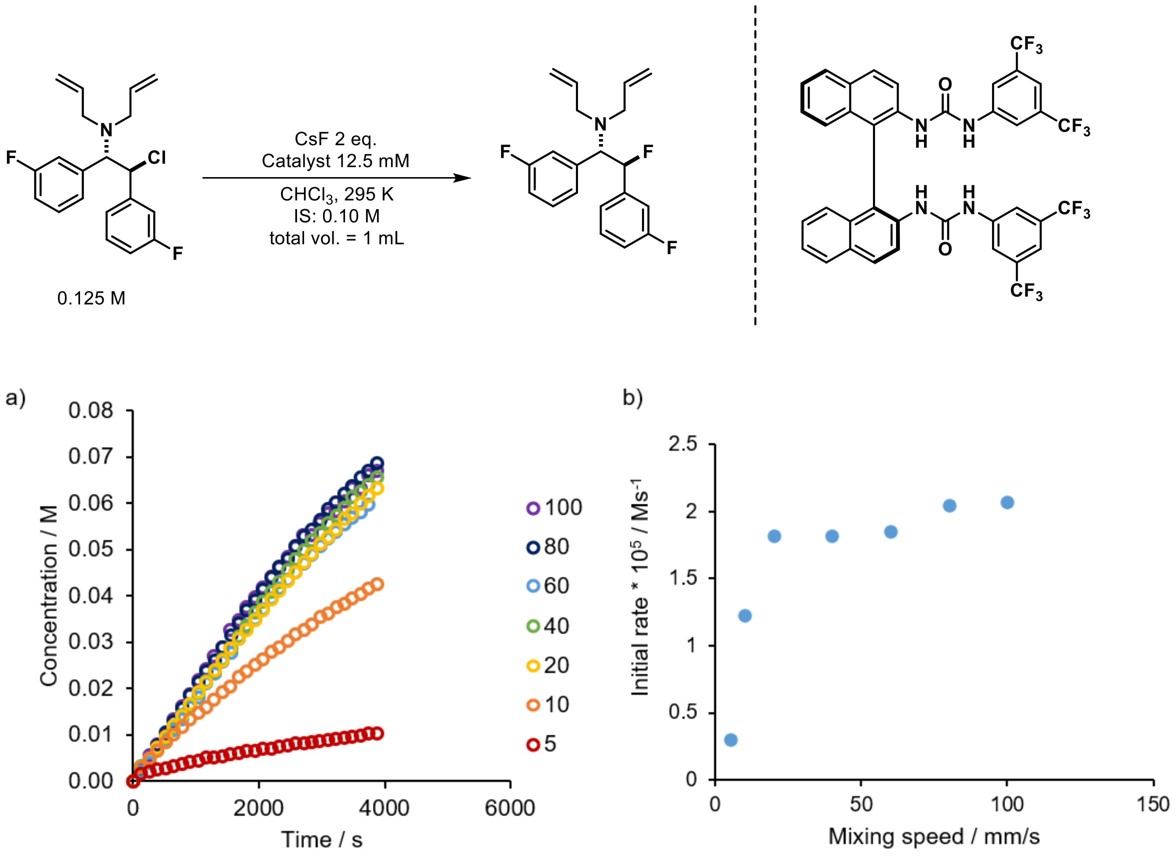

Figure 5.10. Phase-transfer catalysed fluorination of β-chloroamine ([Substrate] = 0.125 M, [Catalyst] = 10 mol%) were monitored using *in-situ* mixing device. a) overlay of percentage yield evolution with varied mixing speed. b) initial rate (*d*[Product]/*dt*) dependence on mixing speed.

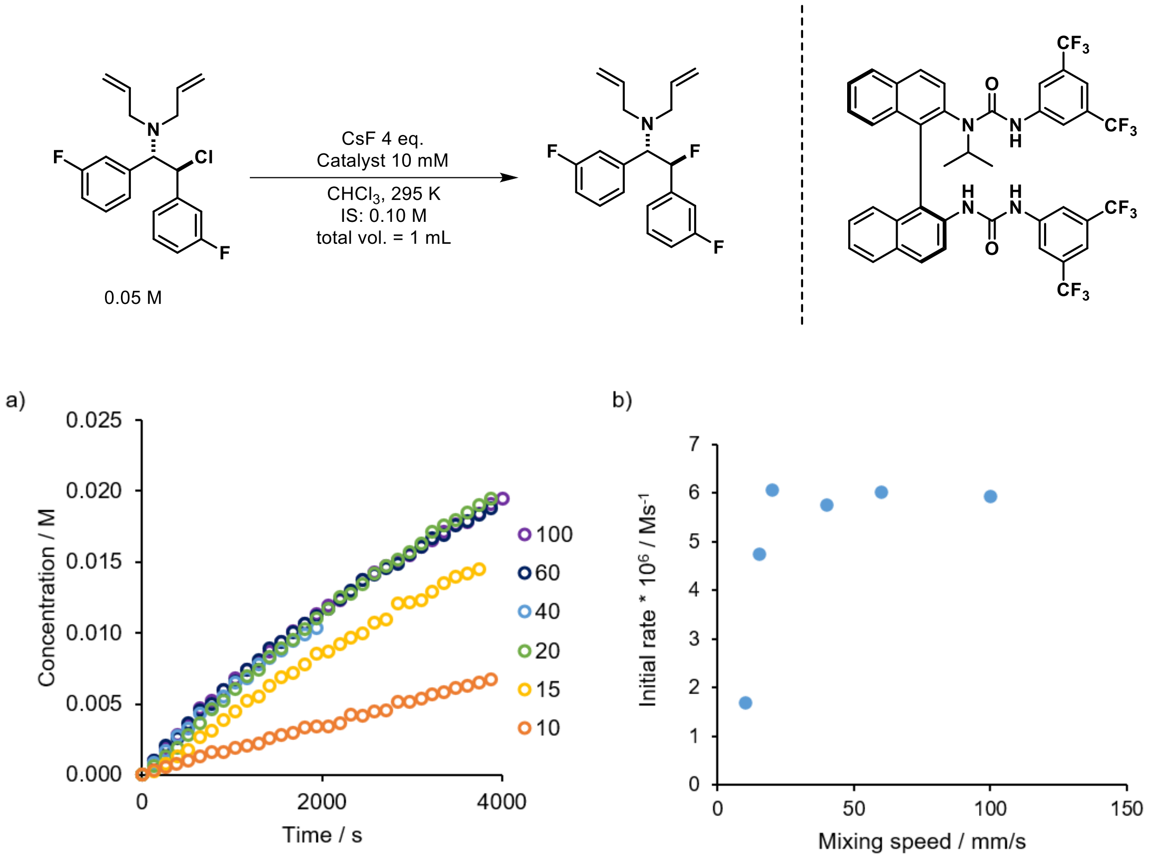

Figure 5.11. Phase-transfer catalysed fluorination of β-chloroamine ([Substrate] = 0.05 M, [Catalyst] = 20 mol%) were monitored using *in-situ* mixing device. a) overlay of percentage yield evolution with varied mixing speed. b) initial rate (*d*[Product]/*d*t) dependence on mixing speed.

5.4.4 Effect of water

5.4.4.1 β-bromosulfide

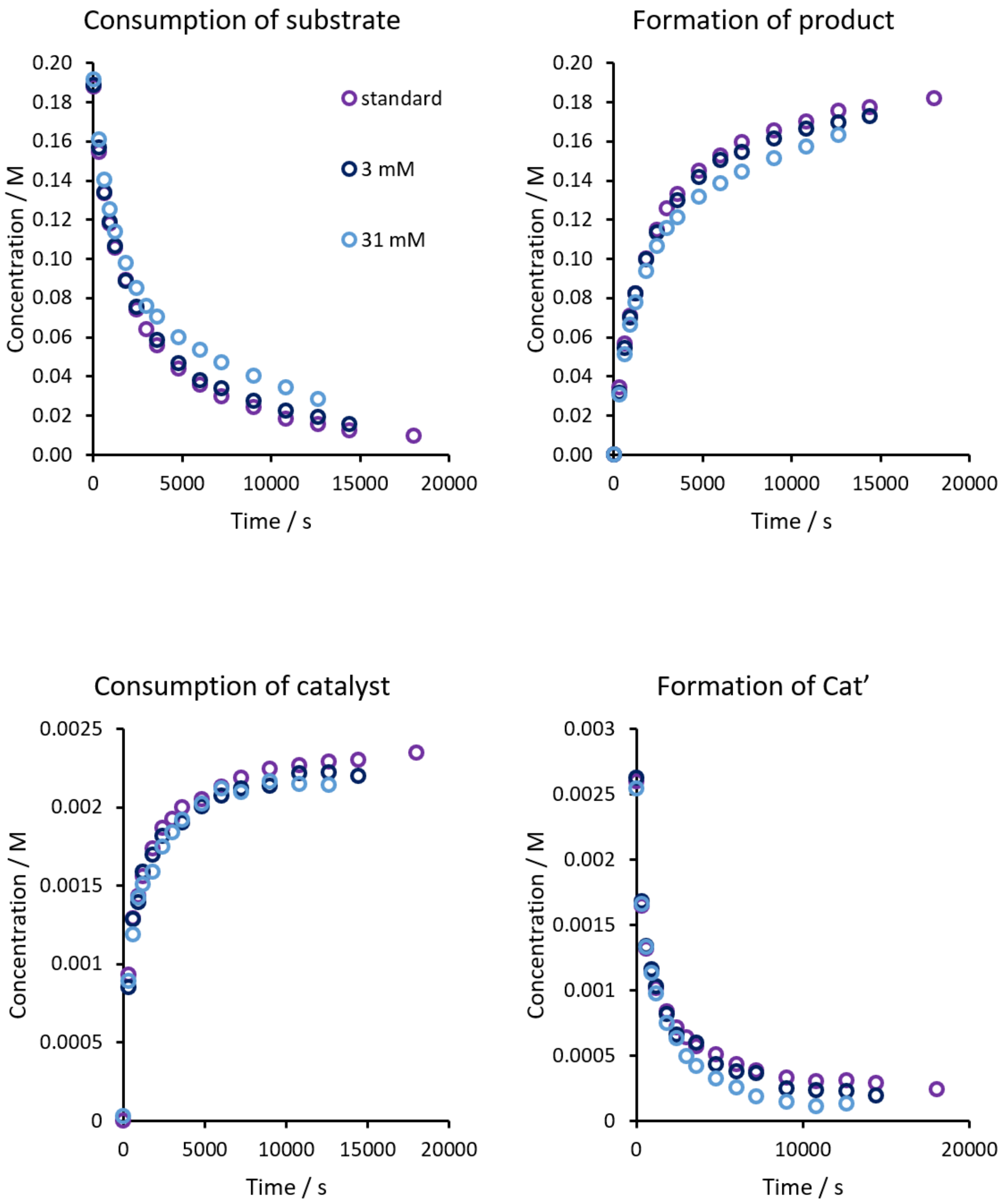

Figure 5.12. Overlaid plots detailing the effect of varying water concentration on the major species present during the reaction against the time. Each color represents a different water concentration with [RBr] = 0.19 M, [**1a**]$_0$ = 2.5 mM. Note that under standard conditions, anhydrous dichloromethane was used as solvent.

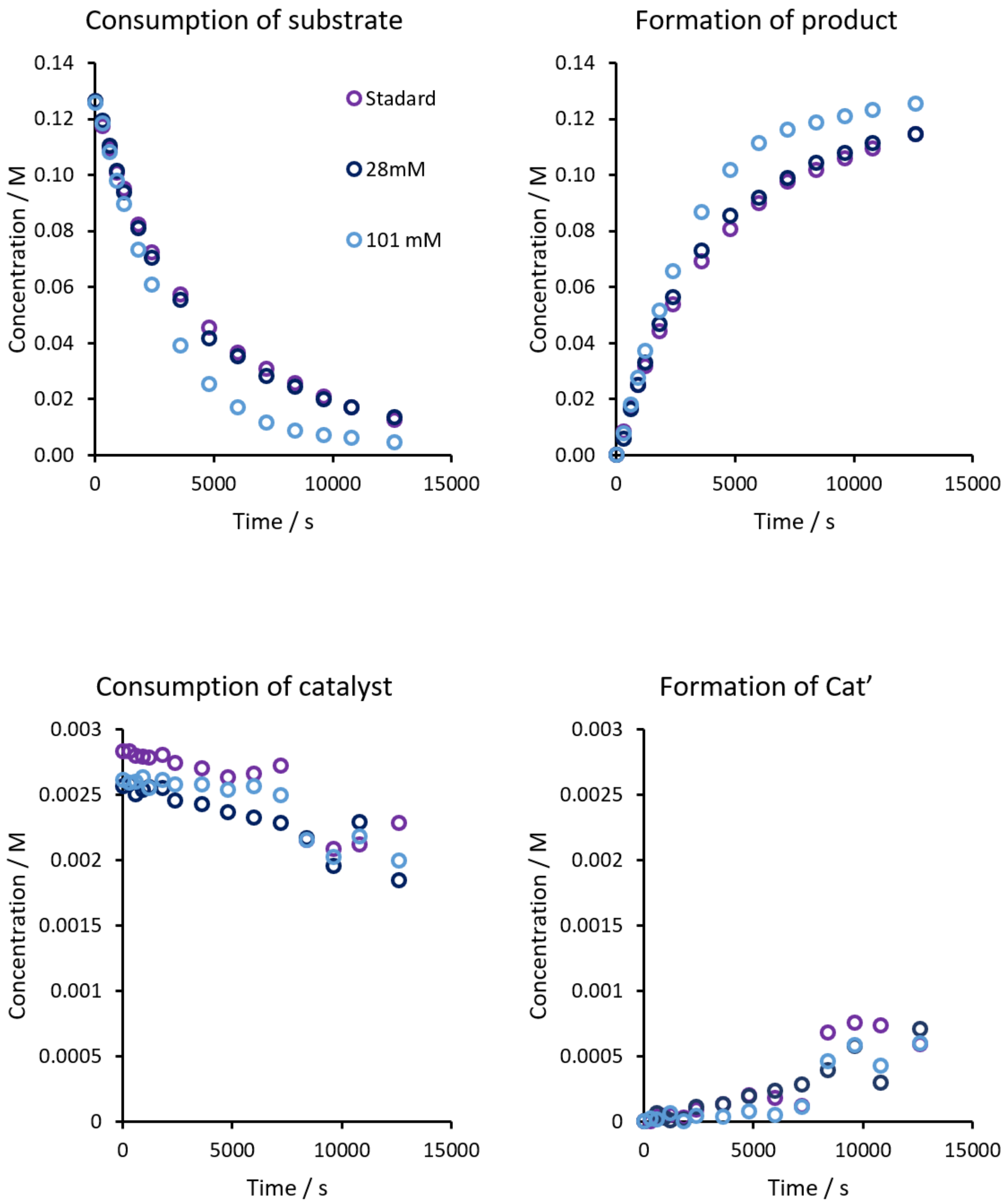

Figure 5.13. Overlaid plots detailing the effect of varying water concentration on the major species present during the reaction against the time. Each color represents a different water concentration with [RBr] = 0.126 M, [**1b**]$_0$ = 2.6 mM. Note that under standard conditions, anhydrous dichloromethane was used as solvent.

5.4.4.2 β-chloroamine

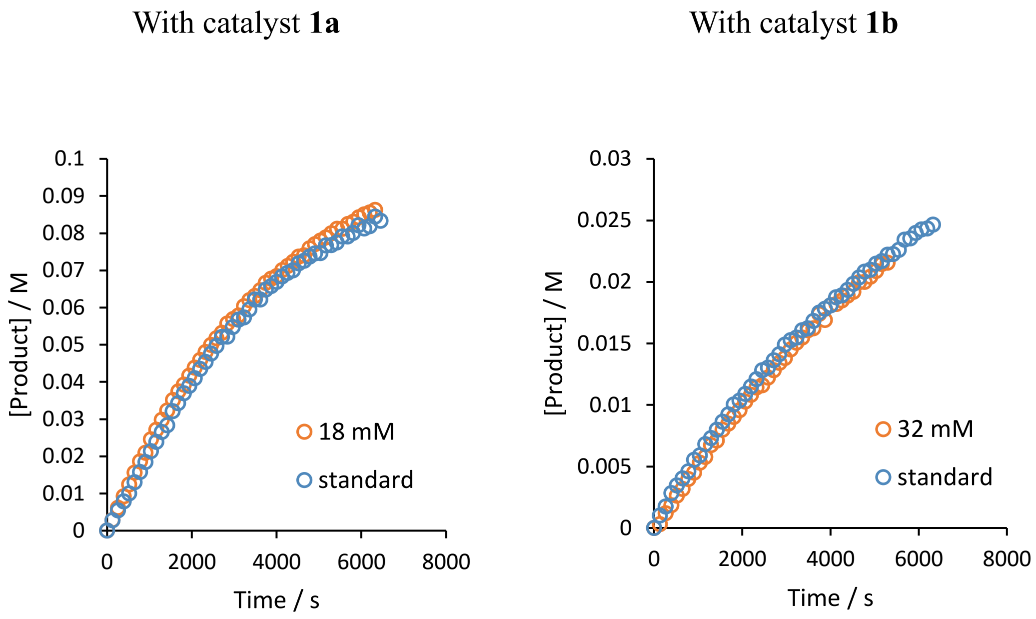

Figure 5.14. Overlaid plots detailing the effect of varying water concentration on the product against the time. Left: $[RCl]_0$ = 125 mM, $[\mathbf{1a}]_0$ = 13 mM; right : $[RCl]_0$ = 50 mM, $[\mathbf{1b}]_0$ = 10 mM.

5.4.5 Substrate-alkylated catalyst

5.4.5.1 NMR spectra

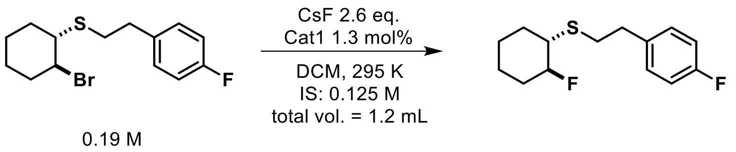

Scheme 5.3. Reaction conditions.

The reaction was conducted following general procedures under the reaction conditions shown in **Scheme 5.3**. The reaction was allowed to reach over 95% conversion to maximize the formation of Cat' species. An aliquot was taken and quenched to make an NMR sample, and a $\{^1H\}^{19}F$ NMR spectrum was acquired. The NMR sample was then poured out, mixed with silica (Merck silica gel 60, 40–63 μm), and stirred for 40 minutes. The solution was filtrated, topped up with dichloromethane, and characterized by $\{^1H\}^{19}F$ NMR (**Figure 5.15**). Similar experiments were conducted with catalyst **1b**, and the results are shown in **Figure 5.16**. In both cases, the formation of Cat' was observed, which was decomposed into the corresponding catalyst and β-hydroxyl sulfide under acidic conditions.

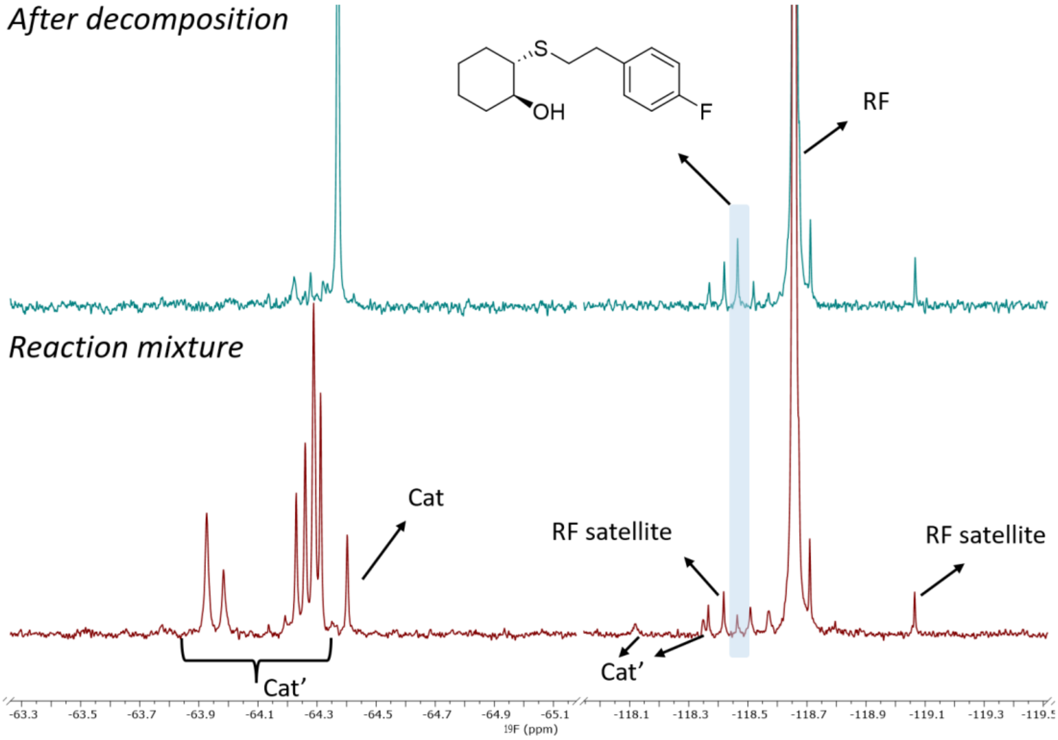

Figure 5.15. Partial $\{^{1}H\}^{19}F$ NMR spectra showing catalyst and aromatic fluoride regions, the chemical shifts were all reference to 1-fluoronaphthalene. Bottom: the reaction mixture reaching near completion. Top: the same mixture after decomposition of Cat'. [RBr] = 0.19 M, [**1a**] = 2.5 mM.

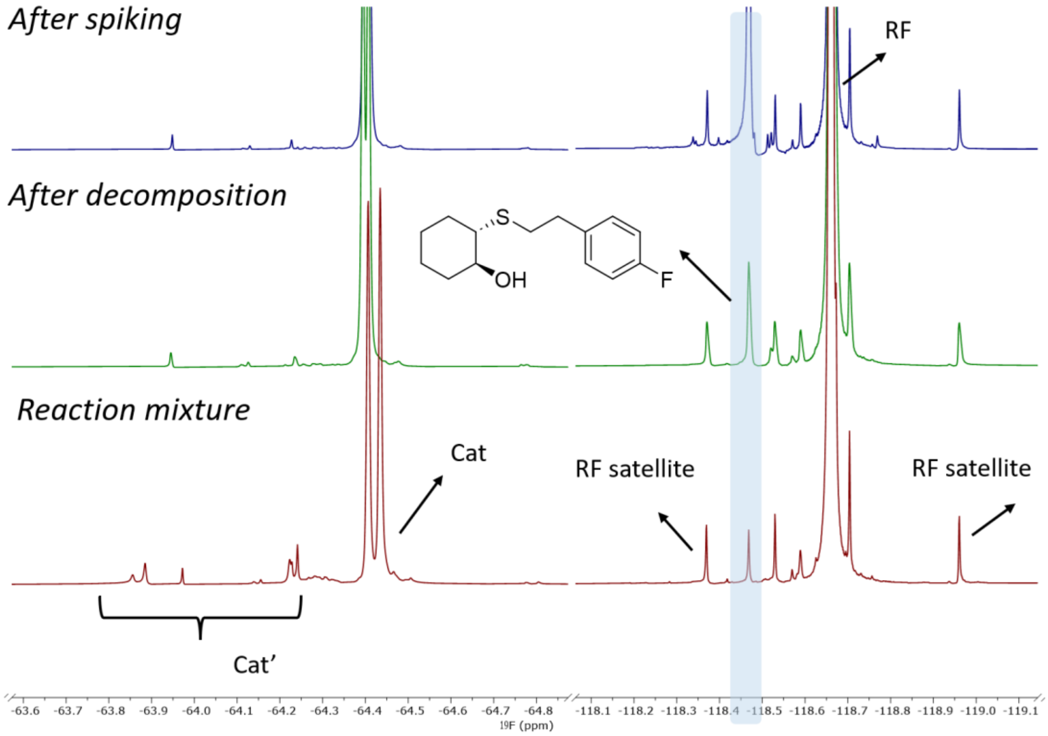

Figure 5.16. Partial $\{^{1}H\}^{19}F$ NMR spectra showing catalyst and aromatic fluoride regions, the chemical shifts were all reference to 1-fluoronaphthalene. Bottom: the reaction mixture reaching near completion. Middle: the

same mixture after decomposition of Cat'. Top: the same mixture after spiking of the β-hydroxyl sulfide. [RBr] = 0.25 M, [**1b**] = 25mM.

5.4.5.2 ESI-MS

The reaction was conducted following general procedures under the reaction conditions shown in **Scheme 5.3**. Three aliquots were taken at t = 0, 90, 240 mins. Each aliquot was separated into two portions, one used for preparation of NMR sample (allow for determination of the yield via NMR), and the other used for preparation of ESI-MS sample. Results are shown in **Figure 5.17**.

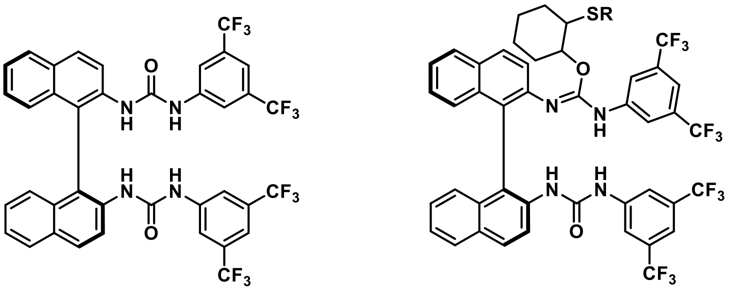

Cat

MW: 794.16

Cat'

MW: 1030.26

Scheme 5.4. Molecular weight (MW) for key species.

(a)

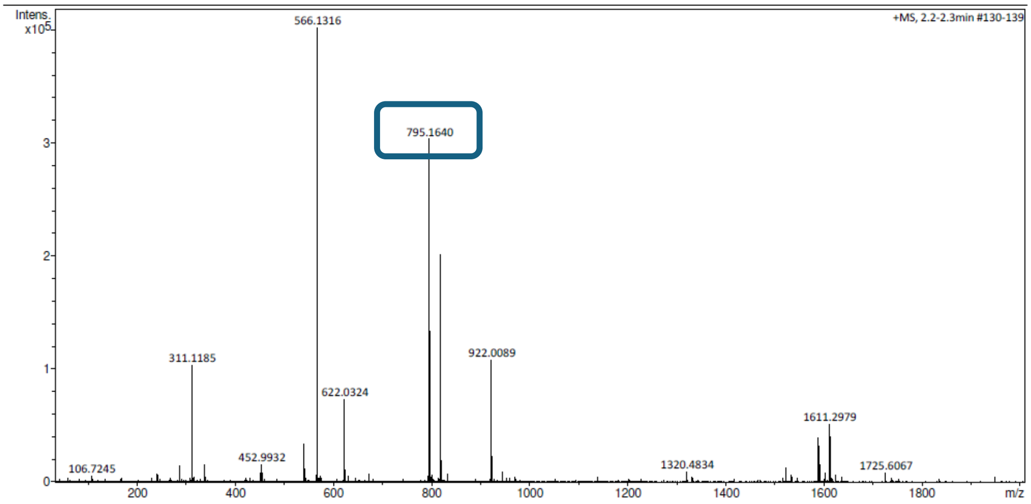

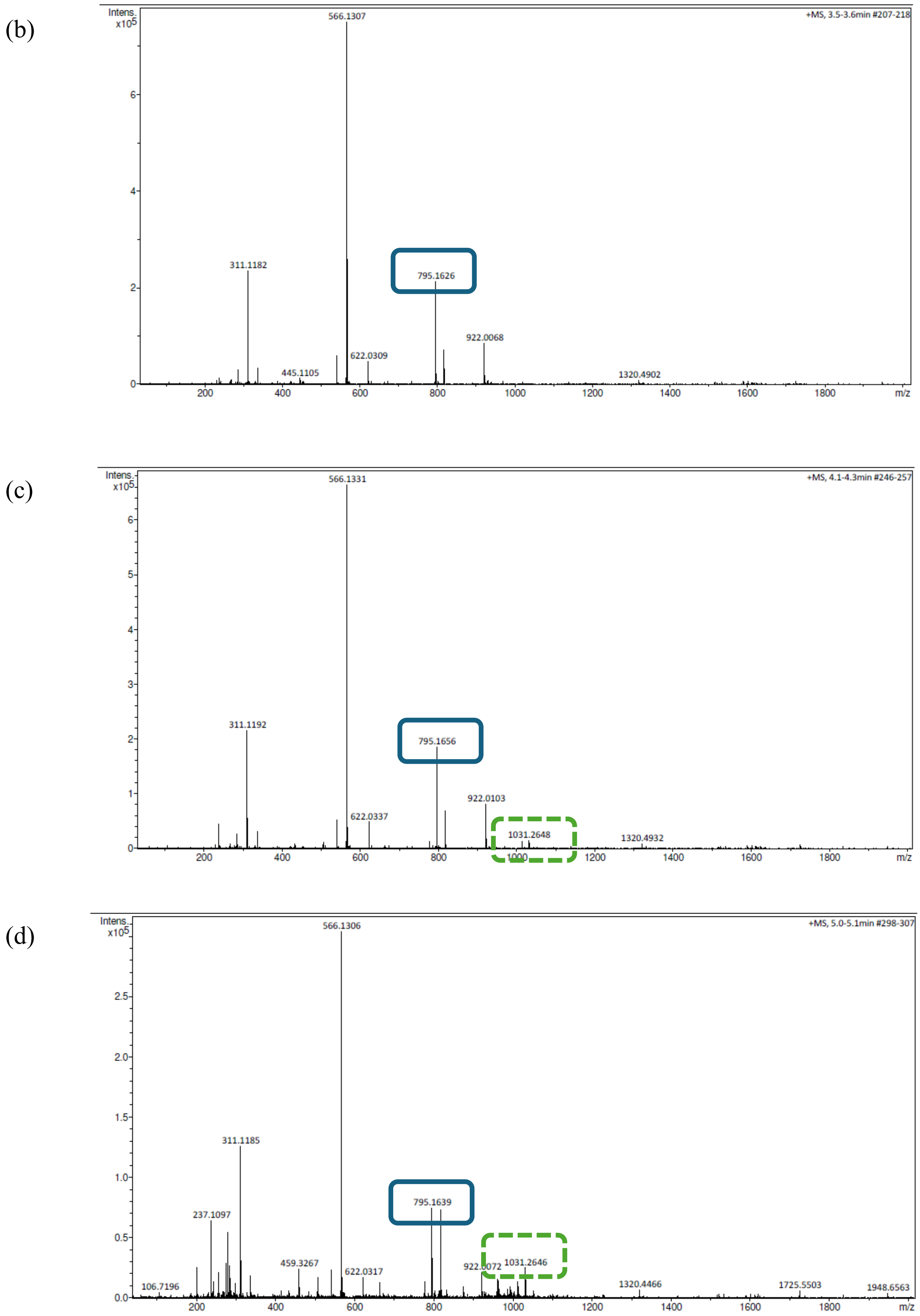

Figure 5.17. The electrospray ionization mass spectrometry spectra of samples of (a) catalyst **1a**, (b) the standard reaction mixture at t = 0, (c) the standard reaction mixture at t = 30 mins, yield = 50%, (d) the standard reaction mixture at t = 240 mins, yield = 90%. The yield was determined by NMR spectroscopy with reference to internal standard. The M+1 peaks for Cat and Cat' were highlighted by blue lines and green dashed lines respectively.

5.4.5.3 Effect of addition of base

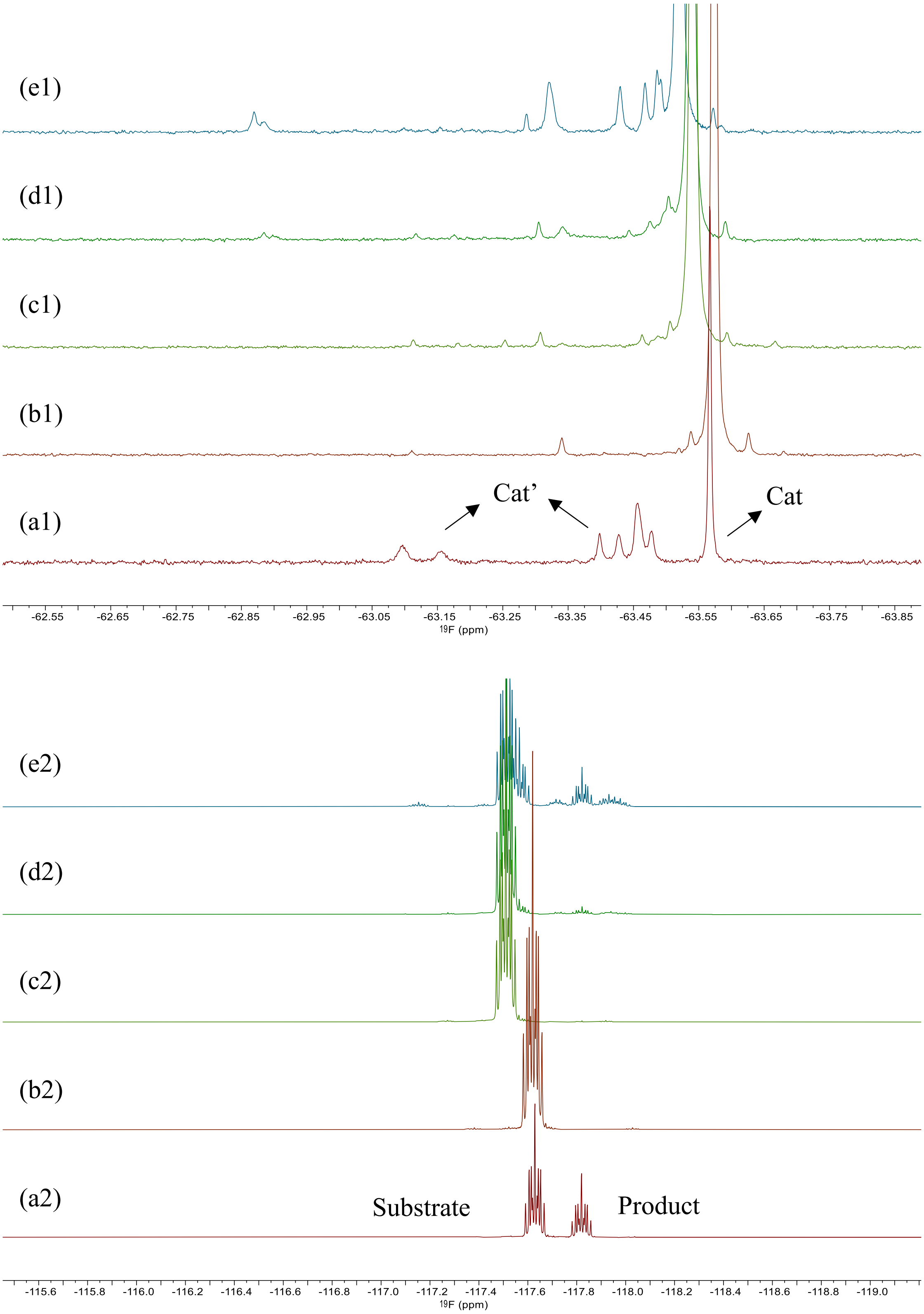

Figure 5.18. Partial ^{19}F NMR spectra showing catalyst and aromatic fluoride regions, the chemical shifts were all reference to 1-fluoronaphthalene (δF = –124.07). (a) sample of reaction mixture at 30% conversion; (b) a solution of catalyst (1.3 mol%), substrate (0.19 M) and 1-fluoronapthalene (0.125 M) in DCM; (c) the same solution directly after addition of tetramethylguanidine (TMG); (d) after 1 hour of addition of TMG; (e) after 16 hours of addition of TMG.

5.4.5.4 Catalytic ability

The reaction was conducted following general procedures with β-bromosulfide (0.181 g, 0.571 mmol, 0.19 M), catalyst 1 (0.00298 g, 0.0038 mmol, 0.7 mol%), and 1-fluoronapthelene (0.0451 g, 0.309 mmol) in anhydrous DCM (3 mL), with excess amount of CsF (0.3463 g, 2.28 mmol). The reaction was stirred for 44 hours to allow full consumption of catalyst, which was verified by ^{19}F NMR (**Figure 5.19**). After that, more β-bromosulfide (0.1575 g, 0.19 M, note that volume is now reduced to 2.6 mL due to ex-situ sampling) was added to the reaction mixture, and the reaction was monitored by *ex situ* sampling method.

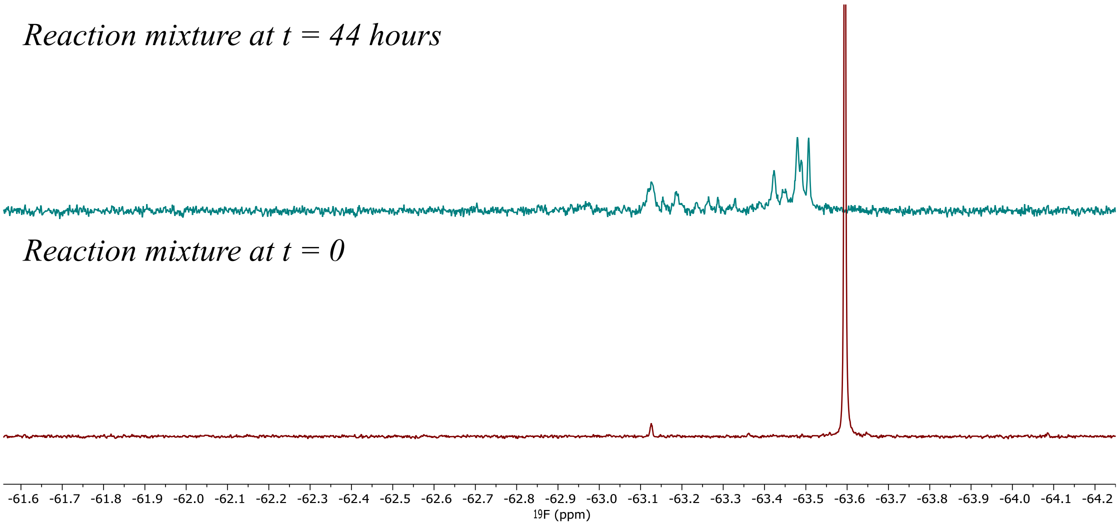

Figure 5.19. Partial ^{19}F NMR spectra showing the catalyst region of the reaction mixtures at t = 0 and t = 44 hours.

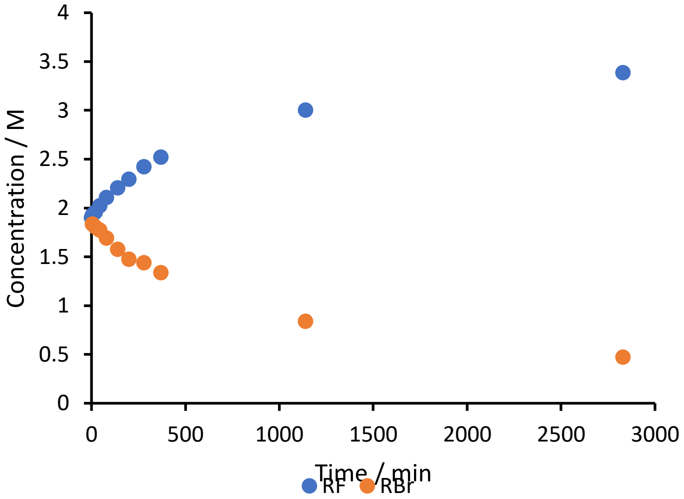

Figure 5.20. Concentration-time profile after addition of more substrate.

5.4.5.5 Effect of ex situ sampling

Two reactions were conducted with the same initial conditions but monitored by different reaction monitoring techniques, i.e. *ex-situ* and *in-situ*, and the results are shown in **Figure 5.21**. There are several catalyst-related species formed during the fluorination of β-bromosulfide catalysed by **1a**, two major species were labelled as Cat'1 and Cat' 2.

When monitored by different techniques the concentrations of substrate, product and catalyst were in good agreement, but the concentration of Cat'1 and Cat'2 was not. We suspected that the concentration of Cat' changes occurred during the quenching and diluting process of the *ex-situ* sampling. Therefore, in all sections, we have only used the concentration of catalyst and treated the rest as Cat'.

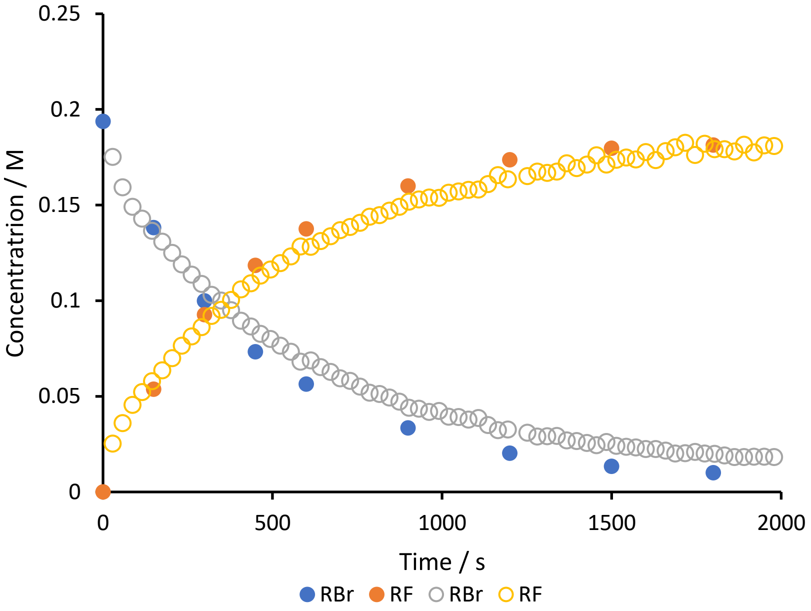

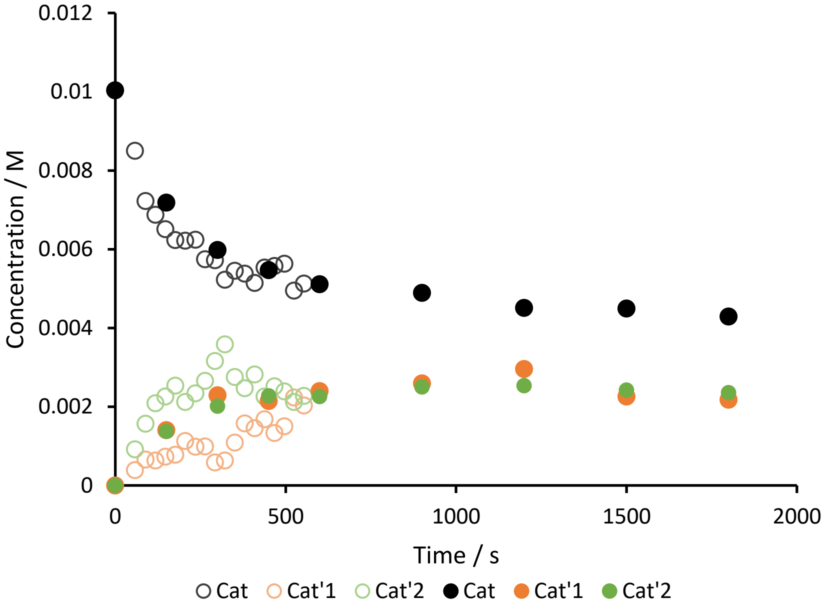

Figure 5.21. Overlayed kinetic profiles of two reactions that were conducted with same initial conditions but monitored by *in situ* (hollow circle) and *ex situ* (solid circle) sampling method. Catalyst related species have lower concentration and are shown in the lower graph. $[RBr]_0 = 0.19$ M, $[1a]_0 = 10$ mM.

5.4.6 Effect of addition of products

5.4.6.1 β-bromosulfide

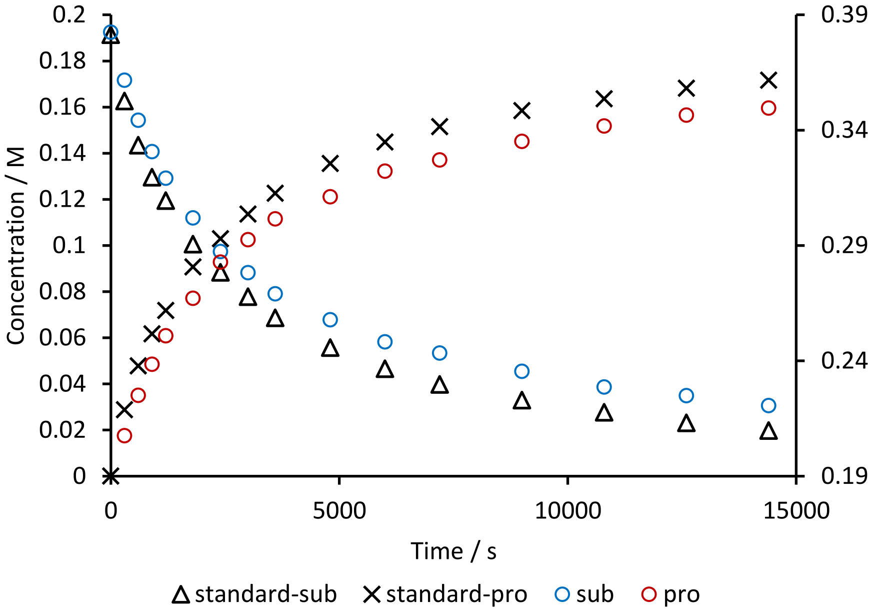

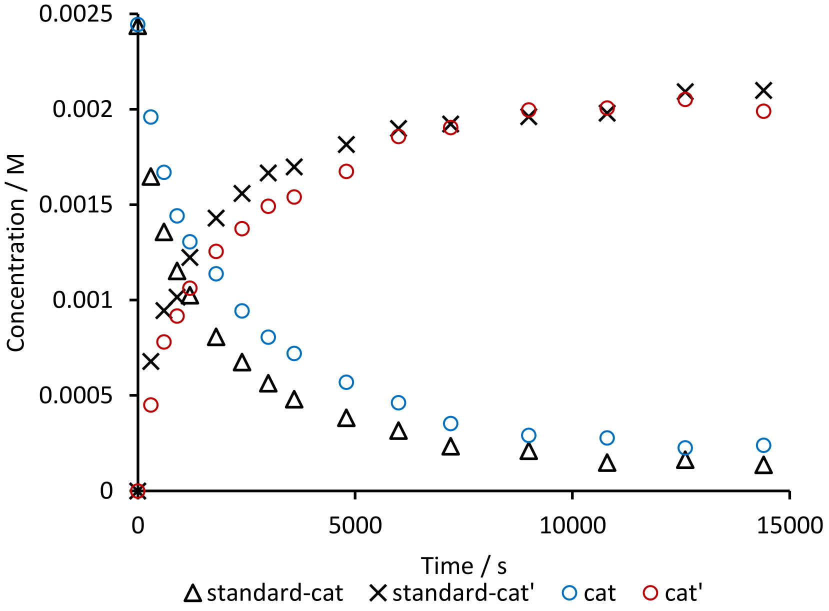

Figure 5.22. Overlayed kinetic profiles of standard reaction and reaction with 1 equivalent addition of products (both RF and CsBr) at the beginning of the reaction. For standard reaction: $[\text{RBr}]_0 = 0.190$ M, $[\mathbf{1a}]_0 = 2.45$ mM. Catalyst related species have lower concentration and are shown in the lower graph.

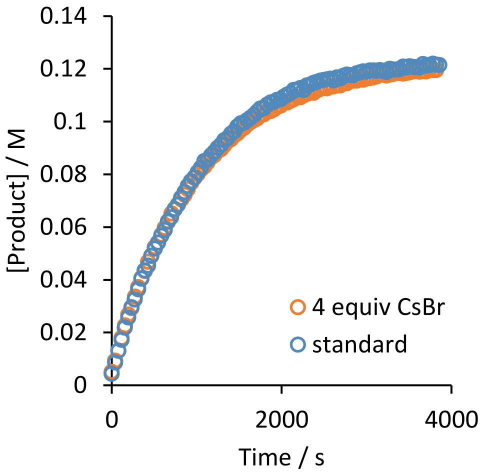

Figure 5.23. Overlaid plots showing the effect of addition of 4 equivalents of ground CsBr on the product against the time. $[RBr]_0$ = 125 mM, $[\mathbf{1b}]_0$ = 6.25 mM.

5.4.6.2 β-chloroamime

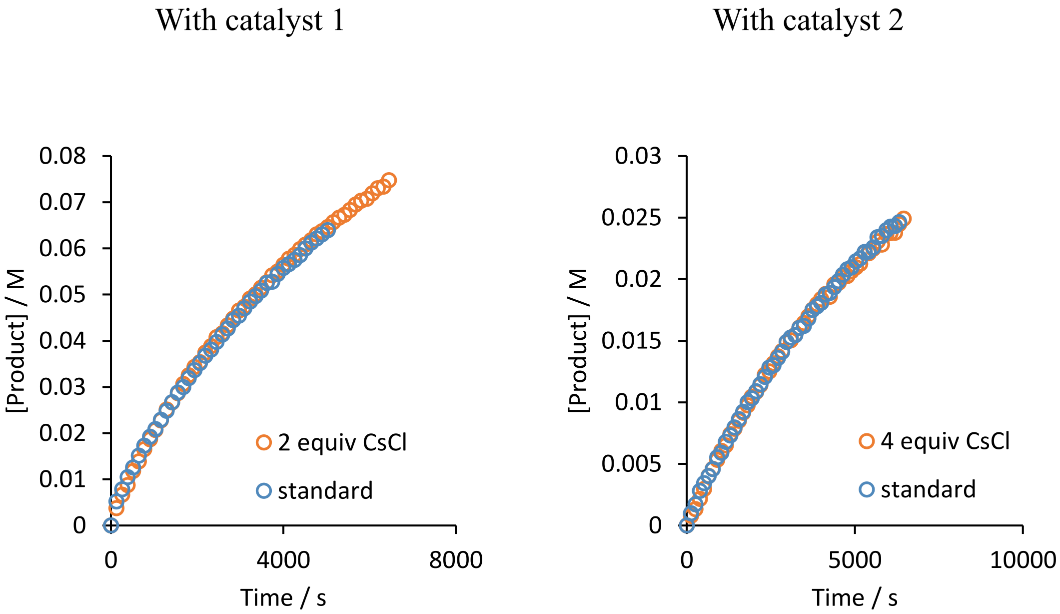

Figure 5.24. Overlaid plots showing the effect of addition of 2 or 4 equivalents of ground CsCl on the product against the time. Left: $[RCl]_0$ = 125 mM, $[\mathbf{1a}]_0$ = 12.5 mM; right : $[RCl]_0$ = 50 mM, $[\mathbf{1b}]_0$ = 10 mM.

5.5 Magnetisation transfer

5.5.1 *General procedures and parameters*

In a dried NMR tube, β-bromosulfide (0.0422 g ,0.133 mmol) and catalyst 1 (0.0199 g, 0.025 mmol) were dissolved in anhydrous deuterated dichloromethane (700 μL). The NMR tube was capped, further sealed by parafilm, and inserted into spectrometer. Pulse calibration was carried prior to the first experiment and the same value was used throughout the day. The experiment was set using following pulse sequence at a temperature range from 284K to 312K. The key parameters are shown in **Table 5.1**.

A selective inversion recovery pulse sequence was used for magnetization transfer experiments: after a relaxation delay, RD, a soft 180º pulse (iSNOB[176] shape, 3750 or 6424 microseconds duration, 0.35 or 0.60 ppm bandwidth) was used to selectively inverted a range of frequencies covering one of the exchange peaks, followed by variable delay VD, during which time the magnetization evolved according to the chemical exchange kinetics and relaxation processes. The resulting longitudinal magnetization was detected using a hard 90º pulse. This pulse sequence was repeated for a series of variable delays (VDLIST) in a random order.

For each set of experiments with the same catalyst loading and temperature, i.e. only differs in VD, the resulting *pseudo*-2D spectrum was split into individual spectra and stacked. The stacked spectra were processed together, in the sequence of apodization, zero-filling, phase correction and baseline correction. An unaffected proton was chosen as internal standard (see Section 5.5.2), and the relative integration of both inverted peak and observed peak were calculated by referring to the integration of the internal standard. Further data processing was discussed in Section 5.5.3.

For experiments where 90° pulse was used, the longitudinal relaxation delay (RD) needs to be larger than 5 x T_1 to allow relaxation over 99%. Therefore, it is essential to get a knowledge of the T_1 values of all the interested peaks under experimental conditions. All T_1 values shown in the following table were determined by following FLIPS method and averaged from 3 runs.[8] Experiments were carried in the temperature ranged from 300 K to 330 K. As the T_1 values appeared to increase with increased temperature, the maximum T_1 values at 312 K or 330 K were used to calculate the required relaxation delay.

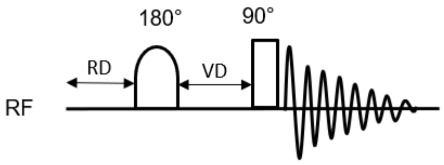

Substrate	β-bromosulfide	β-chloroamine
Number of scans (NS)	8	8
Relaxation delay (RD) / s	30	20
Spectrum centre (O1P) / ppm	4.3	5.5
Spectrum width (SW) / ppm	8.6	11
Selective pulse bandwidth / ppm	0.35	0.6
Selective pulse frequency / ppm	4.32	5.5
Variable delay list (VDLIST)[a]	VD1	VD2
Variable delay list length (1TD)	16	10
Solvent	CD2Cl2	CDCl3

[a] VD1 = 0.5, 1, 1.5, 2, 3, 4, 5, 6, 7, 8, 9, 10, 15, 20, 25, 30 seconds; VD2 = 0.1, 0.5, 1, 2, 3, 4, 6, 10, 15, 20 seconds.

Table 5.1. Typical values of parameters used in automation.

	P1	P2	IS	Temperature / K	[RBr] / M
***T_1* / s**	4.1	3.6	2.2	300	0.19
	4.9	4.2	2.7	312	0.19
	P1	**P2**	**IS**	**Temperature / K**	**[RCl] / M**
	1.8	2.0	1.2	330	0.19
	1.7	2.0	1.1	320	0.19
	1.5	1.7	0.9	310	0.19

Table 5.2. T_1 values for the inverted peak (P1), the observed peak (P2) and the internal standard (IS) under different temperatures. All values are determined by FLIPS and averaged from three runs.

5.5.2 Representative spectra

5.5.2.1 β-bromosulfide

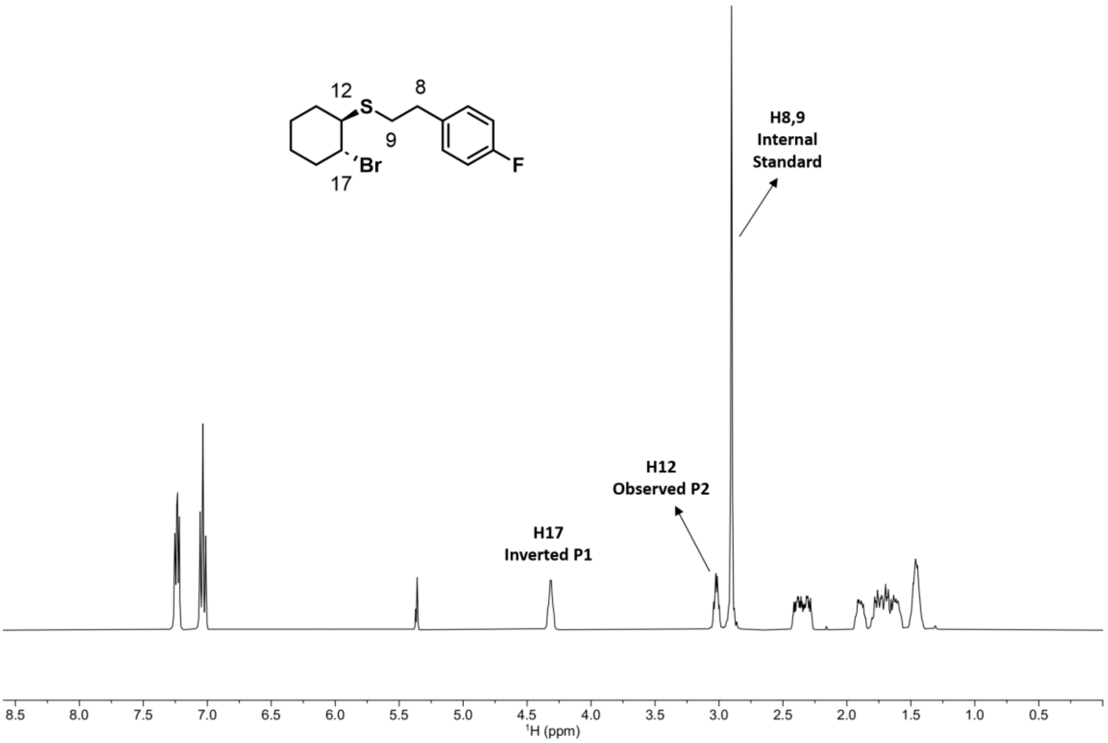

Figure 5.25. Spectrum of NMR sample, showing the locations of key peaks. [RBr] = 0.19 M, T = 300 K.

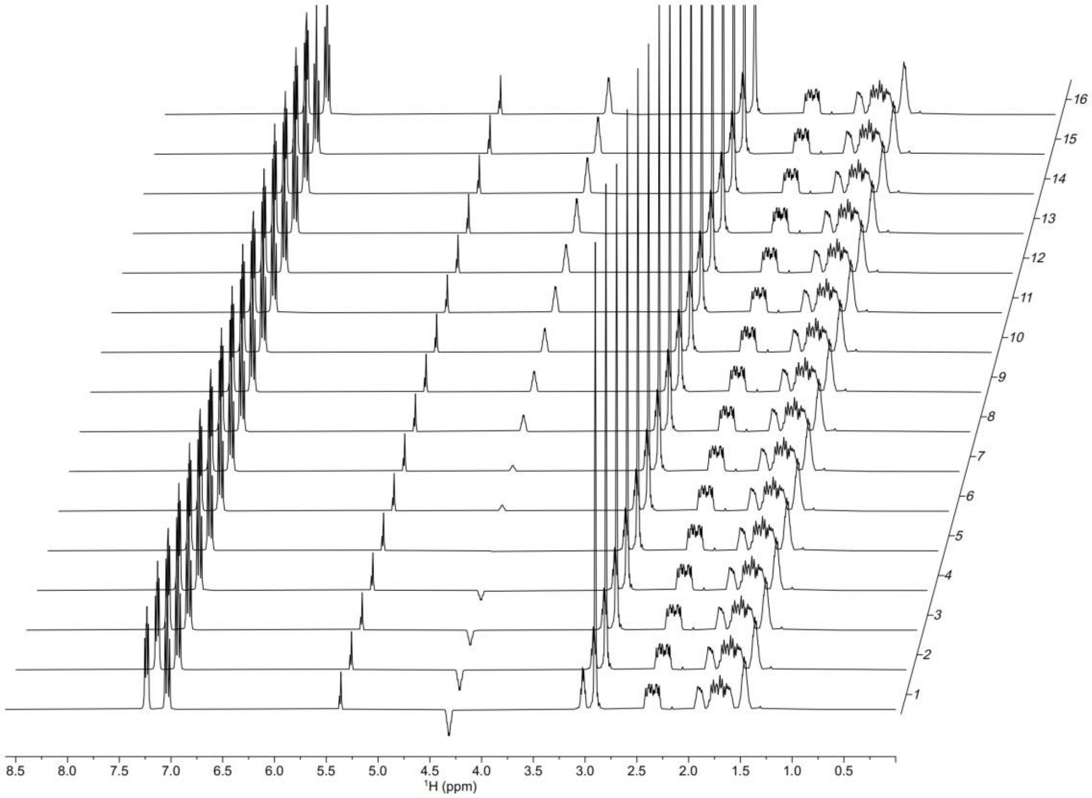

Figure 5.26. The stacked spectra of the same reaction. A random delay list was used during the experiment; the obtained spectra were reordered according to delay time.

5.5.2.2 β-chloroamine

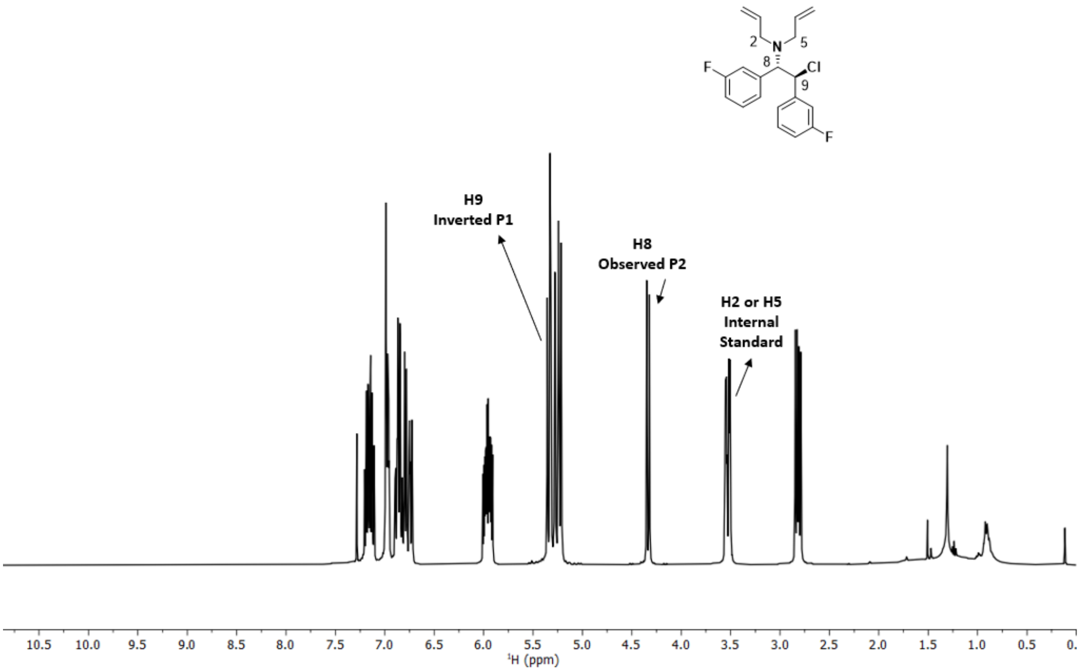

Figure 5.27. Spectrum of NMR sample, showing the locations of key peaks. [RCl] = 0.19 M, T = 320 K.

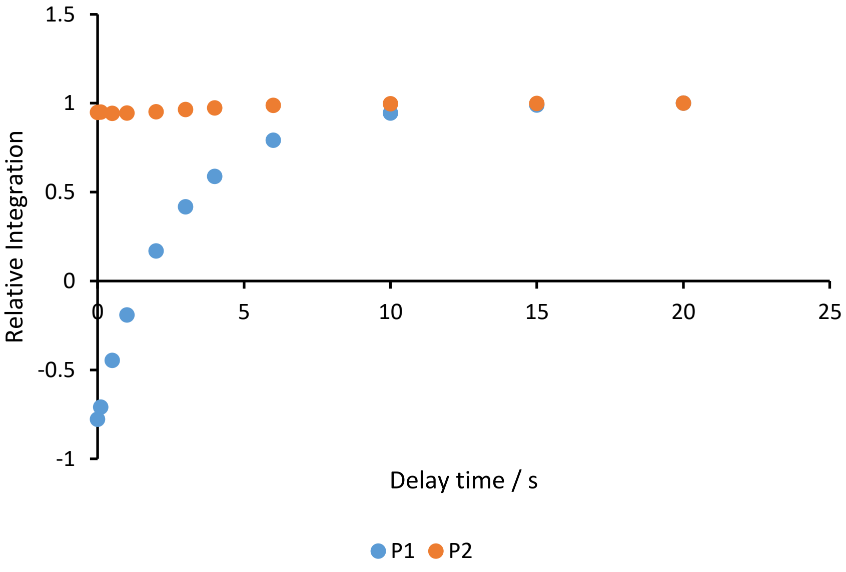

Figure 5.28. A representative integration-time profile with [RCl] = 0.19 M, T = 320 K.

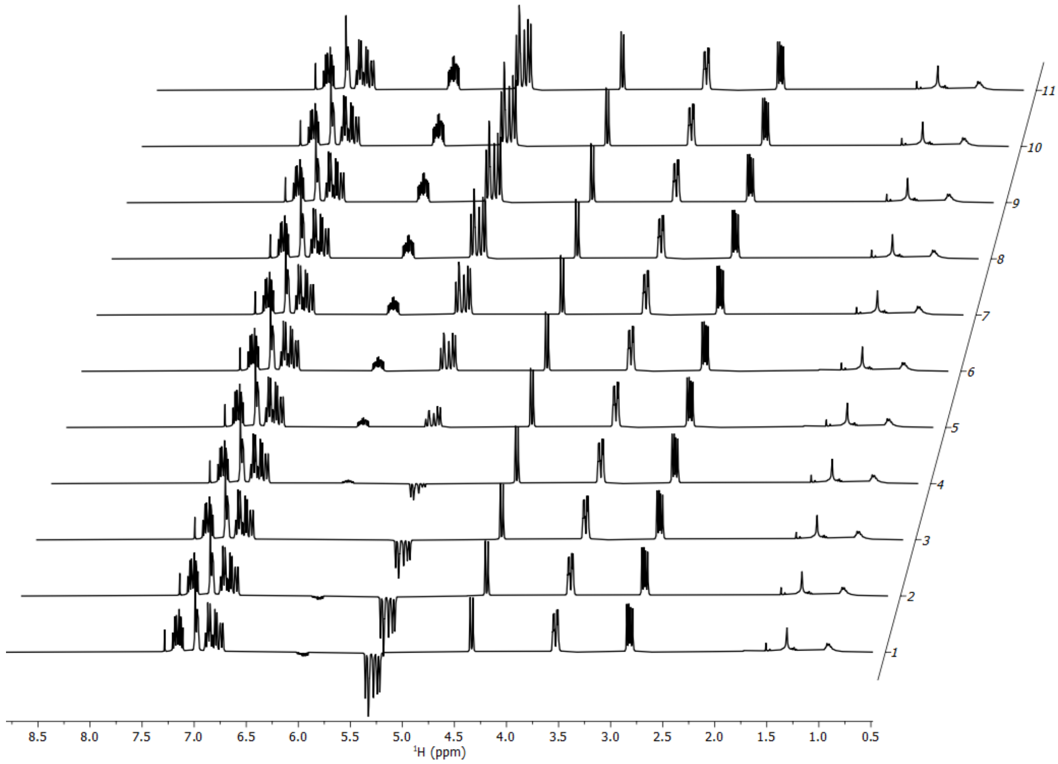

Figure 5.29. The stacked spectra of the same reaction. A random delay list was used during the experiment; the obtained spectra were reordered according to delay time.

5.5.3 *Kinetic model and fitting*

In the case of two-spin system, where spin A and B undergo chemical exchange, the following kinetic model can be constructed, where k_1 is the rate of exchange, T_1^A and T_1^B are longitudinal relaxation time constants of spin A and B respectively. At the beginning of the experiment, the sample is fully magnetized, and both signals A and B are NMR measurable, and their integration represents their concentration. The selective 180° soft pulse inverts the net magnetization of spin A. After a variable delay time, a 90° pulse is applied followed by acquisition. This experiment is repeated with a list of delay times, and the intensities of both signals are recorded and plotted as a function of delay time.

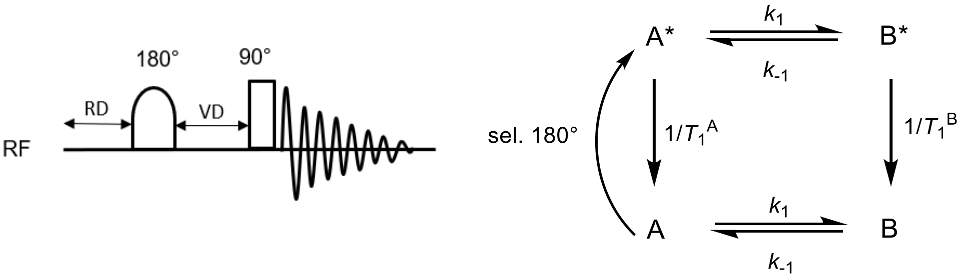

Figure 5.30. Left: pulse sequence for a selective inversion recovery experiment, where RD = relaxation delay, VD = variable delay. Right: kinetic model for a two-spin system, where spin A is inverted by the selective 180° soft pulse to A* and undergoes chemical exchange with B*, and both A* and B* undergo relaxation.

In the case that spin A and B are in the same molecule and undergo chemical exchange via an intermediate, S, the following kinetic model can be constructed. At the beginning of the experiment, the sample is fully magnetized, and signals A, S, and B are NMR measurable. The selective 180° soft pulse inverted the net magnetization of spin A. During a varied delay time, the intensity of peak A, S and B changes as a consequence of relaxation and chemical exchange.

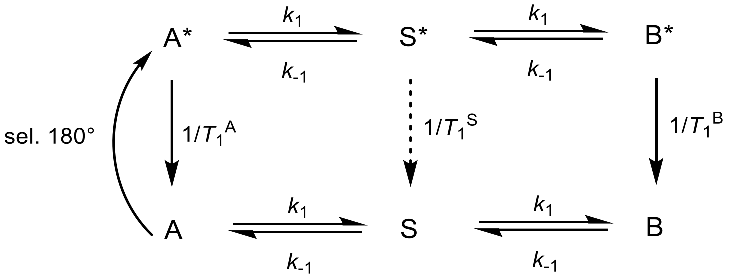

Figure 5.31. Kinetic model when spin A and B are in the same molecule and exchange via formation and dissociation of intermediate S.

For β-bromosulfide, S is the episulfonium intermediate. We didn't observe a separate set of peaks for S during the magnetization transfer experiments, indicating that the concentration of episulfonium intermediate is very low with respect to β-bromosulfide. Therefore, it is reasonable to assume that the relaxation of S* has a negligible effect on the overall kinetics.

The intensity of fully recovered equilibrium magnetization NMR signal of species X is I_{eq}^{X}. The intensity of a signal after selective inversion and a delay time, *t*, is I_t^X. Since the exchange process is intramolecular, we get Eq.5.3.

$$I_t^A = I_{eq}^A \frac{[A] - [A^*]}{[A^*] + [A]} \tag{5.1}$$

$$I_t^B = I_{eq}^B \frac{[B]-[B^*]}{[B^*]+[B]} \tag{5.2}$$

$$I_{eq}^A = I_{eq}^B \tag{5.3}$$

$$\frac{d[S^*]}{dt} = 0 = k_1[A^*] + k_1[B^*] - k_{-1}[S^*] - k_{-1}[S^*] \tag{5.4}$$

Rearrange Eq.5.4 gives Eq.5.5. Combine Eq.5.5 and Eq.5.6 gives Eq.5.7.

$$[S^*] = \frac{k_1([A^*] + [B^*])}{2k_{-1}} \tag{5.5}$$

$$\frac{d[B^*]}{dt} = k_{-1}[S^*] - k_1[B^*] - \frac{1}{T_1^B}[B^*] \tag{5.6}$$

$$\frac{d[B^*]}{dt} = k_{-1}\frac{k_1([A^*] + [B^*])}{2k_{-1}} - k_1[B^*] - \frac{1}{T_1^B}[B^*] \tag{5.7}$$

$$\frac{d[B^*]}{dt} = \frac{k_1[A^*]}{2} - \frac{k_1[B^*]}{2} - \frac{1}{T_1^B}[B^*] \tag{5.8}$$

$$\frac{d[B^*]}{dt} = k_{obs}([A^*] - [B^*]) - \frac{1}{T_1^B}[B^*], \qquad where\ k_1 = 2\ k_{obs} \tag{5.9}$$

Similarly, combine Eq.5.5 and Eq.5.10 gives Eq.5.11, which can be derived into eqn Eq.5.12.

$$\frac{d[A^*]}{dt} = k_{-1}[S^*] - k_1[A^*] - \frac{1}{T_1^A}[A^*] \tag{5.10}$$

$$\frac{d[A^*]}{dt} = k_{-1}\frac{k_1([A^*] + [B^*])}{2k_{-1}} - k_1[A^*] - \frac{1}{T_1^A}[A^*] \tag{5.11}$$

$$\frac{d[A^*]}{dt} = k_{obs}([B^*] - [A^*]) - \frac{1}{T_1^A}[A^*] \tag{5.12}$$

We also have Eq.5.13, which can be rearranged into Eq.5.14. From Eq.5.15 to 5.18, we can get Eq.5.19 and Eq.5.20.

$$\frac{d[S]}{dt} = 0 = k_1[A] + k_1[B] - k_{-1}[S] - k_{-1}[S] \tag{5.13}$$

$$[S] = \frac{k_1([A] + [B])}{2k_{-1}} \tag{5.14}$$

$$\frac{d[B]}{dt} = k_{-1}[S] - k_1[B] + \frac{1}{T_1^B}[B] \tag{5.15}$$

$$\frac{d[B]}{dt} = \frac{k_1[A]}{2} - \frac{k_1[B]}{2} + \frac{1}{T_1^B}[B] \tag{5.16}$$

$$\frac{d[A]}{dt} = k_{-1}[S] - k_1[A] + \frac{1}{T_1^A}[A] \tag{5.17}$$

$$\frac{d[A]}{dt} = k_{-1}\frac{k_1([A] + [B])}{2k_{-1}} - k_1[A] + \frac{1}{T_1^A}[A] \tag{5.18}$$

$$\frac{d[B]}{dt} = k_{obs}([A] - [B]) + \frac{1}{T_1^B}[B] \tag{5.19}$$

$$\frac{d[A]}{dt} = k_{obs}([B] - [A]) + \frac{1}{T_1^A}[A] \tag{5.20}$$

We measured I_t^A and I_t^B with a range of delay time, t, for each set of experimental conditions (**Table 5.3**). All peak intensities were normalized with $I_0^B = 1$. Kinetic simulations were fitted to experimental data using a standard numerical method approach implemented through Excel with a proprietary scale-up systems add-in.

For each data set, the best fit was obtained by setting T_1^A, T_1^B, k_{obs} and I_0^B as variables. The fitted T_1^A and T_1^B were compared with the values that determined experimentally to confirm the validity of the fittings. The fitted I_0^B values are slightly smaller than unity as a complete inversion was not achieved in experiment. The experimental conditions and fitted k_{obs} (k_{fit}) are shown in **Table 5.3**. The rate of formation of episulfonium ring, k_1, was calculated from k_{fit}, and the standard error (S.E.) of k_1 was propagated from the S.E. of k_{fit}. All experimental and simulated kinetic data are shown in **Figure 6.3**.

The same analysis was performed for β-chloroamine. The experimental conditions and fitted k_{obs} (k_{fit}) are shown in **Table 5.4.** Key experimental conditions and key parameters used for fitting. For all groups, [RCl] = 0.19 M.. The rate of formation of aziridinium ring, k_1, was calculated from k_{fit}, and the standard error (S.E.) of k_1 was propagated from the S.E. of k_{fit}. All experimental and simulated kinetic data are shown in **Figure 6.3**.

Entry	**[1a] / mM**	**[1b] / mM**	**Temperature / K**	**k_{fit} / 10^{-2} s^{-1}**	**k_1 / 10^{-2} s^{-1}**	**S.E. / 10^{-2} s^{-1}**
1	-	-	312	0.75	1.5	0.2
2	-	-	309	0.50	1.0	0.2
3	-	-	306	0.39	0.8	0.1
4*	-	-	300	0.14	0.3	-
5*	-	-	296	0.05	0.1	-
6*	-	-	292	0.00	0.0	-
7	-	-	288	0.11	0.2	0.1
8	-	-	284	0.04	0.1	0.0
9	36.1	-	300	2.30	4.6	0.2
10	77.5	-	300	4.54	9.1	0.3
11	77.5	-	296	4.12	8.2	0.4
12	77.5	-	292	2.63	5.3	0.1
13	77.5	-	288	2.21	4.4	0.2
14	77.5	-	284	1.57	3.1	0.2
15	127.9	-	300	7.84	15.7	0.4
16	195.7	-	300	10.65	21.3	0.7
17	195.7	-	296	8.12	16.2	0.6
18	195.7	-	292	6.69	13.4	1.2
19	195.7	-	288	4.35	8.7	0.8
20	195.7	-	284	2.77	5.5	0.8
21	-	19.0	300	2.48	5.0	1.7
22	-	19.0	296	2.67	5.3	0.4
23	-	19.0	292	1.56	3.1	0.3
24	-	19.0	288	1.20	2.4	0.3
25	-	19.0	284	0.77	1.5	0.3
26	-	45.4	300	6.70	13.4	0.3
27	-	73.0	300	7.84	15.7	0.6
28	-	98.4	300	16.05	32.1	0.5
29	-	98.4	296	15.68	31.4	0.7

30	-	98.4	292	10.15	20.3	0.7
31	-	98.4	288	7.57	15.1	0.3
32	-	98.4	284	5.85	11.7	0.5
33	-	127.1	300	24.75	49.5	0.9

*In these groups, the value of k_{fit} has small influence for the final fitting due to a combination of low or negligible exchange and experimental errors.

Table 5.3. Key experimental conditions and key parameters used for fitting. For all groups, [RBr] = 0.19 M.

Entry	**[1a] / mM**	**[1b] / mM**	**Temperature / K**	**k_{fit} / 10^{-2} s^{-1}**	**k_1 / 10^{-2} s^{-1}**	**S.E. / 10^{-2} s^{-1}**
34	-	-	320	3.74	7.5	2.0
35	-	-	315	4.17	8.3	0.5
36	-	-	310	4.06	8.1	0.5
37	-	-	305	4.92	9.8	0.8
38	-	-	300	5.82	11.6	1.4
39	-	-	320	4.03	8.1	0.5
40	-	-	320	4.01	8.0	0.7
41	-	-	320	4.01	8.0	0.5
42	-	-	320	3.89	7.8	0.7
43	-	-	315	4.78	9.6	0.6
44	-	-	310	4.81	9.6	0.7
45	-	-	305	5.59	11.2	0.6
46	-	-	300	3.05	6.1	1.6
47	42.2	-	320	3.88	7.8	0.5
48	42.2	-	315	4.09	8.2	0.7
49	42.2	-	310	4.68	9.4	0.6
50	42.2	-	305	5.25	10.5	0.6
51	42.2	-	300	5.52	11.0	0.8
52	89.9	-	320	4.74	9.5	0.5
53	89.9	-	315	4.24	8.5	1.6
54	89.9	-	310	4.81	9.6	0.9
55	89.9	-	305	4.80	9.6	1.8
56	89.9	-	300	5.21	10.4	1.3
57	129.6	-	320	4.27	8.5	0.9
58	129.6	-	315	4.70	9.4	1.3

59	129.6	-	310	4.89	9.8	1.3
60	129.6	-	305	5.33	10.7	1.8
61	129.6	-	300	3.71	7.4	2.1
62	190.3	-	320	4.38	8.8	0.6
63	190.3	-	315	4.09	8.2	0.6
64	190.3	-	310	4.04	8.1	1.4
65	190.3	-	305	5.43	10.9	0.9
66	190.3	-	300	3.28	6.6	0.8
67	-	44.3	320	4.42	8.8	1.4
68	-	44.3	315	3.61	7.2	0.8
69	-	44.3	310	4.69	9.4	1.0
70	-	44.3	305	3.93	7.9	1.5
71	-	44.3	300	5.79	11.6	1.1
72	-	87.7	320	3.42	6.8	1.2
73	-	87.7	315	4.00	8.0	0.8
74	-	87.7	310	3.85	7.7	1.3
75	-	87.7	305	5.54	11.1	1.9
76	-	87.7	300	4.46	8.9	1.0
77	-	128.5	320	5.79	11.6	2.1
78	-	128.5	315	5.17	10.3	0.9
79	-	128.5	310	4.72	9.4	1.1
80	-	128.5	305	5.91	11.8	1.5
81	-	128.5	300	4.77	9.5	1.3
82	-	192.5	320	3.47	6.9	1.1
83	-	192.5	315	2.32	4.6	1.4
84	-	192.5	310	3.16	6.3	2.0
85	-	192.5	305	2.38	4.8	1.3
86	-	192.5	300	3.07	6.1	1.4

Table 5.4. Key experimental conditions and key parameters used for fitting. For all groups, [RCl] = 0.19 M.

6. Appendix

6.1 Parts and drawings for mixing device

A software was developed in house (**Figure 6.1**A), allows the user to adjust the moving speed, moving distance and acceleration of the mixing device, and to choose between two modes of operation: software trigger, hardware trigger. This software can be downloaded from https://git.ecdf.ed.ac.uk/lloyd-jones-group/NMRmixer. The device was driven by an SLT-0412 linear stepper motor drive with a 150 mm drive length (**Figure 6.1**B). Two PNP induction limit sensors were used as safety precaution. The motor will be halted when moving out of the set range. Tubing and fittings were supplied by IDEX and Cole Parmer. The NMR tube and glass capillary tubes were supplied by Wilmad and truncated in house. The non-magnetic spring was supplied by Lee Springs. Plunger tips were machined by Röchling Industrial UK. The main body of the insert section was machined in house (**Figure 6.1**D). Drawing for the main parts B to D is shown in **Figure 6.2**, and further details can be found in publication 161.

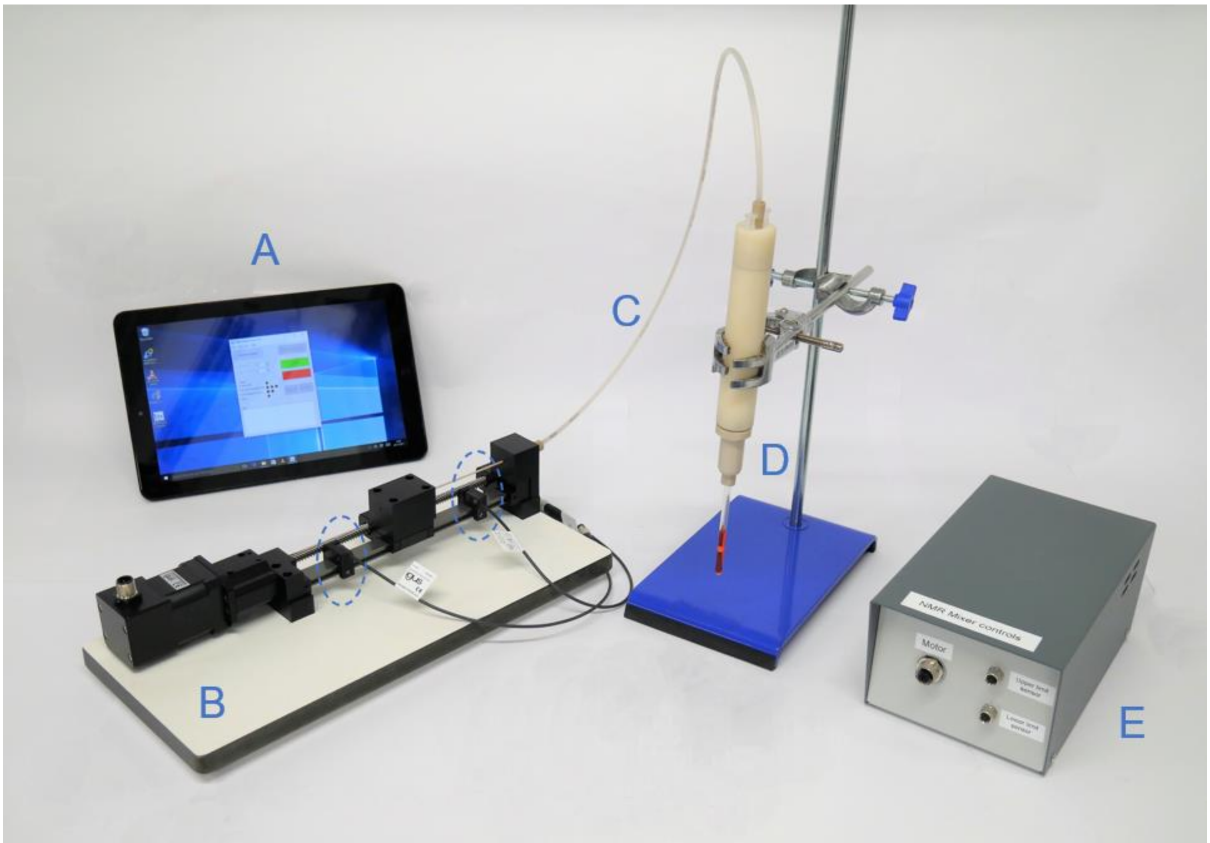

Figure 6.1. Photograph of the main parts of the NMR-based in-situ mixing device. A) Tablet computer for running the control software. B) Linear stepper motor with two limit sensors highlighted by dashed circle. C) Bowden cable. D) The insert section. E) A box containing all the control electronics, including linear motor driver, microcontroller, power supply, TTL inputs and outputs.

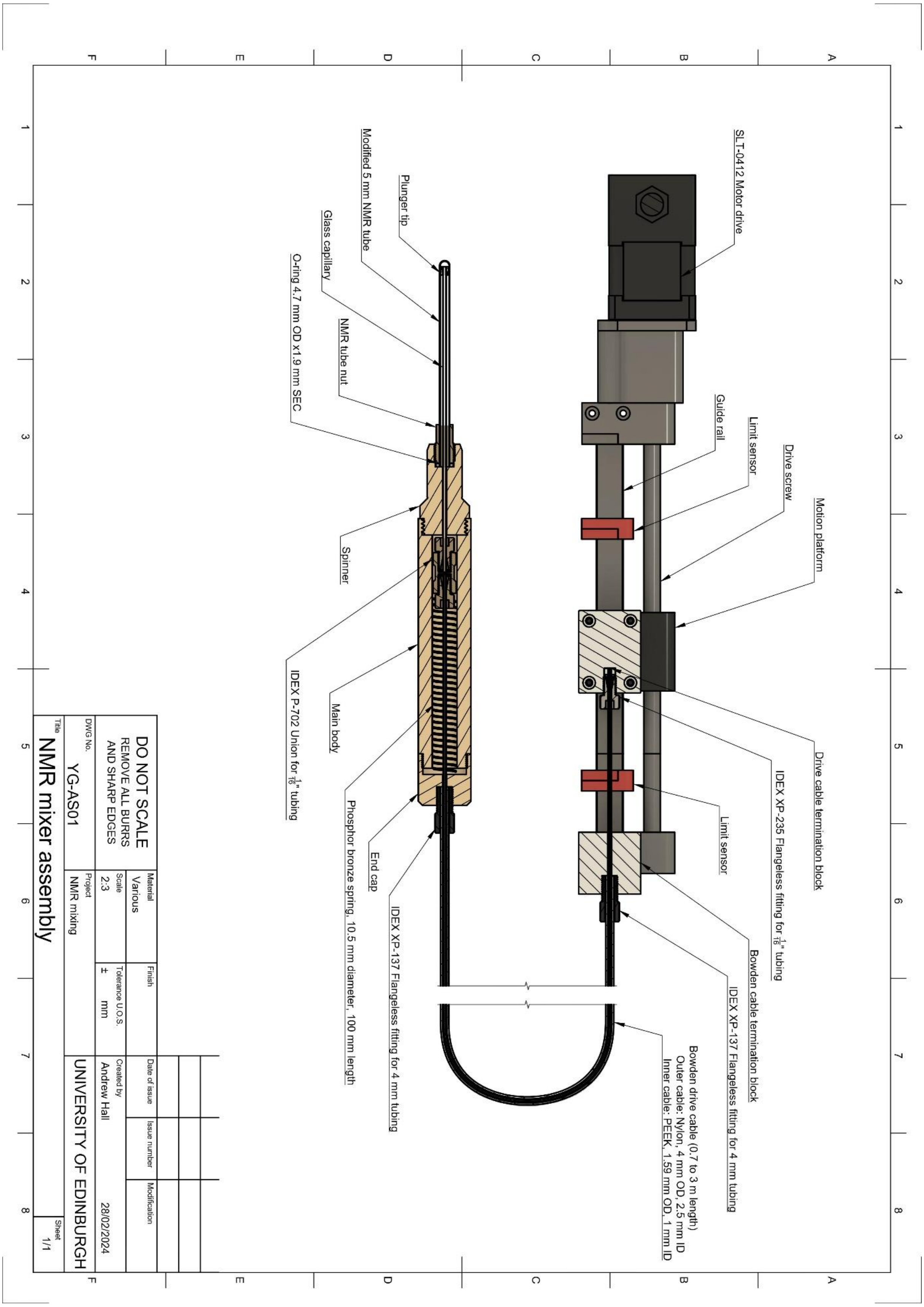

Figure 6.2. Drawing for the full assembly.

6.2 Pulse program for mixing device

The pulse sequences below are coded for Bruker TopSpin® 4.2.0. Data is acquired as pseudo-2D spectra with each row corresponding to a different reaction time point.

```
;zg2dmix
;DELTA to allow interscan delay
;d20 is the time between spectra (mixing + settling + acquisition)
;d2 is the settling time for solids to settle out of solution.
;TTL trigger for mixing device is connected to trigger output V5 or V6 on AQS T-controller:
; output V5 = setnmr4 ^ 13
; output V6 = setnmr4 ^ 14
;modified by Andrew Hall 06112023
;avance-version (12/01/11)
;pseudo 2D sequence
;
;$CLASS=HighRes
;$DIM=2D
;$TYPE=
;$SUBTYPE=
;$COMMENT=

#include <Avance.incl>
#include <Delay.incl>

"DELTA=d20-d2-((d1+aq)*(ns+ds))-30m"
"d11 = 30m"

"acqt0=-p1*2/3.1416"

1 ze
  30m
2 1u setnmr4 ^ 13 ; Set trigger output HIGH (mixing device on)
  DELTA ; Mix the sample
```

```
3 1u setnmr4 | 13 ; Set trigger output LOW (mixing device off)
  d2 ; Wait for solids to settle
4 d1 ; Acquire spectrum
  p1 ph1
  go=4 ph31
  d11 wr #0 if #0 ze
  lo to 2 times td1
exit
ph1=0 2 2 0 1 3 3 1
ph31=0 2 2 0 1 3 3 1

;pl1 : f1 channel - power level for pulse (default)
;p1 : f1 channel - 90 degree high power pulse
;d1 : relaxation delay; 1-5 * T1
;d2 : settling time [typ. 2 - 30 sec]
;d11: delay for disk I/O [30 msec]
;d20: delay between start of different 1D spectra
;ns: 1 * n
;td1: number of spectra to acquire
```

6.3 Full dataset for magnetisation transfer experiments

1.

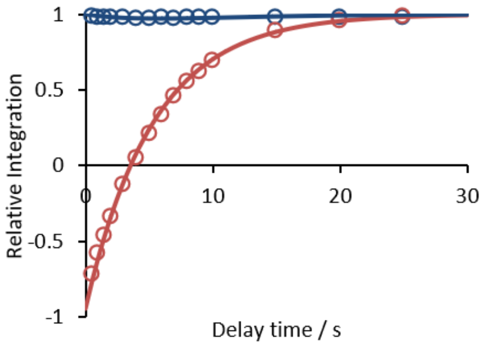

2.

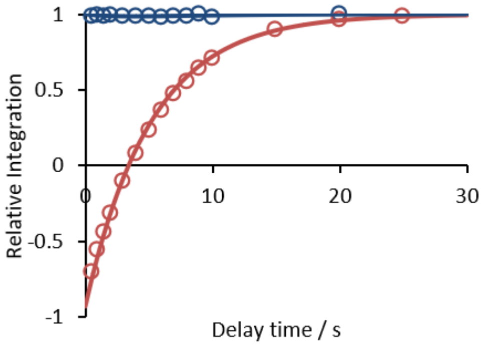

3.

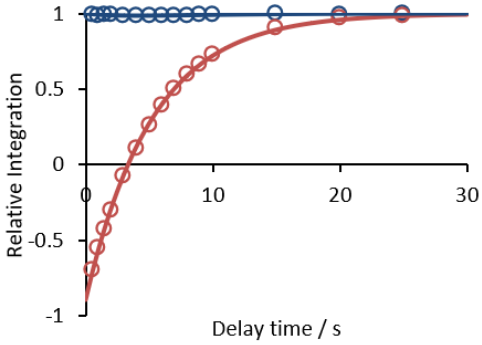

4.

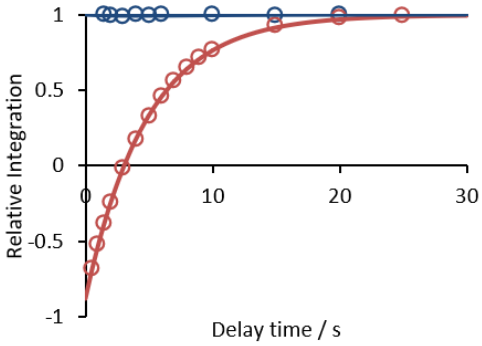

5.

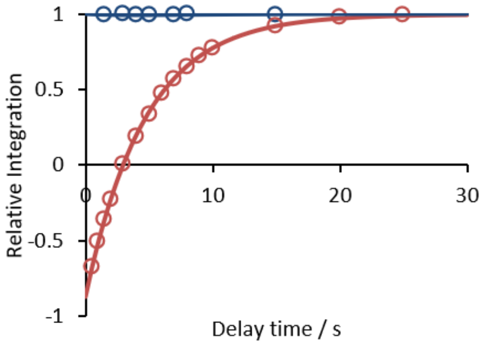

6.

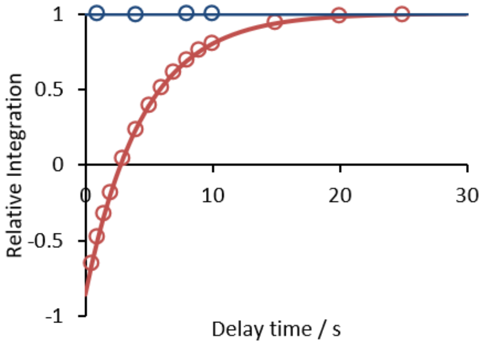

7.

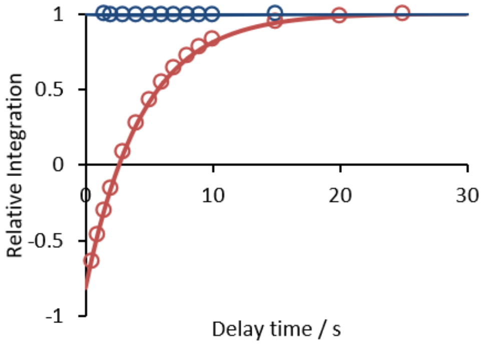

8.

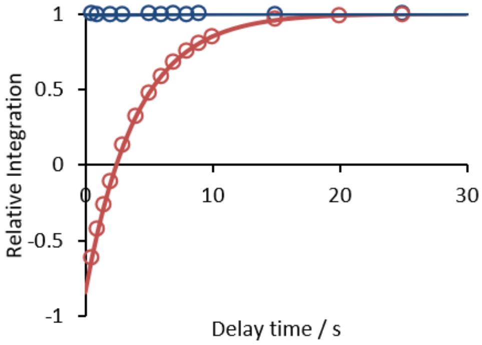

9.

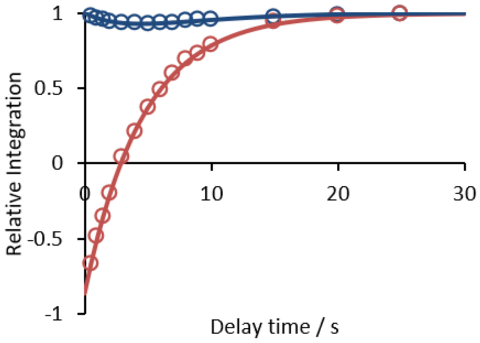

10.

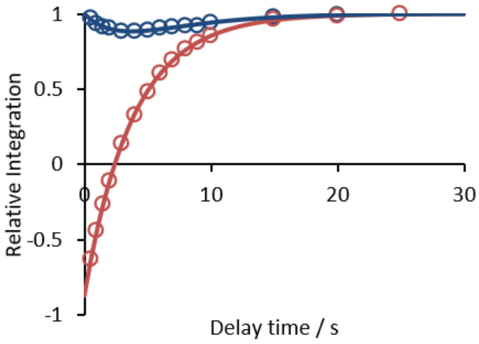

11.

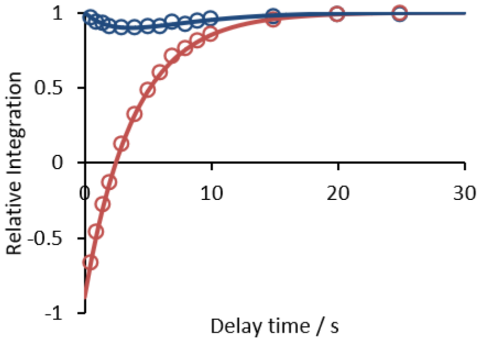

12.

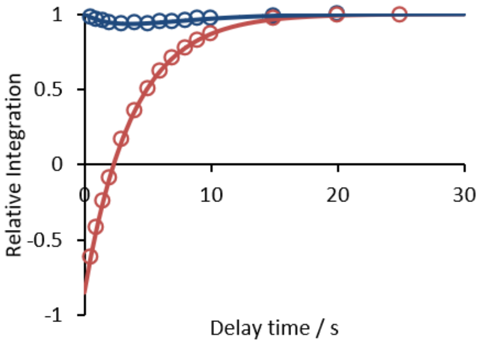

13.

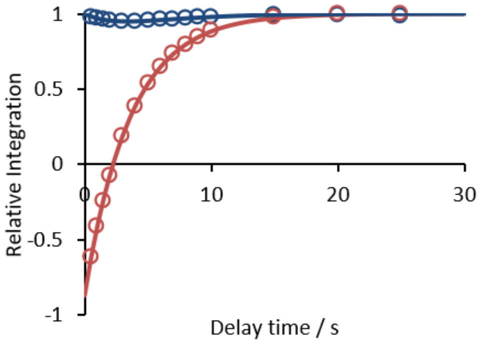

14.

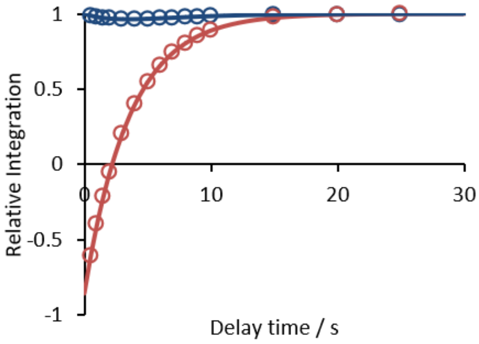

15.

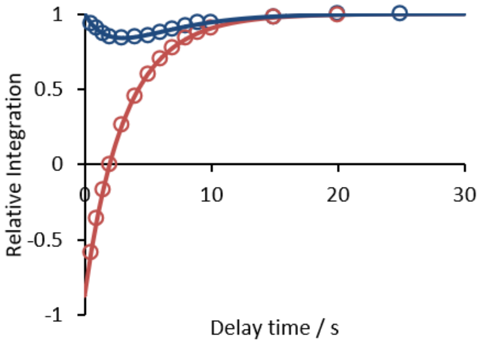

16.

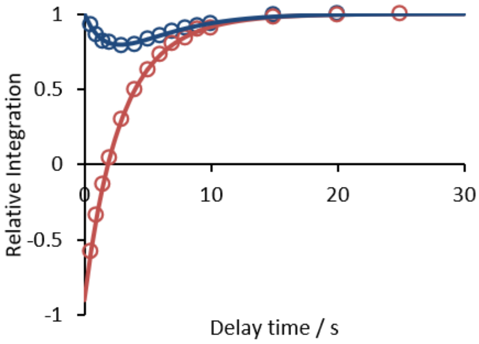

17.

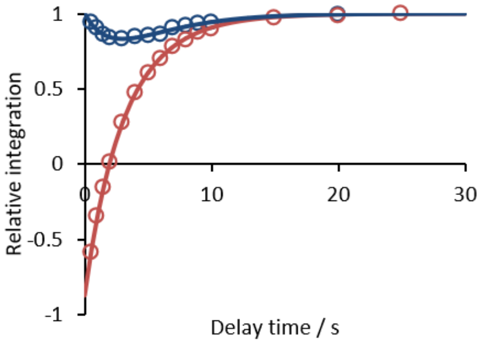

18.

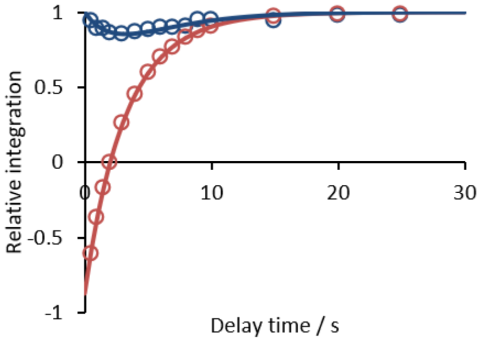

19.

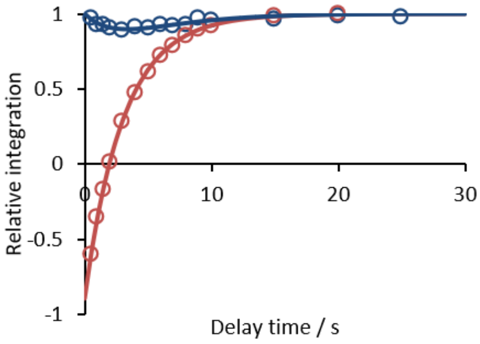

20.

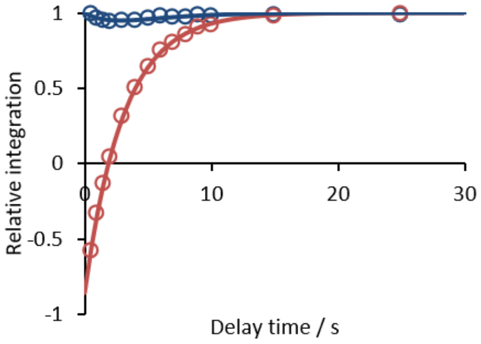

21.

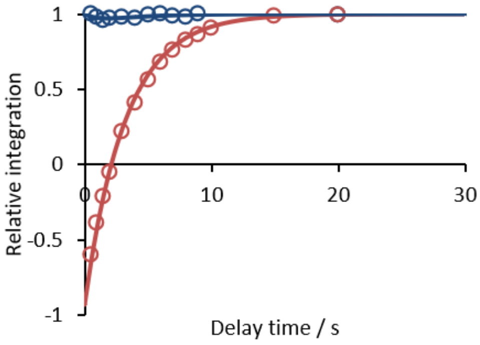

22.

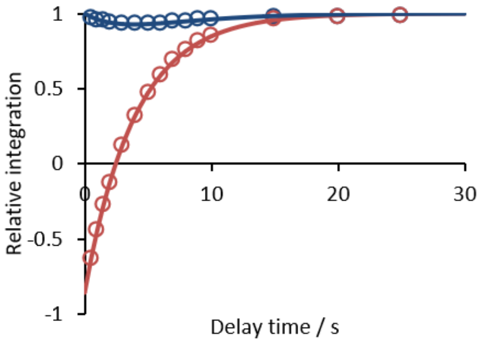

23.

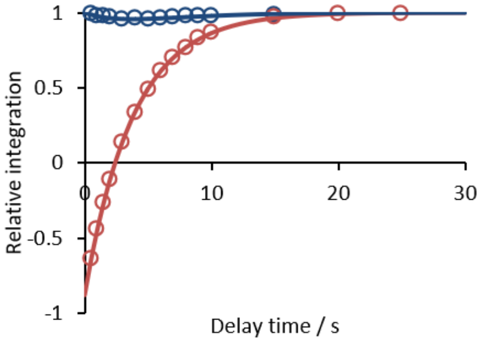

24.

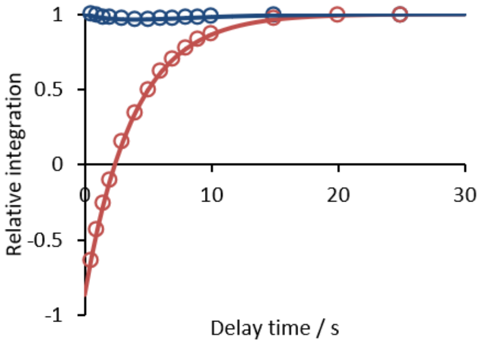

25.

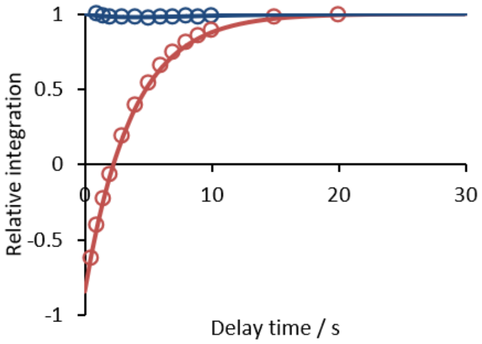

26.

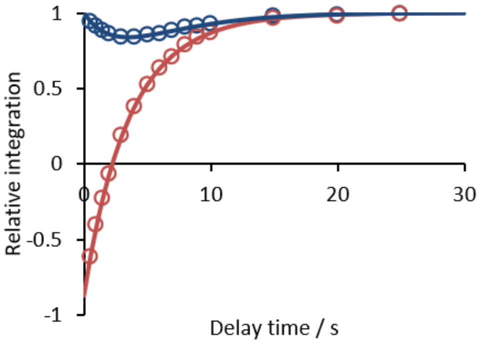

27.

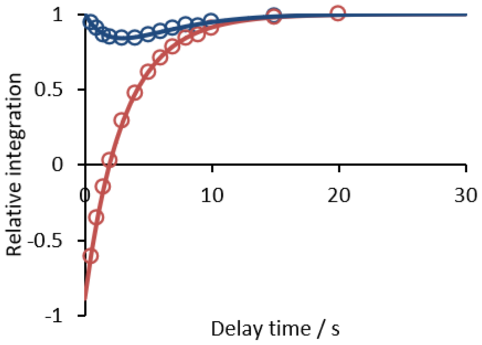

28.

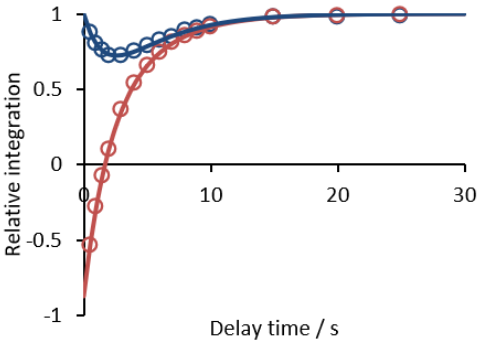

29.

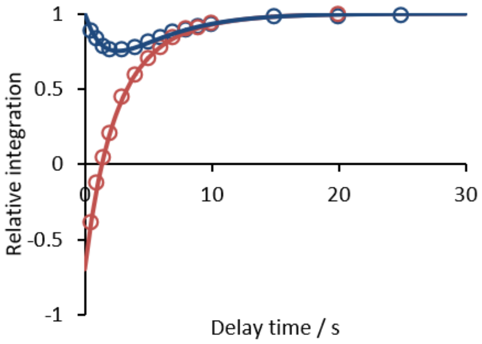

30.

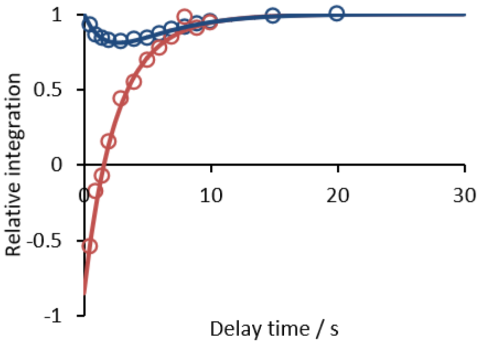

31.

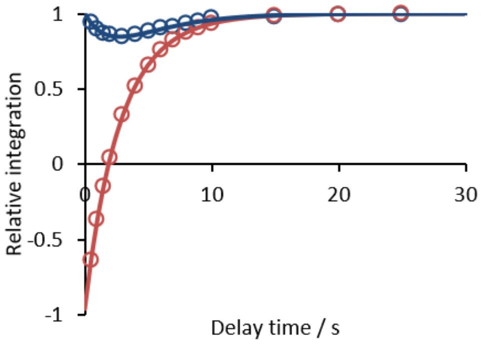

32.

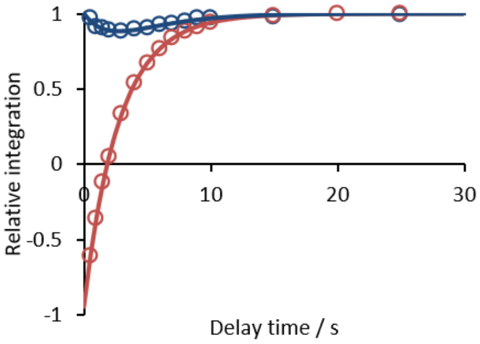

33.

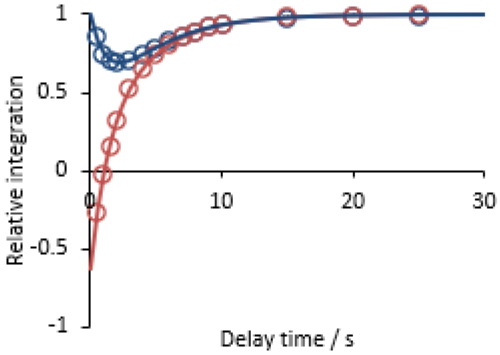

34.

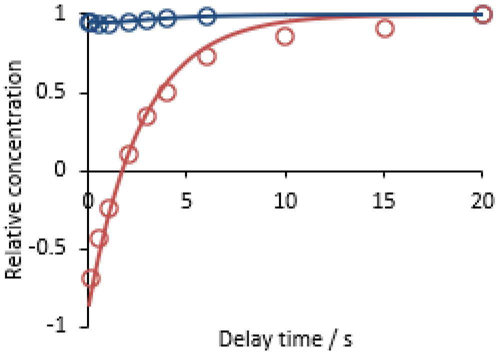

35.

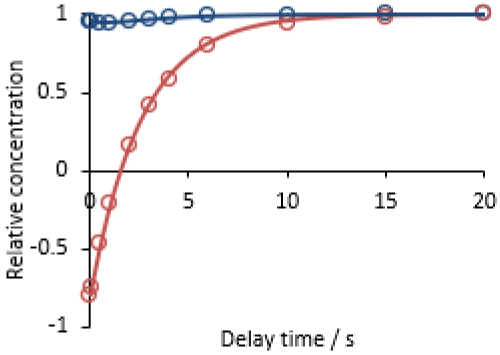

36.

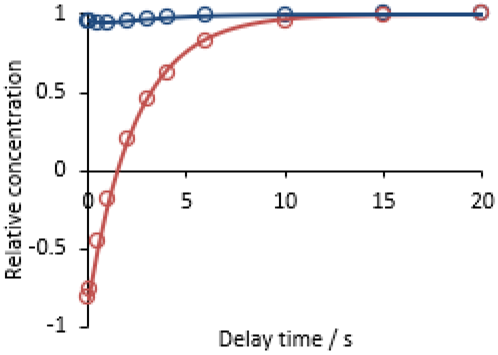

37.

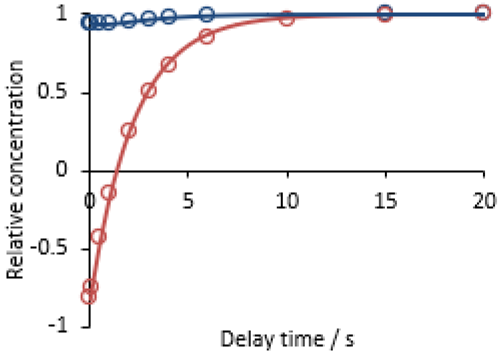

38.

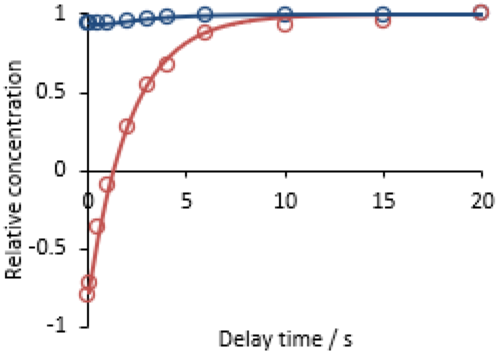

39.

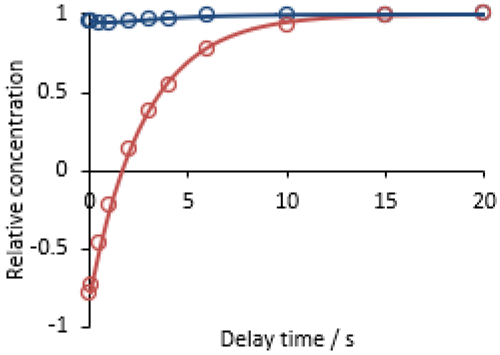

40.

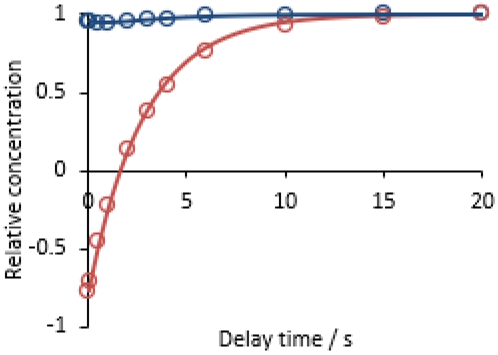

41.

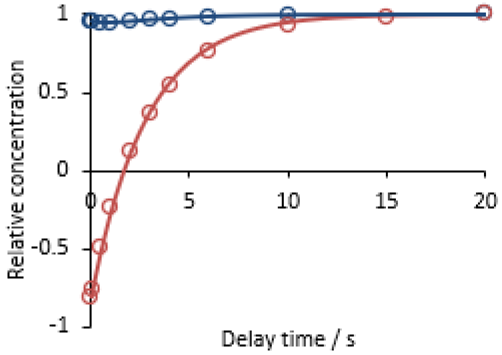

42.

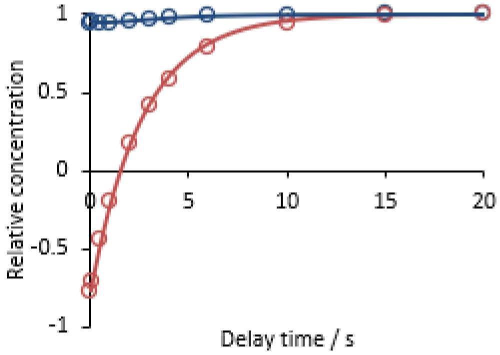

43.

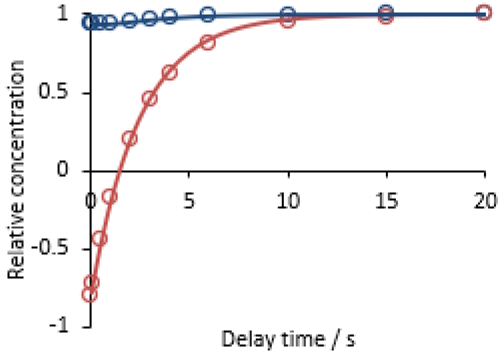

44.

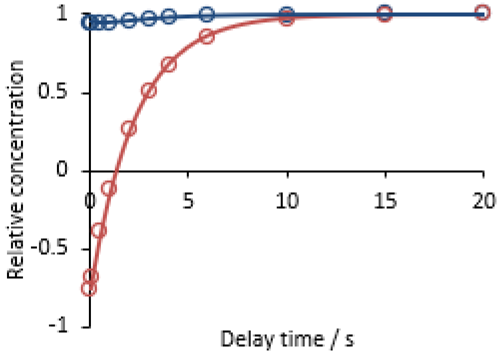

45.

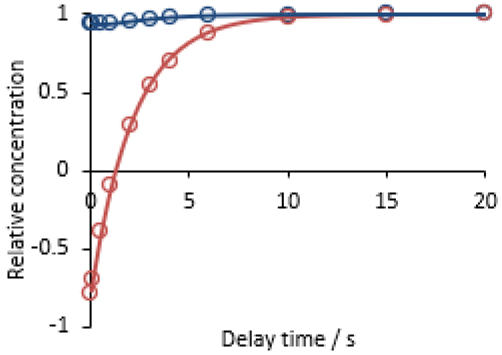

46.

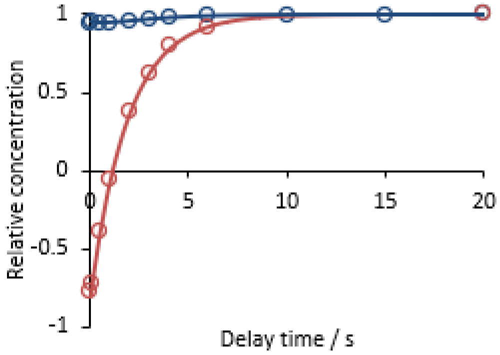

47.

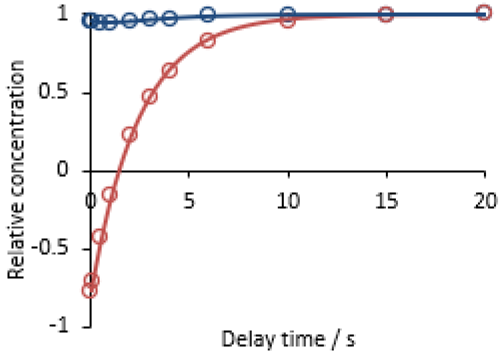

48.

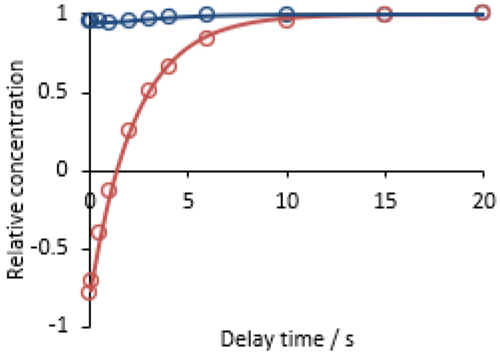

49.

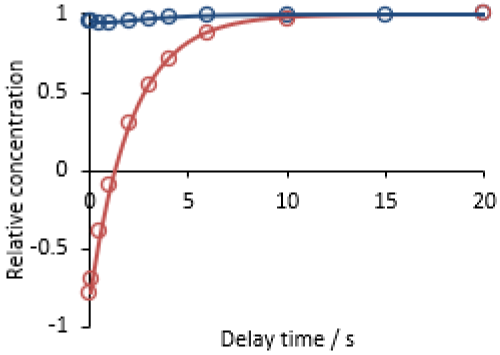

50.

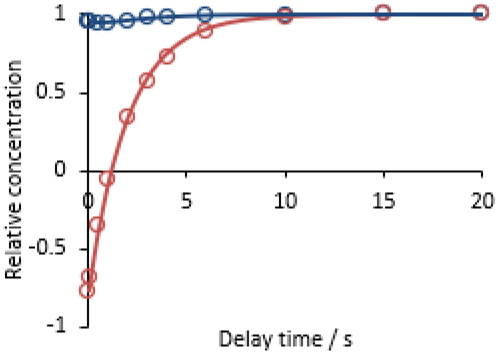

51.

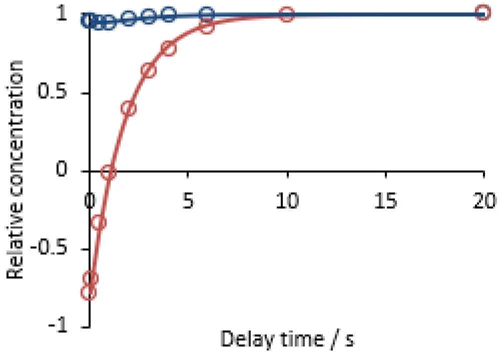

52.

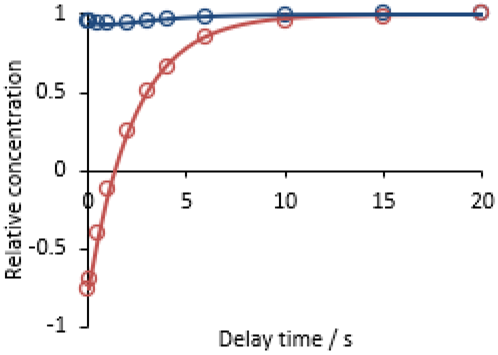

53.

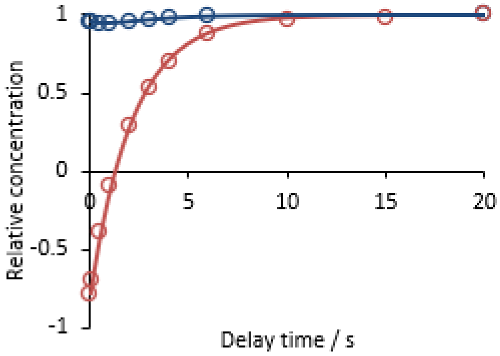

54.

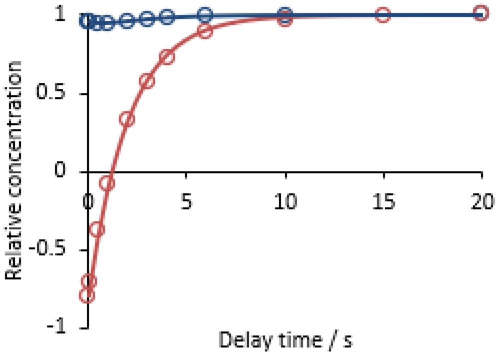

55.

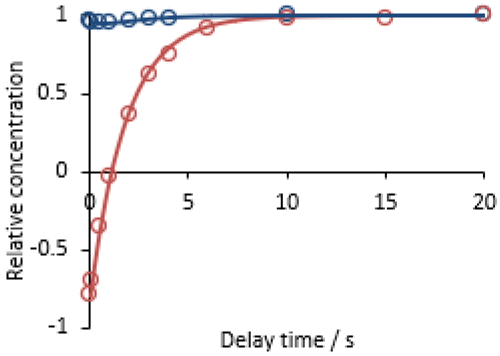

56.

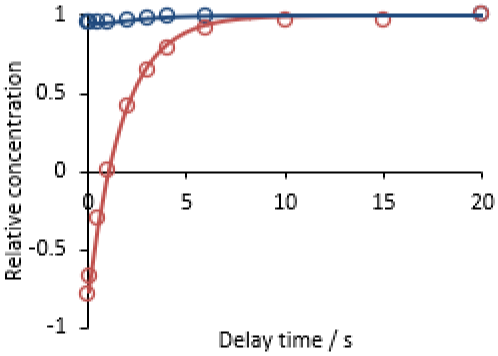

57.

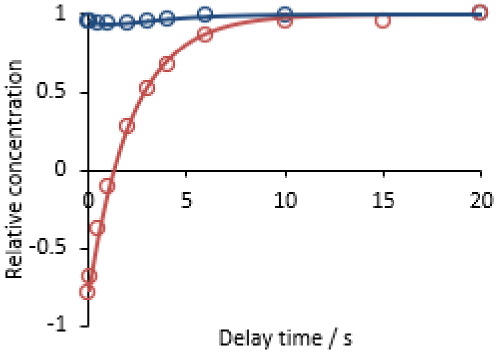

58.

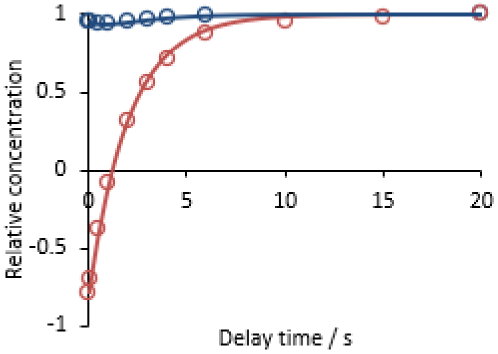

59.

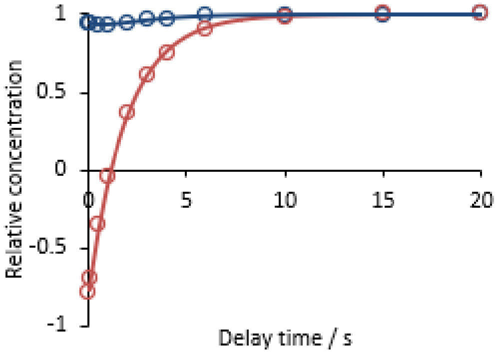

60.

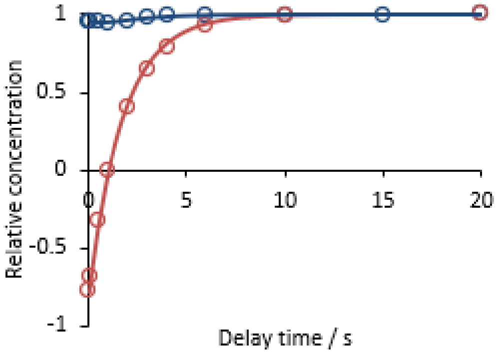

61.

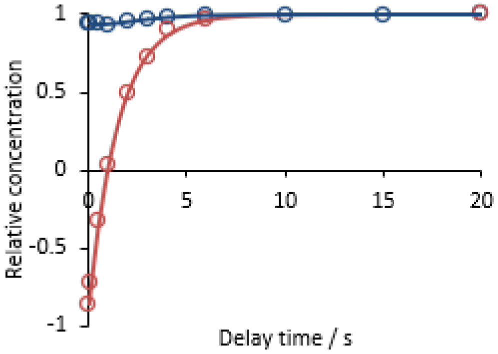

62.

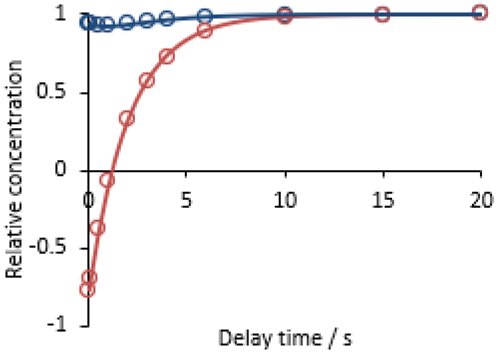

63.

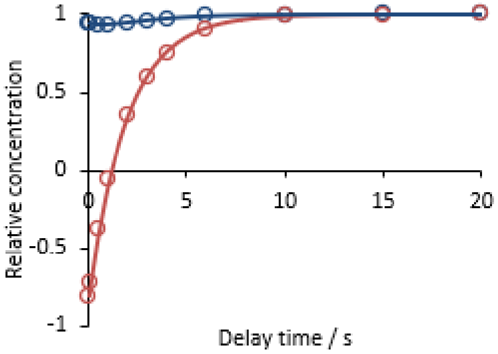

64.

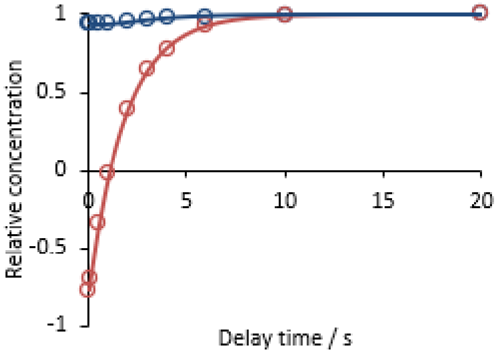

65.

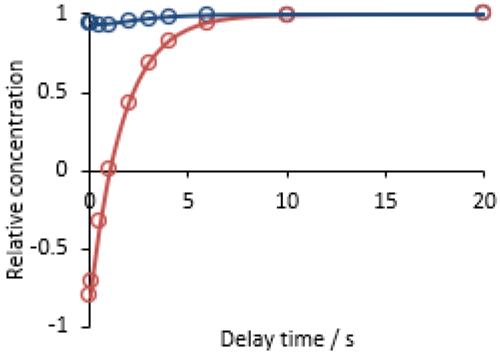

66.

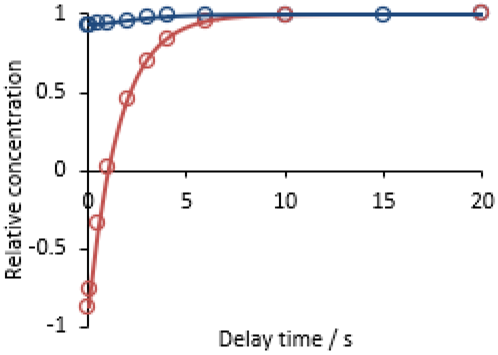

67.

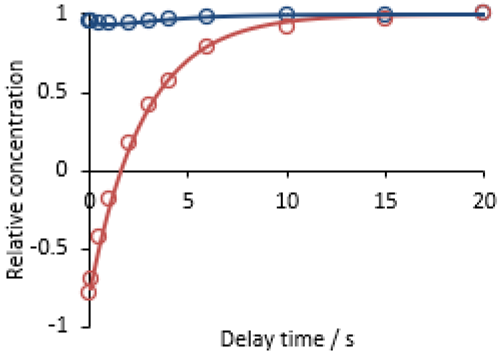

68.

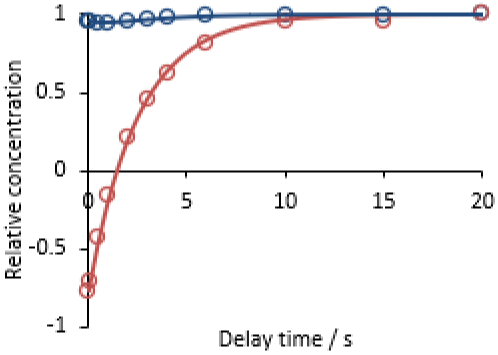

69.

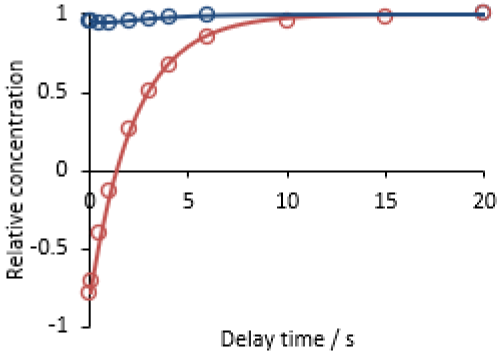

70.

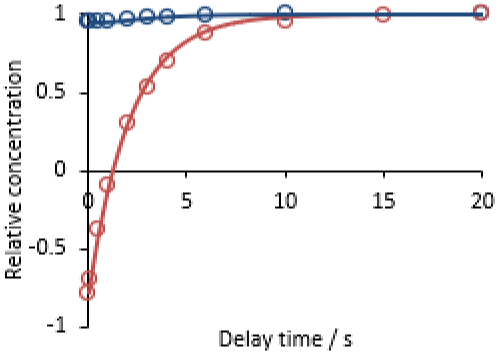

71.

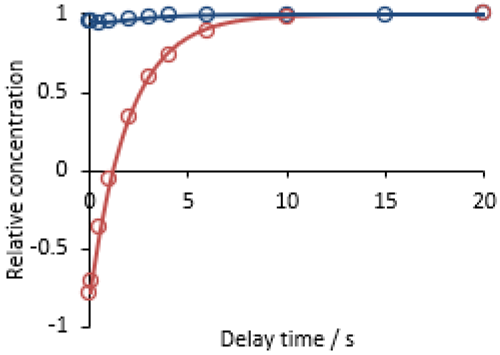

72.

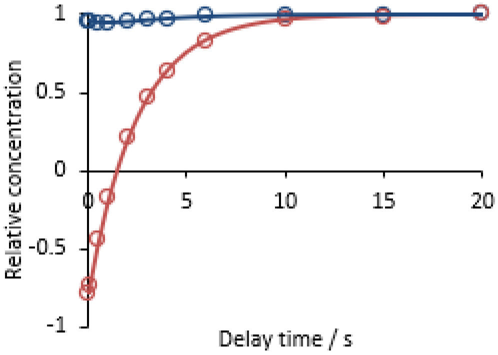

73.

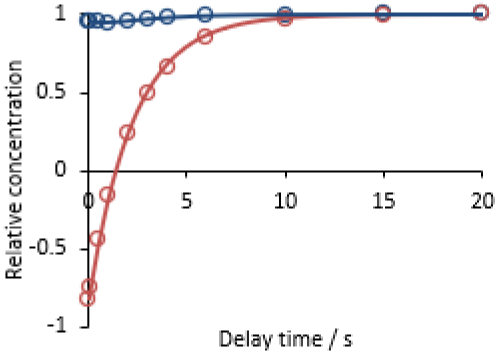

74.

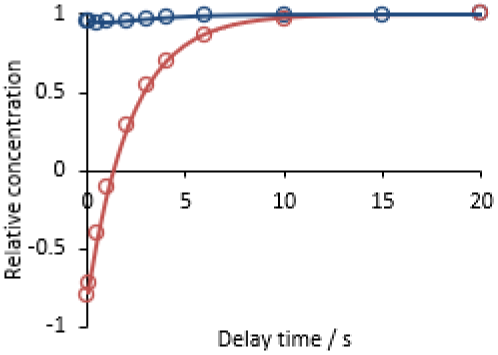

75.

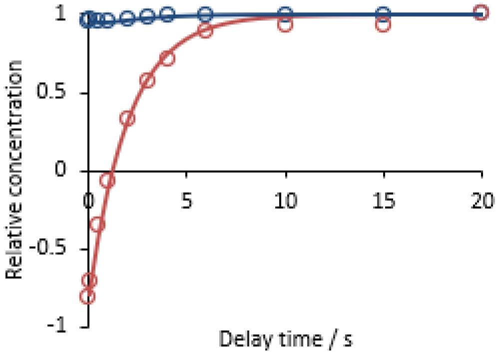

76.

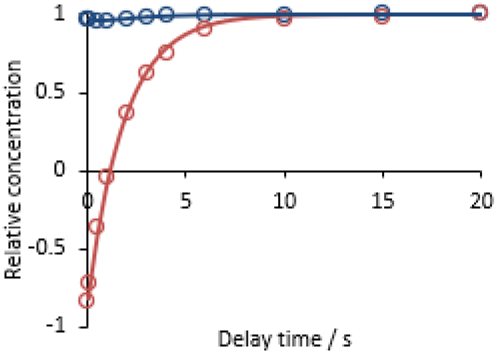

77.

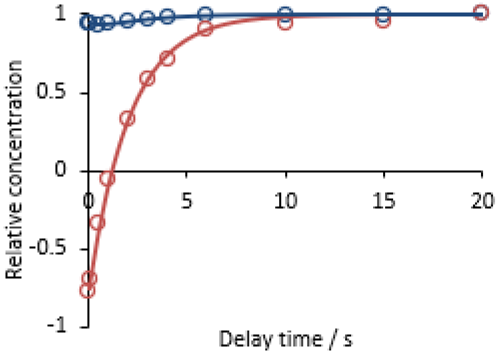

78.

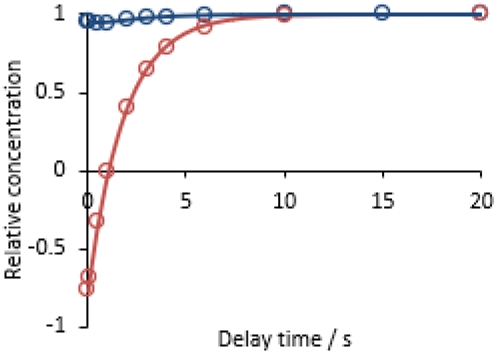

79.

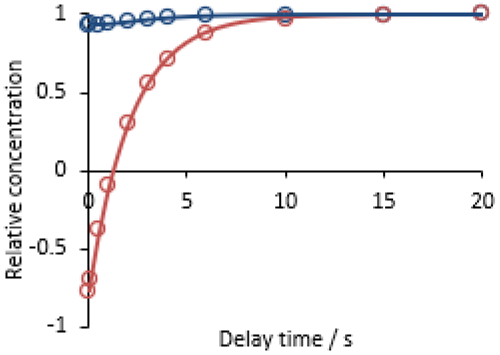

80.

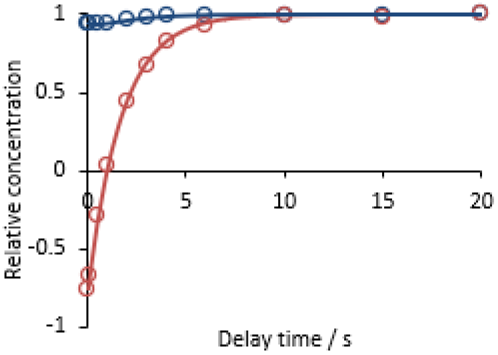

81.

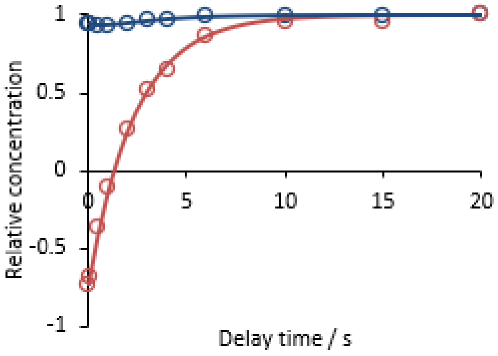

82.

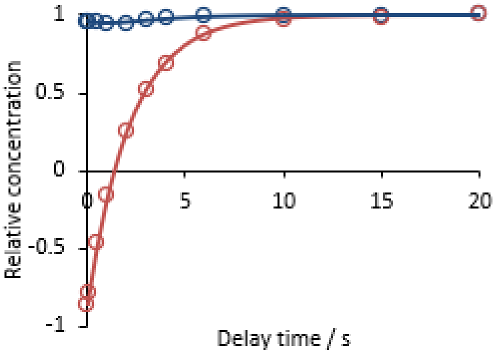

83.

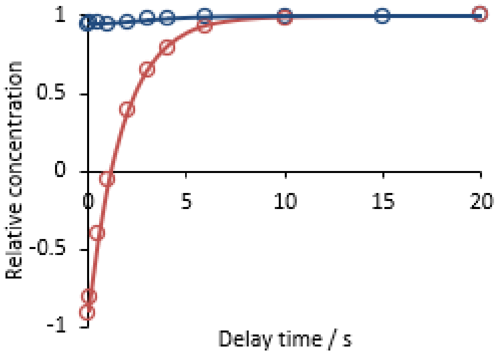

84.

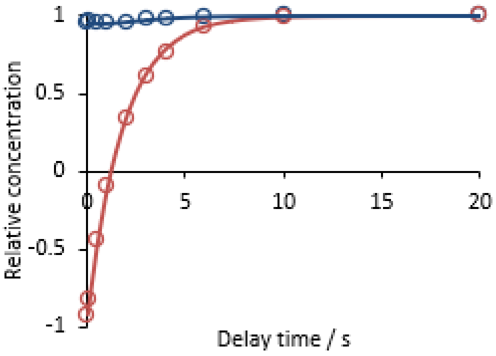

85.

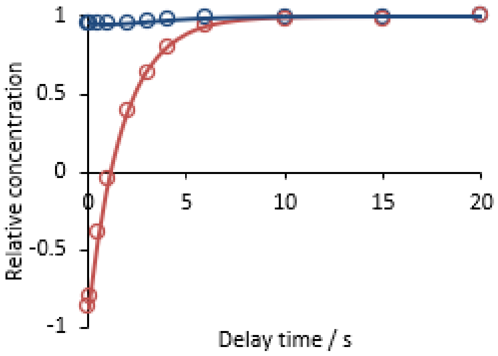

86.

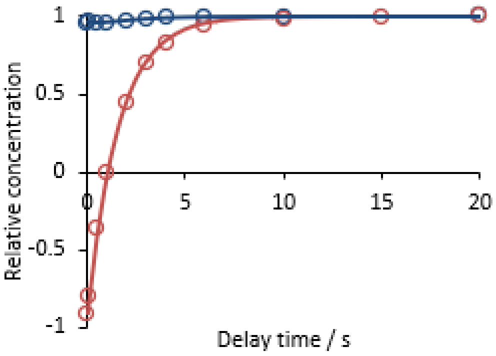

For clarity, below are zoomed in version of the same plots:

1.

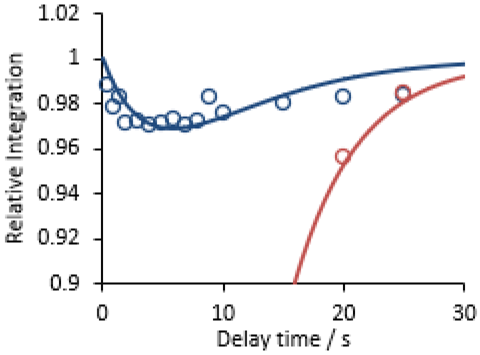
Relative Integration
1.02
1
0.98
0.96
0.94
0.92
0.9
0
10
20
30
Delay time / s

2.

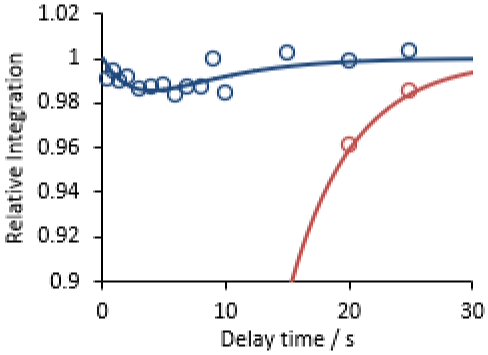
Relative Integration
1.02
1
0.98
0.96
0.94
0.92
0.9
0
10
20
30
Delay time / s

3.

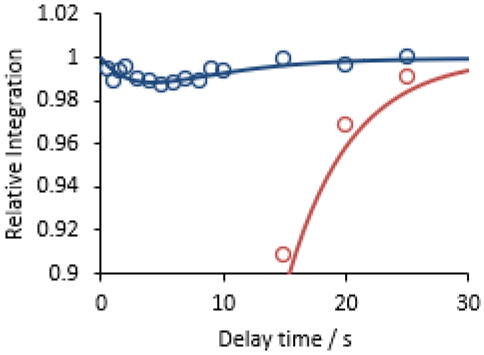
Relative Integration
1.02
1
0.98
0.96
0.94
0.92
0.9
0
10
20
30
Delay time / s

4.

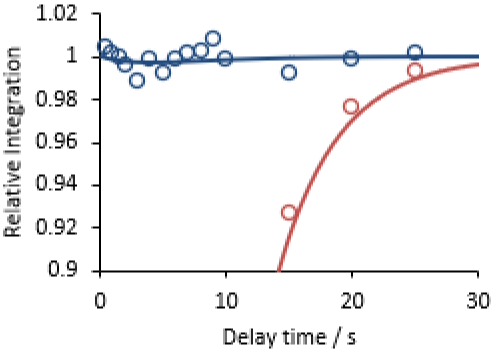
Relative Integration
1.02
1
0.98
0.96
0.94
0.92
0.9
0
10
20
30
Delay time / s

5.

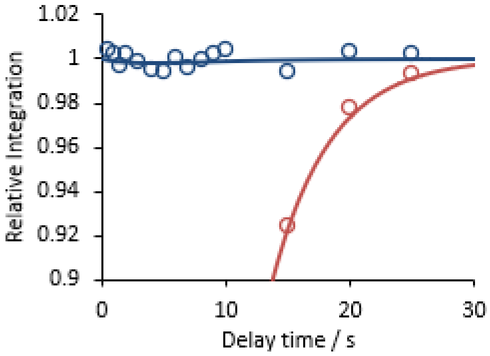
Relative Integration
1.02
1
0.98
0.96
0.94
0.92
0.9
0
10
20
30
Delay time / s

6.

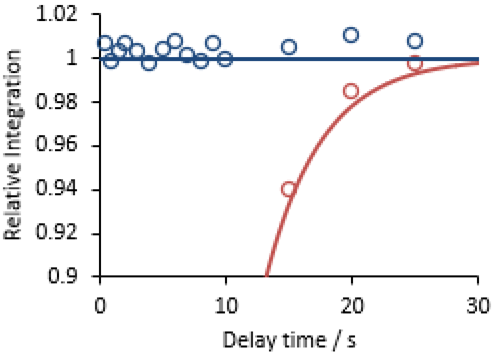
Relative Integration
1.02
1
0.98
0.96
0.94
0.92
0.9
0
10
20
30
Delay time / s

7.

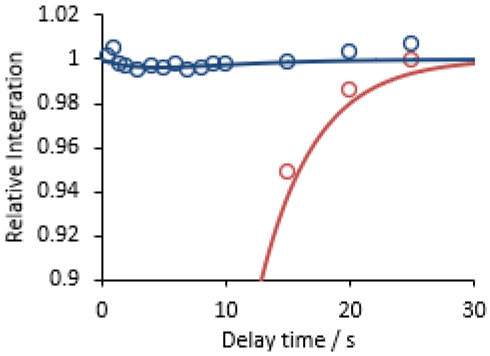
Relative Integration
1.02
1
0.98
0.96
0.94
0.92
0.9
0
10
20
30
Delay time / s

8.

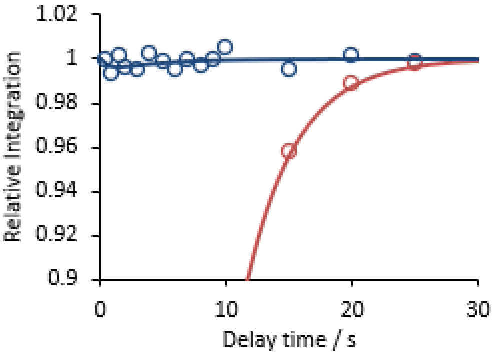
Relative Integration
1.02
1
0.98
0.96
0.94
0.92
0.9
0
10
20
30
Delay time / s

9.

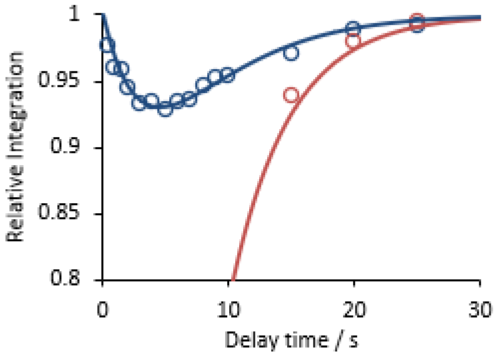

10.

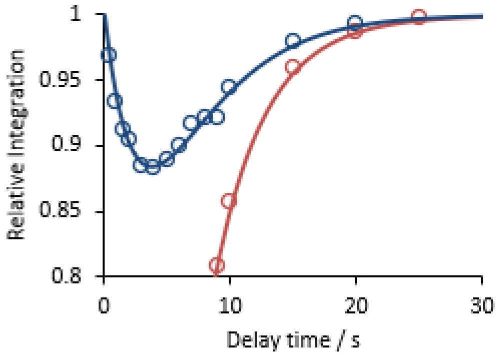

11.

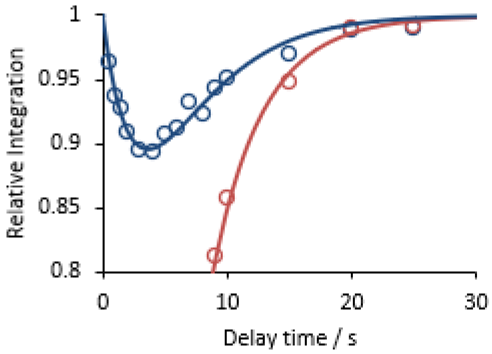

12.

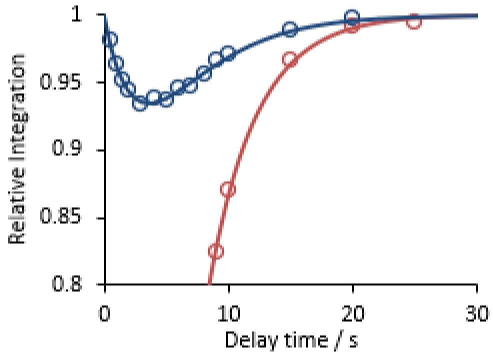

13.

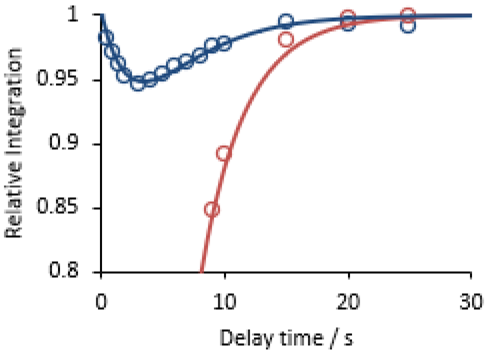

14.

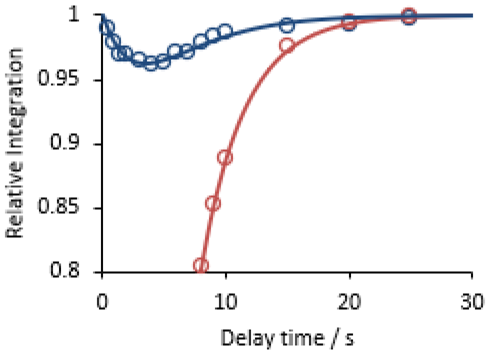

15.

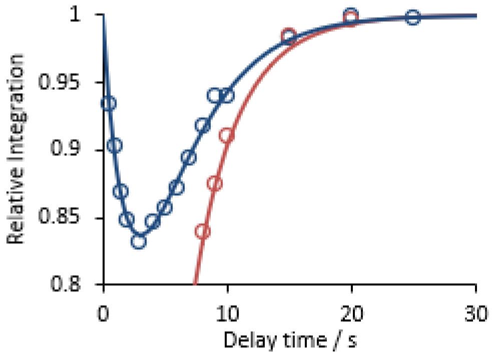

16.

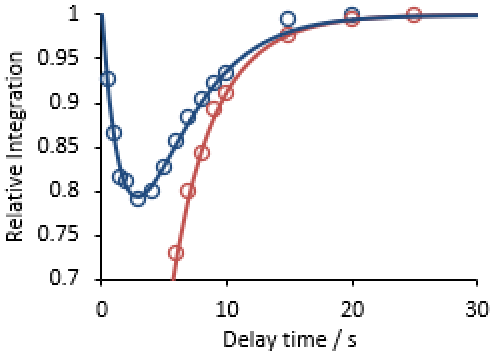

17.

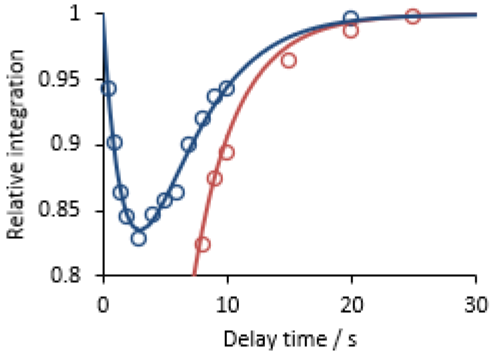

18.

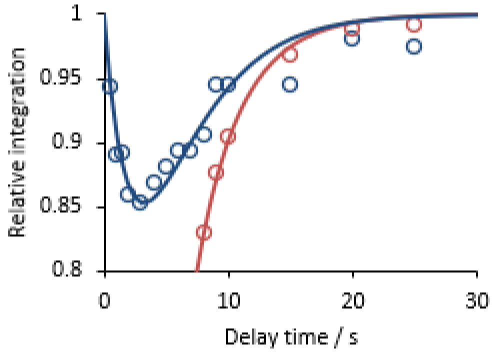

19.

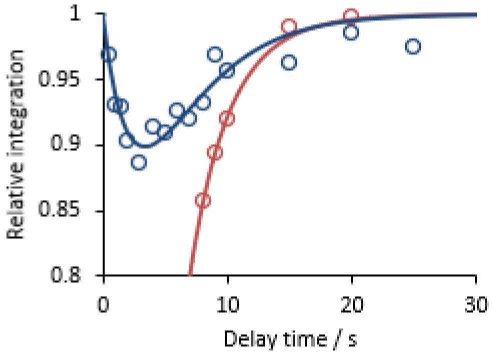

20.

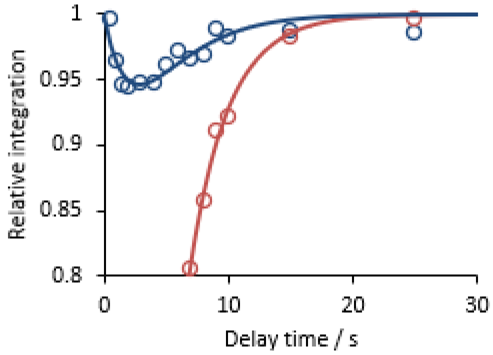

21.

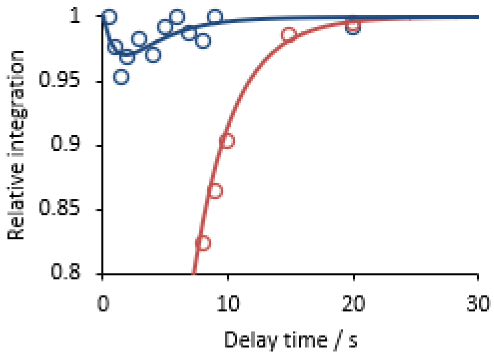

22.

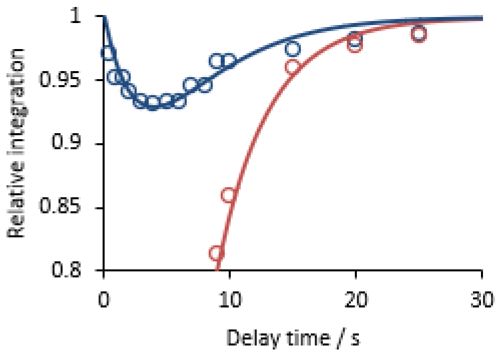

23.

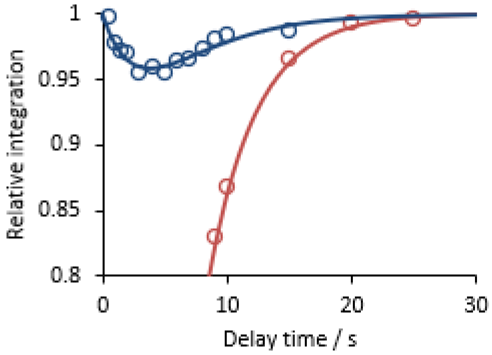

24.

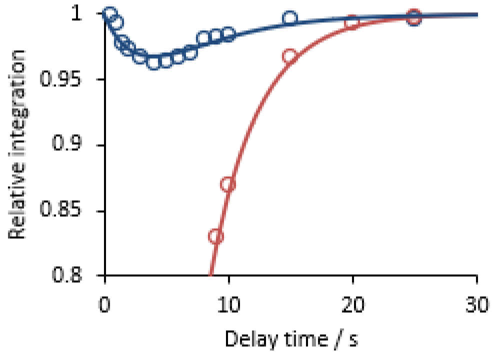

25.

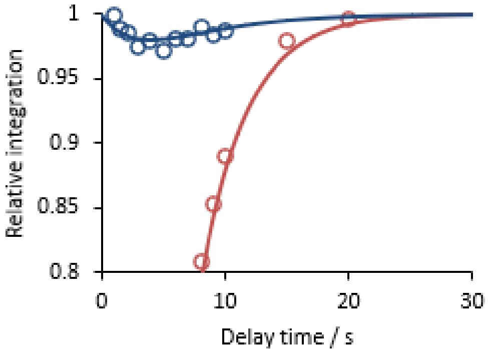

26.

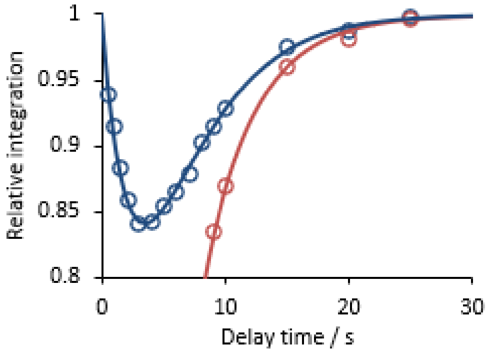

27.

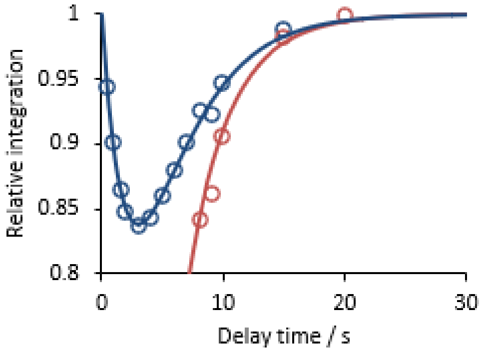

28.

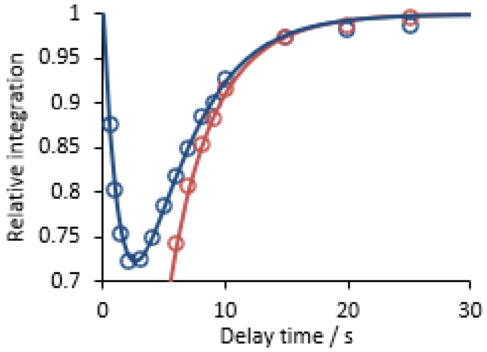

29.

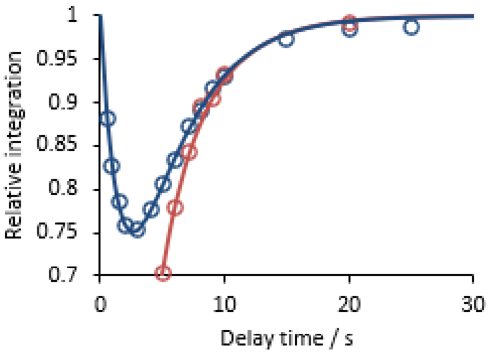

30.

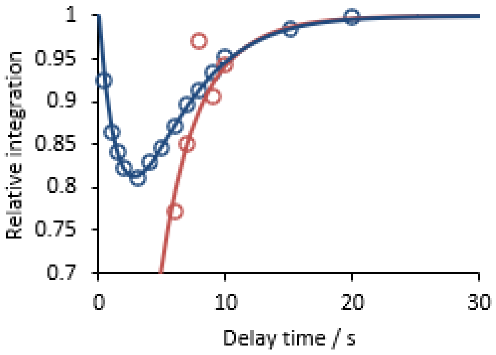

31.

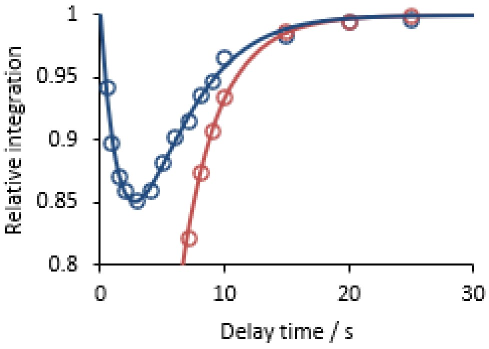

32.

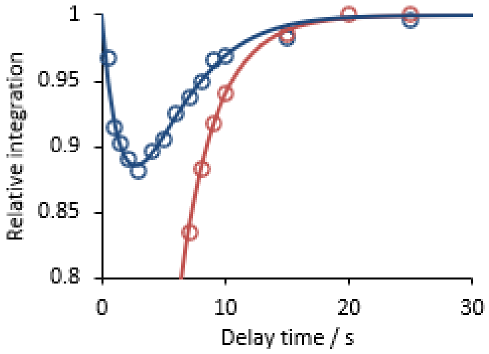

33.

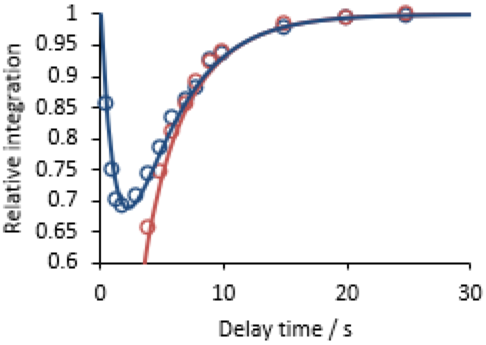

34.

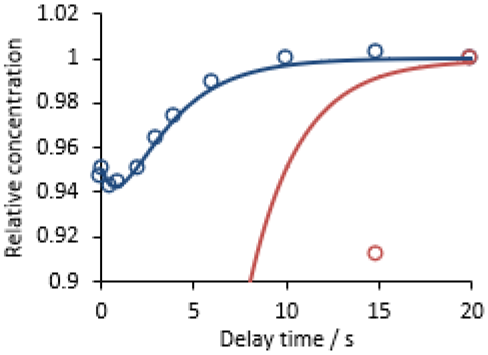

35.

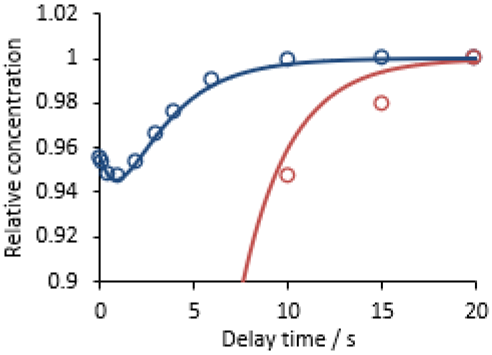

36.

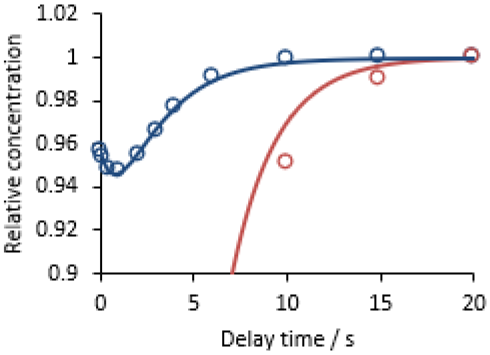

37.

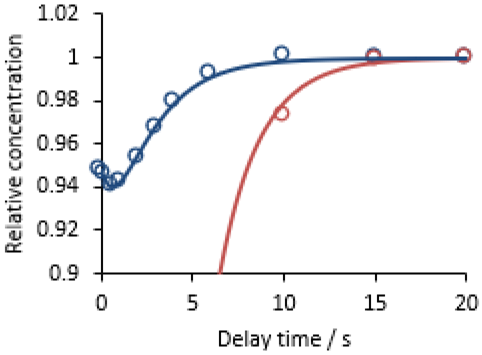

38.

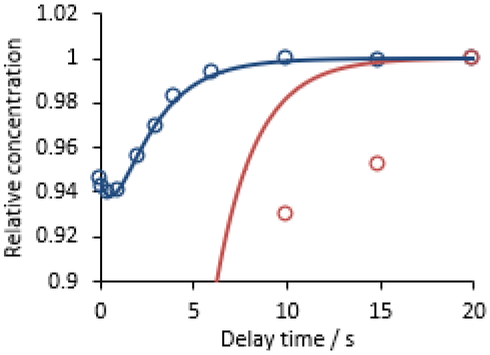

39.

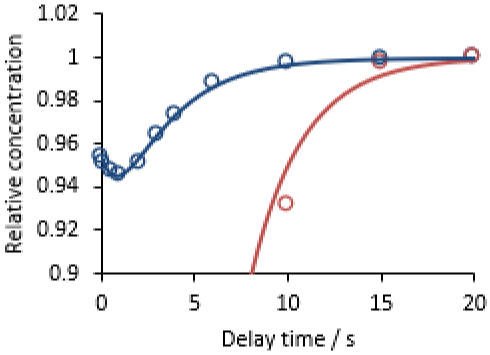

40.

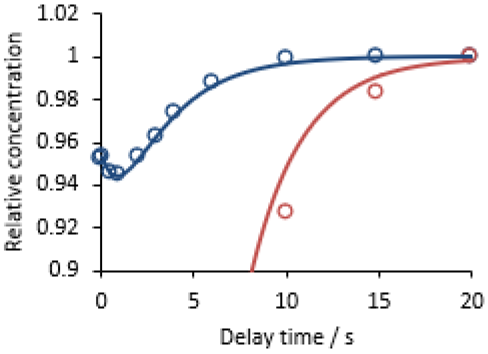

41.

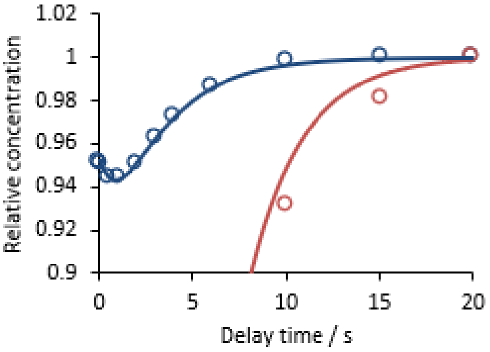

42.

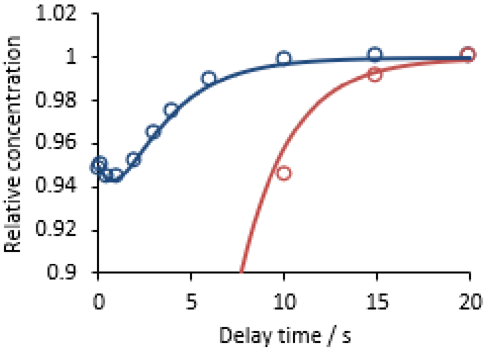

43.

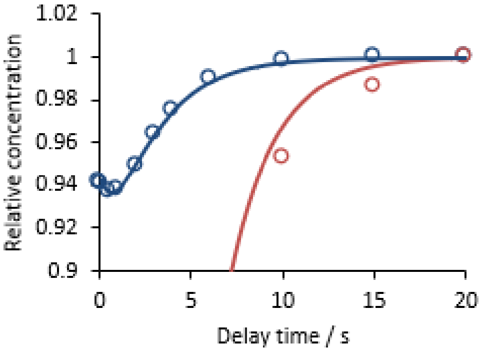

44.

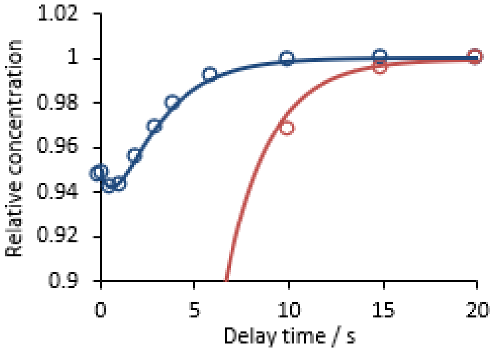

45.

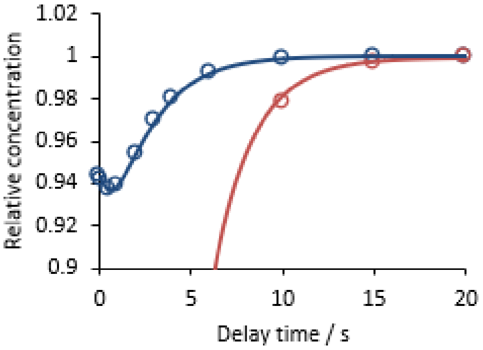

46.

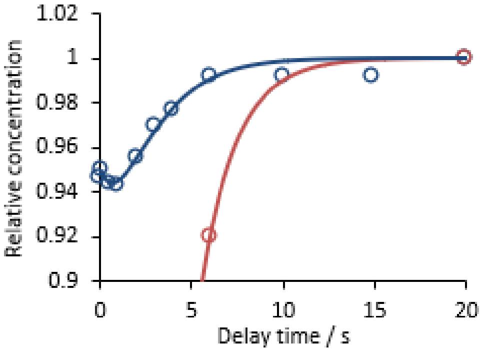

47.

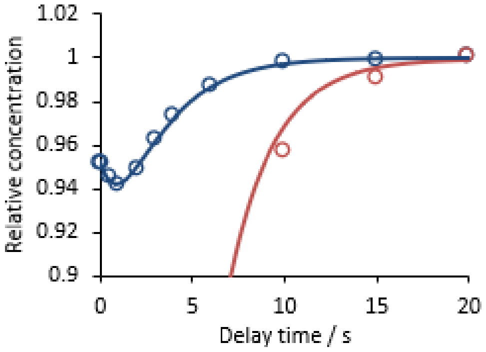

48.

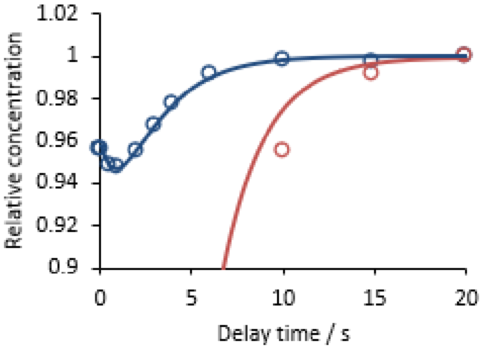

49.

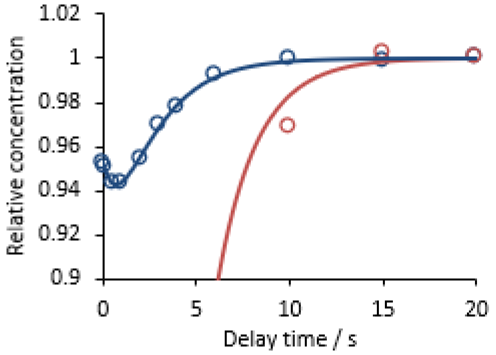

50.

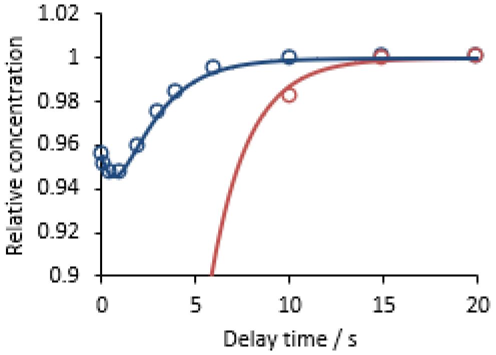

51.

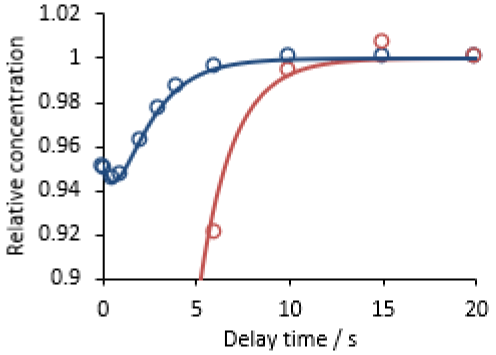

52.

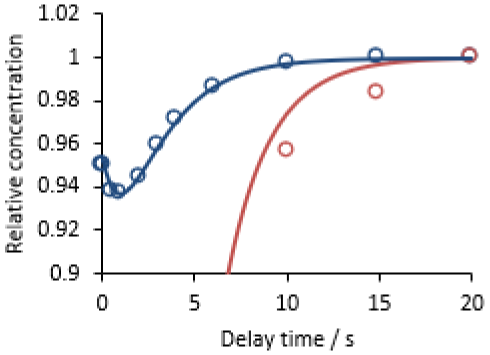

53.

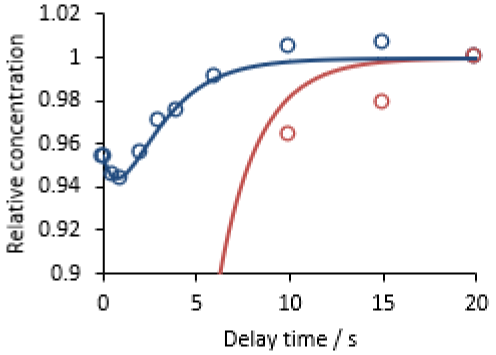

54.

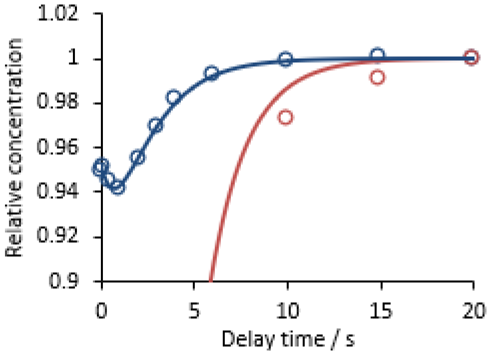

55.

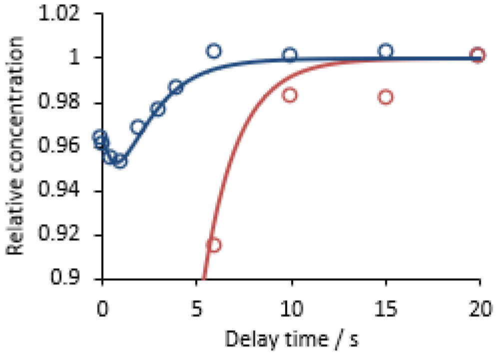

56.

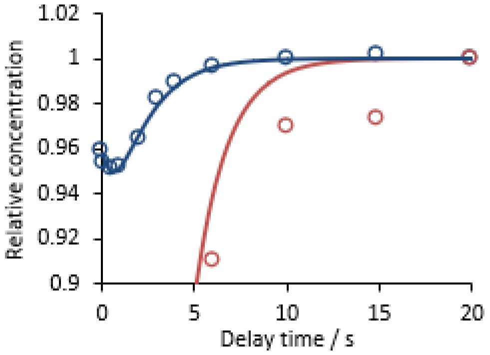

57.

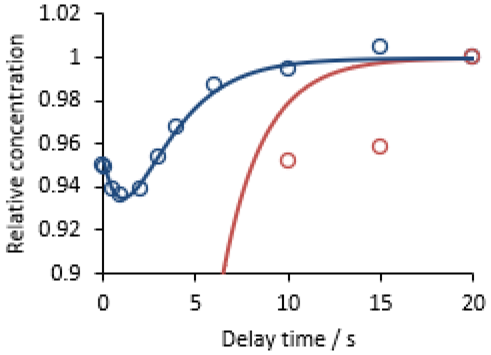

58.

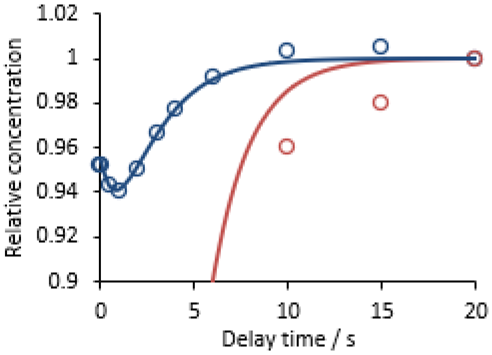

59.

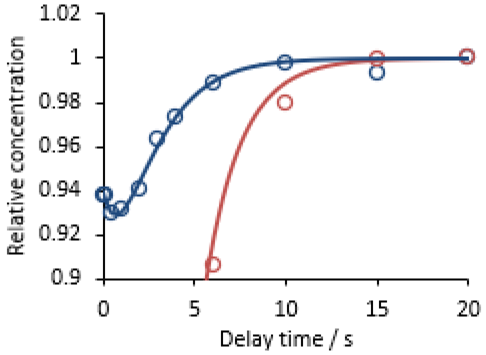

60.

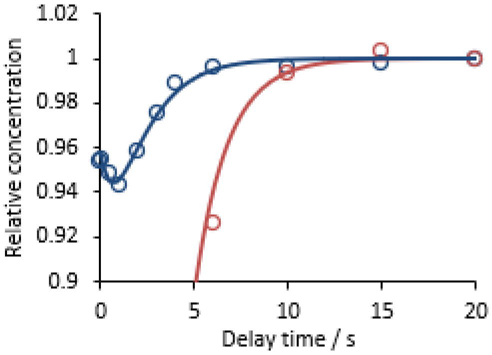

61.

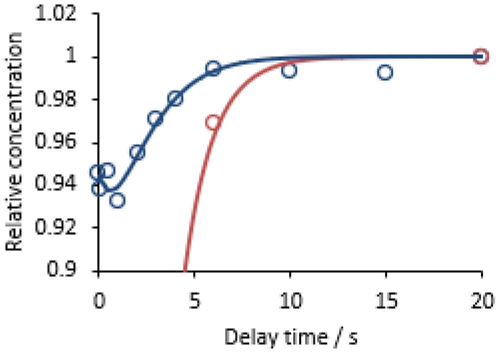

62.

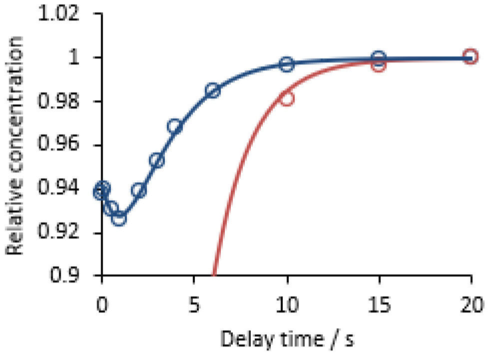

63.

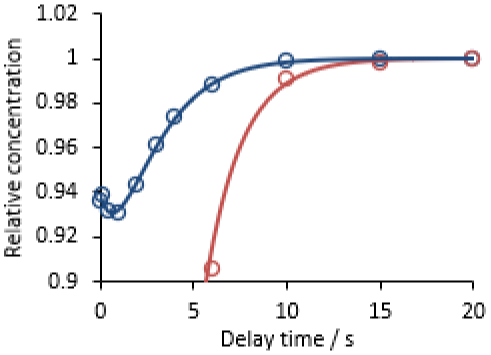

64.

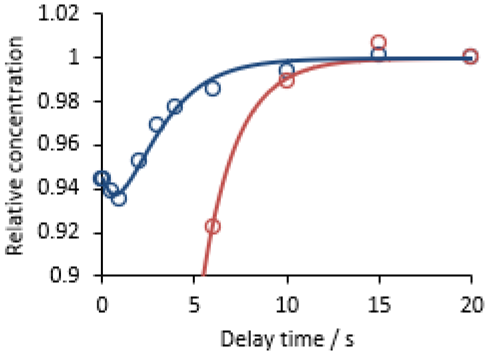

65.

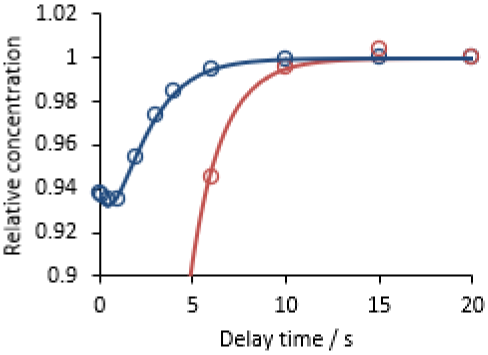

66.

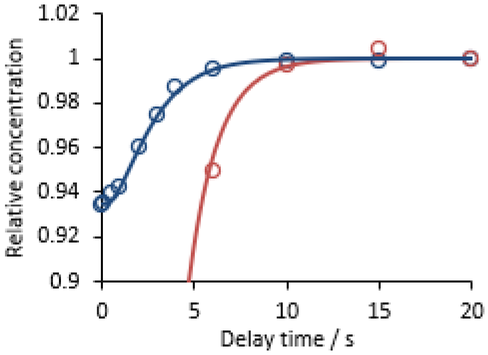

67.

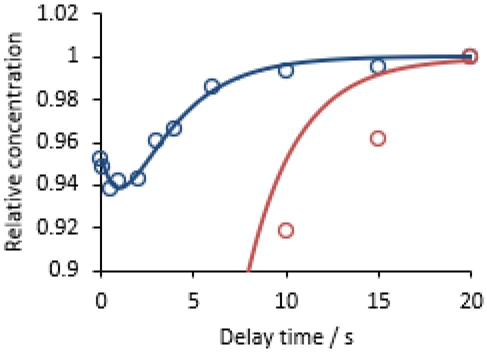

68.

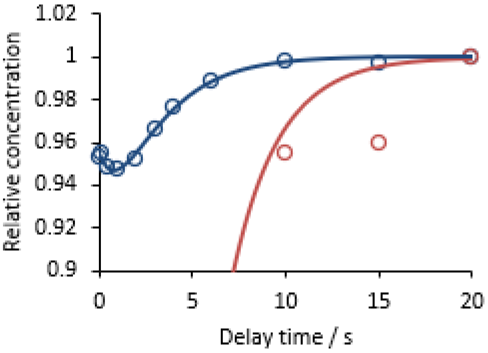

69.

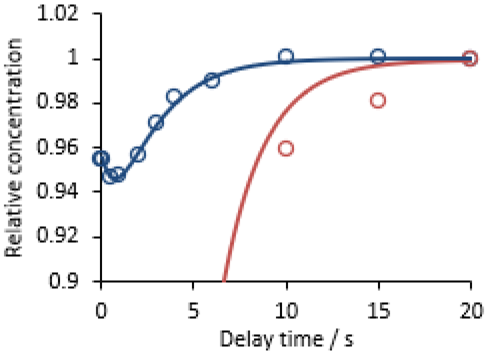

70.

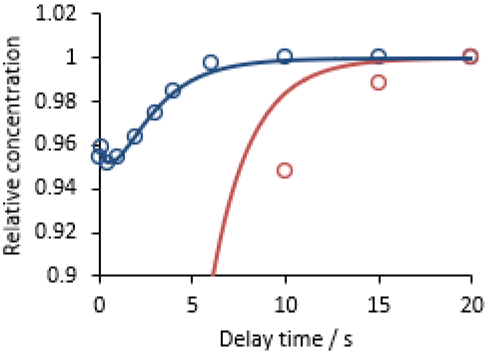

71.

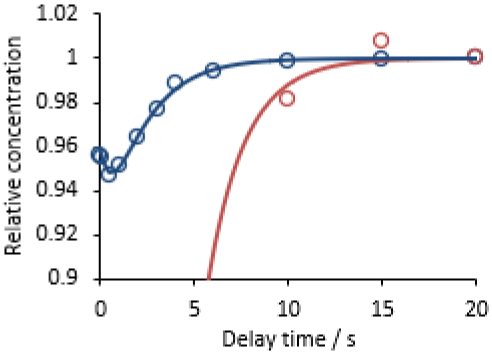

72.

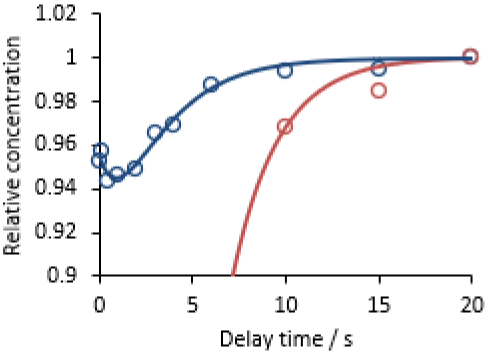

73.

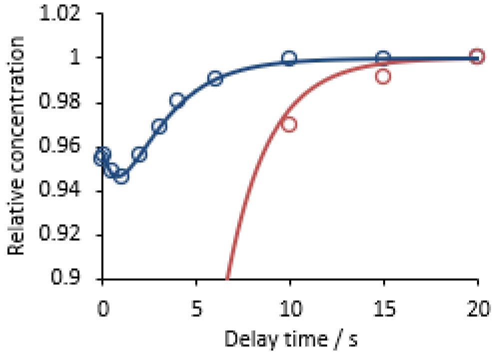

74.

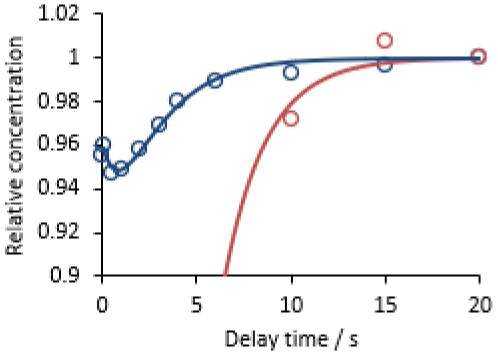

75.

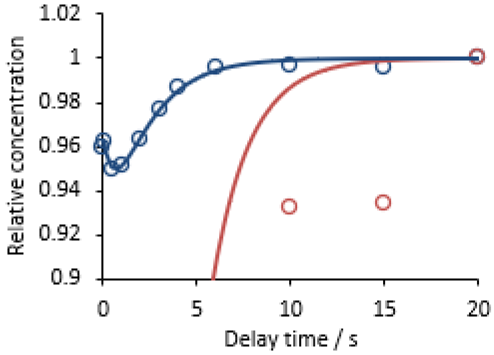

76.

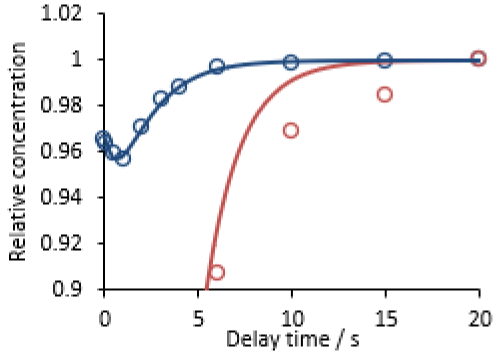

77.

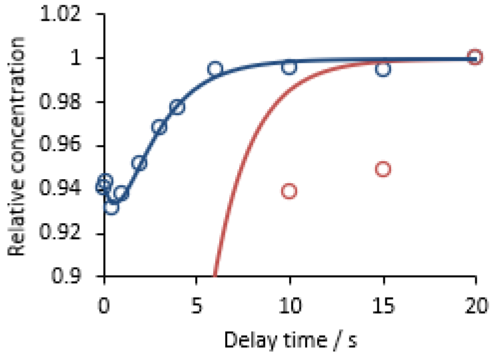

78.

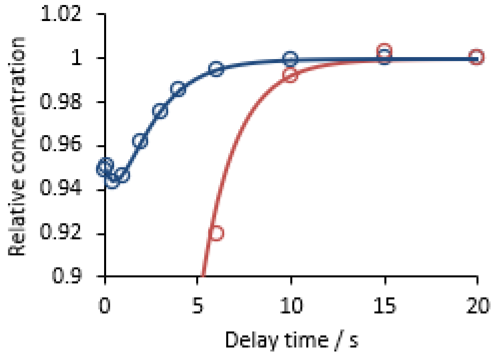

79.

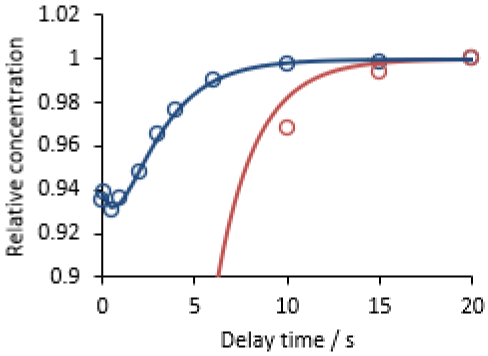

80.

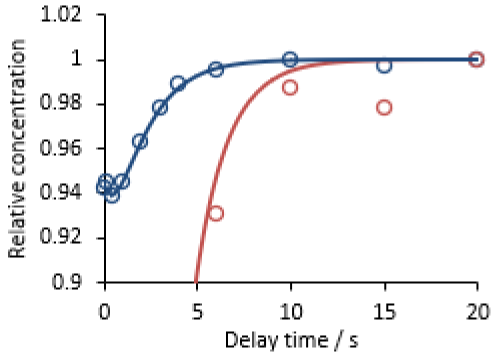

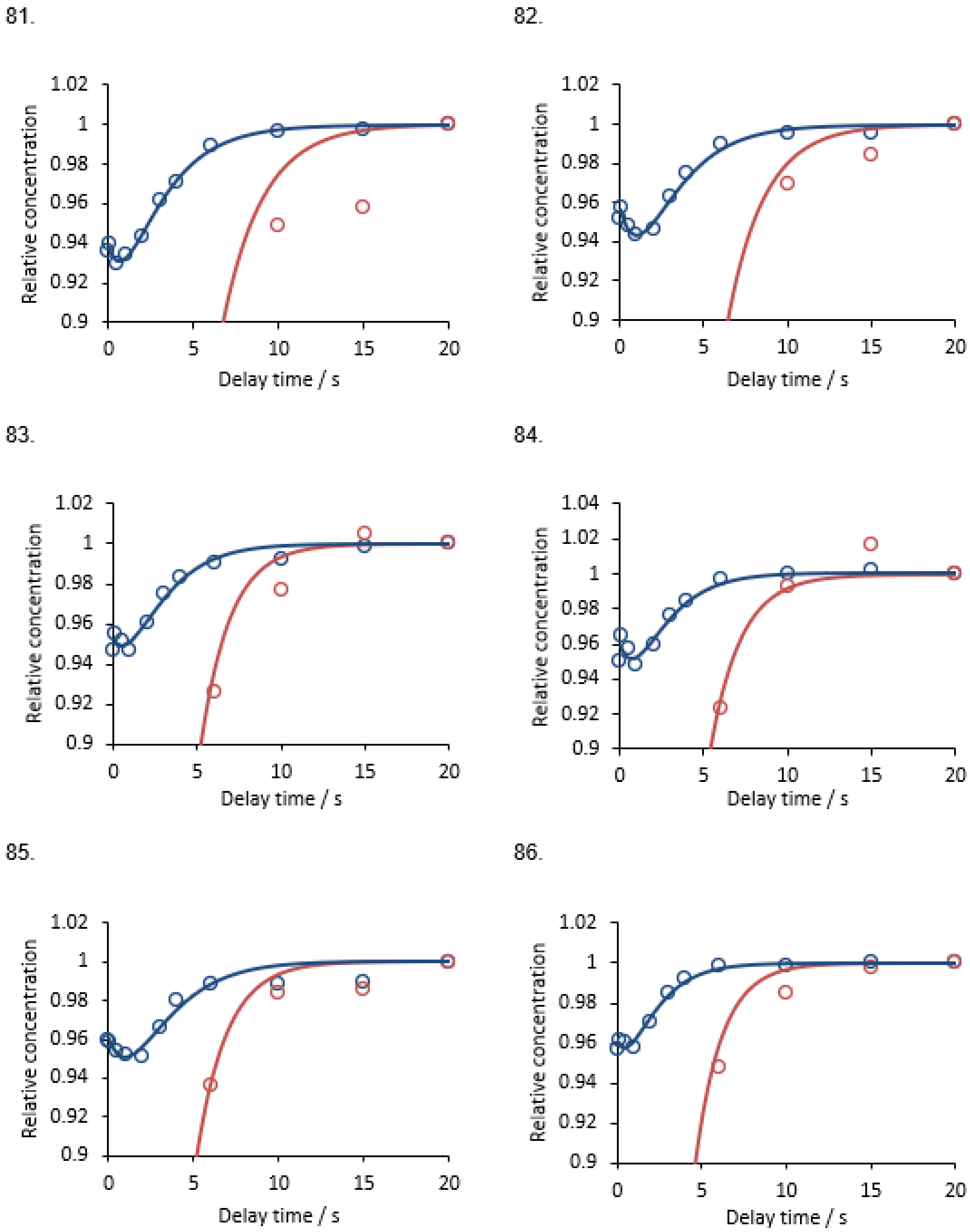

Figure 6.3. Experimental datasets (circles) and kinetic simulations (lines) with conditions and parameters indicated in previous tables.

6.4 Full dataset for phase-transfer catalysed fluorinations

The kinetic models with final rate constants are shown in **Table 6.1** and **Table 6.2** for the fluorination of β-bromosulfide and β-chloroamine, respectively. Some of the rate constants were fitted individually to each dataset, and their values, along with the initial experimental conditions for each dataset, are provided in **Table 6.3** and **Table 6.4**. All experimental and simulated kinetic data are shown in **Figure 6.4**.

It is assumed that the concentration of CsF is approximately constant during the reaction and has a value of a mol·L^{-1}, and the formation of [CatFR] is the rate limiting step. The equilibrium constants, K_c, K_1, K_2 and K_i were each set to an arbitrary value of 0.001. The overall rate of Cat' formation from [CatBrR] was set as k_5.

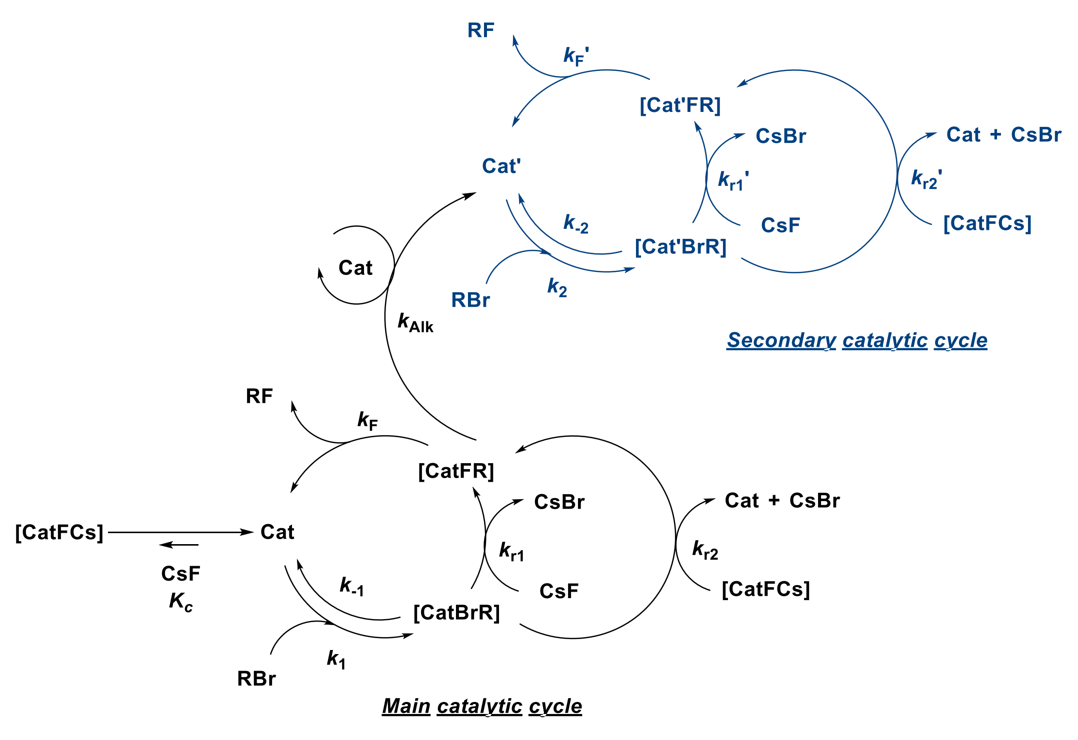

Rate coefficient	Value (1a)	Value (1b)	Unit
k_1	8.16×10^{-1}	2.55	L mol^{-1} s^{-1}
$k_3 = a \cdot k_{r1}$	1.71×10^{2}	4.33×10^{1}	L mol^{-1} s^{-1}
$k_4 = a \cdot k_{r2}$	1.16×10^{8}	1.63×10^{7}	L mol^{-1} s^{-1}
k_2	9.12	0	L mol^{-1} s^{-1}
$k_6 = a \cdot k_{r1}'$	3.44×10^{1}	0	L mol^{-1} s^{-1}
$k_7 = a \cdot k_{r2}'$	0	0	L mol^{-1} s^{-1}

Table 6.1. The proposed kinetic model for fluorination of β-bromosulfide, RBr. The value of the rate constants used in the model for each catalyst were stated.

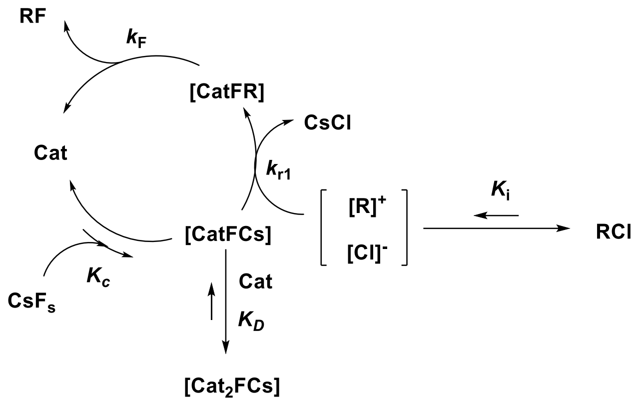

Rate coefficient	Value (1a)	Value (1b)	Unit
k_i	4.5×10^{-2}	4.5×10^{-2}	s^{-1}
k_d	0	2.83×10^{1}	$L\ mol^{-1}\ s^{-1}$
k_{-d}	0	3.09×10^{-3}	s^{-1}

Table 6.2. The proposed kinetic model for fluorination of β-bromosulfide, RBr. The value of the rate constants used in the model for each catalyst were stated.

Entry	[1a] / mM	[1b] / mM	[2b] / M	k_5 / 10^3 L mol^{-1} s^{-1}
1	1.25	-	0.114	6.77
2	2.49	-	0.118	5.80
3	1.30	-	0.189	5.54
4	1.92	-	0.188	4.68
5	2.44	-	0.191	4.37
6	5.87	-	0.185	4.63
7	9.78	-	0.194	5.00
8	1.22	-	0.249	4.26
9	2.56	-	0.224	3.93
10	-	2.66	0.269	0.539
11	-	1.31	0.248	0.40
12	-	1.22	0.125	1.38
13	-	2.84	0.125	0.539
14	-	6.90	0.123	0.539
15	-	12.29	0.126	0.539
16	-	6.73	0.110	0.539

Table 6.3. Key experimental conditions and variable parameter used for fitting.

Entry	**[1a] / mM**	**[1b] / mM**	**[6a] / M**	$\boldsymbol{k_8}$ / 10^4 L mol^{-1} s^{-1}
17	12.8	-	0.122	1.43
18	12.3	-	0.124	1.55
19	23.0	-	0.122	1.34
20	18.2	-	0.124	1.44
21	9.03	-	0.124	1.58
22	6.07	-	0.126	1.50
23	12.5	-	0.247	1.27
24	12.3	-	0.063	1.63
25	-	25.0	0.120	1.34
26	-	12.5	0.126	1.34
27	-	10.0	0.050	1.26
28	-	20.0	0.049	1.15
29	-	15.0	0.050	1.34
30	-	7.50	0.051	1.34
31	-	10.0	0.103	1.34

Table 6.4. Key experimental conditions and variable parameter used for fitting; $k_8 = \mathrm{a} \cdot k_{\mathrm{r1}}$.

1.

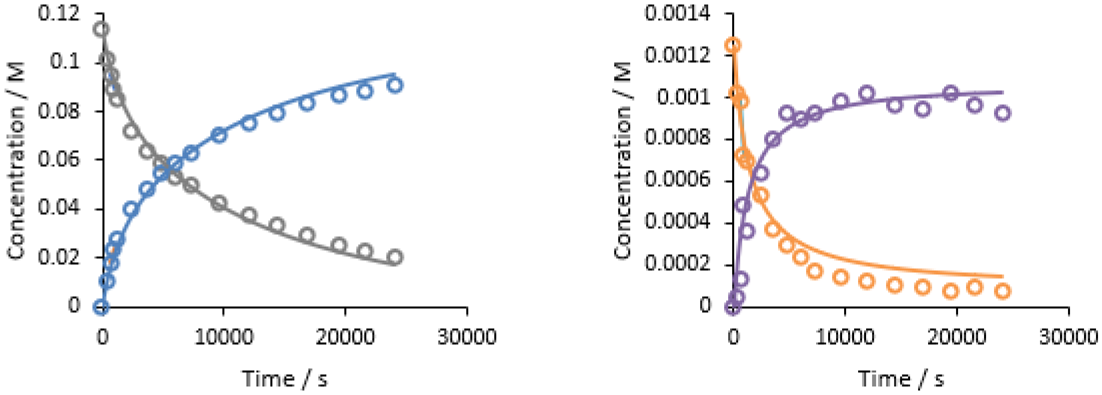
Concentration / M
0.12
0.1
0.08
0.06
0.04
0.02
0
0
10000
20000
30000
Time / s
Concentration / M
0.0014
0.0012
0.001
0.0008
0.0006
0.0004
0.0002
0
0
10000
20000
30000
Time / s

2.

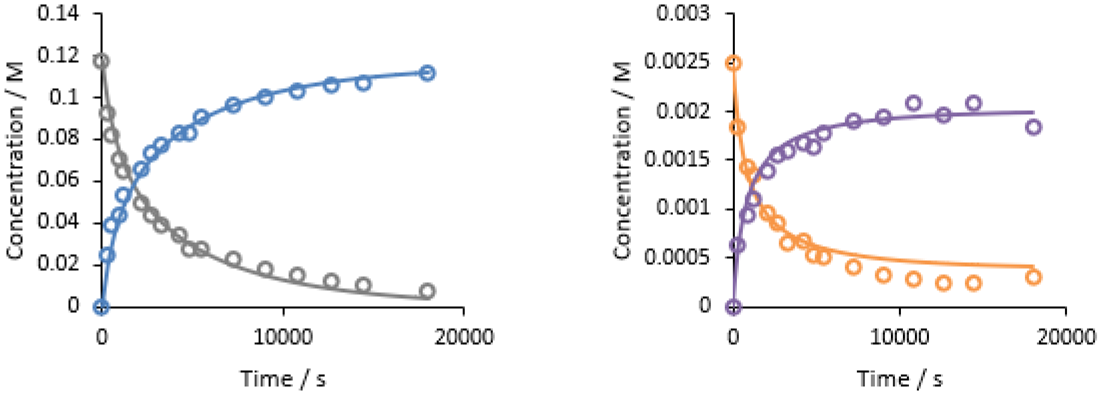
Concentration / M
0.14
0.12
0.1
0.08
0.06
0.04
0.02
0
0
10000
20000
Time / s
Concentration / M
0.003
0.0025
0.002
0.0015
0.001
0.0005
0
0
10000
20000
Time / s

3.

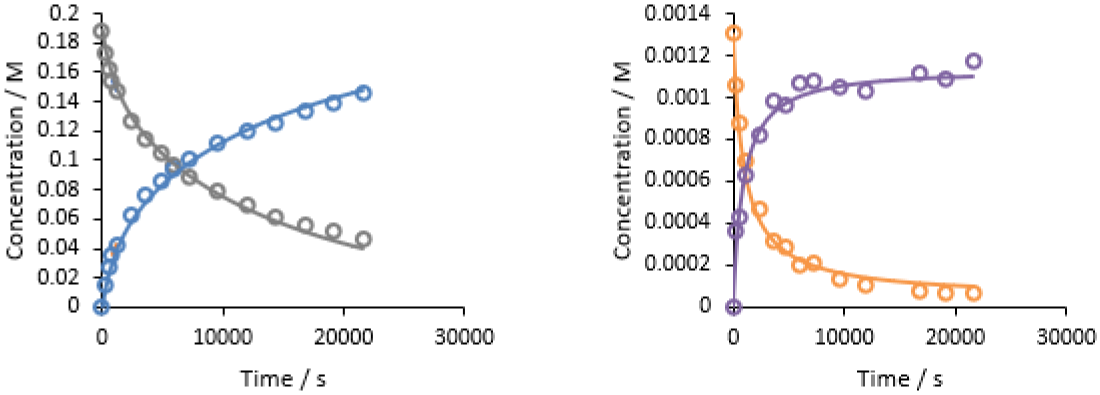
Concentration / M
0.2
0.18
0.16
0.14
0.12
0.1
0.08
0.06
0.04
0.02
0
0
10000
20000
30000
Time / s
Concentration / M
0.0014
0.0012
0.001
0.0008
0.0006
0.0004
0.0002
0
0
10000
20000
30000
Time / s

4.

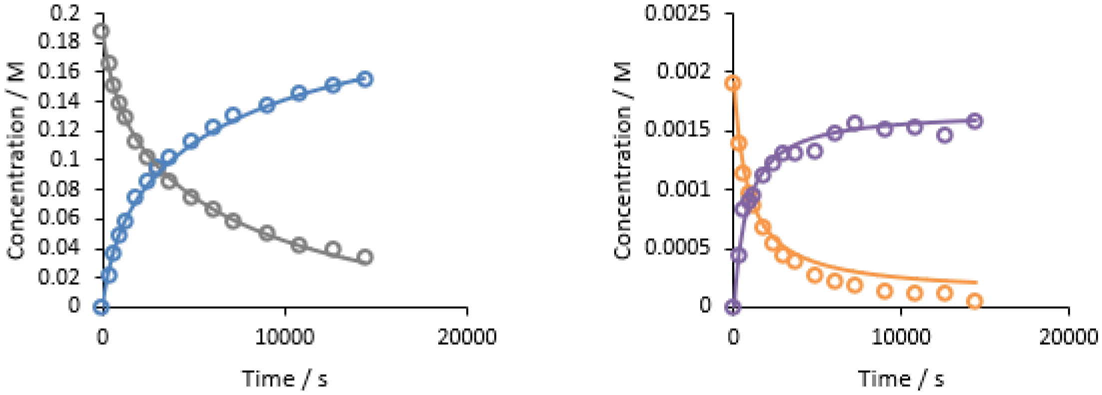
Concentration / M
0.2
0.18
0.16
0.14
0.12
0.1
0.08
0.06
0.04
0.02
0
0
10000
20000
Time / s
Concentration / M
0.0025
0.002
0.0015
0.001
0.0005
0
0
10000
20000
Time / s

5.

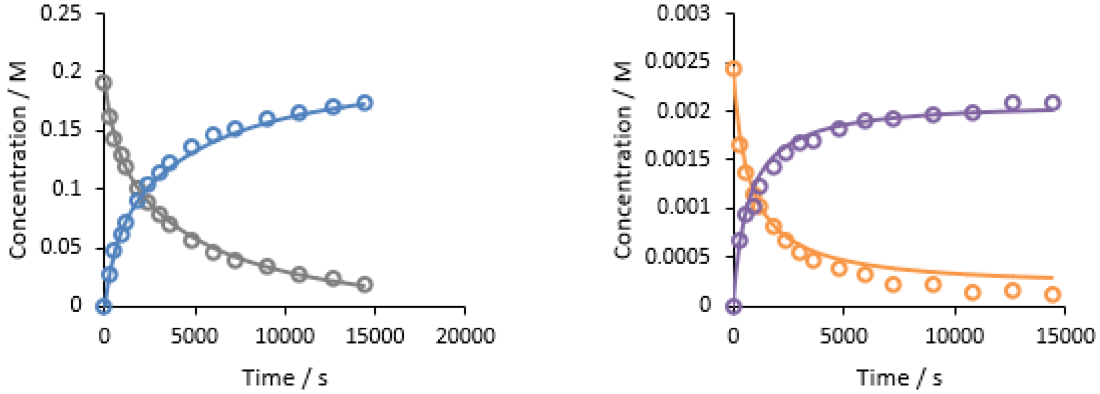
Concentration / M
0.25
0.2
0.15
0.1
0.05
0
0
5000
10000
15000
20000
Time / s
Concentration / M
0.003
0.0025
0.002
0.0015
0.001
0.0005
0
0
5000
10000
15000
Time / s

6.

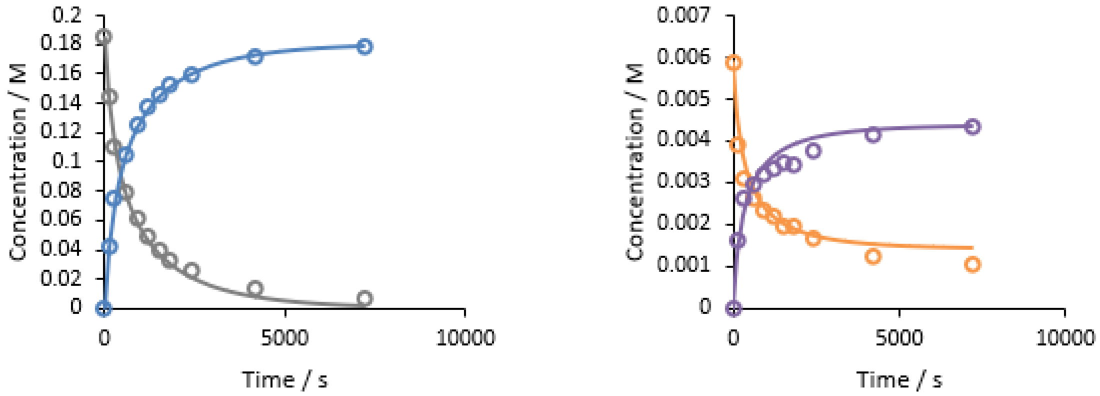
Concentration / M
0.2
0.18
0.16
0.14
0.12
0.1
0.08
0.06
0.04
0.02
0
0
5000
10000
Time / s
Concentration / M
0.007
0.006
0.005
0.004
0.003
0.002
0.001
0
0
5000
10000
Time / s

7.

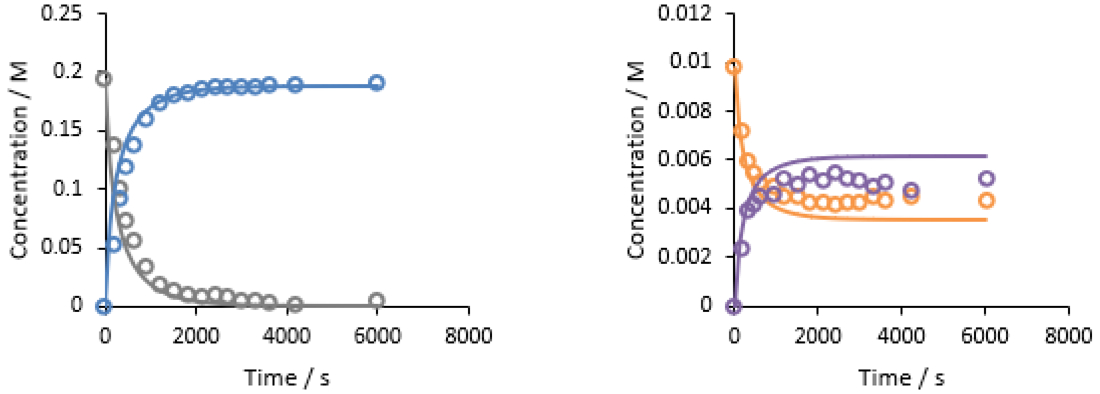
Concentration / M
0.25
0.2
0.15
0.1
0.05
0
0
2000
4000
6000
8000
Time / s
Concentration / M
0.012
0.01
0.008
0.006
0.004
0.002
0
0
2000
4000
6000
8000
Time / s

8.

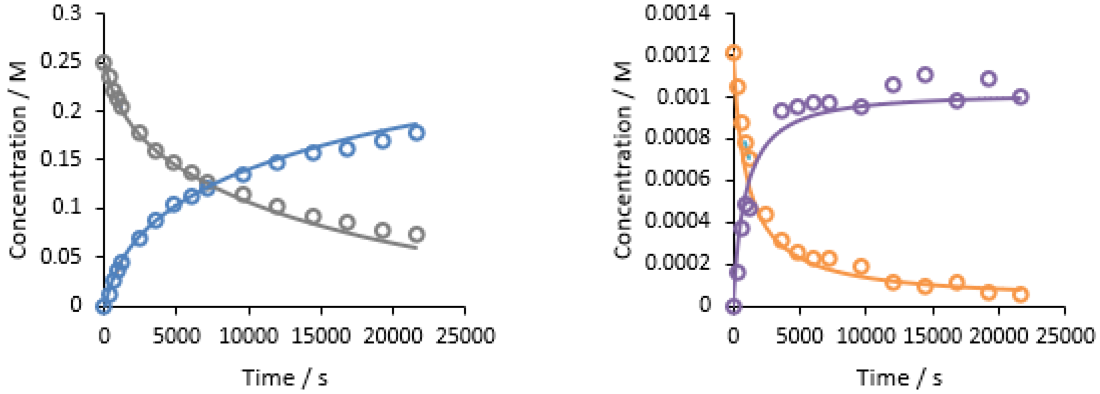
Concentration / M
0.3
0.25
0.2
0.15
0.1
0.05
0
0
5000
10000
15000
20000
25000
Time / s
Concentration / M
0.0014
0.0012
0.001
0.0008
0.0006
0.0004
0.0002
0
0
5000
10000
15000
20000
25000
Time / s

9.

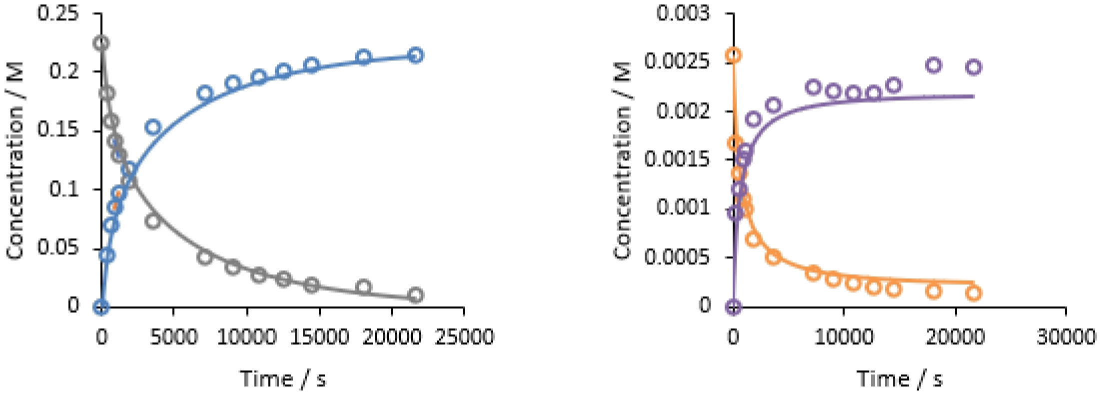
Concentration / M
0.25
0.2
0.15
0.1
0.05
0
0
5000
10000
15000
20000
25000
Time / s
Concentration / M
0.003
0.0025
0.002
0.0015
0.001
0.0005
0
0
10000
20000
30000
Time / s

10.

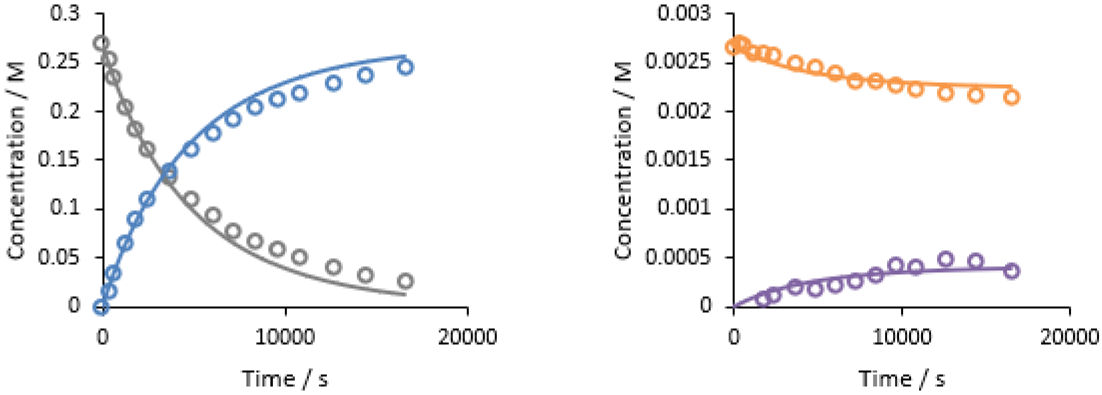
Concentration / M
0.3
0.25
0.2
0.15
0.1
0.05
0
0
10000
20000
Time / s
Concentration / M
0.003
0.0025
0.002
0.0015
0.001
0.0005
0
0
10000
20000
Time / s

11.

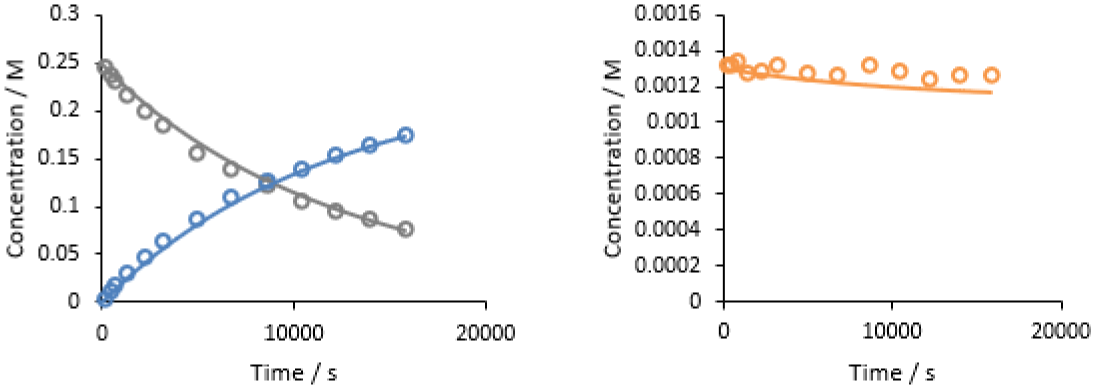
Concentration / M
0.3
0.25
0.2
0.15
0.1
0.05
0
0
10000
20000
Time / s
Concentration / M
0.0016
0.0014
0.0012
0.001
0.0008
0.0006
0.0004
0.0002
0
0
10000
20000
Time / s

12.

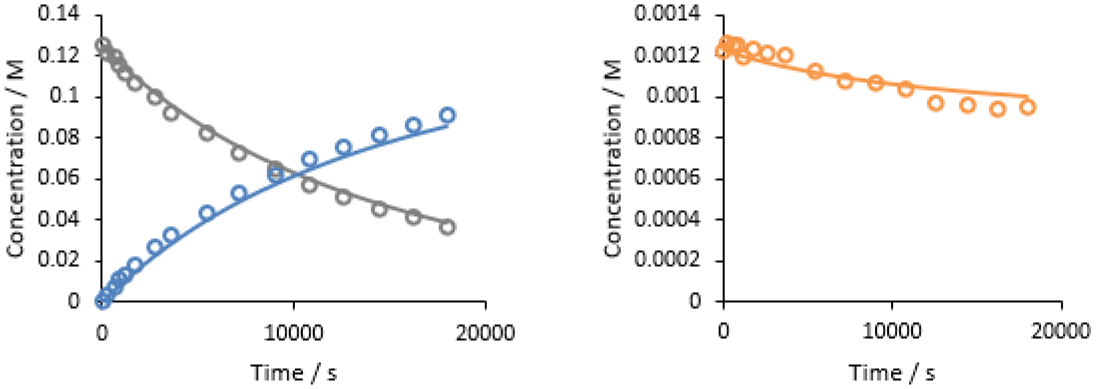
Concentration / M
0.14
0.12
0.1
0.08
0.06
0.04
0.02
0
0
10000
20000
Time / s
Concentration / M
0.0014
0.0012
0.001
0.0008
0.0006
0.0004
0.0002
0
0
10000
20000
Time / s

13.

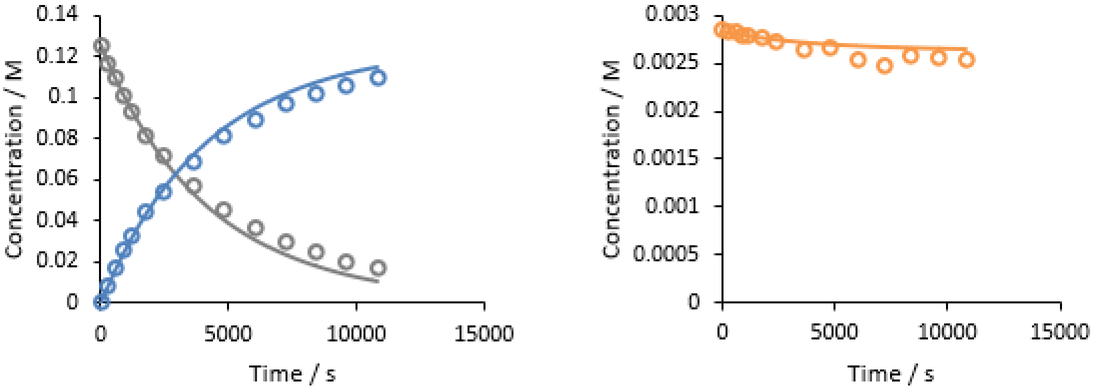

14.

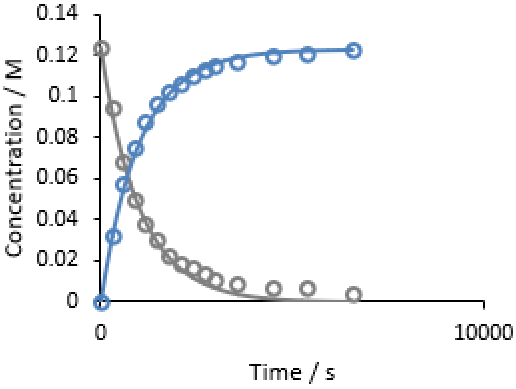

15.

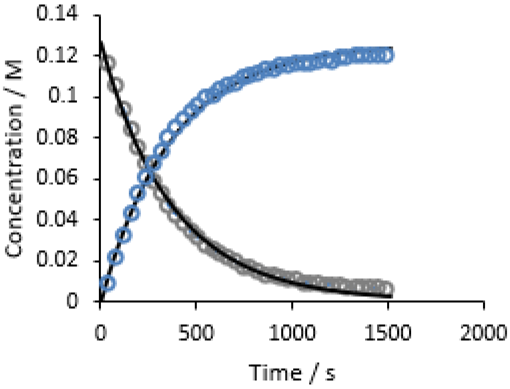

16.

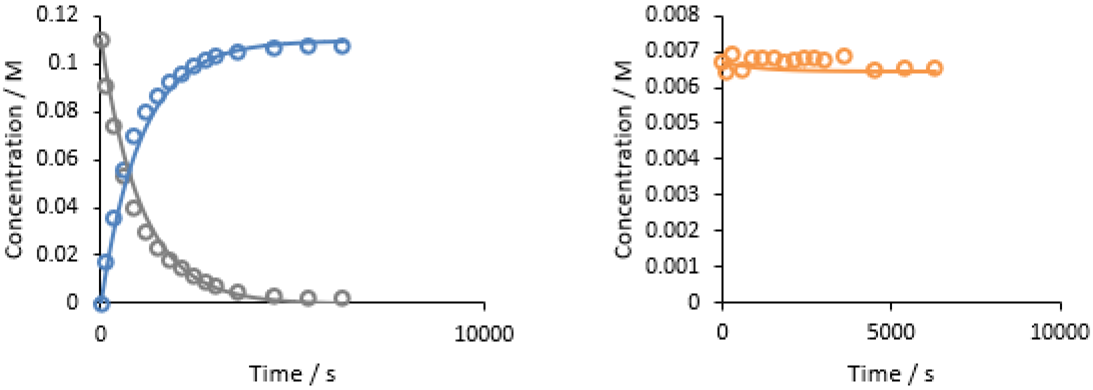

17.

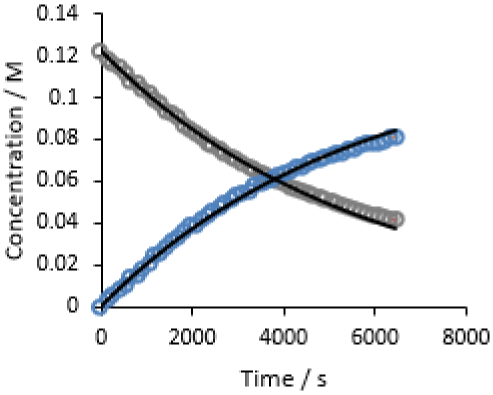

18.

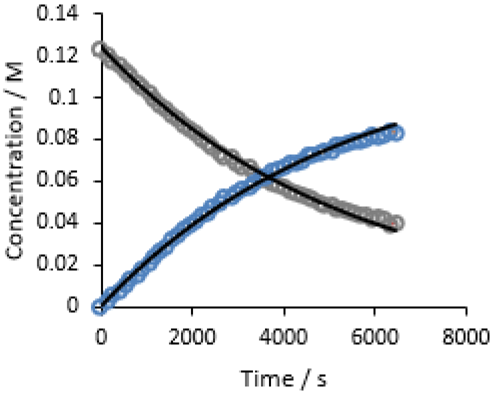

19.

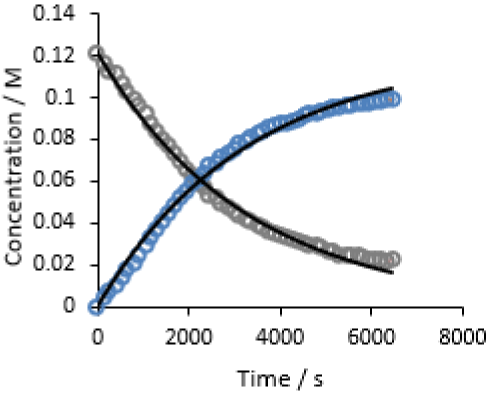

20.

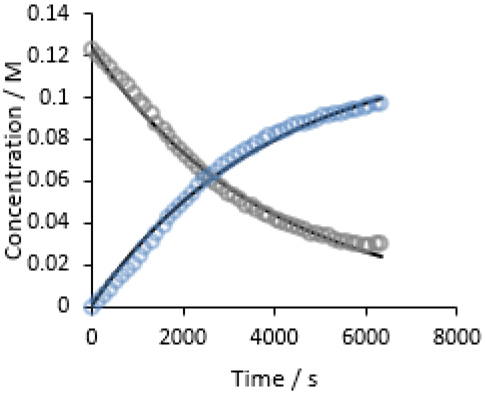

21.

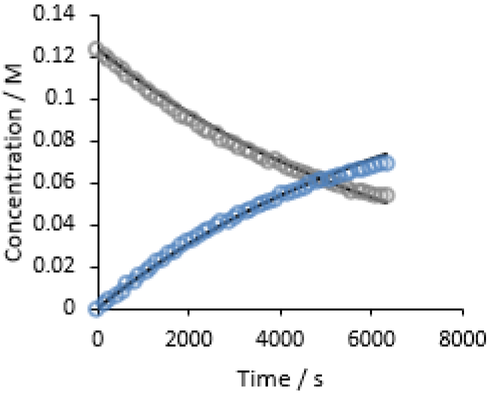

22.

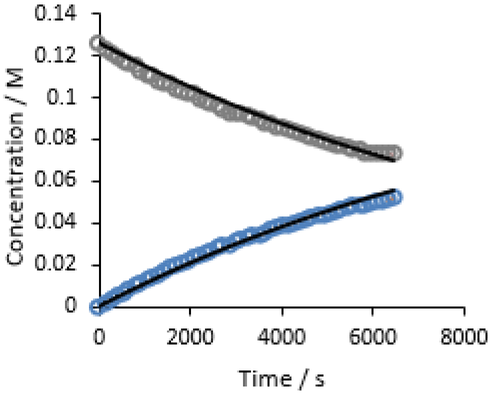

23.

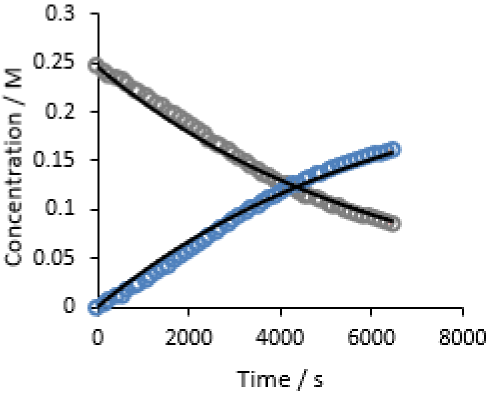

24.

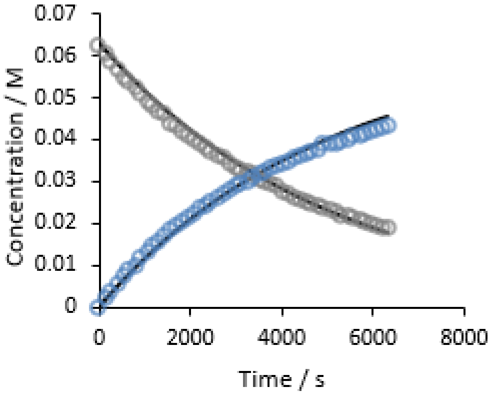

25.

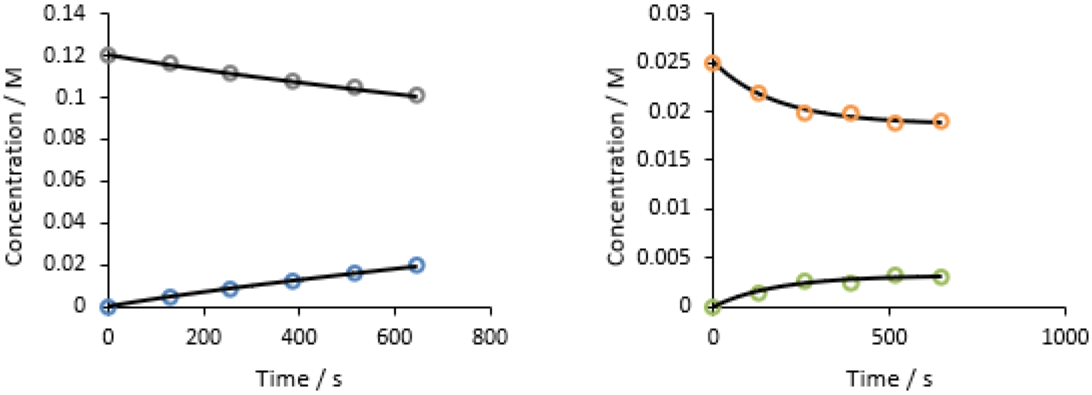

26.

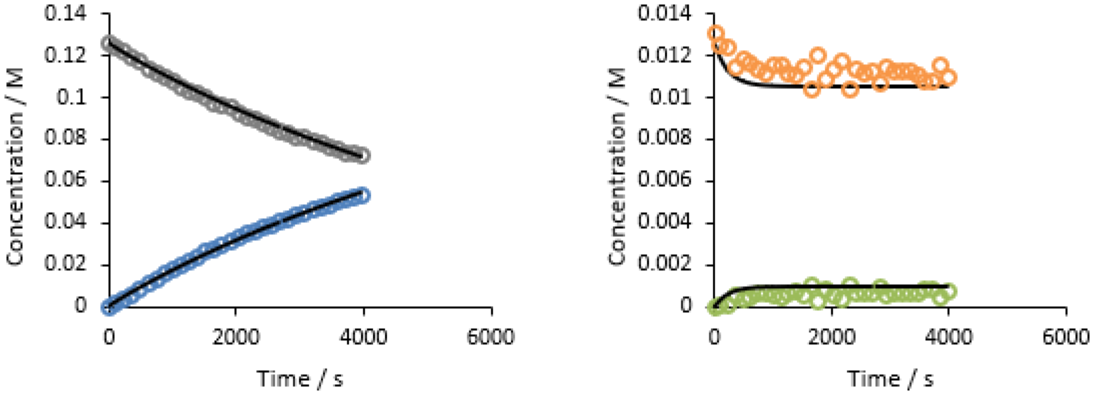
Concentration / M
0.14
0.12
0.1
0.08
0.06
0.04
0.02
0
0
2000
4000
6000
Time / s
Concentration / M
0.014
0.012
0.01
0.008
0.006
0.004
0.002
0
0
2000
4000
6000
Time / s

27.

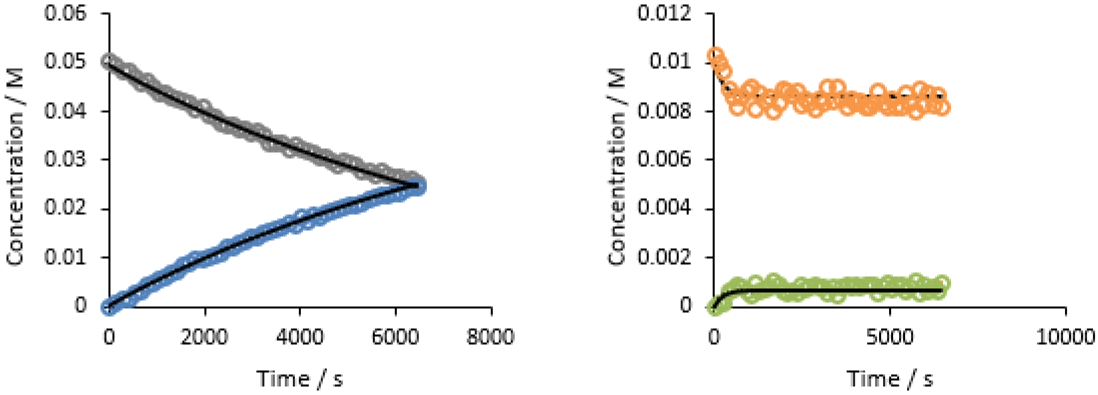
Concentration / M
0.06
0.05
0.04
0.03
0.02
0.01
0
0
2000
4000
6000
8000
Time / s
Concentration / M
0.012
0.01
0.008
0.006
0.004
0.002
0
0
5000
10000
Time / s

28.

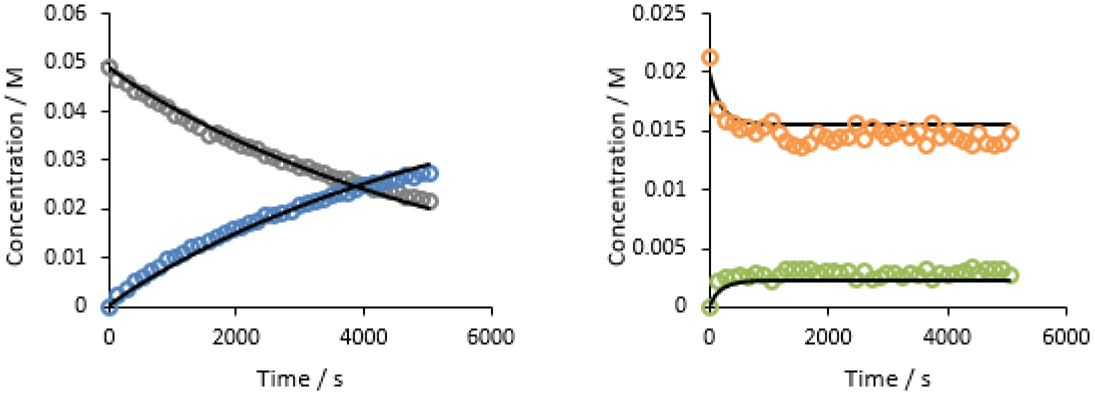
Concentration / M
0.06
0.05
0.04
0.03
0.02
0.01
0
0
2000
4000
6000
Time / s
Concentration / M
0.025
0.02
0.015
0.01
0.005
0
0
2000
4000
6000
Time / s

29.

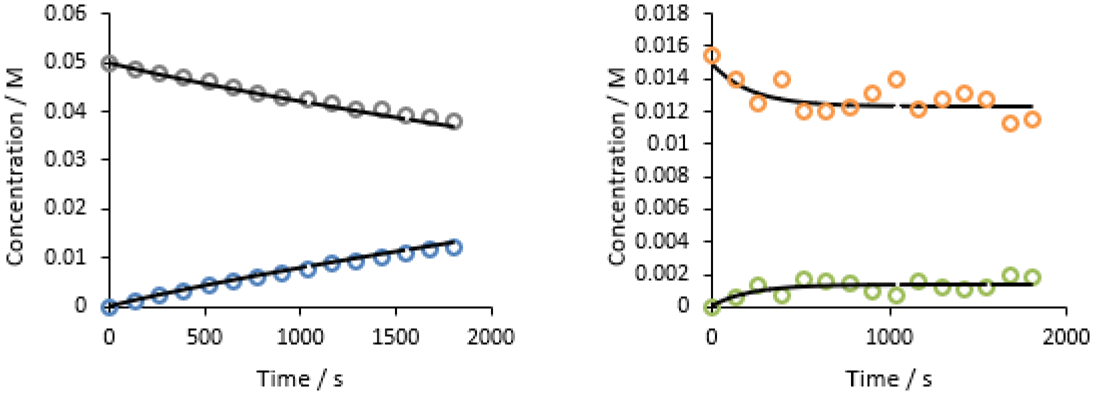
Concentration / M
0.06
0.05
0.04
0.03
0.02
0.01
0
0
500
1000
1500
2000
Time / s
Concentration / M
0.018
0.016
0.014
0.012
0.01
0.008
0.006
0.004
0.002
0
0
1000
2000
Time / s

30.

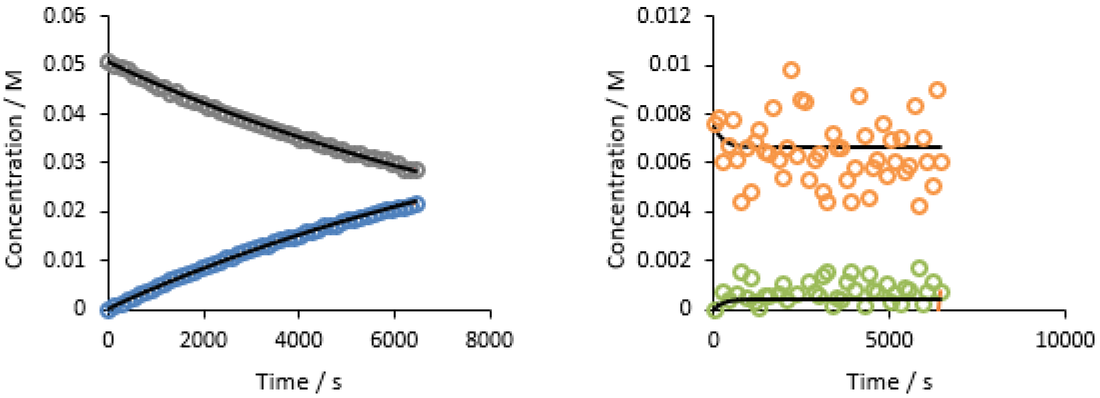

31.

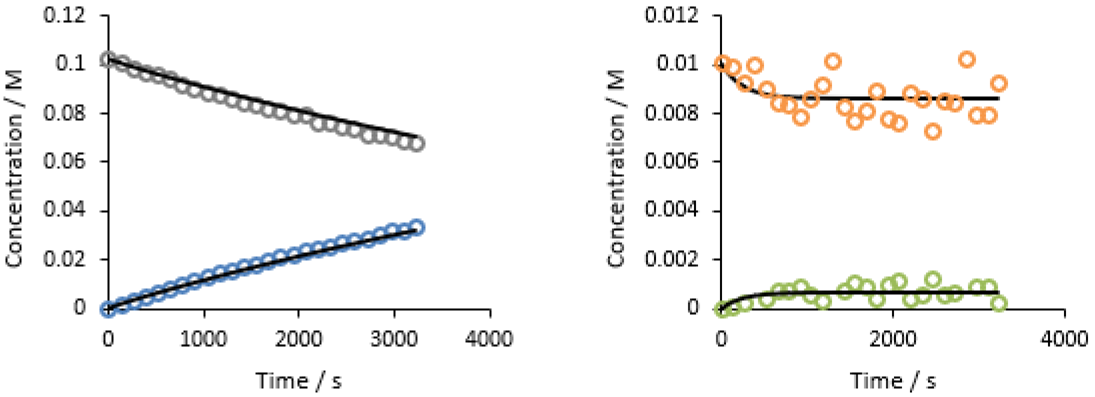

Figure 6.4. From 1 to16: kinetic simulations (solid lines) of [**2b**]$_t$ (grey), [**3b**]$_t$ (blue), [**1a**]$_t$ or [**1b**]$_t$ (orange), and [**Cat'**]$_t$ (purple) for different initial concentrations of β-bromosulfide, **2b**, and bis-urea catalyst as compared to values determined experimentally (open circles; determined by *in-situ* or *ex-situ* ^{19}F NMR spectroscopy). From 17 to 31: kinetic simulations (solid lines) of [**6a**]$_t$ (grey), [**7a**]$_t$ (blue), [**1a**]$_t$ or [**1b**]$_t$ (orange), and [**CatD**]$_t$ (green) for different initial concentrations of β-chloroamine, **6a**, and bis-urea catalyst as compared to values determined experimentally (open circles; determined by *in-situ* or *ex-situ* ^{19}F NMR spectroscopy).

References

(1) Keglevich, G.; Grün, A.; Bálint, E. Microwave Irradiation and Phase Transfer Catalysis in C-, O- and N-Alkylation Reactions. *Curr. Org. Synth.* **2013**, *10* (5), 751–763.

(2) Herchl, R.; Waser, M. Stereoselective Cyclization Reactions under Phase-Transfer Catalysis. *Tetrahedron*. **2014**, *70* (11), 1935–1960.

(3) Wang, C. H.; Liu, C. F.; Rao, G. W. Green Application of Phase-Transfer Catalysis in Oxidation: A Comprehensive Review. *Mini-Rev. Org. Chem.* **2020**, *17* (4), 405–411.

(4) Albanese, D. C. M.; Penso, M. New Trends in Asymmetric Phase Transfer Catalysis. *Eur. J. Org. Chem.* **2023**, *26* (19).

(5) Lee, S.; Chung, W. jin. Enantioselective Halogenation via Asymmetric Phase-Transfer Catalysis. *Bull. Korean Chem. Soc.* 2022, *43* (7), 896–911.

(6) *Handbook of Phase Transfer Catalysis*, 1st ed.; Sasson, Y.; Neumann, R., Eds.; Springer Dordrecht, 1997.

(7) Tan, J.; Yasuda, N. Contemporary Asymmetric Phase Transfer Catalysis: Large-Scale Industrial Applications. *Org. Process Res. Dev.* **2015**, *19* (11), 1731–1746.

(8) Starks, C. M.; Liotta, C. L.; Halpern, M. E. *Phase-Transfer Catalysis - Fundamentals, Applications and Industrial Perspectives.* 1st ed.; Springer, 2012.

(9) Brändström, A.; Junggren, U.; Holm, A.; Nordal, V.; Lindberg, A. A.; Craig, J. C. Ion Pair Extraction in Preparative Organic Chemistry. III. Alkylation of Methyl Cyanoacetate and Related Compounds. *Acta Chem. Scand.* **1969**, *23* (6), 2203–2204.

(10) Brändström, A.; Berntsson, P.; Carlsson, S.; Djurhuus, A.; Gustavii, K.; Junggren, U.; Lamm, B.; Samuelsson, B. Ion Pair Extraction in Preparative Organic Chemistry. II. Preparation of Tetrabutylammonium Salts. *Acta Chem. Scand.* **1969**, *23* (6), 2202.

(11) Makosza, M. Reactions of Organic Anions XVI. Catalytic Nitroarylation of Phenylacetonitrile Derivatives in Aqueous Medium. *Tetrahedron Lett.* **1969**, *10* (9), 673–676.

(12) Makosza, M. Reactions of Organic Anions. XI. Catalytic Alkylation of Indene. *Tetrahedron Lett.* **1966**, *7* (38),4621–4624.

(13) Starks, C. M. Phase-Transfer Catalysis. I. Heterogeneous Reactions Involving Anion Transfer by Quaternary Ammonium and Phosphonium Salts. *J. Am. Chem. Soc.* **1971**, *93* (1), 195–199.

(14) *Phase Transfer Catalysis: Principles and Techniques*, 1st ed.; Starks, M. C., Liotta, C., Eds.; Elsevier Inc.: New York, 1978.

(15) Regen, S. L. Triphase Catalysis. Applications to Organic Synthesis. *J. Org. Chem.* **1977**, *42* (5), 875–879.

(16) Regen, S. L. Triphase Catalysis [New Synthetic Methods (27)]. *Angew. Chem., Int. Ed. Engl.* **1979**, *18* (6), 421–429.

(17) Wang, D. H.; Weng, H. S. Preliminary Study on the Role Played by the Third Liquid Phase in Phase Transfer Catalysis. *Chem. Eng. Sci.* **1988**, *43* (8), 2019–2024.

(18) Neumann, R.; Sasson, Y. Mechanism of Base-Catalyzed Reactions in Phase-Transfer Systems with Poly(Ethylene Glycols) as Catalysts. The Isomerization of Allylanisole. *J. Org. Chem.* **1984**, *49* (19), 3448–3451.

(19) Baur, M.; Frank, M.; Schatz, J.; Schildbach, F. Water-Soluble Calix[n]Arenes as Receptor Molecules for Non-Polar Substrates and Inverse Phase Transfer Catalysts. *Tetrahedron* **2001**, *57* (32), 6985–699.

(20) Tilloy, S.; Bricout, H.; Monflier, E. Cyclodextrins as Inverse Phase Transfer Catalysts for the Biphasic Catalytic Hydrogenation of Aldehydes: A Green and Easy Alternative to Conventional Mass Transfer Promoters. *Green Chem.* **2002**, *4* (3), 188–193.

(21) Jwo, J. J. Phase Transfer Catalysis: Fundamentals and Selected Systems. *Catal. Rev. - Sci. Eng.* **2003**, *45* (3–4), 397–461.

(22) Ito, H.; Kusukawa, T.; Fujita, M. Wacker Oxidation in an Aqueous Phase through the Reverse Phase-Transfer Catalysis of a Self-Assembled Nanocage. *Chem. Lett.* **2000**, *29* (6), 598–599.

(23) Halpern, M. *Phase-transfer Catalysis: Mechanisms and Syntheses*; ACS Publications, 1997.

(24) Yang, H. M.; Wu, H. S. Interfacial Mechanism and Kinetics of Phase-Transfer Catalysis. *Catal. Rev. - Sci. Eng.* **2003**, *45* (3–4), 463–540.

(25) Makosza, M.; Fedoryński, M. Interfacial Processes—The Key Steps of Phase Transfer Catalyzed Reactions. *Catalysts* **2020**, *10* (12), 1436.

(26) Makosza, M.; Wawrzyniewicz, M. Reactions of Organic Anions. XXIV. Catalytic Method for Preparation of Dichlorocyclopropane Derivatives in Aqueous Medium. *Tetrahedron Lett.* **1969**, *10* (53), 4659–4662.

(27) Mąkosza, M.; Fedoryński, M. Phase Transfer Catalysis in Dichlorocarbene Chemistry: Basic Principles and Specific Features. *Russ. Chem. Bull.* **2011**, *60*, 2141–2146.

(28) Zhu, W.; Evgeniy, B.; Vladimir, K. A Minireview of Phase-Transfer Catalysis and Recent Trends. *Biomed. J. Sci. Tech. Res.* **2022**, *45* (4).

(29) Helder, R.; Hummelen, J. C.; Laane, R. W. P. M.; Wiering, J. S.; Wynberg, H. Catalytic Asymmetric Induction in Oxidation Reactions. The Synthesis of Optically Active Epoxides. *Tetrahedron Lett.* **1976**, *17* (21), 1831–1834.

(30) O'Donnell, M. J.; Bennett, W. D.; Wu, S. The Stereoselective Synthesis of α-Amino Acids by Phase-Transfer Catalysis. *J. Am. Chem. Soc.* **1989**, *111* (6), 2353–2355.

(31) O'Donnell, M. J.; Wu, S.; Huffman, J. C. A New Active Catalyst Species for Enantioselective Alkylation by Phase-Transfer Catalysis. *Tetrahedron* **1994**, *50* (15), 4507–4518.

(32) Lygo, B.; Wainwright, P. G. A New Class of Asymmetric Phase-Transfer Catalysts Derived from Cinchona Alkaloids - Application in the Enantioselective Synthesis of α-Amino Acids. *Tetrahedron Lett.* **1997**, *38* (49), 8595–8598.

(33) Corey, E. J.; Xu, F.; Noe, M. C. A Rational Approach to Catalytic Enantioselective Enolate Alkylation Using a Structurally Rigidified and Defined Chiral Quaternary Ammonium Salt under Phase Transfer Conditions. *J. Am. Chem. Soc.* **1997**, *119* (50), 12414–12415.

(34) Cram, D. J.; Sogah, G. D. Y. Chiral Crown Complexes Catalyse Michael Addition Reactions to Give Adducts in High Optical Yields. *J. Chem. Soc., Chem. Commun.,* **1981**, 625–628.

(35) Aoki, S.; Sasaki, S.; Koga, K. Simple Chiral Crown Ethers Complexed with Potassium Tert-Butoxide as Efficient Catalysts for Asymmetric Michael Additions. *Tetrahedron Lett.* **1989**, *30* (51), 7229–7230.

(36) Tőke, L.; Fenichel, L.; Albert, M. Asymmetric Michael Reaction. Deracemization of Enolate by Chiral Crown Ether. *Tetrahedron Lett.* **1995**, *36* (33), 5951–5954.

(37) Ooi, T.; Kameda, M.; Maruoka, K. Molecular Design of a C_2-Symmetric Chiral Phase-Transfer Catalyst for Practical Asymmetric Synthesis of α-Amino Acids. *J. Am. Chem. Soc.* **1999**, *121* (27), 6519–6520.

(38) Ooi, T.; Takeuchi, M.; Kameda, M.; Maruoka, K. Practical Catalytic Enantioselective Synthesis of α,α-Dialkyl-α-Amino Acids by Chiral Phase-Transfer Catalysis. *J. Am. Chem. Soc.* **2000**, *122* (21), 5228–5229.

(39) Ooi, T.; Ohara, D.; Tamura, M.; Maruoka, K. Design of New Chiral Phase-Transfer Catalysts with Dual Functions for Highly Enantioselective Epoxidation of α,β-Unsaturated Ketones. *J. Am. Chem. Soc.* **2004**, *126* (22), 6844–6845.

(40) He, R.; Wang, X.; Hashimoto, T.; Maruoka, K. Binaphthyl-Modified Quaternary Phosphonium Salts as Chiral Phase-Transfer Catalysts: Asymmetric Amination of β-Keto Esters. *Angew. Chem., Int. Ed.* **2008**, *47* (49), 9466-9468.

(41) Lee, H. J.; Maruoka, K. Recent Asymmetric Phase-Transfer Catalysis with Chiral Binaphthyl-Modified and Related Phase-Transfer Catalysts over the Last 10 Years. *Chem. Rec.* **2023**, *23* (7).

(42) Kitamura, M.; Shirakawa, S.; Arimura, Y.; Wang, X.; Maruoka, K. Combinatorial Design of Simplified High-Performance Chiral Phase-Transfer Catalysts for Practical Asymmetric Synthesis of α-Alkyl- and α,α-Dialkyl-α-Amino Acids. *Asian J. Chem.* **2008**, *3* (8–9), 1702–1714.

(43) Eitzinger, A.; Winter, M.; Schörgenhumer, J.; Waser, M. Quaternary $\beta^{2,2}$-Amino Acid Derivatives by Asymmetric Addition of Isoxazolidin-5-Ones to: Para -Quinone Methides. *Chem. Commun.* **2020**, *56* (4), 579–582.

(44) Arai, S.; Tsuji, R.; Nishida, A. Phase-Transfer-Catalyzed Asymmetric Michael Reaction Using Newly-Prepared Chiral Quaternary Ammonium Salts Derived from L-Tartrate. *Tetrahedron Lett.* **2002**, *43* (52), 9535–9537.

(45) Bernal, P.; Fernández, R.; Lassaletta, J. M. Asymmetric Cyanosilylation of Nitroalkenes. *Chem. Eur. J.* **2010**, *16*, 7714–7718.

(46) Schettini, R.; Nardone, B.; De Riccardis, F.; Sala, G. Della; Izzo, I. Cyclopeptoids as Phase-Transfer Catalysts for the Enantioselective Synthesis of α-Amino Acids. *Eur. J. Org. Chem.* **2014**, *2014* (35), 7793–7797.

(47) Pupo, G.; Ibba, F.; Ascough, D. M. H.; Vicini, A. C.; Ricci, P.; Christensen, K. E.; Pfeifer, L.; Morphy, J. R.; Brown, J. M.; Paton, R. S.; Gouverneur, V. Asymmetric Nucleophilic Fluorination under Hydrogen Bonding Phase-Transfer Catalysis. *Science* **2018**, *360* (6389), 638–642.

(48) Otevrel, J.; Waser, M. Asymmetric Phase-Transfer Catalysis - From Classical Applications to New Concepts. In *Asymmetric Organocatalysis: New Strategies, Catalysts, and Opportunities: Volume 2*; 1st ed.; John Wiley & Sons, 2022; pp 70–120.

(49) Carter, C.; Fletcher, S.; Nelson, A. Towards Phase-Transfer Catalysts with a Chiral Anion: Inducing Asymmetry in the Reactions of Cations. *Tetrahedron Asymmetry* **2003**, *14* (14), 1995–2004.

(50) Hamilton, G. L.; Kanai, T.; Toste, F. D. Chiral Anion-Mediated Asymmetric Ring Opening of Meso-Aziridinium and Episulfonium Ions. *J. Am. Chem. Soc.* **2008**, *130* (45), 14984–14986.

(51) Rauniyar, V.; Lackner, A. D.; Hamilton, G. L.; Toste, F. D. Asymmetric Electrophilic Fluorination Using an Anionic Chiral Phase-Transfer Catalyst. *Science* **2011**, *334* (6063), 1681–1684.

(52) Egami, H.; Asada, J.; Sato, K.; Hashizume, D.; Kawato, Y.; Hamashima, Y. Asymmetric Fluorolactonization with a Bifunctional Hydroxyl Carboxylate Catalyst. *J. Am. Chem. Soc.* **2015**, *137* (32), 10132–10135.

(53) Egami, H.; Hamashima, Y. Asymmetric Fluorofunctionalizations with Carboxylate-Based Phase-Transfer Catalysts. *Chem. Rec.* **2023**, *23* (7).

(54) O'Hagan, D. Understanding Organofluorine Chemistry. An Introduction to the C–F Bond. *Chem. Soc. Rev.* **2008**, *37* (2), 308–319.

(55) Peyroux, J.; Dubois, M.; Tomasella, E.; Petit, E.; Flahaut, D. Enhancement of Surface Properties on Commercial Polymer Packaging Films Using Various Surface Treatment Processes (Fluorination and Plasma). *Appl. Surf. Sci.* **2014**, *315* (1), 426–431.

(56) Guzman-Puyol, S.; Tedeschi, G.; Goldoni, L.; Benítez, J. J.; Ceseracciu, L.; Koschella, A.; Heinze, T.; Athanassiou, A.; Heredia-Guerrero, J. A. Greaseproof, Hydrophobic, and Biodegradable Food Packaging Bioplastics from C6-Fluorinated Cellulose Esters. *Food Hydrocoll.* **2022**, *128*.

(57) Holoubek, J.; Yu, M.; Yu, S.; Li, M.; Wu, Z.; Xia, D.; Bhaladhare, P.; Gonzalez, M. S.; Pascal, T. A.; Liu, P.; Chen, Z. An All-Fluorinated Ester Electrolyte for Stable High-Voltage Li Metal Batteries Capable of Ultra-Low-Temperature Operation. *ACS Energy Lett.* **2020**, *5* (5), 1438–1447.

(58) Wang, Y.; Li, Z.; Hou, Y.; Hao, Z.; Zhang, Q.; Ni, Y.; Lu, Y.; Yan, Z.; Zhang, K.; Zhao, Q.; Li, F.; Chen, J. Emerging Electrolytes with Fluorinated Solvents for Rechargeable Lithium-Based Batteries. *Chem. Soc. Rev*. **2023**, *52* (8). 2713–2763.

(59) Wang, Y.; Wu, Z.; Azad, F. M.; Zhu, Y.; Wang, L.; Hawker, C. J.; Whittaker, A. K.; Forsyth, M.; Zhang, C. Fluorination in Advanced Battery Design. *Nat. Rev. Mater*. **2024**, *9*, 119–133.

(60) Donchev, A.; Mengis, L.; Couret, A.; Mayer, S.; Clemens, H.; Galetz, M. Effects of Tungsten Alloying and Fluorination on the Oxidation Behavior of Intermetallic Titanium Aluminides for Aerospace Applications. *Intermetallics.* **2021**, *139*.

(61) Jiang, C.; Cheng, Z.; Li, X.; Li, C.; Liu, X. Thermally Robust Bendable Silicon Dioxide/Polyimide Layered Composite Film through Catalytic Fluorination. *ACS Appl. Polym. Mater.* **2019**, *1* (4).

(62) Purser, S.; Moore, P. R.; Swallow, S.; Gouverneur, V. Fluorine in Medicinal Chemistry. *Chem. Soc. Rev.* **2008**, *37* (2).

(63) Zhou, Y.; Wang, J.; Gu, Z.; Wang, S.; Zhu, W.; Acenã, J. L.; Soloshonok, V. A.; Izawa, K.; Liu, H. Next Generation of Fluorine-Containing Pharmaceuticals, Compounds Currently in Phase II-III Clinical Trials of Major Pharmaceutical Companies: New Structural Trends and Therapeutic Areas. *Chem. Rev.* **2016**, *116* (2), 422–518.

(64) Gillis, E. P.; Eastman, K. J.; Hill, M. D.; Donnelly, D. J.; Meanwell, N. A. Applications of Fluorine in Medicinal Chemistry. *J. Med. Chem.* **2015**, *58* (21).

(65) Mei, H.; Han, J.; Klika, K. D.; Izawa, K.; Sato, T.; Meanwell, N. A.; Soloshonok, V. A. Applications of Fluorine-Containing Amino Acids for Drug Design. *Eur. J. Med. Chem*. **2020**, *186*.

(66) Shi, L.; Zhang, N. Applications of Solution NMR in Drug Discovery. *Molecules*. **2021**, *26* (3).

(67) Gronenborn, A. M. Small, but Powerful and Attractive: 19F in Biomolecular NMR. *Structure*. **2022**, *30* (1), 6–14.

(68) Gimenez, D.; Phelan, A.; Murphy, C. D.; Cobb, S. L. 19F NMR as a Tool in Chemical Biology. *Beilstein J. Org. Chem.* 2021, *17,* 293–318.

(69) Ajenjo, J.; Destro, G.; Cornelissen, B.; Gouverneur, V. Closing the Gap between 19F and 18F Chemistry. *EJNMMI Radiopharm. Chem.* **2021**, *6*.

(70) Haveman, L. Y. F.; Vugts, D. J.; Windhorst, A. D. State of the Art Procedures towards Reactive [18F]Fluoride in PET Tracer Synthesis. *EJNMMI Radiopharm. Chem*. **2023**, *8*.

(71) Nerella, S. G.; Bhattacharya, A.; Thacker, P. S.; Tulja, S. Synthetic Methodologies and PET Imaging Applications of Fluorine-18 Radiotracers: A Patent Review. *Expert Opin. Ther. Pat*. **2022**, *32* (4), 455–473.

(72) O'Hagan, D.; Harper, D. B. Fluorine-Containing Natural Products. *J. Fluor. Chem.* **1999**, *100* (1–2), 127–133.

(73) Chan, K. K. J.; O'Hagan, D. The Rare Fluorinated Natural Products and Biotechnological Prospects for Fluorine Enzymology. In *Methods in Enzymology*; 2012; Vol. 516.

(74) Harsanyi, A.; Sandford, G. Organofluorine Chemistry: Applications, Sources and Sustainability. *Green Chem.* **2015**, *17* (4).

(75) Britton, R.; Gouverneur, V.; Lin, J. H.; Meanwell, M.; Ni, C.; Pupo, G.; Xiao, J. C.; Hu, J. Contemporary Synthetic Strategies in Organofluorine Chemistry. *Nat. Rev. Methods Primers*. **2021**, *47*.

(76) Politanskaya, L. V.; Selivanova, G. A.; Panteleeva, E. V.; Tretyakov, E. V.; Platonov, V. E.; Nikul'shin, P. V.; Vinogradov, A. S.; Zonov, Y. V.; Karpov, V. M.; Mezhenkova, T. V.; Vasilyev, A. V.; Koldobskii, A. B.; Shilova, O. S.; Morozova, S. M.; Burgart, Y. V.; Shchegolkov, E. V.; Saloutin, V. I.; Sokolov, V. B.; Aksinenko, A. Yu.; Nenajdenko, V. G.; Moskalik, M. Yu.; Astakhova, V. V.; Shainyan, B. A.; Tabolin, A. A.; Ioffe, S. L.; Muzalevskiy, V. M.; Balenkova, E. S.; Shastin, A. V.; Tyutyunov, A. A.; Boiko, V. E.; Igumnov, S. M.; Dilman, A. D.; Adonin, N. Yu.; Bardin, V. V.; Masoud, S. M.; Vorobyeva, D. V.; Osipov, S. N.; Nosova, E. V.; Lipunova, G. N.; Charushin, V. N.; Prima, D. O.; Makarov, A. G.; Zibarev, A. V.; Trofimov, B. A.; Sobenina, L. N.; Belyaeva, K. V.; Sosnovskikh, V. Ya.; Obydennov, D. L.; Usachev, S. A. Organofluorine Chemistry: Promising Growth Areas and Challenges. *Russ. Chem. Rev.* **2019**, *88* (5).

(77) Reddy, P. *Organofluorine Chemistry: Synthesis and Applications*; Elsevier, 2020.

(78) *Organofluorine Chemistry: Synthesis, Modeling, and Applications*; 1st ed.; Szabó, K.; Selander, N., Eds.; Wiley-VCH, 2021.

(79) Qing, F. L.; Liu, X. Y.; Ma, J. A.; Shen, Q.; Song, Q.; Tang, P. A Fruitful Decade of Organofluorine Chemistry: New Reagents and Reactions. *CCS Chemistry*. **2022**, *4*, 2518–2549.

(80) Hintermann, L.; Togni, A. Catalytic Enantioselective Fluorination of β-Ketoesters. *Angew. Chem. Int. Ed.* **2000**, *39* (23).

(81) Bertogg, A.; Hintermann, L.; Huber, D. P.; Perseghini, M.; Sanna, M.; Togni, A. Substrate Range of the Titanium TADDOLate Catalyzed Asymmetric Fluorination of Activated Carbonyl Compounds. *Helv. Chim. Acta.* **2012**, *95* (3), 353–403.

(82) Hamashima, Y.; Yagi, K.; Takano, H.; Tamás, L.; Sodeoka, M. An Efficient Enantioselective Fluorination of Various β-Ketoesters Catalyzed by Chiral Palladium Complexes. *J. Am. Chem. Soc.* **2002**, *124* (49).

(83) Hamashima, Y.; Suzuki, T.; Takano, H.; Shimura, Y.; Tsuchiya, Y.; Moriya, K. ichi; Goto, T.; Sodeoka, M. Highly Enantioselective Fluorination Reactions of β-Ketoesters and β-Ketophosphonates Catalyzed by Chiral Palladium Complexes. *Tetrahedron* **2006**, *62* (30).

(84) Cho, M. J.; Kang, Y. K.; Lee, N. R.; Kim, D. Y. Catalytic Asymmetric Fluorination of α-Chloro-β-Ketoesters in the Presence of Chiral Palladium Complexes. *Bull. Korean Chem. Soc.* **2007**, *28* (12).

(85) Shibata, N.; Ishimaru, T.; Nagai, T.; Kohno, J.; Toru, T. First Enantio-Flexible Fluorination Reaction Using Metal-Bis(Oxazoline) Complexes. *Synlett.* **2004**, 10, 1703–1706.

(86) Reddy, D. S.; Shibata, N.; Nagai, J.; Nakamura, S.; Toru, T.; Kanemasa, S. Desymmetrization-like Catalytic Enantioselective Fluorination of Malonates and Its Application to Pharmaceutically Attractive Molecules. *Angew. Chem. Int. Ed.* **2008**, *47* (1).

(87) Ma, J. A.; Cahard, D. Copper(II) Triflate-Bis(Oxazoline)-Catalysed Enantioselective Electrophilic Fluorination of β-Ketoesters. *Tetrahedron Asymm.* **2004**, *15* (6).

(88) Shibata, N.; Ishimaru, T.; Reddy, D. S.; Horikawa, T.; Nakamura, S.; Toru, T. DBFOX-Ph/Metal Complexes: Evaluation as Catalysts for Enantioselective Fluorination of 3-(2-Arylacetyl)-2-Thiazolidinones. *Beilstein J. Org. Chem.* **2008**, *4*.

(89) Reddy, D. S.; Shibata, N.; Horikawa, T.; Suzuki, S.; Nakamura, S.; Toru, T.; Shiro, M. A DBFOX-Ph-Based Combinatorial Catalyst for Enantioselective Fluorination of Aryl Acetyl and 3-Butenoyl Thiazolidinones. *Asian J. Chem.* **2009**, *4* (9).

(90) Kim, D. Y.; Park, E. J. Catalytic Enantioselective Fluorination of β-Keto Esters by Phase-Transfer Catalysis Using Chiral Quaternary Ammonium Salts. *Org. Lett.* **2002**, *4* (4).

(91) Wang, X.; Lan, Q.; Shirakawa, S.; Maruoka, K. Chiral Bifunctional Phase Transfer Catalysts for Asymmetric Fluorination of β-Keto Esters. *Chem. Commun.* **2010**, *46* (2).

(92) Luo, J.; Wu, W.; Xu, L. W.; Meng, Y.; Lu, Y. Enantioselective Direct Fluorination and Chlorination of Cyclic β-Ketoesters Mediated by Phase-Transfer Catalysts. *Tetrahedron Lett.* **2013**, *54* (21).

(93) Enders, D.; Hüttl, M. R. M. Direct Organocatalytic α-Fluorination of Aldehydes and Ketones. *Synlett.* **2005**, *6*.

(94) Beeson, T. D.; MacMillan, D. W. C. Enantioselective Organocatalytic α-Fluorination of Aldehydes. *J. Am. Chem. Soc.* **2005**, *127* (24).

(95) Steiner, D. D.; Mase, N.; Barbas, C. F. Direct Asymmetric α-Fluorination of Aldehydes. *Angew. Chem. Int. Ed.* **2005**, *44* (24).

(96) Marigo, M.; Fielenbach, D.; Braunton, A.; Kjærsgaard, A.; Jørgensen, K. A. Enantioselective Formation of Stereogenic Carbon - Fluorine Centers by a Simple Catalytic Method. *Angew. Chem. Int. Ed.* **2005**, *44* (24).

(97) Ishimaru, T.; Shibata, N.; Horikawa, T.; Yasuda, N.; Nakamura, S.; Toru, T.; Shiro, M. Cinchona Alkaloid Catalyzed Enantioselective Fluorination of Allyl Silanes, Silyl Enol Ethers, and Oxindoles. *Angew. Chem. Int. Ed.* **2008**, *47* (22).

(98) Baudequin, C.; Loubassou, J. F.; Plaquevent, J. C.; Cahard, D. Enantioselective Electrophilic Fluorinations: A Study of the Fluorine-Transfer from Achiral N-F Reagents to Cinchona Alkaloids. *J. Fluor. Chem.* **2003**, *122* (2).

(99) Greedy, B.; Paris, J. M.; Vidal, T.; Gouverneur, V. Regio- and Enantioselective Synthesis of Allylic Fluorides by Electrophilic Fluorodesilylation of Allyl Silanes. *Angew. Chem. Int. Ed.* **2003**, *42* (28).

(100) Wu, J.; Wang, Y. M.; Drljevic, A.; Rauniyar, V.; Phipps, R. J.; Dean Toste, F. A Combination of Directing Groups and Chiral Anion Phase-Transfer Catalysis for Enantioselective Fluorination of Alkenes. *Proc. Natl. Acad. Sci. U. S. A.* **2013**, *110* (34), 13729–13733.

(101) Phipps, R. J.; Hiramatsu, K.; Toste, F. D. Asymmetric Fluorination of Enamides: Access to α-Fluoroimines Using an Anionic Chiral Phase-Transfer Catalyst. *J. Am. Chem. Soc.* **2012**, *134* (20).

(102) Phipps, R. J.; Toste, F. D. Chiral Anion Phase-Transfer Catalysis Applied to the Direct Enantioselective Fluorinative Dearomatization of Phenols. *J. Am. Chem. Soc.* **2013**, *135* (4).

(103) Liang, X. W.; Liu, C.; Zhang, W.; You, S. L. Asymmetric Fluorinative Dearomatization of Tryptamine Derivatives. *Chem. Commun.* **2017**, *53* (40).

(104) Liang, X. W.; Cai, Y.; You, S. L. Asymmetric Fluorinative Dearomatization of Tryptophol Derivatives by Chiral Anion Phase-Transfer Catalysis. *Chin. J. Chem.* **2018**, *36* (10), 925–928.

(105) Honjo, T.; Phipps, R. J.; Rauniyar, V.; Toste, F. D. A Doubly Axially Chiral Phosphoric Acid Catalyst for the Asymmetric Tandem Oxyfluorination of Enamides. *Angew. Chem. Int. Ed.* **2012**, *51* (38).

(106) Zi, W.; Wang, Y. M.; Toste, F. D. An in Situ Directing Group Strategy for Chiral Anion Phase-Transfer Fluorination of Allylic Alcohols. *J. Am. Chem. Soc.* **2014**, *136* (37).

(107) Rozatian, N.; Ashworth, I. W.; Sandford, G.; Hodgson, D. R. W. A Quantitative Reactivity Scale for Electrophilic Fluorinating Reagents. *Chem. Sci.* **2018**, *9* (46).

(108) Satyanarayana, T.; Abraham, S.; Kagan, H. B. Nonlinear Effects in Asymmetric Catalysis. *Angew. Chem. Int. Ed.* **2009**, *48* (3).

(109) Bruns, S.; Haufe, G. Enantioselective Introduction of Fluoride into Organic Compounds: First Asymmetric Ring Opening of Epoxides by Hydrofluorinating Reagents. *J. Fluor. Chem.* **2000**, *104* (2).

(110) Haufe, G.; Bruns, S. (Salen)Chromium Complex Mediated Asymmetric Ring Opening of Meso- And Racemic Epoxides with Different Fluoride Sources. *Adv. Synth. Catal.* **2002**, *344* (2).

(111) Kalow, J. A.; Doyle, A. G. Enantioselective Ring Opening of Epoxides by Fluoride Anion Promoted by a Cooperative Dual-Catalyst System. *J. Am. Chem. Soc.* **2010**, *132* (10).

(112) Kalow, J. A.; Doyle, A. G. Mechanistic Investigations of Cooperative Catalysis in the Enantioselective Fluorination of Epoxides. *J. Am. Chem. Soc.* **2011**, *133* (40).

(113) Kalow, J. A.; Doyle, A. G. Enantioselective Fluoride Ring Opening of Aziridines Enabled by Cooperative Lewis Acid Catalysis. *Tetrahedron* **2013**, *69* (27–28).

(114) Pupo, G.; Vicini, A. C.; Ascough, D. M. H.; Ibba, F.; Christensen, K. E.; Thompson, A. L.; Brown, J. M.; Paton, R. S.; Gouverneur, V. Hydrogen Bonding Phase-Transfer Catalysis with Potassium Fluoride: Enantioselective Synthesis of β-Fluoroamines. *J. Am. Chem. Soc.* **2019**, *141* (7).

(115) Roagna, G.; Ascough, D. M. H.; Ibba, F.; Vicini, A. C.; Fontana, A.; Christensen, K. E.; Peschiulli, A.; Oehlrich, D.; Misale, A.; Trabanco, A. A.; Paton, R. S.; Pupo, G.; Gouverneur, V. Hydrogen Bonding Phase-Transfer Catalysis with Ionic Reactants: Enantioselective Synthesis of γ-Fluoroamines. *J. Am. Chem. Soc.* **2020**, *142* (33).

(116) Liang, S.; Hammond, G. B.; Xu, B. Hydrogen Bonding: Regulator for Nucleophilic Fluorination. *Chem. Eur. J.* **2017**, *23* (71), 17850–17861.

(117) Ibba, F.; Pupo, G.; Thompson, A. L.; Brown, J. M.; Claridge, T. D. W.; Gouverneur, V. Impact of Multiple Hydrogen Bonds with Fluoride on Catalysis: Insight from NMR Spectroscopy. *J. Am. Chem. Soc.* **2020**, *142* (46).

(118) Katcher, M. H.; Doyle, A. G. Palladium-Catalyzed Asymmetric Synthesis of Allylic Fluorides. *J. Am. Chem. Soc.* **2010**, *132* (49).

(119) Katcher, M. H.; Sha, A.; Doyle, A. G. Palladium-Catalyzed Regio- and Enantioselective Fluorination of Acyclic Allylic Halides. *J. Am. Chem. Soc.* **2011**, *133* (40).

(120) Ben-Tal, Y.; Boaler, P. J.; Dale, H. J. A.; Dooley, R. E.; Fohn, N. A.; Gao, Y.; García-Domínguez, A.; Grant, K. M.; Hall, A. M. R.; Hayes, H. L. D.; Kucharski, M. M.; Wei, R.; Lloyd-Jones, G. C. Mechanistic Analysis by NMR Spectroscopy: A Users Guide. *Prog. Nucl. Magn. Reason. Spectrosc.* **2022**, *129*, 28–106.

(121) Chung, R.; Hein, J. E. The More, The Better: Simultaneous *In* Situ Reaction Monitoring Provides Rapid Mechanistic and Kinetic Insight. *Top. Catal.* **2017**, *60* (8).

(122) Blackmond, D. G. Kinetic Profiling of Catalytic Organic Reactions as a Mechanistic Tool. *J. Am. Chem. Soc.* **2015**, *137* (34).

(123) Zhao, Y.; Adiyeri Saseendran, D. P.; Huang, C.; Triana, C. A.; Marks, W. R.; Chen, H.; Zhao, H.; Patzke, G. R. Oxygen Evolution/Reduction Reaction Catalysts: From In Situ Monitoring and Reaction Mechanisms to Rational Design. *Chem. Rev.* **2023**, *123* (9).

(124) Ye, S.; Yang, S.; Ni, L.; Qiu, W.; Xu, Q. Mechanism and Kinetic Study of Paal-Knorr Reaction Based on in-Situ MIR Monitoring. *Spectrochim. Acta – A: Mol. Biomol. Spectrosc.* **2022**, *264*.

(125) Wang, J.; Horwitz, M. A.; Dürr, A. B.; Ibba, F.; Pupo, G.; Gao, Y.; Ricci, P.; Christensen, K. E.; Pathak, T. P.; Claridge, T. D. W.; Lloyd-Jones, G. C.; Paton, R. S.; Gouverneur, V. Asymmetric Azidation under Hydrogen Bonding Phase-Transfer Catalysis: A Combined Experimental and Computational Study. *J. Am. Chem. Soc.* **2022**, *144* (10).

(126) Grabow, K.; Bentrup, U. Homogeneous Catalytic Processes Monitored by Combined in Situ ATR-IR, UV-VIS, and Raman Spectroscopy. *ACS Catal.* **2014**, *4* (7).

(127) Madani, A.; Pieber, B. In Situ Reaction Monitoring in Photocatalytic Organic Synthesis. *ChemCatChem*. **2023**, *15* (7).

(128) Sung, S.; Sale, D.; Braddock, D. C.; Armstrong, A.; Brennan, C.; Davies, R. P. Mechanistic Studies on the Copper-Catalyzed N-Arylation of Alkylamines Promoted by Organic Soluble Ionic Bases. *ACS Catal.* **2016**, *6* (6).

(129) Bharti, S. K.; Roy, R. Quantitative 1H NMR Spectroscopy. *TrAC, Trends Anal. Chem.* **2012**, *35*.

(130) Khalil, A.; Kashif, M. Nuclear Magnetic Resonance Spectroscopy for Quantitative Analysis: A Review for Its Application in the Chemical, Pharmaceutical and Medicinal Domains. *Crit. Rev. Anal. Chem.* **2023**, *53* (5).

(131) Jaworski, J. N.; Kozack, C. V.; Tereniak, S. J.; Knapp, S. M. M.; Landis, C. R.; Miller, J. T.; Stahl, S. S. Operando Spectroscopic and Kinetic Characterization of Aerobic Allylic C-H Acetoxylation Catalyzed by Pd(OAc)2/4,5-Diazafluoren-9-One. *J. Am. Chem. Soc.* **2019**, *141* (26).

(132) Wright, A. M.; Pahls, D. R.; Gary, J. B.; Warner, T.; Williams, J. Z.; Spring, S. M.; Allen, K. E.; Landis, C. R.; Cundari, T. R.; Goldberg, K. I. Experimental and Computational Investigation of the Aerobic Oxidation of a Late Transition Metal-Hydride. *J. Am. Chem. Soc.* **2019**, *141* (27).

(133) Rollet, A. L.; Bessada, C. NMR Studies of Molten Salt and Room Temperature Ionic Liquids. In *Annual Reports on NMR Spectroscopy*; 2013; Vol. 78.

(134) Bramham, J. E.; Golovanov, A. P. Sample Illumination Device Facilitates in Situ Light-Coupled NMR Spectroscopy without Fibre Optics. *Chem. Commun.* **2022**, *5* (1).

(135) Seegerer, A.; Nitschke, P.; Gschwind, R. M. Combined *In Situ* Illumination-NMR-UV/Vis Spectroscopy: A New Mechanistic Tool in Photochemistry. *Angew. Chem. Int. Ed.* **2018**, *57* (25).

(136) Lakhani, P.; Modi, C. K. Shaping Enantiochemistry: Recent Advances in Enantioselective Reactions via Heterogeneous Chiral Catalysis. *Mol. Catal.* **2023**, *548*.

(137) Butler, R. N.; Coyne, A. G. Organic Synthesis Reactions On-Water at the Organic-Liquid Water Interface. *Org. Biomol. Chem.* **2016**, *42*.

(138) Murzin, D.; Salmi, T. Mass Transfer and Catalytic Reactions. In *Catalytic Kinetics*; Elsevier Science: Amsterdam, 2006; pp 341–481.

(139) Naik, S. D.; Doraiswamy, L. K. Phase Transfer Catalysis: Chemistry and Engineering. *AIChE J.* **1998**, *44* (3), 612–646.

(140) A., P.; Wang, M.-L. Role of Mass Transfer in Phase Transfer Catalytic Heterogeneous Reaction Systems. In *Mass Transfer - Advanced Aspects*, 1st ed.; IntechOpen, 2011; pp 685–708.

(141) Beach, N. J.; Knapp, S. M. M.; Landis, C. R. A Reactor for High-Throughput High-Pressure Nuclear Magnetic Resonance Spectroscopy. *Rev. Sci. Instrum.* **2015**, *86* (10).

(142) Huang, Y.; Cao, S.; Yang, Y.; Cai, S.; Zhan, H.; Tan, C.; Lin, L.; Zhang, Z.; Chen, Z. Ultrahigh-Resolution NMR Spectroscopy for Rapid Chemical and Biological Applications in Inhomogeneous Magnetic Fields. *Anal. Chem.* **2017**, *89* (13).

(143) Foroozandeh, M.; Morris, G. A.; Nilsson, M. PSYCHE Pure Shift NMR Spectroscopy. *Chem. Eur. J.* **2018**, *24* (53).

(144) Zangger, K. Pure Shift NMR. *Prog. Nucl. Magn. Reson. Spectrosc.* **2015**, *86–87*, 1–20.

(145) Jones, A. B.; Lloyd-Jones, G. C.; Uhrín, D. SHARPER Reaction Monitoring: Generation of a Narrow Linewidth NMR Singlet, without X-Pulses, in an Inhomogeneous Magnetic Field. *Anal. Chem.* **2017**, *89* (18).

(146) Davy, M.; Dickson, C. L.; Wei, R.; Uhrín, D.; Butts, C. P. Monitoring Off-Resonance Signals with SHARPER NMR - the MR-SHARPER Experiment. *Analyst* **2022**, *147* (8).

(147) Davy, M. J. Development of Pure Shift NMR Spectroscopy Techniques through Novel Acquisition Schemes, Ph.D. Dissertation, University of Bristol, Bristol, UK, 2021.

(148) Morris, G. A.; Barjat, H.; Horne, T. J. Reference Deconvolution Methods. *Prog. Nucl. Magn. Reson. Spectrosc.* **1997**, *31* (2–3), 197–257.

(149) Metz, K. R.; Lam, M. M.; Webb, A. G. Reference Deconvolution: A Simple and Effective Method for Resolution Enhancement in Nuclear Magnetic Resonance Spectroscopy. *Con. Magn. Reason.* **2000**, *12* (1).

(150) Keller, W. D.; Lusebrink, T. R.; Sederholm, C. H. NMR Spectrum of 3-Chlorothietane, an Example of Complete NMR Spectral Analysis by Computer Techniques. *J. Chem. Phys.* **1966**, *44* (2).

(151) Ernst, R. R.; Freeman, R.; Gestblom, B.; Lusebrink, T. R. Detection of Very Small N.M.R. Spin Coupling Constants by Resolution Enhancement. *Mol. Phys.* **1967**, *13* (3).

(152) Taquin, J. Line-Shape and Resolution Enhancement of High-Resolution F.T.N.M.R. in an Inhomogeneous Magnetic Field. *Rev. Phys. Appl. (Paris)* **1979**, *14* (6), 669–681.

(153) Wouters, J. M.; Petersson, G. A. Reference Lineshape Adjusted Difference NMR Spectroscopy. I. Theory. *J. Magn. Reason.* **1977**, *28* (1).

(154) Rougeot, C.; Situ, H.; Cao, B. H.; Vlachos, V.; Hein, J. E. Automated Reaction Progress Monitoring of Heterogeneous Reactions: Crystallization-Induced Stereoselectivity in Amine-Catalyzed Aldol Reactions. *React. Chem. Eng.* **2017**, *2* (2).

(155) Daponte, J. A.; Guo, Y.; Ruck, R. T.; Hein, J. E. Using an Automated Monitoring Platform for Investigations of Biphasic Reactions. *ACS Catal.* **2019**, *9* (12).

(156) Christensen, M.; Adedeji, F.; Grosser, S.; Zawatzky, K.; Ji, Y.; Liu, J.; Jurica, J. A.; Naber, J. R.; Hein, J. E. Development of an Automated Kinetic Profiling System with Online HPLC for Reaction Optimization. *React. Chem. Eng.* **2019**, *4* (9).

(157) Sato, Y.; Liu, J.; Ndukwe, I. E.; Silva Elipe, M. V.; Griffin, D. J.; Murray, J. I.; Hein, J. E. Liquid/Liquid Heterogeneous Reaction Monitoring: Insights into Biphasic Suzuki-Miyaura Cross-Coupling. *Chem. Catal.* **2023**, *3* (7).

(158) Baumann, W.; Mansel, S.; Heller, D.; Borns, S. Gas Bubbles in the Tube: An Easy Way to NMR Investigate Reactions with Gases in the Liquid Phase. *Magn. Reson. Chem.* **1997**, *35*, 701–706.

(159) De Souza Braga Neto, A.; Rigaud, B.; Mériguet, G.; Rollet, A. L.; Sirieix-Plénet, J. Efficient Method for in Situ Agitation of Liquids Directly inside NMR Spectrometer. *MethodsX* **2023**, *11*.

(160) Gao, Y.; Hall, A. M. R.; Fohn, N. A.; King, E. J.; Mitchell, L. A. L.; Steedman, G. A.; Lloyd-Jones, G. C. A Simple Device for Automated Mixing of Heterogeneous Solid-Liquid Reactions During In-Situ Monitoring by NMR Spectroscopy. *Eur. J. Org. Chem.* **2024**, *27* (20).

(161) Kasat, G. R.; Pandit, A. B. Review on Mixing Characteristics in Solid-Liquid and Solid-Liquid-Gas Reactor Vessels. *Can. J. Chem. Eng*. **2005**, *83* (4), 618–643.

(162) Paul, E. L.; Atiemo-Obeng, V. A.; Kresta, S. M. *Handbook of Industrial Mixing: Science and Practice;* John Wiley & Sons, 2003.

(163) Khajeh, M.; Bernstein, M. A.; Morris, G. A. A Simple Flowcell for Reaction monitoring by NMR. *Magn. Reson. Chem.* **2010**, *48* (7).

(164) Grosu, S.; Rodriguez-Guerrero, C.; Grosu, V.; Vanderborght, B.; Lefeber, D. Evaluation and Analysis of Push-Pull Cable Actuation System Used for Powered Orthoses. *Front. Robot. AI* **2018**, *5*.

(165) Affrossman, S.; Murray, J. P. Kinetics of the Hydrolysis in 1: 3 Water–Acetone of Aliphatic Esters Having Substituents in the Alkyl Group, Catalysed by an Acid Resin or an Acidic Solution. *J. Chem. Soc. B* **1968**, 579–582.

(166) Colon, I.; Kelsey, D. R. Coupling of Aryl Chlorides by Nickel and Reducing Metals. *J. Org. Chem.* **1986**, *51* (14).

(167) Nelson, T. D.; Crouch, R. D. Cu, Ni, and Pd Mediated Homocoupling Reactions in Biaryl Syntheses: The Ullmann Reaction. In *Organic Reactions*; 2004.

(168) Fohn, N. A.; Gao, Y.; Sproules, S.; Nichol, G. S.; Brennan, C. M.; Robinson, A. J.; Lloyd-Jones, G. C. Kinetics and Mechanism of PPh_3/Ni-Catalyzed, Zn-Mediated, Aryl Chloride Homocoupling: Antagonistic Effects of $ZnCl_2/Cl^-$. *J. Am. Chem. Soc.* **2024**.

(169) Vicini, A. C.; Pupo, G.; Ibba, F.; Gouverneur, V. Multigram Synthesis of N-Alkyl Bis-Ureas for Asymmetric Hydrogen Bonding Phase-Transfer Catalysis. *Nat. Protoc*. **2021**, *16*, 5559–5591.

(170) Vicini, A. C.; Alozie, D. M.; Courtes, P.; Roagna, G.; Aubert, C.; Certal, V.; El-Ahmad, Y.; Roy, S.; Gouverneur, V. Scalable Synthesis of (*R,R*)-N,N-Dibenzyl-2-Fluorocyclohexan-1-Amine with CsF under Hydrogen Bonding Phase-Transfer Catalysis. *Org. Process Res. Dev.* **2021**, *25* (12).

(171) Wei, R.; Hall, A. M. R.; Behrens, R.; Pritchard, M. S.; King, E. J.; Lloyd-Jones, G. C. Stopped-Flow ^{19}F NMR Spectroscopic Analysis of a Protodeboronation Proceeding at the Sub-Second Time-Scale. *Eur. J. Org. Chem.* **2021**, *2021* (17), 2331–2342.

(172) Mostert, S.; Mentz, W.; Petzer, A.; Bergh, J. J.; Petzer, J. P. Inhibition of Monoamine Oxidase by 8-[(Phenylethyl)Sulfanyl]Caffeine Analogues. *Bioorg. Med. Chem.* **2012**, *20* (24).

(173) Orrell, K. G.; Šik, V.; Stephenson, D. Quantitative Investigations of Molecular Stereodynamics by 1D and 2D NMR Methods. *Prog. Nucl. Magn. Reson. Spectrosc.* **1990**, *22* (2), 141–208.

(174) Broghammer, F.; Brodbeck, D.; Junge, T.; Peters, R. Cooperative Lewis Acid-Onium Salt Catalysis as Tool for the Desymmetrization of Meso-Epoxides. *Chem. Commun.* **2017**, *53* (6).

(175) Mio, M. J.; Kopel, L. C.; Braun, J. B.; Gadzikwa, T. L.; Hull, K. L.; Brisbois, R. G.; Markworth, C. J.; Grieco, P. A. One-Pot Synthesis of Symmetrical and Unsymmetrical Bisarylethynes by a Modification of the Sonogashira Coupling Reaction. *Org. Lett.* **2002**, *4* (19).

(176) Kupče, Ē.; Boyd, J.; Campbell, I. D. Short Selective Pulses for Biochemical Applications. *J. Magn. Reson. B* **1995**, *106* (3).

(177) Wang, J.; Horwitz, M. A.; Dürr, A. B.; Ibba, F.; Pupo, G.; Gao, Y.; Ricci, P.; Christensen, K. E.; Pathak, T. P.; Claridge, T. D. W.; Lloyd-Jones, G. C.; Paton, R. S.; Gouverneur, V. Asymmetric Azidation under Hydrogen Bonding Phase-Transfer Catalysis: A Combined Experimental and Computational Study. *J. Am. Chem. Soc.* **2022**, 144 (10), 4572–4584.

(178) Jagtap, S. Heck Reaction—State of the Art. *Catalysts.* **2017**, 7 (9), 267.

(179) Beller, M.; Kühlein, K. First Heck Reactions of Aryldiazonium Salts Using Heterogeneous Catalysts. *Synlett 1995*, 1995 (5), 441–442.

(180) Houpis, I. N.; Shilds, D.; Nettekoven, U.; Schnyder, A.; Bappert, E.; Weerts, K.; Canters, M.; Vermuelen, W. Utilization of Sequential Palladium-Catalyzed Cross-Coupling Reactions in the Stereospecific Synthesis of Trisubstituted Olefins. *Org. Process. Res. Dev.* **2009**, 13 (3), 598–606.

(181) Walker, S. D.; Borths, C. J.; Divirgilio, E.; Huang, L.; Liu, P.; Morrison, H.; Sugi, K.; Tanaka, M.; Woo, J. C. S.; Faul, M. M. Development of a Scalable Synthesis of a GPR40 Receptor Agonist. *Org. Process. Res. Dev.* **2011**, 15 (3), 570–580.

(182) Mpungose, P. P.; Vundla, Z. P.; Maguire, G. E. M.; Friedrich, H. B. The Current Status of Heterogeneous Palladium Catalysed Heck and Suzuki Cross-Coupling Reactions. *Molecules* **2018**, 23 (7), 1676.

(183) Bechtloff, B.; Jüsten, P.; Ulrich, J. The Kinetics of Heterogeneous Solid-Liquid Reaction Crystallizations - An Overview and Examples. *Chem. Ing. Tech.* **2001**, 73 (5), 453–460.